BULGARIAN CHEMICAL COMMUNICATIONS

IN MEMORIAM

Prof. Eng. Georgi A. Peev, *PhD, DSc*

(1935-2020)

Professor Georgi Peev (1935-2020) is an outstanding Bulgarian scientist who has taught chemical engineering to students at different Universities for many years. Combining erudition, precision, creativity and exceptional passion for science, until the last breath he impressed his colleagues and the general public with his infinite energy and the quality of his research. Dedicated to science but also a person with a broad general culture, fresh sense of humour and poetic talent, he bequeathed to us many wonderful poems. Prof. Peev was a truly noble man with an exceptional sense of responsibility towards his family and friends, his colleagues and his country.

His career began back in 1958 when he graduated with honours (summa cum laude) from the department of "Technology of Inorganic Materials" at the University of Chemical Technology and was recruited as a senior chemist at DPM-Rosen in Bourgas and later as a Head of laboratory at DIP-Hemus.

His scientific career began in October 1960 at the High Institute of Chemical Technology (nowadays University of Chemical Technology and Metallurgy) where he won the competition for assistant professor lectureship of Processes and Apparatus in the Chemical Industry. For many years Professor Peev was a valuable member of the Department of Processes and Apparatus in the Chemical Industry (nowadays Department of Chemical Engineering) where he gradually undertook the positions of lecturer, senior lecturer, associate professor (from 1972 onward) and a full professor (from 1982 onward). He was a longstanding member of the faculty and the Academic Council of the University and Dean of the Faculty of Organic Technology (from 1979 onward, two terms). As such he introduced two new advanced courses at the University of Chemical Technology, namely Chemical Engineering and Biotechnology, which nowadays are highly popular among students. As Vice Rector of education (1987-1989) Professor Peev dedicated his time and efforts to introducing widely computer-based methods of education and new approaches toward student exams.

During the period 1984-1993 he was elected twice Head of Department of Chemical Technology and Materials in Microelectronics at University of Chemical Technology and Metallurgy. During this period, he won a TEMPUS European grant - SJEP-07316-94 Development and Spreading of Education in Material Science and Technology. This project entirely supervised by Professor Peev laid the foundations of modern course of Technology of Materials and Material Science at University of Chemical Technology and Metallurgy which is still in the ongoing curriculum. A second European project - CME-03618-97 Dissemination of Education in Materials Science and Technology submitted again by Professor Peev as a Coordinator and Scientist in charge was funded by the EC and provided wide opportunities for collaboration and students and staff exchange between universities in Romania, North Macedonia and Bulgaria.

For his contribution towards university education and science he was awarded the prestige medal "St. St. Cyril and Methodius" in 1985. His dedication to science and education continued even after his retirement in 2001.

During his long-term career as a University Professor he prepared and delivered the following courses:

Processes and Apparatus in Chemical Technology at the: University of Chemical Technology and Metallurgy – (for many years); University Asen Zlatarov Burgas (2 years); Southwest University Blagoevgrad – 12 years; Military Academy Georgi Rakovski – 4 years.

Fluid Mechanics – at the University of Chemical Technology and Metallurgy (for many years); at the Faculty of Chemistry – Sofia University St. Kliment Ohridski – 3 years.

Heat and Mass Transfer in Non-Newtonian liquids - at the University of Chemical Technology and Metallurgy (for many years).

Reactors in Biotechnology - at the University of Chemical Technology and Metallurgy (for 2 years)

Chemical Technology – at the Southwest University Blagoevgrad (3 years).

As Deputy Head of the Academy of Environmental Protection he delivered a course on Mechanical, Extraction and Evaporation Methods for Waste Waters Treatment.

Professor Peev's professional development includes many achievements amongst which are – PhD thesis - awarded PhD in 1970; DSc thesis - awarded DSc in 1980; international specializations at Bradford University - United Kingdom and Volgograd State Technical University – Russia. Professor Peev is an author and co-author of 11 patents and an impressive number of publications in various areas of chemical engineering science - more than 120 papers mainly in high impact factor peer-reviewed international journals, and more than 720 citations of his works by international authors including in books, handbooks and encyclopaedias.

Professor Peev's passion for science and his broad research interests resulted in considerable scientific achievements in many areas of Chemical Engineering including – Rheology of Non-Newtonian Fluids; Processes of liquid-liquid extraction, dissolution, absorption, solid-liquid extraction, and also in the areas of Biotechnology, Environmental Protection (Waste waters and gaseous treatment); Chemical Vapor Deposition;

Membrane technology – in particularly – Organic solvent nanofiltration.

Professor Peev was a Coordinator and Scientist in charge of multiple projects with industry; European projects – TEMPUS (2 projects) and multiple projects financed *via* The Bulgarian National Science Fund, MINISTRY OF EDUCATION AND SCIENCE OF BULGARIA.

As an Emeritus Professor he submitted, got funded and coordinated the participation of UCTM in another international project under EC FP7 program - EC Maria Curie project Industry-Academia network under FP7, IMETI-PIAP-GA-2008-218068 /Implementation of membrane technology to industry, involving 7 European partners from Academia and Industry. One of the papers published by Prof. Peev under this project was awarded first place by Elsevier as the most cited paper of Chemical Engineering Research and Design journal for the period 2011-2012.

Professor Peev was an invited lecturer at many international conferences, a permanent reviewer for 7 scientific journals and a member of organising committees of multiple international forums. He was an active member of the Bulgarian Scientific Union and the Bulgarian Chemists Union.

Professor Peev is considered the founder of research on implementation of membrane processes for separation and concentration of biologically active substances from natural extracts using organic solvent nanofiltration membranes in Bulgaria.

This issue of Bulgarian Chemical Communications is in memory of Professor Peev – A man who devoted himself to chemical engineering

A.Nikolova
D. Peshev

Ultrasound-assisted extraction of thymol from *Zataria multiflora* Boiss.: Optimization by response surface methodology and comparison with conventional Soxhlet extraction

N. Alirezapour, A. Haghighi Asl*, M. Khajenoori

School of Chemical, Gas and Petroleum Engineering, Semnan University, Iran

This study focuses on the extraction of thymol from the medicinal plant *Zataria multiflora* Boiss. leaves by ultrasound technique and by the Soxhlet method. The effects of several parameters including time, temperature, solid-to-solvent ratio, ultrasound power, and duty cycle on the amount of thymol extracted from *Z. multiflora* leaves were investigated and optimized using response surface methodology (RSM). The optimized circumstances for the extraction were as follows: extraction time 30 min, temperature 34°C, ultrasound power 340 watts, solid-to-solvent ratio 1:35 g/ml and duty cycle 20%. The amount of thymol extracted at the above-mentioned parameters was 7.195 mg/g which was consistent with the predicted amount of 7.31 mg/g by RSM. Furthermore, Peleg's model was used to predict the kinetics of ultrasound-assisted extraction (UAE) of thymol. The results proved the good agreement of the model with the experimental data. Moreover, UAE was found to be more efficient, faster and easier to manipulate compared to the Soxhlet method. To the best of researchers' knowledge, this is the first report on the extraction of essential oils from *Z. multiflora* using ultrasound technique.

Keywords: Ultrasound-assisted extraction; *Zataria multiflora* Boiss.; Thymol; Response surface methodology.

INTRODUCTION

Oil essences are natural aromatic compounds of plants, which are widely utilized in perfume, pharmaceutical and food industries [1]. Essences are commonly prepared from different parts of fresh or dried herbal organs. These compounds have physiological and medicinal properties, the most common and well known of which are antimicrobial, antifungal, analgesic and antioxidant [2].

Essences, especially Thyme essential oils, are useful in preserving food. *Z. multiflora* Boiss. (Shirazi Thyme) is one of the species of thyme classified in the Mints group. It belongs to the southwestern part of Asia, Iran, and is the most important species of thymes after *Thymus vulgaris L.,* [2, 3]. Thymol is the most important compound of this plant, which accounts for 30-70% of oil essence. It is a white aromatic substance with antibacterial and antiseptic properties [4]. Anti-bacterial feature of thymol is the cause for thyme essence's anti-bacterial trait. For this reason, it is commonly used in mouthwashes and toothpastes. In addition, thymol can reduce bacterial resistance to antibiotics and eliminate fungi and it can function as a general medical disinfector [5-7]. Thymol's anti-fungal effect has led to its use in alcoholic solutions to treat fungal infections, as well as intestinal infections in the United States [8]. Also Middle

Easters consume *Z. multiflora* to reduce and remove internal parasites [9].

In recent years, in order to obtain valuable compounds from plants and to prevent their decomposition, various technologies have been evaluated to provide an efficient extraction method. Conventional methods are divided into three categories, namely distillation, solvent extraction and cold compression [10]. These methods, which have been repeatedly used since long time ago, have many drawbacks. The mechanism of the aforementioned methods is that when the plant is placed in the solvent, the compounds enter the solvent due to the concentration gradient introduced inside and outside. This process sometimes takes up to a month to reach the equilibrium [11]. Other disadvantages of these methods include degradation of volatile and unsaturated compounds, low yield, and solvent toxicity [2].

Today, for the extraction of various compounds in various industries, such as food industry, ultrasound technology is used, the driving force of which is the cavitation phenomenon [12, 13]. In this process, due to the oscillation of the bubbles and their collapse, the solvent faster targets the plant's material and causes an increase in the temperature. This results in tissue destruction, as well as increased extraction efficiency and mass transfer rate [14-16].

Many studies have been carried out on the extraction of oil essences from *Z. multiflora*. For instance, the comparison made between the supercritical fluid extraction of *Z. multiflora* essence

---
* To whom all correspondence should be sent:
E-mail: ahaghighi@semnan.ac.ir

and steam distillation revealed that although supercritical fluid extraction takes less time than the steam distillation (half an hour vs. 1 hour), the amount of extracted thymol equals 44.6% of that in steam distillation. Furthermore, the resulting mixtures from the two methods slightly differed, but with the supercritical fluid method under higher pressure and by changing extraction parameters, there will be better selectivity while compared to steam distillation [17]. Additionally, Golmakani and Rezaei (2008) have illustrated that the extraction of *Z. multiflora* essence by Microwave-Assisted hydrodistillation (MAHD) took less time than hydrodistillation (1 hour *vs*. 4 hours) [3]. In addition, the resulting mixtures have been more similar, but the MAHD method yielded a higher output and costed less. Moreover, using a subcritical water extraction method carried out by Khajenoori *et al.* (2009) [2] it has been shown that this method is more efficient and provides more valuable oxygenated compounds of essence compared to Soxhlet extraction (a conventional method used in the present study). Considering all above mentioned approaches, it is demonstrated that despite novel methods' supremacy over the traditional ones, these differences are insignificant.

According to the literature review on extraction by ultrasound method and the importance of thymol, which is a valuable compound of *Z. multiflora*, the main objective of the present study is to evaluate the efficiency of this method and calculate the maximum amount of extracted substances. In order to optimize the extraction of the valuable compound of *Z. multiflora* by ultrasound waves, the effective parameters including temperature, power, time, duty cycle and solvent-to-solid ratio were investigated by a 3-level and 5-factor Box–Behnken design of response surface methodology (RSM). In addition, since minimizing time and expenses is an all-the-time concern in industry, kinetic studies play a significant role in extraction processes allowing predicting of their speed. Despite the broad considerations about ultrasound-assisted extraction, there is a huge gap concerning the kinetics of this process. That is why the kinetics of extracting thymol out of *Z. multiflora* using ultrasound-assisted Peleg's equation, and the RSM model were investigated. Eventually, the obtained results were compared with those of the Soxhlet method.

MATERIALS AND METHODS

Plant materials and chemicals

In June 2017, dried leaves of *Z. multiflora* were procured from the Bamu area in the Zagros mountains located in Fars province (south of Iran). Moisture was measured according to a standard method using a laboratory oven at 150 ºC to reach constant weight at 5 wt% (dry basis). Samples were powdered using a mill and were kept in a refrigerator until use. *n*-Hexane (extra pure) was purchased from Daejung (Korea). Thymol (Roth, Datteln, Germany) was used as a reference for identifying the thymol peak.

Soxhlet extraction

Soxhlet extraction of 10 g *Z. multiflora* powder was done for 6 hours using 250 ml of hexane. The extract was filtered using a filter paper under vacuum (Whatman No. 1, England) and was centrifuged at 3600 rpm for 15 min. Hexane was then removed by a rotary evaporator (HAHNSHIN, Korea) at 35 °C. The extracted essential oil was transferred into a volumetric flask, using three rinses of hexane prior to the GC. **10** µl of naphthalene solution was added to the concentrate as an internal standard and 1 µl of this mixture was directly injected into the GC (Fig. 1).

Ultrasound-assisted extraction (UAE)

To extract thymol from *Z. multiflora* leaves, ultrasound equipment (Adecco, Iran) (Fig. 2) was used at a constant frequency of 20 KHz. It has a capacity of 800 watts with a titanium alloy flat tip probe (diameter 13 mm). Based on the design of the experiment (DOE), 5 g of *Z. multiflora* powder was mixed with different volumes of hexane. The effects of solid-to-solvent ratio (1:15-1:35 g/ml), temperature (20-40 ºC) extraction time (15-30 min), ultrasound power (150-350 watt), and duty cycle (20-80%), were examined. After conducting every test, the sample obtained was filtered and prepared for GC analysis, as mentioned in the previous section.

Experimental design

In order to optimize the conditions for the extraction of thymol from *Z. multiflora*, the response surface method was used as an effective statistical model. This allows determination of the favorable conditions of UAE. As previously reported, studying the effects of variables at the same time is more efficient than when the variables are separately examined [18, 19].
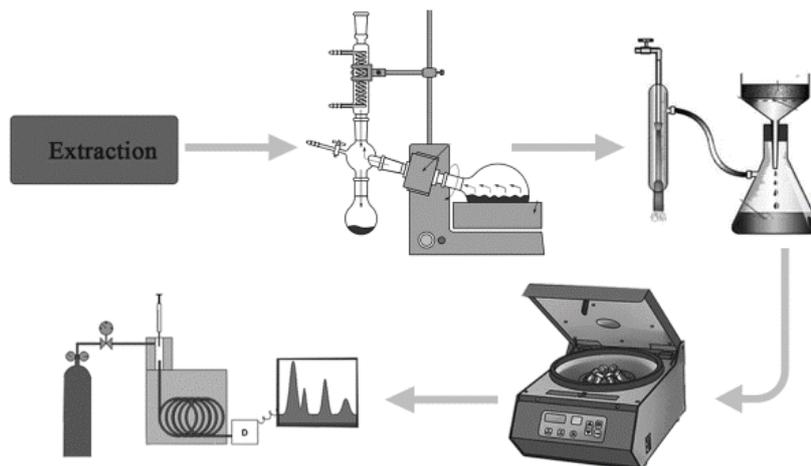
Figure 1. Schematic representation of the ultrasound-assisted extraction process.

Box-Behnken is a spherical design of the RSM family, which includes one central point and several midpoints [20, 21]. A 5-factor 3-level version of Box-Behnken design was used to attain the highest efficiency. One of the features of this model is minimizing the effect of kinematic errors. The plan includes 46 tests. To prevent errors and minimize the effects of unexpected changes, the tests were done randomly. The five independent variables include solid-to-solvent ratio (X1), temperature (X2), extraction time (X3), ultrasound power (X4), and duty cycle (X5) (Table 1), while the amount of thymol extracted is the response variable. The entire test design matrix is shown in Table 2. Statistical analysis was performed on the experimental data and the thymol response obtained from different extractions of the *Z. multiflora* was entered into a quadratic polynomial equation (Equation 1). This equation shows the relationship between the dependent and independent variables:

$$Y = b_0 + \sum_{i=1}^{n} b_i X_i + \sum_{\substack{i=1 \\ j>i}}^{n-1} \sum_{j=2}^{n} b_{ij} X_i X_J + \sum_{i=1}^{n} b_{ii} X_i^2 \qquad (1)$$

where Y is the thymol response expected, b_0 is a constant of model, b_i denote linear coefficients, b_{ij} are interactive coefficients, b_{ii} are second-order coefficients, and X_i and X_j are independent variables. Statistical significance of this equation was investigated by analysis of variance (ANOVA). Furthermore, the quality of the fitted model and significance of each coefficient were evaluated through R^2 and P-value, respectively.
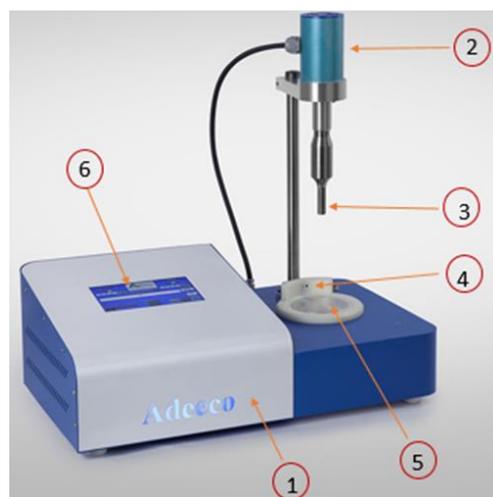
Figure 2. Ultrasound equipment: (1) ultrasonic generator; (2) ultrasonic transducer; (3) titanium probe; (4) IR sensor; (5) temperature control module; (6) touch screen.

Table 1. Coding of independent variables and their levels for Box-Behnken design (BBD).

Parameter	Symbol	Levels		
		-1	0	1
Solid-to-solvent ratio (g/ml)	X_1	1:15	1:25	1:35
Temperature (ºC)	X_2	20	30	40
Extraction time (min)	X_3	15	22.5	30
Ultrasonic power (watts)	X_4	150	250	350
Duty cycle (%)	X_5	20	50	80

Table 2. Box-Behnken design matrix with experimental results.

Run	Parameters					Response
	Ratio X_1	Temp. X_2	Time X_3	Power X_4	Duty cycle X_5	Y Thymol value (mg/g)
1	15.00	30.00	22.50	350.00	50.00	4.83
2	25.00	30.00	22.50	150.00	20.00	5.257
3	25.00	30.00	15.00	350.00	50.00	5.63
4	15.00	30.00	22.50	250.00	80.00	4.96
5	25.00	30.00	22.50	150.00	80.00	5.49
6	35.00	30.00	15.00	250.00	50.00	4.9
7	25.00	30.00	22.50	250.00	50.00	5.01
8	15.00	30.00	30.00	250.00	50.00	4.63
9	15.00	40.00	22.50	250.00	50.00	4.345
10	35.00	30.00	22.50	250.00	80.00	5.1
11	25.00	20.00	30.00	250.00	50.00	4.48
12	25.00	20.00	22.50	250.00	80.00	4.45
13	35.00	20.00	22.50	250.00	50.00	4.24
14	25.00	30.00	22.50	350.00	20.00	6.13
15	25.00	30.00	30.00	350.00	50.00	5.86
16	25.00	30.00	15.00	250.00	20.00	4.5
17	15.00	20.00	22.50	250.00	50.00	3.3
18	25.00	40.00	22.50	150.00	50.00	5.09
19	25.00	30.00	22.50	250.00	50.00	4.985
20	35.00	30.00	22.50	250.00	20.00	5.64
21	25.00	30.00	22.50	250.00	50.00	4.98
22	25.00	20.00	22.50	150.00	50.00	3.99
23	25.00	40.00	22.50	350.00	50.00	5.56
24	25.00	20.00	22.50	250.00	20.00	4.36
25	25.00	30.00	30.00	150.00	50.00	5.46
26	35.00	40.00	22.50	250.00	50.00	4.84
27	25.00	40.00	22.50	250.00	80.00	5.315
28	25.00	30.00	30.00	250.00	20.00	6.2
29	25.00	30.00	30.00	250.00	80.00	5.01
30	25.00	40.00	15.00	250.00	50.00	4.95
31	25.00	30.00	15.00	250.00	80.00	5.85
32	25.00	40.00	22.50	250.00	20.00	5.22
33	35.00	30.00	22.50	150.00	50.00	4.78
34	25.00	30.00	22.50	250.00	50.00	4.99
35	25.00	30.00	22.50	350.00	80.00	5.95
36	25.00	30.00	22.50	250.00	50.00	5.02
37	25.00	30.00	15.00	150.00	50.00	4.79
38	15.00	30.00	22.50	150.00	50.00	4.63
39	25.00	30.00	22.50	250.00	50.00	4.995
40	15.00	30.00	22.50	250.00	20.00	4.35
41	15.00	30.00	15.00	250.00	50.00	4.15
42	25.00	20.00	22.50	350.00	50.00	4.86
43	35.00	30.00	22.50	350.00	50.00	5.95
44	35.00	30.00	30.00	250.00	50.00	5.34
45	25.00	40.00	30.00	250.00	50.00	5.12
46	25.00	20.00	15.00	250.00	50.00	3.85

Gas chromatographic analysis

The compounds of *Z. multiflora* were proven by means of gas chromatography (GC). Separation and identification of the essence compounds were carried out by a GC (ACME 6100, 6000 series) equipped with a TRB-WAX capillary column (60 m × 0.25 mm i.d.) with a 0.5 μ m polyethylene glycol film. Helium (Roham Gas Co, Iran, 99.999%) was used as the carrier gas with a constant flow rate of 1 ml/min. Both detector and injector temperatures were set at 250 ºC. The volume of each sample injected was 1.0 µl and the total time spent for each injection was 20 min. The GC temperature program was as follows: oven temperature increased from 60 ºC to 200 ºC with a rate of 4 ºC/min using splitless mode injection. Naphthalene was used as internal

standard, and the amount reported as relative peak area is based on this (peak area of thymol to peak area of naphthalene (p_T/p_N)).

Extraction kinetics

Mathematic modeling can play a crucial role in designing extraction processes, predicting their rate, and controlling them. So different empirical and semi-empirical equations have been presented such as the Peleg's equation [22]. This equation is widely used for solid-liquid extraction of biological material out of plants. The present model equation is as follows:

$$C_t = C_0 + \frac{t}{K_1 + K_2 t} \tag{2}$$

where C_t is the concentration of thymol at time t (mg of thymol/g of dried sample), K_1 is Peleg's initial rate constant (min.g of dried sample/mg of thymol), $K_2 t$ is Peleg's capacity constant (g of dried sample/mg of thymol) and C_0 is initial concentration of thymol.

Supposing that the initial concentration of thymol is zero, as a fresh solvent is used, the equation will be as follows:

$$C_t = \frac{t}{K_1 + K_2 t} \tag{3}$$

According to the equation, K_1 and K_2, respectively, the slope and the intercept of $\frac{1}{C_t}$ *vs.* $\frac{1}{t}$ are calculated.

RESULTS AND DISCUSSION

Analysis of response surface methodology

Extracting thymol from *Z. multiflora* was done using UAE, entering the resulting lab data in the quadratic equation. The significance of model coefficients and compatibility of the design have also been reviewed using variance analysis (ANOVA). The obtained results show that linear coefficients for all independent variables as well as all quadratic coefficients are significant. The observed value for all effects is as $p < 0.0001$. The results also demonstrate a significant interaction between independent variables, except for temperature, and duty cycle, time and solvent-to-solid ratio. Eliminating non-significant variables, the final predictive equation coefficients will be as follows (Table 3).

Variance analysis was conducted for the regression equation, validating the model using ANOVA. This analysis proves that while F-value=1048.54 ($p < 0.0001$), the model is significant.

Table 3. Predicted equation coefficients.

Factor	Coefficient
b_0	-7.98027
A=time	+0.19606
B=temp	+0.42275
C=power	-0.013230
D=s/s	+0.21840
E=duty cycle	+0.060220
time * temp	-1.53333E-003
time * power	-1.46667E-004
time * duty cycle	-2.82222E-003
temp * power	-1.00000E-004
temp * s/s	-1.11250E-003
power * s/s	+4.16667E-006
power * duty cycle	+2.42500E-004
s/s * duty cycle	-3.44167E-005
time^2	-9.58333E-004
temp^2	+1.33444E-003
power^2	-4.87438E-003
s/s^2	+3.69813E-005
duty cycle^2	-3.19521E-003

Model quality was assessed using the R^2 correlation coefficient and the value for lack-of-fit. P-value of lack-of-fit ($p > 0.05$) and F-value show that this factor which is used to verify model adequacy is not significant. Correlation coefficient equaled 0.9788 (R^2), signifying that more than 97.8 % of the changes are explainable by the regulated model. R^2_{adj} coefficient which shows the level of correlation between predicted and real attained values equaled 0.9479. In addition, the predicting functions of the model considering variance inflation factor (VIF) have not been decreased (< 4). Given the results discussed above, it is arguable that this model describes well the connection between response and the independent variables.
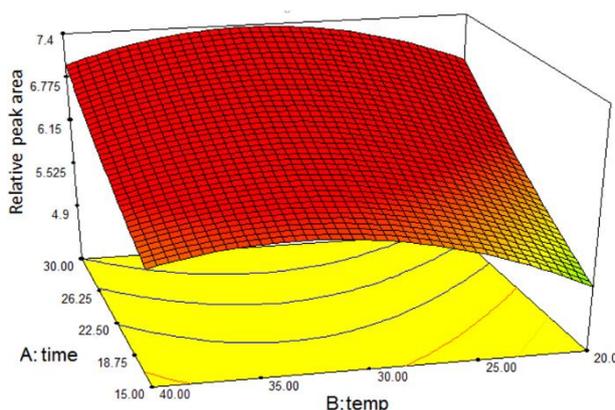
Effects of independent variables on extraction yield in the RSM model

The effects of various parameters on total thymol content in the form of three-dimensional graphs of surface response are depicted in Figs. 3a-3h. In each diagram, changes in the amount of the extracted thymol, shown in the vertical axis, are displayed in terms of the two specific variables, which are independent of each other, while other parameters are kept constant. Fig. 3a depicts the interactive effect of temperature and time. As it can be seen, the highest amount of thymol is extracted at 30 ºC and 30 min. The effects of time and power are shown in Fig. 3b. It is seen that in the first 30 min, with increasing power (about 350 watts), the amount of thymol extracted is still rising. In another study, (see Fig. 3c) the interaction between duty cycle and time parameters was examined. In fact, a decrease in duty cycle from 80 to 20% causes an increase in thymol
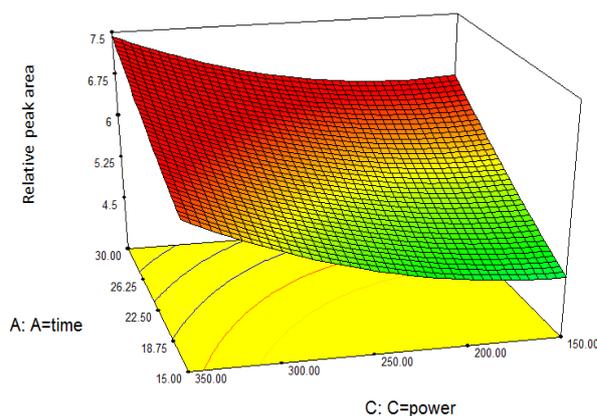
extraction. Furthermore, the interaction between power and temperature is shown in Fig. 3d. As seen, with increasing power, more thymol is extracted.

In this way, with increasing power from 150 to 250 w, the slope of the extraction is negligible; however, from 250 to 350 w, the process of increasing extraction is considerable. Thymol extraction changes in terms of temperature variations are such that before reaching 30º, the extraction is initially increased and then reduced. The interactive effect of temperature and solid-to-solvent ratio is shown in Fig. 3e. As can be seen, by increasing the solvent-to-solid ratio, thymol extraction is increased, so that in the range of 1:15 to 1:30, the slope of the extraction increase is greater than that at 1:30 to 1:35. In fact, increasing the solid-to-solvent ratio from 1:30 to 1:35 has no significant effect on thymol extraction. The effect of the interaction between power and the solid-to-solvent ratio is shown in Fig. 3f. As it can be seen, the extraction of thymol increases with increasing both the power and the solid-to-solvent ratio.

In Figs. 3g and 3h, respectively, the interactive effects of power and of the solid-to-solvent ratio with the duty cycle are shown. Again, with the reduction of the duty cycle, and the increase in the power and the solid-to-solvent ratio, the extraction of thymol from *Z. multiflora* is increased. The striking feature of the graphs is that with increasing power from 250 to 350 watts and reducing the duty cycle from 50 to 20%, the extraction is significant. The results show that all five parameters studied on the thymol extraction are effective.

Figure 3(b). Response surface analysis for thymol from *Z. multiflora* with ultrasound-assisted extraction: time and power.
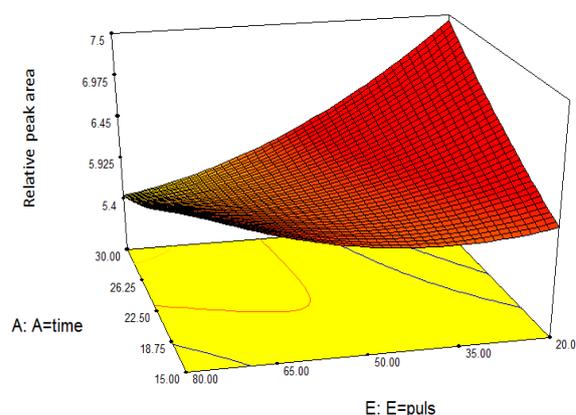
Figure 3(c). Response surface analysis for thymol from *Z. multiflora* with ultrasound-assisted extraction: time and duty cycle.
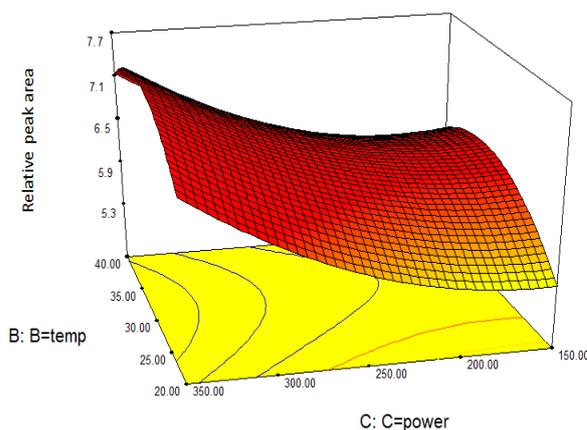
Figure 3(d). Response surface analysis for thymol from *Z. multiflora* with ultrasound-assisted extraction: temperature and power.

Figure 3(a). Response surface analysis for thymol from *Z. multiflora* with ultrasound-assisted extraction: time and temperature.
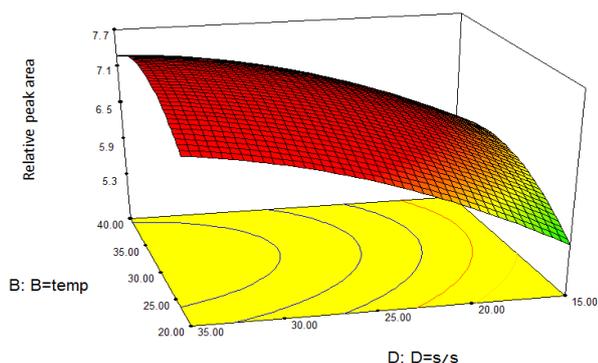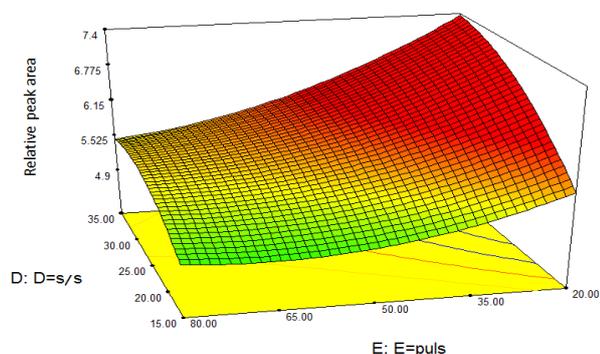
Figure 3(e). Response surface analysis for thymol from *Z. multiflora* with ultrasound-assisted extraction: temperature and solvent-to-solid ratio.
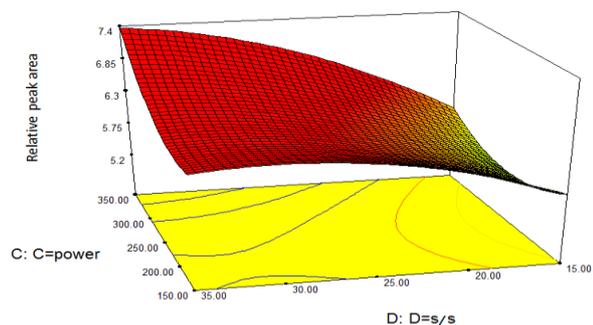
Figure 3(f). Response surface analysis for thymol from *Z. multiflora* with ultrasound-assisted extraction: power and solid-to-solvent ratio.
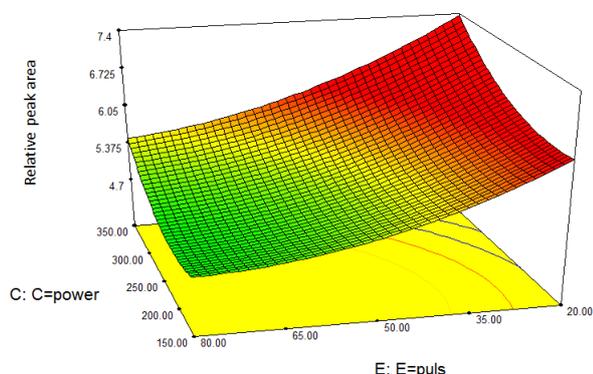
Figure 3(g). Response surface analysis for thymol from *Z. multiflora* with ultrasound-assisted extraction: power and duty cycle.

Figure 3(h). Response surface analysis for thymol from *Z. multiflora* with ultrasound-assisted extraction: solvent-to-solid ratio and duty cycle.

Validation of the predicted value

Different methods have been used to optimize the process. The most common method is to change one of the parameters while retaining the rest in constant levels. Such methods are time consuming, difficult, and impractical due to numerous experiments needed, moreover that these methods do not guarantee optimal situations in most cases [18, 23, 24]. As a result of this, RSM predictions have been applied and are known for attaining the best possible circumstances needed for maximum extraction efficiency. After designing the experiment, the predicted values were examined for results in optimal situation. According to the results, optimal conditions are as follows: time: 30 min, temperature: 34 ºC, ultrasound power: 340 watts, solid-to-solvent ratio: 1:35, and duty cycle: 20%. According to the optimal extraction conditions, the experimental amount of thymol achieved was 7.195 which was acceptable in comparison with the predicted value of 7.31 using the polynomial model.

Therefore, it can be concluded that the model developed can successfully predict thymol extraction from *Z. multiflora* using UAE.

Comparison of ultrasound-assisted extraction with Soxhlet extraction method

To represent the benefits of utilizing UAE over conventional methods, a comparison was done between the results of this experiment and those of the Soxhlet extraction method. As shown in table 4, the amount of thymol obtained using UAE for 30 min, is higher than that using Soxhlet extraction for 6 hours, so the efficiency of the former is higher. The reason for this is the destruction of plant's cellular texture due to the use of high-frequency waves which cause cavitation resulting in mass transfer to the solvent. Finally, having spent less time, showing higher efficiency, lower temperature, and less consumption of solvent compared to traditional methods such as Soxhlet extraction, UAE proves to be more efficient [25-27].

Effect of time

Since minimizing costs has always been an important point regarded by industries, in this experiment, the kinetics of the process of extracting thymol under optimal circumstances (described in the former section), was analyzed. In this section, six experiments with constant values for temperature, power, solid-to-solvent ratio, and duty cycle parameters were done while varying the time parameter.

Table 4. Comparison of Soxhlet extraction with UAE.

Extracting method	Temperature	Time	Thymol value, (mg/g)
Ultrasonic	34 °C	30 min	7.195
Soxhlet	68 °C	6 h	5.216

Empirical and predicted results concerning the amount of extracted thymol are demonstrated in Fig. 4, in which the bullets are the empirical results and the line shows the values predicted by the Peleg's equation. It can be observed that the model can perform the prediction well. Using the data obtained from the previous section, we have analyzed the RSM predicting procedure. Based on the results, it can be perceived that more than 85% of the extracted thymol is obtained during the first 20 min (Fig. 5). Also, the findings of this section show that the model resulted from the RSM can predict the process of thymol extraction with proper accuracy.
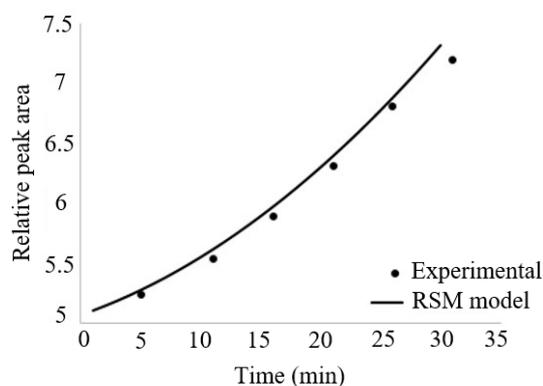
Figure 4. Experimental data of thymol extraction from *Z. multiflora* and comparison with Peleg model.
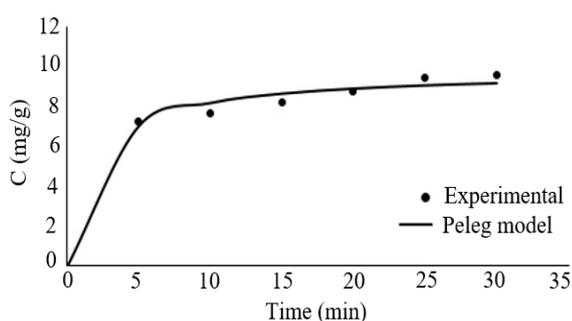
Figure 5. Kinetic extraction of thymol from *Z. multiflora* and comparison with RSM model.

CONCLUSION

In this study, UAE was successfully applied using RSM to extract thymol from *Z. multiflora* Boiss. Five factors, namely time, temperature, power, solid-to-solvent ratio, and duty cycle were examined and it was revealed that these parameters have significant effects on thymol extraction. The optimal circumstances were reported to be 30 min, 34 °C, 340 watts of power, solid-to-solvent ratio of 1:35 g/ml, and a duty cycle equaling 20% with extracted thymol value of 7.195 mg/g as compared to the predicted value of 7.31 mg/g using the polynomial model. This shows that this model works well in predicting the amount of thymol extracted from *Z. multiflora*. In comparison to the Soxhlet method, it is shown that UAE significantly reduces the time of extraction (30 min *vs.* 6 h). Reviewing the kinetic extraction, it was shown that under optimal conditions it is possible to extract more than 85% of thymol in less time; moreover, Peleg's model showed a good agreement with the experimental results. Generally, it can be argued that as a modern technology, UAE is an appropriate and easy way of extracting essences.

REFERENCES

1. J. M. Roldán-Gutiérrez, J. Ruiz-Jiménez, M. L. De Castro, *Talanta*, **75**(5), 1369 (2008).
2. M. Khajenoori, A. Haghighi Asl, F. Hormozi, M. H. Eikani, H. Noori Bidgoli, *Journal of Food Process Engineering*, **32**(6), 804 (2009).
3. M. T. Golmakani, K. Rezaei, *European Journal of Lipid Science and Technology*, **110**(5), 448 (2008).
4. M. Khajenoori, A. Haghighi Asl, M. H. Eikani, *J. Essent. Oil-Bear. Plants*, **18**, 1165 (2015).
5. G. Zarrini, Z. B. Delgosha, K. M. Moghaddam, A. R. Shahverdi, *Pharmaceutical Biology*, **48**(6), 633 (2010).
6. K. Palaniappan, R. A. Holley, *International Journal of Food Microbiology*, **140**(2), 164 (2010).
7. G. Nieto, *Medicines*, **4**(3), 63 (2017).
8. J. A. Ferrell, The rural school and hookworm disease (No. 20). US Government Printing Office (1914).
9. S. K. Marwat, M. A. Khan, I. U. Bhatti, *Pakistan Journal of Nutrition*, **8**(9), 1472 (2009).
10. M. Vinatoru, T. J. Mason, I. Calinescu, *TrAC Trends in Analytical Chemistry*, **97**, 159 (2017).
11. M. Vinatoru, M. Toma, O. Radu, P. I. Filip, D. Lazurca, T. J. Mason, *Ultrasonics Sonochemistry,* **4**(2), 135 (1997).
12. B. Verhaagen, D. F. Rivas, *Ultrasonics Sonochemistry*, **29**, 619 (2016).
13. W. Lauterborn, C. D. Ohl, *Ultrasonics Sonochemistry*, **4**(2), 65 (1997).
14. P. Kiełczyński, M. Szalewski, A. Balcerzak, K. Wieja, A. Malanowski, R. Kościesza, R. Tarakowski, A. J. Rostocki, R. M. Siegoczyński, *Ultrasonics*, **54**, 2134 (2014).

15. J. Jordens, B. Gielen, L. Braeken, T. Van Gerven, *Chemical Engineering and Processing: Process Intensification*, **84**, 38 (2014).
16. B. H.Samani, H. Zareiforoush, Z. Lorigooini, B. Ghobadian, S. Rostami, E. Fayyazi, *Fuel*, **168**, 22 (2016).
17. H.Ebrahimzadeh, Y. Yamini, F. Sefidkon, M. Chaloosi, S. M. Pourmortazavi, *Food Chemistry*, **83**(3), 357 (2003).
18. A. DeLean, P. J. Munson, D. Rodbard, American *Journal of Physiology-Endocrinology & Metabolism,* **235**(2), E97. (1978).
19. M. A. M. García, M. Á. P. Lage, *PLoS One*, **8**(4), e61391 (2013).
20. Y. Ding, J. Zheng, X. Xia, T. Ren, J. Kan, *LWT-Food Science and Technology*, **67**, 206 (2016).
21. M.Khajenoori, A. Haghighi Asl, M. H. Eikani, *J. Essent. Oil-Bear. Plants*. **18**, 1310 (2015).
22. M. Peleg, *Journal of Food Science*, **53**(4), 1216 (1988).
23. M. A. Prieto, J. A. Vázquez, M. A. Murado, *Food Chemistry*, **167**, 299 (2015).
24. G. E. Box, J. S. Hunter, W. G. Hunter, Statistics for experimenters, in: Wiley Series in Probability and Statistics, Hoboken, NJ, Wiley. 2005.
25. M. D. Esclapez, J. V. García-Pérez, A. Mulet, J. A. Cárcel, *Food Engineering Reviews*, **3**(2), 108 (2011).
26. U.Vajic, J. Grujic-Milanovic, J. Živkovic, K. Šavikin, D. Gođevac, Z. Miloradovic, B. Bugarski, N. Mihailovic-Stanojevic, *Industrial Crops and Products*, **74,** 912 (2015).
27. L. Wang, C. L. Weller*, Trends in Food Science & Technology,* **17**(6), 300 (2006).

Yield and chemical composition of oil isolated from Algerian *Hypericum perforatum* L. as influenced by the plant habitat, harvesting date and plant organ

M. Abdelhadi[1,2], A. Hassani[1], H. Boudjella[3], S.-A. Rezzoug[4]*

[1]*Laboratoire des molécules bio actives et valorisation de la biomasse, Ecole Normale Supérieure, BP 92 Kouba, Algiers, Algeria*
[2]*Département des Energies Renouvelables, Faculté de Technologie - Université de Blida, 1. Route de Soumaa, BP 270, Blida, Algeria*
[3]*Laboratoire de Biologie des Systèmes Microbiens, Ecole Normale Supérieure, BP 92, Kouba, Algiers, Algeria*
[4]*LaSIE, UMR CNRS 7356, Université de La Rochelle – Faculté des Sciences et Technologies, Bâtiment Marie Curie, Avenue Michel Crépeau, 17042 La Rochelle, France*

The changes in volatile oil chemical composition of *Hypericum perforatum* L. from Algeria were investigated according to harvesting locality and period, as well as plant organ. Aerial parts were collected from three different regions (Algiers, Medea and Blida), from 2009 to 2014. All oils were extracted by hydrodistillation and analyzed by GC and GC/MS. The main compounds were α-pinene and 2-methyl-octane. The flower and fruit parts gave the best yield (0.30%- 0.39%) and the highest concentrations of monoterpenes (32.7% to 35.9% of isolated oil) and non-oxygenated compounds (89.6% - 90.2%), while leave oils contained the highest concentrations of sesquiterpenes (52.9% to 59.5%) and oxygenated compounds (40.5% to 48.4%). From the aerial parts, the best oil yields were obtained for Blida (2014) and Medea (2011) samples. Volatile oil isolated from aerial partsof the Blida-2014 sample was examined for its antimicrobial activity.

INTRODUCTION

The genus *Hypericum* (Hypericaceae) is widely distributed through temperate regions and depicted by approximately 450 species [1]. *Hypericum perforatum* L., commonly known as St. John's wort, is used in traditional medicine since ancient times [2]. Nowadays, most of the investigations on *Hypericum perforatum* L. focused on the anti-depressant properties of the isolated substances [3], as well as on their anti-inflammatory, antimicrobial and anti-proliferative activities [4]. Research also concerned the bioactive compound classes including naphthodianthrone derivatives (hypericin and pseudohypericin), acylated phloroglucinol derivatives (hyperforin and adhyperforin), and flavonoids such as quercetin, quercitrin, hyperoside, rutin, kaempferol, biapigenin, and amentoflavone [5]. Numerous scientific studies investigated the chemical composition [6] or the changes in chemical composition of volatile oils of *Hypericum perforatum* L. extracted by hydrodistillation [7]. The influence of geographical distribution on the chemical composition of oils was also scrutinized [8, 9]. Beside this, other aspects [10-12] were examined as the phenological cycle [13] and the type of plant organ [14-16]. However, little research is reported on the effect of the seasonal variations on the chemical composition of the essential oil except Smelcerovic *et al.* [17] who investigated the changes in chemical composition of *Hypericum perforatum* L. oil extracted by steam distillation during three nonconsecutive years, namely 1998, 2001 and 2003. Moreover, *Hypericum perforatum* L. from the Mediterranean area as Turkey [18], Tunisia [19], France [20] or Greece [21] was investigated, but to the best of our knowledge, no study was reported on Algerian species apart from our recent study [22]. The present contribution concerns the influence of (a) three harvesting localities in the north of Algeria (Algiers, Blida and Medea); (b) the harvesting year between 2009 and 2014 (year per year); (c) the plant organ (whole aerial part, leaves, flowers-fruits) on the chemical composition of volatile oils extracted by hydrodistillation. This study also characterizes the antimicrobial activity. The originality of the work is the simultaneous study of the influence of harvesting period, harvesting region and the plant organ subjected to hydrodistillation on the composition of volatile oil.

EXPERIMENTAL

Plant material and chemicals

To investigate the effect of plant habitat,

---

* To whom all correspondence should be sent:
E-mail: sarezzou@univ-lr.fr

Table 1. Basic characterization of sites where *Hypericum perforatum* L. (aerial parts) was collected. All harvesting areas have a warm and temperate climate.

Locality	Blida	Algiers	Medea
Altitude(m)	260	200	486
Latitude	36°28'12" N	36°44'11" N	36°24'46" N
Longitude	2°49'39" E	3°02'31" E	2°45'14" E
Mean annual temperature (°C)	17.9	17.7	14.4

Hypericum perforatum L. was collected from three different places in north Algeria (Algiers, Blida and Medea) (Table 1). For Blida locality, samples were typically harvested every year between May 25th and June 4th (flowering period) for six consecutive years (2009-2014). The plant samples were identified by the Head of the Herbarium of the National Institute of Agronomy (INA, El-Harrach-Algiers-Algeria) and dried in a shaded room at a temperature not exceeding 25 °C. Herbal scissors were used during the harvesting process and to separate leaves and flowers-fruits.

Hydrodistillation apparatus and procedure

Conventional hydrodistillation apparatus (Clevenger-type) according to the *European Pharmacopeia* [23] was employed. A quantity of 300 g of *Hypericum perforatum* for 1.5 to 2 L of distilled water was used during 240 min hydrodistillation from the first drop of distillate until the raw material has been completely exhausted. The essential oil was collected, dried over anhydrous sodium sulfate, and stored in a dark place at 4°C for further analysis. Each extraction was performed at least three times, and a standard deviation was calculated. The extraction yield was calculated according to eq. 1.

$$\text{Extraction yield (\%)} = \left(\frac{\text{mass of collected oil}}{\text{mass of dry material}}\right) \times 100$$
(eq.1)

GC and GC-MS identification

GC analysis of volatile compounds was carried out using Hewlett Packard HP6890 series II system coupled to an ionization flame detector (FID). The compounds were separated on a HP-5 capillary column (5 % phenylmethylpolysiloxane, 30 m × 0.25 mm i.d., 0.25 μm film thickness). The gas chromatographic parameters were set up as follows: initial temperature 60°C for 5 min, rate 2°C min^{-1}, final temperature 250°C, held for 10 min; injector and transfer line temperatures were set at 250°C. Nitrogen was used as the carrier gas at a flow rate of 1 mL/min; injection volume, 1 μL; split ratio, 1:20. The percent compositions were determined from electronic integration measurements using flame ionization detection (FID, 250°C). GC–MS

analysis was carried out using Varian 3900 chromatograph coupled to a Saturn 2100T mass spectrometer. Samples were analyzed on a fused-silica capillary column. The non-polar column was HP-5MS (30 m × 0.25 mm × 0.25 μm film thickness). The spectra were obtained using the following conditions: carrier gas helium at a flow rate of 1 mL/min; split mode 1:20; 1 μL injection volume; injection temperature 250°C. The oven temperature program was: 60°C for 5 min, rate 2°C/min to 250°C and held for 10 min. The ionization mode used was electronic impact at 70 eV. The constituents were identified by comparison of their GC linear retention indices (RI), determined with reference to a homologous series of C_5–C_{32} n-alkanes. The identification was confirmed by computer matching against commercial libraries (Wiley and NIST) and by comparison with mass spectra from literature data [24].

Antimicrobial activity

The antimicrobial activity of the essential oil obtained by hydrodistillation of the plant sample collected at Blida in 2014 was examined by the paper disk diffusion method [25] and by determination of the minimal inhibitory concentrations (MICs) according to the recommendations of the European Committee on Antimicrobial Susceptibility Testing [26]. The antibacterial activity of *Hypericum perforatum* L. essential oil was tested against four bacterial strains including Gram-positive bacteria: *Micrococcus luteus* ATCC 9314 (Ml), *Bacillus subtilis* ATCC 6633 (Bs), *Staphylococcus aureus* CIP 7625 (Sa) and the Gram-negative bacterium: *Klebsiella pneumoniae* (CIP 8291 (Kp1). The antifungal activity of the essential oil was investigated using two filamentous fungi: *Fusarium oxysporum albedinis* CURZA (Foa) and *Aspergillus carbonarius* M333 (Ac), and two yeast strains: *Candida albicans* (Ca) and *Candida glabrata* (Cg). All tests were performed in triplicate. The microorganisms were regenerated twice before use in the manipulations by culturing bacterial strains on Mueller-Hinton, and fungal strains on Sabouraud agar. The paper disk diffusion assay was

performed according to the protocol described by Lass-Flörl *et al.* [27] The minimal inhibitory concentrations (MICs) were determined by the conventional agar dilution method described in [27].

Statistical considerations

The data were analyzed using Statgraphics software (Centurion version). One-way analysis of variance with p≤0.05 was performed to identify significant differences among the different samples. All results presented are the mean of triplicate.

RESULTS AND DISCUSSION

Variability in oil chemical composition of Hypericum perforatum L.

Influence of the plant habitat. Samples of *Hypericum perforatum* L. aerial parts from three different regions, Blida, Algiers and Medea (Table 2), collected during 2011 season and subjected to hydrodistillation, were investigated. From Table 2, it is clear that there is a significant difference in the obtained yields and percentages of chemical classes, namely total oxygenated, total non-oxygenated monoterpenes and sesquiterpenes according to the plant habitat. The oil yields varied from 0.049 % for the Blida sample to 0.136 % for the Medea sample. These values are in agreement with those of Pirbalouti *et al.* [28] for *Hypericum perforatum* L. oil extracted by hydodistillation from Iranian species and with those of Cossuta *et al.* [29] for Hungarian species isolated by supercritical fluid extraction. The more important compounds were: 2-methyl-octane (13.8 %), α-pinene (15.9 %), α-

amorphene (14.6 %) for the Blida sample and α-pinene (11.04 %), α-amorphene (16.6 %) and n-tetradecanol (10.7 %) for the Algiers sample. For the Medea sample the major compounds were 2-methyl-octane (12.1 %), α-pinene (22.03 %) and β-selinene (10.9%). α-Pinene appears to be one of the most abounded compounds in the oils originating from the three investigated regions while α-amorphene is the major compound in the volatile oil isolated from Blida and Algiers samples.

On the other hand, the concentration of 2-methyl-octane is higher in the Blida and Medea samples. It should be noted that there seems to be a relation between the altitude of the harvesting region and the proportion of α-pinene in the extracted oil. The content of α-pinene was proportional to the altitude of the sample collection site. The higher the altitude, the higher amounts of α-pinene were detected (Table 1). An inverse trend was observed for n-tetradecanol and α-amorphene for which the proportions in the extracted oil decreased with altitude. Table 2 also indicates that volatile oil extracted from Algiers sample is rich in sesquiterpenes (62 %) and oxygenated compounds (31 %) and that those from both Blida and Medea are rich in sesquiterpenes (44.4 % and 48.9 %, respectively). Hajdari *et al.* [12] showed that the altitude of the harvesting locality has an effect on oil composition. Marrelli *et al.* [30] tested the phototoxicity of Italian (south Apennine) *Hypericum perforatum* L. extracts harvested in several altitudes.
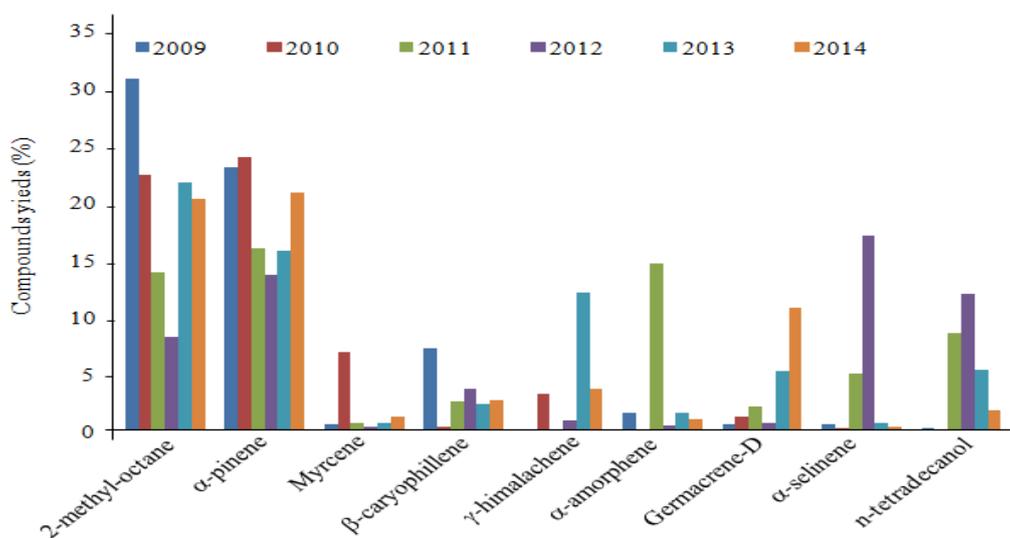
Table 2. Percentage of classes of compounds identified in the volatile oils from *Hypericum perforatum* L. (aerial parts) originated from the three investigated regions.

Classes of chemical compounds/ regions	Blida	Algiers	Medea
Total monoterpenes	21.2	12.6	25.7
Hydrogenated monoterpenes	20.4	12.3	25.5
Oxygenated monoterpenes	0.9	0.3	0.2
Total sesquiterpenes	44.4	61.7	49.0
Hydrogenated sesquiterpenes	34.0	45.8	39.9
Oxygenated sesquiterpenes	10.4	15.8	9.1
Total non-terpenes	34.2	24.2	25.1
Oxygenated non-terpenes	11.9	15.0	6.7
Non oxygenated non-terpenes	22.4	9.3	18.4
Total oxygenated compounds	23.1	31.1	16.0
Total non-oxygenated compounds	76.7	67.4	83.8
Total identified%	99.8	98.5	99.7
Yield %	0.049	0.055	0.136

The values in the table represent the relative percentages (relative content %) against the total percentage of identified compounds. All results presented are the mean of triplicate. The standard deviations were systematically less than 1%.

The results showed that the best antiradical and antioxidant activities are obtained for the plants collected at an altitude of 370 m, which is close to the height (486 m) of the collection site of our Medea samples.

Xenophontos *et al.* [31] pointed out a great difference in total hypericins content according to altitude of habitat. A clear trend showing an increase of the total hypericins content with increasing altitude was observed.

Influence of harvesting year between 2009 and 2014. Volatile oil composition of *Hypericum perforatum* L. aerial parts from the locality of Blida, according to six consecutive years (2009-2014) are presented in Table 3 as classes of compounds. The obtained yields, ranging between 0.050 % and 0.131 %, are in agreement with those obtained by Helmja *et al.* [11] for Estonian species (from 0.068 % to 0.188 %). Year per year, the major compounds are displayed in Table 4. It should be stated that two compounds are systematically present with high proportions: 2-methyl-octane and α-pinene apart from 2012, where 2-methyl-octane is present in lower proportions (Figure 1). Non-terpene compounds were also identified. For example, in 2011 and 2012, the oil contained between 22.4 % and 15.9 % of alkanes and between 9.5 % and 12.3 % of alcohols, between 34.2 % and 29 % of non-terpenes, for the two years, respectively.

Table 3 shows that the six oils are rich in sesquiterpenes (from 25.3 to 52.2%), especially hydrogenated sesquiterpenes (from 17.5 to 42.9%), as well as in non-oxygenated compounds (from 76.3 to 89.2%) while they are poor in oxygenated monoterpenes (from 0.4% to 3.2%). These ranges are in agreement with those of Hosni *et al.* [9] who studied the extraction of Tunisian *Hypericum perforatum* L. oil harvested in 2006. The obtained oil was composed from 38.3% of hydrogenated sesquiterpenes and 20.5% of hydrogenated monoterpenes. As in our study, the authors reported low proportions in oxygenated monoterpenes (2%) and oxygenated sesquiterpenes (3.6%). More recently, Hajdari *et al.* [12] pointed out low proportions in oxygenated monoterpenes (from 1.3 to 2.4%) in *Hypericum perforatum* L. essential oil originating from Kosovo.

Variability in the chemical composition according to the plant organ. To investigate the influence of plant part subjected to extraction on oil composition a study was conducted on two parts of the plant: leaves and flowers-fruits in 2011 for the localities of Medea (M) and Blida (B). As it was expected, the extraction of volatile oils from flowers-fruit gave a higher oil yield ranging from 0.3% to 0.4% with high proportions of α-pinene (24.6% - 28.9%) and 2-methyl-octane (13.6% - 15.3%). Akhbari *et al.* [14] also reported a high proportion in α-pinene (11.34 %) for the oil extracted from fruits of Iranian *Hypericum perforatum* L. species together with α-amorphene (15.9%).

Table 3. Percentage of classes of compounds identified in volatile oils of *Hypericum perforatum* L. (whole aerial parts – region of Blida) obtained by hydrodistillation between 2009 and 2014

Classes of chemical compounds / years	2009	2010	2011	2012	2013	2014
Total monoterpenes	27.1	38.7	21.2	18.6	24.4	32.8
Hydrogenated monoterpenes	26.7	35.5	20.4	17.4	21.7	31.2
Oxygenated monoterpenes	0.4	3.2	0.9	1.2	2.7	1.6
Total sesquiterpenes	27.8	25.3	44.4	52.2	37.6	36.8
Hydrogenated sesquiterpenes	20.1	17.5	34.0	42.9	31.6	32.2
Oxygenated sesquiterpenes	7.7	7.7	10.4	9.3	6.0	4.6
Total non-terpenes	44.2	34.1	34.2	29.0	36.3	29.4
Oxygenated non-terpenes	3.6	1.2	11.9	13.0	8.2	3.7
Non oxygenated non-terpenes	40.6	32.9	22.4	16.0	28.1	25.7
Total oxygenated compounds	11.6	12.1	23.1	23.5	16.9	9.8
Total non-oxygenated compounds	87.6	85.9	76.7	76.3	81.4	89.2
Total identified %	99.2	98.1	99.8	99.8	98.2	99.0
Yield %	0.050	0.048	0.049	0.082	0.064	0.131

The values in the table represent the relative percentages (relative content %) against the total percentage of identified compounds. All results presented are the mean of triplicate. The standard deviations were systematically less than 1%.

Table 4: Major identified compounds in volatile oils extracted from *Hypericum perforatum* L. between 2009 and 2014.

Year	Major compounds
2009	2-Methyl-octane (30.67%),α-Pinene (23.01%),β-Caryophyllene (7.20%)
2010	2-Methyl-octane (22.32%),α-Pinene (23.83%),Myrcene (6.81%)
2011	2-Methyl-octane (13.79%),α-Pinene (15.89%), α-Amorphene (14.59%)
2012	α- Pinene (13.65%), α-Selinene (16.98%), n-Tetradecanol(11.9%)
2013	2-Methyl-octane (21.67%),α-Pinene (15.74%), γ-Himachalene (12.053%)
2014	2-Methyl-octane (20.21%),α-Pinene (20.77%),Germacrene-D (10.768%)

Figure1. Main compounds identified in volatile oils from *Hypericum perforatum* L. (aerial parts) between 2009 and 2014.

Table 5. Percentage of classes of compounds identified in volatile oils from *Hypericum perforatum* L. Leaves-B and flowers-fruit-B are plants that originated from Blida and leaves-M and flowers-fruit-M that originated from Medea

Classes of chemical compounds /Organs	Leaves-B	Flowers & Fruits-B	Leaves-M	Flowers & Fruits-M
Total monoterpenes	7.6	32.7	3.6	36.0
Hydrogenated monoterpenes	6.9	32.2	3.3	35.3
Oxygenated monoterpenes	0.7	0.5	0.3	0.6
Total sesquiterpenes	53.0	41.6	59.5	37.0
Hydrogenated sesquiterpenes	36.4	36.1	39.8	31.2
Oxygenated sesquiterpenes	16.5	5.5	19.8	5.8
Total non-terpenes	34.9	24.1	32.5	25.7
Oxygenated non-terpenes	23.3	2.7	28.4	2.1
Non oxygenated non-terpenes	11.7	21.4	4.2	23.6
Total oxygenated compounds	40.5	8.7	48.4	8.6
Total non-oxygenated compounds	55.0	89.6	42.2	90.2
Total identified %	95.5	98.4	95.6	98.7
Yield %	0.062	0.39	0.067	0.301

The values in the table represent the relative percentages (relative content %) against the total percentage of identified compounds. All results presented are the mean of triplicate. The standard deviations were systematically less than 1%.

Oxygenated monoterpenes exhibited the lowest percentages whatever the plan organ considered (from 0.23% to 0.87%). This is in accordance with the results presented by Radusiene *et al.* [16] in which the oxygenated monoterpenes in oils isolated from flowers varied from 0.1% to 0.9 % and almost the same percentages (from traces to 0.9%) in oils from leaves. However, for sesquiterpene hydrocarbons, our results showed equivalent percentages in the two plant parts (from 31.2 % to 39.8%) while according to Radusiene *et al.* [16] they were higher in flowers than in leaves.

Antimicrobial activity

The antimicrobial activity of *Hypericum perforatum* L. (aerial parts collected from Blida in 2014) oil was tested against eight microorganisms using the paper disc diffusion method and by determining the minimal inhibitory concentrations (MIC). The results (Table 6) showed that it exhibited weak antibacterial (against Gram-positive bacteria) and antifungal (against filamentous fungi) activities. The Gram-negative bacteria and the yeast strains tested were resistant. The MIC values of the collected oils against all target microorganisms were higher than 100 μg/ml, confirming the weak activity of the extracted oil. The weak antimicrobial activity of the volatile oils could be related to the presence of hydrogenated monoterpenes (31.23%) including α-pinene (20.77%) and *β*-pinene (3.19%). Moreover, oxygenated monoterpenes and 2-methyl-octane (20.21%) as alkane, as well as germacrene-D (10.77%) as hydrogenated sesquiterpene may explain the slight antimicrobial properties.

Some studies reported that a good antimicrobial activity was often related to the presence of oxygenated terpenes, especially oxygenated monoterpenes [32, 33]. These compounds were detected in small percentages (0.23 – 0.87%) in this study. The weak antimicrobial activity of essential oils isolated from *Hypericum perforatum* L. was reported by Rančić *et al.* [34] against seven strains of bacteria and six strains of fungi. The diameters of inhibition zones obtained against the Gram-positive bacteria were weak; 6 mm (1 μl) and 10 mm (5 μl) for *Micrococcus luteus*, 5 mm (1 μl) and 11 mm (5 μl) for *Staphylococcus aureus*, 4 mm (1 μl) and 9 mm (5 μl) against *Staphylococcus epidermidis*. In the same work, weak activity against four Gram-negative bacteria (*Escherichia coli. Pseudomonas tolaasii. Salmonella enteritidis. S. typhimurium*) was also reported. Values of inhibition zone diameters ranging between 7 and 12 mm were obtained. The authors attributed the weak antimicrobial activity of the *Hypericum perforatum* L. volatile oil to its chemical composition, which is characterized by the dominance of nonane (63.8%).

Table 6: Antimicrobial activity of *Hypericum perforatum* L. essential oil by the paper disc diffusion method and minimal inhibitory concentrations.

Microorganisms	Diameters of the inhibitions zones (mm)		Minimal inhibitory concentrations (μg/ml)	
Gram-positive bacteria	Volatile oil	Gentamicin	Volatile oil	Gentamicin
Micrococcus luteus	11	28	> 100	1
Bacillus subtilis	10	27	> 100	2
Staphylococcus aureus	13	27	> 100	2
Gram-negative bacteria				
Klebsiellapneumoniae	0	25	> 100	2
Filamentous fungi	Volatile oil	Amphotericin B	Volatile oil	Amphotericin B
Aspergillus carbonarius	9	15	> 100	2
Fusarium oxysporum albedinis	11	14	> 100	1.5
Yeasts	Volatile oil	Itraconazole	Volatile oil	Itraconazole
Candida albicans	0	18	> 100	1
Candida glabrata	0	16	> 100	1.5

Values of inhibition zones include the diameter of disk (6 mm).. All results presented are the mean of triplicate. The standard deviations were systematically less than 1%.

CONCLUSIONS

The aim of this study was to assess the variability of chemical composition of *Hypericum perforatum* L. essential oil according to plant organ subjected to extraction. 2-Methyl-octane and α-pinene were identified as the most abundant constituents. Considerable

habitat, to the harvesting year between 2009 and 2014 and to plant organ subjected to extraction. 2-Methyl-octane and α-pinene were identified as the most abundant constituents. Considerable

qualitative and quantitative variations were observed in the chemical profile of essential oils. The harvesting localization reflected by the altitude of the plant habitat favorized the global yield of essential oil. The monitoring of the essential oil composition between 2009 and 2014 indicated that the above compounds were predominantly present but according to the harvesting year other important compounds may be present, as α-selinene, α-amorphene and γ-himachalene.

As found in our previous study on Algerian species originated from Blida [35], these compounds greatly contribute to the antioxidant activity of *Hypericum perforatum* L. essential oil making this plant an important source of natural antioxidants.

REFERENCES

1. B. Karakashov, S. Grigorakis, S. Loupassaki, D. P. Makris, *J. Appl. Res. Med. Arom. Plant.*, **2,** 1 (2015).
2. A. C. Carvalho, G. Franklin, A. C. P. Dias, C. F. Lima, *Ind. Crop. Prod.,* **59**, 177 (2014).
3. N. Ramalhete, A. Machado, R. Serrano, T. E. Gomes, H. Mota-Filipe, O. Silva, *Ind. Crop. Prod.,* **82**, 29 (2016).
4. E. Bagdonaite, P. Mártonfi, M. Repčák, J. Labokas, *Ind. Crop. Prod.,* **35**, 302 (2012).
5. J. Zhao, W. Liu, J.-C. Wang, *Chem.Biodivers.,***12**, 309(2015).
6. M. R. Morshedloo, A. Ebadi, M. R. Fatahi-Moghaddam, D. Yazdani, *J. Med. Plants,* **11**, 218 (2012).
7. M. R. Morshedloo, A. Ebadi, F. Maggi, R. Fattahi, D. Yazdani, M. Jafari, *Ind. Crop. Prod*., **76**, 565 (2015).
8. F. S. Sharopov, I. S. Gulmurodov, W. N. Setzer, *J. Chem. Pharm. Res.,***2**, 284 (2010).
9. K. Hosni, K. Msaad̂a, M. Ben Taarît, T. Chahed, B. Marzouk, *Nat. Prod. Commun.,***6**, 1731(2011).
10. D. Mockute, G. Bernotiene, A. Judzentiene*, J. Essent. Oil Res*., **20**, 128 (2008).
11. K. Helmja, M. Vaher, T. Pussa, A. Orav, A. Viitak, T. Levandi, M. Kaljurand, *Nat. Prod. Res.,* **25**, 496 (2011).
12. A. Hajdari, B. Mustafa, D. Nebija, A. Kashtanjeva, J. Widelski, K. Glowniak, J. Novak, *Curr. Issues Pharm. Med. Sci*., **27**, 51 (2014)
13. I. Schwob, J. M. Bessiere, V. Masotti, J. Viano, *Biochem. Syst. Ecol*., **32**, 735 (2004).
14. M. Akhbari, H. Batooli, *Am-Eurasian J. Sustain. Agric.,* **3,** 107 (2009).
15. A. M. Kakhky, A. Rustaiyan, S. Masoudi, M. Tabatabaei-Anaraki, J. Aboly, *Essent. Oil Bear. Pl.,* **11**, 548 (2008).
16. J. Radusiene, A. Judzentiene, G. Bernotiene, *Biochem. Syst. Ecol*., **33**, 113 (2005).
17. A. Smelcerovic, M. Spiteller, A. P. Ligon, Z. Smelcerovic, N. Raabe, *Biochem. Syst. Ecol.,* **35** (2007).
18. T. Şerbetçi, N. Özsoy, B. Demirci, A. Can, Ş. Kültür, C. K. H. Başer, *Ind. Crop Prod*., **36**, 599 (2012).
19. Z. Rouis, A. Laamari, N. Abid, A. Elaissi, P. L. Cioni, G. Flamini, M. Aouni, *Parasitol. Res*., **112**, 9 (2013).
20. I. Schwob, J. M. Bessière, J. Viano, *CR. Biol*., **325**, 781 (2002).
21. E. M. Gioti, Y. C. Fiamegos, D. C. Skalkos, C. D. Stalikas, *Food Chem.,***117**, 398 (2009).
22. M. Abdelhadi, A. Meullemiestre, A. Gelicus, A. Hassani, S. A. Rezzoug, *Chem. Eng. Res. Des.,* **93**, 621 (2015).
23. *European Pharmacopeia*. (2012). http://online6. edqm.eu/ep705/; accessed December 2017.
24. R. P. Adams, Identification of essential oil components by gas chromatography/mass spectrometry, 4ᵗʰ edn., Allured Publishing Corporation, Carol Stream*, IL, 2007.
25. A. W. Bauer, W. M. M. Kirby, J. C. Sherris, M. Turk, *Am. J. Clin. Pathol*., **45**, 493 (1966).
26. EUCAST (2013). www.eucast.org. Web resource document accessed November 2017.
27. C. Lass-Flörl, A. Mayr, S. Perkhofer, G. Hinterberger, J. Hausdorfer, C. Speth, M. Fille, *Antimicrob. Agents Chemother*., **52**, 3637 (2008).
28. A. Gh. Pirbalouti, M. Fatahi-Vanani, L. Craker, H. Shirmardi, *Pharm. Biol.,* **52**, 175 (2014).
29. D. Cossuta. T. Vatai, M, Báthori, J, Hohmann, T. Keve, B. Simándi, *J. Food Process. Eng.,* **35**, 222 (2012).
30. M. Marrelli, F. Conforti, C. Toniolo, M. Nicoletti, G. Statti, F. Menichini, *Pharm. Biol.,* **52,** 909 (2014).
31. M. Xenophontos, I. Stavropoulos, E, Avramakis, E. Navakoudis, D. Dörnemann, K. Kotzabasis, *Planta Medica,* **74**, 1496 (2008).
32. V. Saroglou, P. D. Marin, A. Rancic, M. Veljic, H. Skalts, *Biochem. Syst. Ecol.,* **35**, 146 (2007).
33. A. P. Guedes, G. Franklin, M. Fernandes-Ferreira, *Photochem. Rev*., **11**, 127 (2012).
34. A. Rančić, M. Soković, J. Vukojević, A. Simić, P. Marin, S. Duletić-Lausěvić, D. Djoković, *J. Essent. Oil Res.,* **17**, 341 (2005).
35. M. Abdelhadi, Ph.D Thesis, High Normal School (ENS) of Kouba, Algiers, Algeria, 2016.

Influence of the sparger in a down flow jet loop reactor on the neutralization of alkaline solution by carbon dioxide absorption

G. Mugaishudeen*, K. Saravanan

Department of Chemical Engineering, Kongu Engineering College, Perundurai, Erode-638060, Tamil Nadu, India

The gas absorption efficiency in an absorption tower is largely affected by the gas residence time and the absorption rate. Because of some major setbacks of packed columns, spray towers, bubble columns and agitated vessels such as high power consumption in an agitated vessel, huge pressure drop in a packed column and poor absorption rate in a bubble column, an alternative in the form of jet loop reactor has been developed by the researchers. In the jet loop reactor, the liquid jet performs the functions of distributing and dispersing the gas as fine bubbles in the liquid and also in circulating the gas liquid mixture by momentum transfer. To investigate the performance of a jet loop sparged reactor with a straight-throat ejector, CO_2 absorption experiments in alkaline solution were performed. In our study, we analyzed the performance of a jet loop sparged reactor based on alkaline solution neutralization time and CO_2 absorption by changing influent flow rates of the alkaline solution. We observed that due to the presence of sparger down the straight-throat ejector, the neutralization time of the alkaline solution by CO_2 in the reactor was reduced up to 50% when compared with that in a reactor with a conventional straight-throat ejector. Also, the absorption of CO_2 and production of Na_2CO_3 in the reactor with sparger was higher by about 10-15% than those in a reactor with conventional straight-throat ejector.

Keywords: Jet loop reactor, Jet loop sparged reactor, Straight-throat ejector, CO_2 absorption, Neutralization time.

INTRODUCTION

The gas absorption efficiency in an absorption tower is largely affected by the gas residence time and the absorption rate [1]. In order to achieve maximum absorption efficiency developments were made on many types of absorption equipment such as packed column, spray tower, bubble column and agitated vessel which are used in various applications. Because of some major setbacks of the above said systems such as high power consumption in an agitated vessel, huge pressure drop in a packed column and poor absorption rate in a bubble column an alternative in the form of a jet loop reactor has been developed by the researchers.

Bohner [2] developed a jet loop reactor that can form very small bubbles to achieve a higher absorption rate and to improve the turbulence intensity of the gas-liquid absorption system. The liquid jet performs the functions of distributing and dispersing the gas as fine bubbles in the liquid and also in circulating the gas-liquid mixture by momentum transfer. The majority of investigations reported on jet loop reactors considered a central draft tube and two fluid nozzles installed at the bottom of the reactor [3, 4]. This type of construction was characterized by a jet or an annular nozzle in which the liquid jet enters the reactor space through a nozzle which is in the centre of a gas jet. The operational difficulties such as blockage of nozzle and lower residence time of the gaseous phase led to the development of a new jet propelled loop reactor where gas was introduced from the top of the reactor [5].

Raghavan [6] reported that using the Venturi ejector in a reactor for air-water system, internal circulation and turbulence in the main holding tank, as well as external circulation of the dispersion were found to be low when compared with the straight-throat ejector. Secondary dispersion in the main tank was less uniform. In addition, the opposing buoyancy force of the gas bubbles resulted in relatively low internal and external circulation of the dispersion. When Venturi ejectors are used in the reactor to handle an electrolytic aqueous solution, the bubble sizes are much smaller because of shrinkage and breakage of primary bubbles at the exit of the throat.

Various authors have investigated the absorption of CO_2 in an alkaline solution by a down flow jet loop reactor with two fluid nozzles and also two fluid swirl nozzles [7-11]. However, no systematic investigation of the CO_2 absorption characteristics of a jet loop sparged reactor with a down flow straight-throat ejector nozzle has been reported in the literature.

---

* To whom all correspondence should be sent:
E-mail: g.mugaishudeen@gmail.com

The present work was undertaken to study the performance of a jet loop sparged reactor based on alkaline solution neutralization time and CO_2 absorption by changing influent flow rates of the alkaline solution.

EXPERIMENTAL

The schematic diagram of the experimental setup used for the absorption of CO_2 in alkaline solution is shown in Fig. 1. The apparatus is made of an acrylic column of 14.2 cm i.d. and 60 cm height. The jet loop reactor consists of two sections, top gas induction tube of straight-throat ejector type and middle cylindrical tube. The gas induction tube is a Gi pipe of 3 cm diameter with CO_2 entry on top whereas the alkaline solution enters tangentially. The dimensions of the straight-throat ejector used in this work fell within the dimensional range of ejectors studied by Ogawa [12]. A sparger of 4 mm diameter as shown in Fig. 1 is attached at the bottom of the induction tube. According to Henry's law, the water pressure is greater at higher flow rate, which indicates that the increased pressure from the sparger allows greater dissolution of gases into the water [16]. The sparger used definitely determines the bubble sizes observed in the column. Perforated plates with small orifice, as shown in Fig. 1, enable the formation of smaller sized bubbles and greater gas hold up [17-19]. The solution is continuously withdrawn from the reactor and circulated back to the reactor through the gas induction tube by means of a liquid circulation pump *via* a calibrated flow meter. The high-velocity liquid flow through the nozzle sets up the suction of the gas into the reactor, which is the principle of the ejector mode operation.
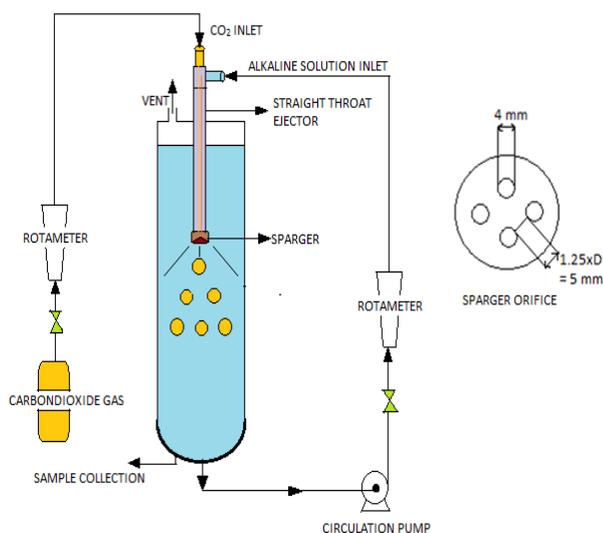
Fig. 1. Schematic diagram of the jet loop reactor

To operate the reactor, the jet loop sparged reactor was filled manually with 9 L of alkaline solution having a pH value of 11. The alkaline solution flowed into the liquid induction tube with the straight-throat ejector using the circulation pump. Simultaneously, the gas containing CO_2 was supplied through the gas induction tube. With the commencement of recirculation flow, the high velocity of the jet created a low pressure in the suction chamber which, when connected to the gas space, entrained the gas across the diffuser. It was subsequently dispersed in the circulating liquid both in the diffuser region and in the main holding vessel, depending on the operating variables such as gas and liquid flow rates and the pressure difference between the exit from the diffuser throat and the gas inlet. A good amount of the dispersed gas was also recirculated through the external pipeline as a gas-liquid mixture. The gas was separated and discharged through the gas discharge valve in the upper part of the reactor [13] and the liquid was recirculated through the circulation pump to outside the reactor and discharged again through the straight-throat ejector.

To compare the performance of the reactor containing a straight-throat ejector with and without sparger in the semi-batch mode, the straight-throat ejector with and without sparger was placed separately in the reactor initially filled with 9 L of the alkaline solution. The circulation flow rates (Q_R) of the alkaline solution were changed from 4 to 8 LPM, and the pH variations of the alkaline solution were measured at a constant gas flow rate $(Q_G = 2$ LPM$)$. The time taken for the pH of the alkaline solution to be neutralized from 11.0 to 7.0 was defined as the neutralization time. In addition, the CO_2 absorption in moles per litre was continuously measured at constant time intervals by a standard titration method. About 10 ml of sample was collected at regular time intervals and titrated with 0.1 N HCl. Two indicators (phenolphthalein and methyl orange) were added to estimate the amount of CO_2 absorbed in the sample of alkaline solution.

RESULTS AND DISCUSSION

Neutralization time dependence on changes in the liquid circulation flow rate

To compare the performance of the straight-throat ejector with sparger and without sparger in the semi-batch mode, the pH variation characteristics affected by the changes in the liquid circulation flow rates $(Q_R = 4-8$ LPM$)$ were measured. This took place while the gas was continuously being injected into the jet loop

reactors without sparger and with sparger separately at a constant gas flow rate (Q_G= 2 LPM). Figs. 2 and 3 show the tendency of the alkaline solution to be neutralized and of the pH to decrease during the continuous injection of the gas with an inlet CO_2 flow rate of 2 LPM. This was attributed to the absorption of the CO_2 in the gas into the alkaline solution, its reaction with OH-, and the neutralization of the solution. Based on such results, the time required for the pH of the initial alkaline solution to change from 11 to 7.0 due to the changes in the liquid circulation flow rate (Q_R) in the cases with and without sparger in a straight-throat ejector, that is, the neutralization time, was measured. The results are shown in Fig. 4.
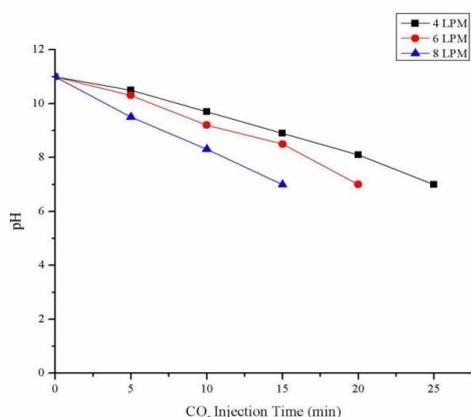
Fig. 2. pH changes with respect to the liquid circulation flow rates in the reactor without sparger at Q_G= 2 LPM.
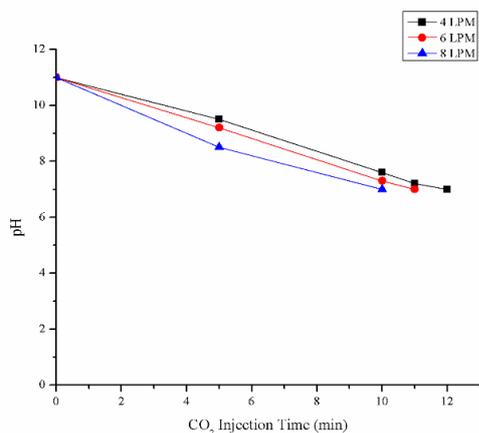
Fig. 3. pH changes with respect to the liquid circulation flow rates in the reactor with sparger at Q_G= 2 LPM.

The straight-throat ejectors without and with sparger presented above show different neutralization times (Fig. 4). The neutralization time decreased with the increase in the liquid circulation flow rate (Q_R), reaching its lowest value at 8 LPM. Because of the increase in the turbulence

intensity as the liquid circulation flow rate increased and due to the increase in the mass transfer rate in the gas-liquid system, the neutralization time decreased. In all cases, the neutralization time was shorter for the reactor with sparger than without sparger at the same liquid circulation flow rate (Fig. 4).
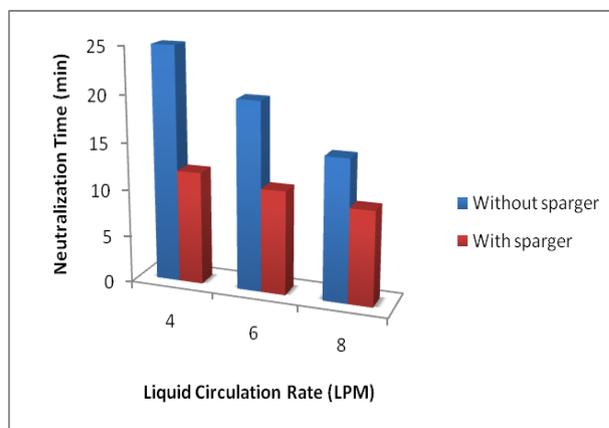
Fig. 4. Effect of the liquid circulation flow rate on the neutralization time at Q_G= 2 LPM.

This result was attributed to the turbulent flow formed at the sparger tip of the straight throat ejector. By design, the sparged reactor forms a turbulent flow and enhances the turbulence intensity in the gas and liquid films, thus resulting in an improved mass transfer rate between the gas and the liquid.

Carbon dioxide absorption

Absorption of CO_2 in the alkaline solution was estimated by a standard titration method. Sodium carbonate and water will be formed when CO_2 reacts with sodium hydroxide according to the following reaction (1):

$$2 \text{ NaOH} + CO_2 \text{ (g)} \Rightarrow Na_2CO_3 + H_2O \qquad (1)$$

When a known volume of the sample is titrated with 0.1 N HCl in presence of phenolphthalein, the acid reacts with all of the sodium hydroxide and only half of the carbonate. Similarly, when the sample is titrated with HCl in presence of methyl orange, the acid reacts with all of the hydroxide and all of the carbonate. Thus, we may be able to estimate the amount of CO_2 absorbed in the alkaline solution sample at regular time intervals once we calculate the amount of sodium carbonate produced. From Figs. 5 and 6 it is clear that CO_2 absorption shows an increasing trend with respect to flow rate and gas injection time. The one with sparger shows better absorption of CO_2 (about 0.653 moles / litre, see Fig. 6) for the same flow rate of 8 LPM and injection time of 20 min.

Sodium carbonate produced

Sodium carbonate (Na_2CO_3) produced as a result of CO_2 injection in alkaline solution was measured in order to predict the behaviour of the reactor without sparger and that with sparger as discussed in previous cases.
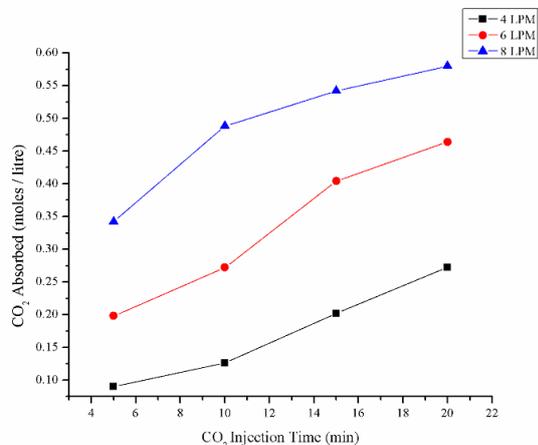
Fig. 5. Effect of CO_2 injection time on CO_2 absorption in alkaline solution with respect to the liquid circulation flow rates in the reactor without sparger at Q_G= 2 LPM.
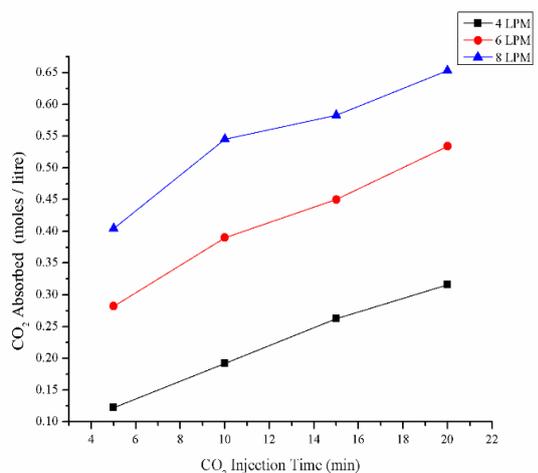
Fig. 6. Effect of CO_2 injection time on CO_2 absorption in alkaline solution with respect to the liquid circulation flow rates in the reactor with sparger at Q_G= 2 LPM.

The results presented in Figs. 7 and 8 show that the influence of the sparger in a straight-throat ejector for liquid flow rates (Q_R=4-8 LPM) towards the production of Na_2CO_3 is higher by about 10-15% for the reactor with a sparger compared to that without sparger.

Carbon dioxide mole fraction in the outlet gas stream

The mole fraction of CO_2 in the outlet gas stream increased as the solution pH decreased by th3 following reactions during the absorption of CO_2 in the alkaline solution [14, 15]:

$$CO_2 \,(g) + H_2O \Leftrightarrow CO_2 \,(aq) \qquad (2)$$
$$CO_2 \,(aq) + OH^- \Leftrightarrow HCO_3^- \qquad (3)$$
$$HCO_3^- + OH^- \Leftrightarrow CO_2^{2-} + H_2O \qquad (4)$$
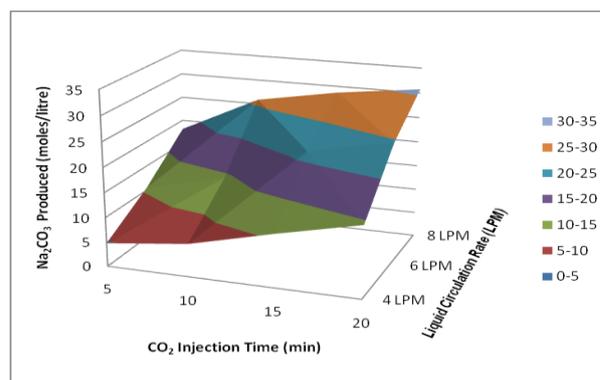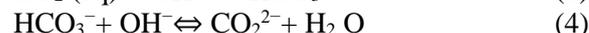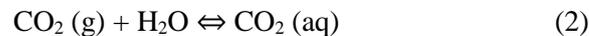
Fig. 7. Effect of CO_2 injection time and liquid circulation flow rates on Na_2CO_3 produced in the alkaline solution for the reactor without sparger at Q_G= 2 LPM.

In the alkaline solution with higher pH, the aqueous CO_2 absorbed in the solution by reaction (2) was rapidly consumed by reactions (3) and (4) because of the high OH^- concentration. However, reaction (3) was limited by the lower OH^- concentration in the solution with lower pH, as shown in Fig. 9. Therefore, the mole fraction of CO_2 in the outlet gas increased with the lower pH of the alkaline solution.
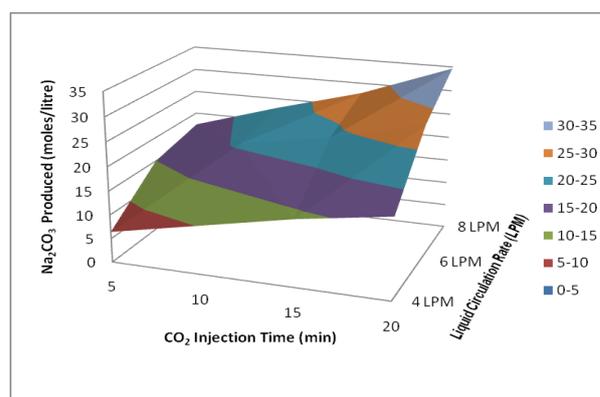
Fig. 8. Effect of CO_2 injection time and liquid circulation flow rates on Na_2CO_3 produced in the alkaline solution for the reactor with sparger at Q_G= 2 LPM.
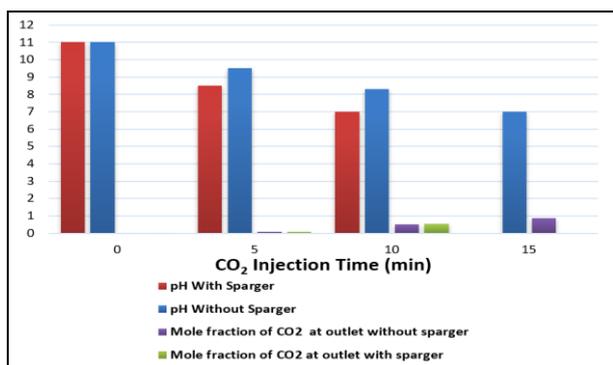
Fig. 9. Comparision of pH value and mole fraction of CO_2 in the outlet gas stream at Q_R= 8 LPM and Q_G= 2 LPM.

CONCLUSIONS

To investigate the performance of a jet loop reactor with a sparged straight throat ejector, CO_2 absorption experiments in the reactor were performed in an alkaline solution. The results obtained were compared with an equally sized jet loop reactor with a conventional straight-throat ejector. The following conclusions were made, summarized in Table 1.

1. At a constant gas flow rate (Q_G=2 LPM), the neutralization time in the jet loop reactor without and with sparger decreased with the liquid circulation flow rate (Q_R), reaching the minimum value at Q_R=8 LPM. Furthermore, the neutralization time decreased in the case of the straight-throat ejector with sparger compared to that without sparger at the same Q_R.

2. When CO_2 gas was continuously injected into the jet loop reactor without and with sparger, at an arbitrary time t, the CO_2 absorption was higher by about 10-15% when the straight-throat ejector with sparger was used compared to the one without sparger.

3. At a constant gas flow rate (Q_G=2 LPM) into the jet loop reactor without and with sparger, at an arbitrary time t, the Na_2CO_3 produced was found to be higher by about 10-15% when the straight-throat ejector with sparger was used compared to the one without sparger.

Table 1. Comparison of straight-throat ejector with and without sparger in a down flow jet loop reactor

S.No	Straight-Throat Ejector				
	Name of the investigation	Process variables	Without sparger (@ 8 LPM & 20 min)	With sparger (@ 8 LPM & 20 min)	Inference
1	Neutralization time (min)	Liquid flow rate (4,6,8 LPM)	15	10	50% decrease
2	CO_2 absorption (moles / litre)	CO_2 Injection time (5,10,15,20 min)	0.58	0.653	11% increase
3	Na_2CO_3 produced (moles / litre)		30.74	34.65	11% increase

REFERENCES

1. Z. W. Cao, Z. X. Li, H. X. Yuan, *Environ. Eng.,* **1**, 102 (2007).
2. K. Bohner, H. Blenke, *Chemie Ingenieur Technik,* **6**, 50 (1972).
3. H. Blenke, *Advances in Biochemical Engineering,* **13**,121 (1979).
4. K. H. Tebel, P. Zehner, *J. Chem. Eng. Technology,* **12**, 274 (1989).
5. M. Velan, T. K. Ramanujam, *J. Chem. Eng. Sci.,* **47**, 2871 (1992).
6. N. N. Dutta, K. V. Raghavan, *Chem. Eng. J.,* **36**, 111 (1987).
7. N. Degermenci, O. N. Ata, E. Yildiz, *J. Ind. Chem. Eng.,* **18**, 399 (2012).
8. S. H. Kang, K. S. Song, J. M. Lim, *J. Korean Solid Wastes Engineering Society,* **16**, 554 (1999).
9. P. Maurizio, E. Ana, F. Federico, *Process Biochem.,* **37**, 821 (2002).
10. M. K. Son, H. J. Sung, J. K. Lee, *J. Korean Society of Combustion,* **18**, 17 (2013).
11. J. K. Lee, M. K. Son, *Korean Patent*, KR-B-10-2012-0056631 (2012).
12. S. Ogawa, M. Kobayashi, S. Tone, T. Otake, *J. C&M Eng. Jpn.,* **15**, 469 (1982).
13. K. Y. Prasad, T. K. Ramanujam, *Can. J. Chem. Eng.,* **73**, 190 (1995).
14. G. Astarita, Mass transfer with chemical reactions, Amsterdam, London, Elsevier, 1967.
15. P. V. Danckwerts, Gas-liquid reactions, McGraw-Hill, New York, 1970.
16. M. Benjamin, D. Lawler, Water Quality Engineering: Physical / Chemical Treatment Processes, John Wiley & Sons Inc., New Jersey, 2013.
17. X. Luo, D. J. Lee, R. Lau, G. Yang, L. Fan. *J. AIChE J.,* **45**, 665 (1999).
18. M. Bouaifi, G. Hebrard, D. Bastoul, M. Roustan, *J. Chem. Eng. Process.,* **40**, 97 (2001).
19. A. Schumpe, G. Grund, *Can. J. Chem. Eng.,* **64**, 891 (1986).

Spectroscopic (FT-IR & FT-Raman), Fukui function and molecular docking analysis of 6-amino-7,9-dihydropurine-8-thione by DFT approach

P. Chakkaravarthy[1], V. Vetrivelan[2*], S. Syed Shafi[3], S. Muthu[4]

[1]*Department of Chemistry, Government Thirumagal Mills College Gudiyattam, Tamilnadu, India*
[2]*Department of Physics, Thanthai Periyar Government Institute of Technology, Vellore, Tamilnadu, India*
[3]*Department of Chemistry, Thiruvalluvar University, Vellore, Tamilnadu India*
[4]*Department of Physics, Aringar Anna Govt Arts College, Cheyyar, Tamilnadu, India*

The title compound 6-amino-7,9-dihydropurine-8-thione (ADHPT) was analyzed using FT-IR and FT-Raman spectroscopy. The fundamental vibrational wavenumbers, IR and Raman intensities for the optimized structure of the investigated molecule were calculated and compared with the experimental vibrational spectra. The vibrational assignment of the molecule was done using potential energy distribution analysis. The electron density-based local reactivity descriptor such as Fukui function was calculated in order to explain the chemical selectivity of the reactive site in ADHPT. Frontier molecular orbitals are also reported. The MEP map was used to detect the possible electrophilic and nucleophilic sites in the molecule. All the calculations were carried out by the B3LYP/6-311++G (d,p) method. To assess the biological activity of ADHPT, molecular docking was done to recognize the hydrogen bond lengths and binding energy with antibacterial protein (5MLA – human RAS protein).

INTRODUCTION

Despite the enormous progress in medicinal chemistry, communicable diseases continue to be a major threat to our society and have provided a new challenge to researchers worldwide. The new molecular manipulation aims to approach the development of new drugs. Among various diseases, malaria and microbial infections are the widest spreading in nature. As a result, antimicrobial studies are the best way to overcome microbial resistance and to develop effective therapies. Our title compound consists of the distinctive moieties purine and thione. The title compound ADHPT and its derivatives have been studied by Gunasekaran *et al.* [1] and Latosinska *et al.* in recent years [2]. Literature survey reveals that to the best of our knowledge no DFT wavenumber calculations, complete vibrational analysis and molecular properties of ADHPT have been reported so far. In the present work, we reported a detailed theoretical and experimental vibrational spectral investigation of the given molecule with a view to identify the various normal modes with greater wavenumber accuracy. In addition, Fukui function, HOMO-LUMO, MEP and molecular docking studies were calculated. The title compound and its derivatives possess high biological activity as anti-cancer, lymphoblastic leukemia drugs, against malignancies, inflammatory bowel disease, rheumatic diseases, dermatologic conditions and solid organ transplant rejection. Their incorporation into the DNA to bring about a cytotoxic effect and their pharmacokinetics have been examined in several studies [3-5]. Previous studies revealed the ability of inhibiting the above-said diseases; in addition to that the title compound inhibits the antibacterial diseases with a higher potential compared to the purine and thione derivatives of previously synthesized compounds.

Vibrational spectroscopy is highly sensitive to structural changes and is useful for the study of pharmacological properties [6]. Thus, in order to understand the relationship between molecular structure and biological activity, the knowledge of the electronic structure and the complete vibrational spectra is mostly significant. Information about the geometry and structure of the molecule and its electrostatic potential surfaces, together with a complete analysis of the vibrational spectra using Raman and infrared techniques, based on frequency, intensity and potential energy distribution over the internal coordinates helps in understanding the structural and spectral characteristics, by allowing to obtain both qualitative and quantitative understanding of energy distribution. DFT calculations have been individually performed, as they form the basis of the assignment of the vibrational spectrum. In addition, intra- and intermolecular interactions are analyzed by different techniques, e.g. NBO analysis.

---

* To whom all correspondence should be sent:
E-mail: vetri.tpgit@gmail.com

The frontier molecular orbital theory is employed to predict the molecule reactivity. The complete assignments of experimental IR and Raman spectra were performed by comparison of experimental IR and Raman spectra with the corresponding theoretical ones based on the potential energy distribution (PED) and the normal internal coordinates of the ADHPT species. The treatment of solvated systems was an issue which we were unable to address. Dougherty *et al.*, [6] argued that different solvation-desolvation effects will be minor if the ion is held constant while the neutral host is varied, and that gas phase calculations may therefore be of value for prediction of solution phase binding preferences. Molecular dynamics simulations in solvent boxes have proved to be successful and are undoubtedly most promising.

Owing to the increased resistance to the available drugs by antimicrobial pathogens it is essential to synthesize new drugs. According to literature, the title compound consists of effective antimicrobial moieties.

The extensive use of common antibiotics leads to a growing number of defiant bacteria through gene transfer and mutation. Based on pharmacological investigation, *in silico* binding mode of ADHPT ligand to the human RAS protein (5MLA) was also investigated by a docking procedure in this paper.

As the potential applications of the title compound evidence its biological and medicinal importance, so we carried out this study.

MATERIAL AND METHODS

Experimental details

6-Amino-7,9-dihydropurine-8-thione (ADHPT) was purchased from Sigma–Aldrich chemical company with a stated purity of 97% and was used without further purification. The FT-IR spectrum of the sample was recorded in the region of 4000–450 cm^{-1} in a KBr pellet using Spectrum Two FT-IR/Sp10 Perkin Elmer FT-IR spectrometer. The resolution of the spectrum was 4 cm^{-1}. The FT-Raman spectrum was obtained in the range of 4000–100 cm^{-1} using Bruker RFS 100/S FT-Raman spectrophotometer with a 1064 nm Nd: YAG laser source of 100 mW power.

Computational details

The optimized geometrical parameters were used in the vibrational frequency computations at the DFT levels to describe all stationary points as minima. At the optimized structure of the studied species, no imaginary frequency modes were obtained proving that a true minimum on the potential energy surface was found. We have used the gradient-corrected density functional theory [7] with a three-parameter hybrid functional (B3) [8] for the exchange part and the Lee–Yang–Parr (LYP) correlation function [9], accepted as a cost-effective approach for the computation of molecular structure, vibrational frequencies and energies of optimized structures.

By connecting the outcome of the Gauss view program [10] with symmetry considerations, assignments of vibrational frequency were finished with a high degree of accuracy. Then, the spectra were analyzed with respect to potential energy distribution (PED) contributions by the Vibrational Energy Distribution Analysis (VEDA) program [11]. Finally, the calculated normal mode vibrational frequencies provide thermodynamic properties by the way of statistical mechanics. We have scaled the numbers with a standard scaling factor 0.961 [12] to compensate for the errors originating from the basis set in completeness and avoid vibrational anharmonicity, because in the experimental method the compound is analyzed in solid phase whereas in the DFT method that is carried out in gas phase.

Entire theoretical calculations of ADHPT were worked out by the DFT/B3LYP method with the 6-311++G (d, p) basis set using Gaussian 09 software package [13]. Gauss view molecular visualization program [14] was used to visualize the geometry structure. The theoretical vibrational assignments were interpreted by means of PED (Potential Energy Distribution) using VEDA 4 program [11]. Molecular docking studies give vital details about the orientation of ADHPT (ligand) which regulate the binding affinity between the ligand and their protein target. Molecular docking studies were carried out using Auto Dock 4.2 software [15].

Prediction of Raman intensities

The calculated Raman activities (S_i) were converted to relative Raman intensities (I_i) using the following relations [16]:

$$I_i = \frac{f(\upsilon_0 - \upsilon_i)^4\, S_i}{\upsilon_i\, [1 - \exp(hc\upsilon i/k_b T)]} \tag{1}$$

where, υ_0 is the exciting frequency in cm^{-1}, υ_i is the vibrating wavenumber of the ith normal mode, f is a normalization factor for all peak intensities, *h*, c and k_b are Plank's constant, velocity of light and Boltzmann's constant, respectively.

Molecular docking

Molecular docking was employed to elucidate the binding modalities of the investigated ligand towards its target. The three-dimensional structure of human RAS protein was downloaded from the RCSB Protein Data Bank (PDB) with PDB Id 5MLA. The molecular docking program Auto dock 4.2 was used to determine the potential binding mode between the compounds and the selected protein. For the preparation of 5MLA, first crystallographically observed water molecules were eliminated from the protein crystal structure. Then, hydrogen atoms were added using Kollman united atom charges and solvation parameters as provided by Auto Dock Tools [15]. Ligand structures were developed by unifying non-polar atoms of hydrogen, adding Gasteiger partial charges and defining rotatable bonds. A grid box sized 76×74×76 Å was created to conceal the binding site of 5MLA using Auto Grid with points separated by 0.375 Å. The grid box was apportioned for protein using x, y, and z coordinates of 2.765, 25.11 and 39.49, respectively. Docked complexes were pictured and depictions of protein-ligand interactions were engendered using software BIOVIA, Discovery Studio Modeling Environment, Release 4.5 [17].

RESULTS AND DISCUSSION

Molecular geometry

The fundamental structural parameters (bond angles, bond lengths) of the ADHPT values are listed in Table S1 using the B3LYP/6-311G++ (d,p) basis set. In accordance with the atom numbering scheme as obtained from CHEMCRAFT software the optimized structure is shown in Figure 1. The ADHPT has one C-H bond, two C-C bonds, nine C-N bonds, four N-H bonds and one C-S bond. The C-C bond length value of the ring was found to be around 1.396 Å and agrees well with the experimental value of a structurally related compound [1, 2, 18]. The C-H calculated bond length was found to be 1.085 Å and the N-H bond length value was around 1 Å. The C-N bond length values vary from 1.326 to 1.393 Å. The C-S calculated bond length value was 1.659 Å and the experimental value was 1.576 Å. This decrease in bond length may be due to the electronegativity of oxygen atom with neighboring atoms. The bond C-C lengths are greater than C-H bond lengths. The calculated geometries represent a good approximation and they were the bases for calculating vibrational frequencies and thermodynamic properties.
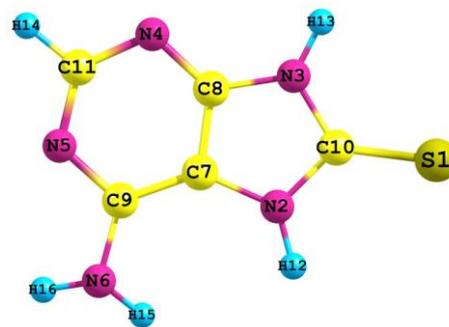
Figure 1. Optimized geometric structure with atoms numbering of ADHPT.

Vibrational assignments

Experimental and theoretical comparative FT-IR and FT-Raman spectra of ADHPT molecule are shown in Figures 2 and 3. The ADHPT molecule consists of 16 atoms, therefore, they have 42 vibrational normal modes. The vibrational frequencies are scaled by 0.961 [12] for B3LYP/6-311++G(d,p) in order to compensate for the errors arising from the basis set incompleteness and neglect the vibrational anharmonicity. The measured (FT-IR and FT-Raman) wavenumbers and assigned wavenumbers values are given in Table S2. They reveal a good correspondence between theory and experiment in the main spectral features.

C-H vibrations

The C-H stretching vibrations are generally identified in the region of 3100-2800 cm^{-1} which is the characteristic region for the ready identification of C-H stretching vibrations [19, 20]. These vibrations are found to be affected by the nature and position of the substituents. In the present study, the IR band was observed at 2854 cm^{-1} and the Raman band at 2976 cm^{-1}. Theoretically computed C-H vibrations values approximately coincide with the experimental values.
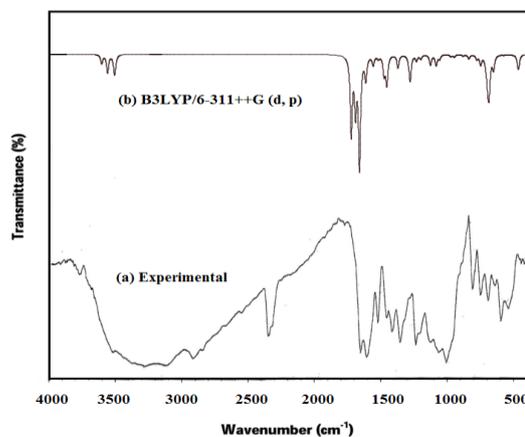
Figure 2. FT-IR spectra of ADHPT (a) Experimental and (b) Theoretical.
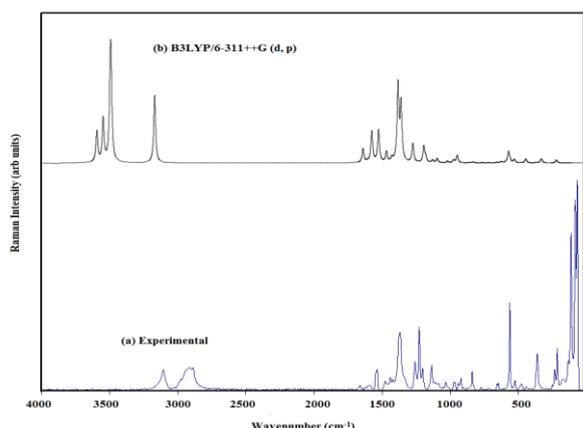
Figure 3. FT-Raman spectra of ADHPT. (a) Experimental and (b) Theoretical.

As indicated by PED, this mode involves 99% of the contribution suggesting that it is a pure stretching mode. The C-H in-plane bending vibrations normally occur as a number of strong- to weak-intensity sharp bands in the region of 1300-1000 cm^{-1} [21] and are very useful for characterization purposes. The bands identified at 1072, 1166, 1230 and 1262 cm^{-1} in the IR spectra and the bending vibrations identified at 1034, 1136, 1209, 1239 and 1268 cm^{-1} in the Raman spectra were assigned to C-H in-plane bending.

C=N and C-N vibrations

The stretching vibrations of C=N occur at 1615-1575 cm^{-1} and those of C-N occur at 1200-1020 cm^{-1} [22]. In this study, the bands identified at 1636, 1482 and 1436 cm^{-1} in the FT-IR spectra and at 1586, 1479, 1440, 1380 and 1372 cm^{-1} in the FT-Raman spectra were assigned to C=N stretching vibrations. For C-N stretching, the bands were identified at 1262, 1230, 1174, 1166 and 1072 cm^{-1} in the FT-IR spectra and at 1268, 1234, 1204 and 837 cm^{-1} in the FT-Raman spectra. The theoretically scaled wave numbers at 1570, 1444, 1431, 1411, 1333, 1312, 1284, 1261 and 1212 cm^{-1} by the DFT method, corresponding to C-N stretching vibrations, coincide with the experimental values with a PED of 57, 58, 59, 62, 63, 69, 73, 77 and 70%, respectively. For C=N stretching vibration, the theoretically scaled wavenumber was at 1570 cm^{-1} with PED of 64%. The remaining vibrations of fundamental modes were also assigned and are listed in Table S2.

Fukui function

Local quantities such as Fukui function and local softness describe the reactivity/selectivity of a specific site in a molecule. The Fukui function is defined in [23]:

$$f_N^+(r) = (\partial \rho(r)/\partial N)_{v(r)}^+ = \rho_{N+1}(r) - \rho_N(r) \qquad (2)$$

where, $\rho_{N+1}(r)$ and $\rho_N(r)$ are the electron densities of the N + 1 and N electron systems evaluated at the geometry, v(r), of the N electron system; the superscript plus sign on the derivative indicates that we are considering the derivative from above (right-hand derivative).

The individual atomic charges calculated by Mulliken population analysis (MPA) were used to calculate the Fukui function. Fukui functions $(f^+(\vec{r}), f^-(\vec{r}), f^0(\vec{r}))$, (s_r^+, s_r^-, s_r^0) [22] for all atomic sites in ADHPT are listed in Table 1. Yang and Mortier [24] have given a simple procedure to calculate the atomic condensed Fukui function indices based on MPA and on three possible forward, backward, and central finite difference approximations to the derivatives [25]. Fukui functions were calculated using the following equations:

$$f^+(\vec{r}) = q_r(N + 1) - q_r(N) \qquad (3)$$

for nucleophilic attack;

$$f^-(\vec{r}) = q_r(N) - q_r(N - 1) \qquad (4)$$

for electrophilic attack;

$$f^0(\vec{r}) = (q_r(N + 1) - q_r(N - 1))/2 \qquad (5)$$

for radical attack.

In these equations, q_r is the atomic charge (evaluated from Mulliken population analysis, electrostatic derived charge, etc.) at the rth atomic site is the neutral (N), anionic (N+1), cationic (N-1) chemical species.

In Table 1 the values of the Fukui function obtained from the Mulliken charges are reported. From the values reported in Table 1, the reactivity order for the electrophilic case is $H_{15} > H_{14} > H_{16} > S_{10} > N_{11} > C_8 > H_{13} > H_{12} > N_3$. On the other hand, for nucleophilic attack we observe $S_{10} > N_5 > C_9 > H_{13} > N_3 > C_2 > H_{12} > H_{14} > N_{11} > H_{15} > H_{16} > N_1 > N_7 > C_4$. If one compares the three kinds of attack it may be concluded that the nucleophilic attack is more active in comparison with the electrophilic and radical attack.

HOMO-LUMO energy

The energy gap between HOMO and LUMO is a critical parameter to determine molecular electrical transit properties. HOMO (logical valence bond) can be thought of as the outermost electron containing orbital that tends to give these electrons away as an electron donor or nucleophilic site [26-29].

Table 1. Values of the Fukui function of ADHPT.

Atoms	Mulliken atomic charges			Fukui functions			Local softness		
	0,1 (N)	N +1 (-1, 2)	N-1 (1,2)	fr_+	fr_-	fr_0	$sr_+ fr_+$	$sr_- fr_-$	$sr_0 \, fr_0$
N1	-0.3106	0.0906	-0.2373	0.4012	-0.0733	0.1639	0.0839	-0.0153	0.0343
N3	-0.1268	-0.0317	-0.0913	0.0950	-0.0355	0.0298	0.0199	-0.0074	0.0062
C4	0.3742	-0.6728	0.3917	-1.0470	-0.0175	-0.5323	-0.2189	-0.0037	-0.1113
N5	-0.1636	-0.1604	-0.0931	0.0032	-0.0705	-0.0337	0.0007	-0.0147	-0.0070
C6	0.0991	0.3480	0.1483	0.2489	-0.0492	0.0999	0.0520	-0.0103	0.0209
N7	-0.2416	-0.0974	-0.1723	0.1442	-0.0693	0.0375	0.0302	-0.0145	0.0078
C8	0.0332	-1.7244	0.0415	-1.7576	-0.0083	-0.8829	-0.3675	-0.0017	-0.1846
C9	-0.3150	3.1289	-0.2668	3.4439	-0.0483	1.6978	0.7201	-0.0101	0.3550
S10	-0.6700	-0.7636	-0.3419	-0.0936	-0.3281	-0.2109	-0.0196	-0.0686	-0.0441
N11	-0.3978	-0.3000	-0.3251	0.0979	-0.0728	0.0125	0.0205	-0.0152	0.0026
H12	0.2775	-0.1124	0.3367	-0.3899	-0.0592	-0.2246	-0.0815	-0.0124	-0.0470
H13	0.3410	-0.3449	0.3938	-0.6859	-0.0528	-0.3694	-0.1434	-0.0110	-0.0772
H14	0.1988	0.0561	0.2686	-0.1428	-0.0698	-0.1063	-0.0299	-0.0146	-0.0222
H15	0.2420	-0.6405	0.2684	-0.8825	-0.0264	-0.4545	-0.1845	-0.0055	-0.0950
H16	0.3380	-0.2497	0.3923	-0.5877	-0.0543	-0.3210	-0.1229	-0.0114	-0.0671
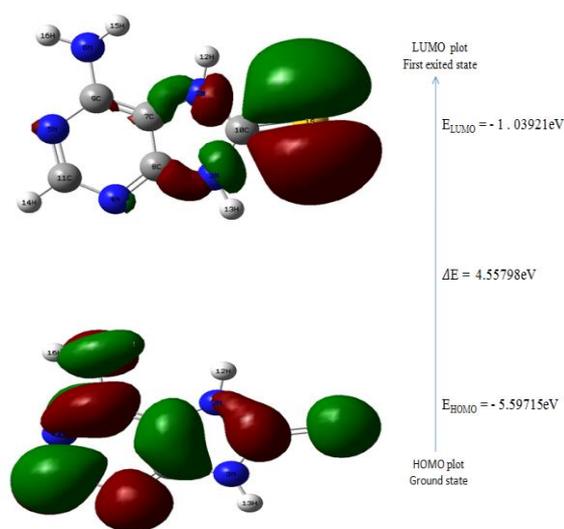
Figure 4. HOMO - LUMO plots of ADHPT.

LUMO (logical conduction band) can be thought of as the innermost orbital containing free sites to electrophilic or accept electrons are of fundamental eminence as it forms the basis of understating the chemical stability and reactivity of a given molecule. The 3D plots of the frontier orbitals HOMO and LUMO figures for the ADHPT are shown in Figure 4.

Pauling introduced the concept of electronegativity as the power of an atom in a molecule to attract electrons to itself. Hardness (η), chemical potential (μ) and electronegativity (χ) and softness (S) are defined as follows:

$$\eta = \frac{1}{2}\left(\frac{\partial_2 E}{\partial N_2}\right)V(r) = \frac{1}{2}\left(\frac{\partial \mu}{\partial N}\right)V(r) \quad (6)$$

$$\eta = \left(\frac{\partial E}{\partial N}\right)V(r)$$

$$\chi = -\mu = -\left(\frac{\partial E}{\partial N}\right)V(r) \quad (7)$$

where, V(r) and E are external potential and electronic energy of an N-electron system, respectively. Softness (S) is a property of molecule that estimates the extent of chemical reactivity. It is the reciprocal of hardness (η).

$$S = 1/2\eta \quad (8)$$

Using Koopman's theorem for closed-shell molecules, η, μ and χ can be defined as:

the hardness of the molecule

$$\eta = (I-A)/2 \quad (9)$$

the chemical potential of the molecule

$$\mu = - (I+A)/2 \quad (10)$$

the electronegativity of the molecule

$$\chi = (A+I)/2 \quad (11)$$

where, I and A are the ionization potential and electron affinity of the molecule, respectively. The ionization energy (I) and electron affinity (A) can be expressed by HOMO and LUMO orbital energies as I = - E_{HOMO} and A = - E_{LUMO}. Electron

affinity (A) relates to the efficiency of a ligand to accept in particular one electron from a donor. The ionization potential calculated by the B3LYP/6-311++G (d,p) method for ADHPT is 5.59715 eV. Considering the chemical hardness, large frontier orbital gap (HOMO–LUMO) means a hard molecule and small frontier orbital gap (HOMO–LUMO) means a soft molecule. A molecule with small frontier gap is generally associated with a low kinetic stability and high chemical reactivity. Recently Parr *et al.* [26] have defined a new descriptor electrophilicity index (ω), which describes a quantitative classification of the global electrophilic nature of a molecule. They defined the electrophilicity index (ω) as follows:

$$\omega = \mu^2/2\eta \qquad (12)$$

Using the above equations, the chemical potential, hardness and electrophilicity index were calculated for ADHPT and their values are shown in Table 2. The usefulness of this new reactivity quantity has been recently proved in understanding the toxicity of various pollutants concerning their site selectivity and reactivity [30-31]. The calculated value of the electrophilicity index describes the biological activity of ADHPT.

Molecular Electrostatic Potential (MEP)

The three-dimensional MEP of ADHPT is illustrated in Figure 5. The MEP is related to the electronic density which is a very useful descriptor for determining the sites for electrophilic attack and nucleophilic reactions, as well as hydrogen-bonding interactions [32, 33]. MEP clearly exhibits molecular size, shape in terms of color grading.

Table 2. Calculated energy values of ADHPT.

Basis set	B3LYP/6-311++G(d, p)
E_{HOMO}(eV)	-5.59715
E_{LUMO}(eV)	-1.03921
Ionization potential	5.59715
Electron affinity	1.03921
Energy gap(eV)	4.55794
Electronegativity	3.31818
Chemical potential	-3.31818
Chemical hardness	2.27897
Chemical softness	0.21940
Electrophilicity index	2.41564

As can be seen from the MEP of the title compound, while the regions having negative potential are over the electronegative atoms (nitrogen and sulfur), the regions having positive potential are the hydrogen atoms. From this result, we can conclude that the hydrogen atom indicates the strongest repulsion and nitrogen and sulfur atoms indicate the attraction.
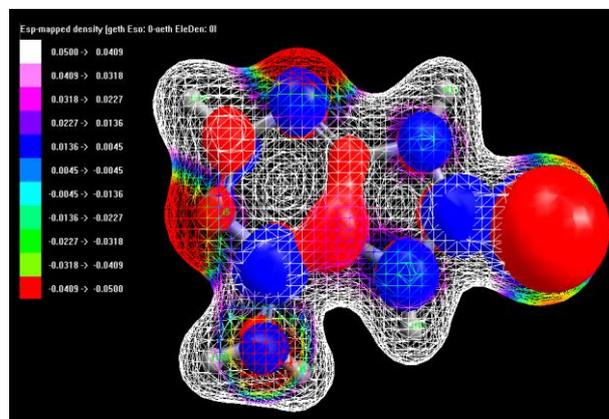
Figure 5. MEP on ADHPT.

Molecular docking

The low toxicity levels of ADHPT calculated in terms of the softness value and the electrophilicity index that act as a biological descriptor, led to molecular docking investigations.

Molecular docking was performed against 5MLA and its purpose was to estimate the binding modalities of ADHPT. Hydrogen bonding plays an important role in the structure and function of biological molecules, the ligand-receptor interactions were inspected on the basis of hydrogen bonding. Table 3 shows the corresponding binding energy, interactions, distance and bonding type. It is evident from Table 3 that the ligand molecule ADHPT is tightly fitted with the active position of 5MLA with very good binding energy - 5.99 kcal/mol, as shown in Figure 6.
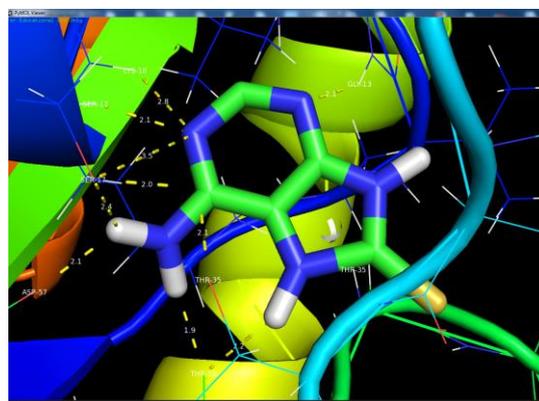
Figure 6. Docking and hydrogen bond interaction of ADHPT with 5MLA.

In molecular docking, the actual requirement is not to find out only RMSD and binding energy values. The molecular interactions like hydrogen bonds, hydrophobic interactions, van der Waal interactions, ionic bonds, etc. are also playing important roles. So, based on RMSD and binding energy the selection of a compound or ligand is not a true way. In some cases, it is possible that the best pose has good binding energy due to the presence of more hydrophobic and van der Waal interactions but it does not contain the stronger hydrogen bond while in the next pose 3-7 hydrogen bonds are present and there are less hydrophobic and van der Waal interactions compared to the best pose. So, in this case the binding energy of the first best pose is -5.43 kcal/mol and of the second is -5.99 kcal/mol. In this way, the second pose is superior because of stronger hydrogen bond interaction between protein and ligand. The docked poses for each controlled inhibitor were evaluated and the pose with the lowest binding free energy and inhibition constant was thereby chosen. The lowest binding free energy (i.e. best docking score) and inhibition constant indicated the highest ligand/protein affinity.

The hydrogen bond lengths and binding energies of the title molecule with different proteins were identified. A minimum binding energy of -5.99 kcal/mol was found for the interaction of protein 5MLA with the bonded residues GLY13, LYS16, SER17, ASP57 and THR58.

Table 3. Molecular docking with 5MLA.

Protein (PDB ID)	Bonded residues	No. of hydrogen bonds	Bond distance (Å)	Estimated inhibition constant (μm)	Binding energy (kcal/mol)	Torsional free energy
5MLA	GLY13	7	2.1	40.45	-5.99	0.3
	LYS16		2.8			
	SER17		2.1			
	SER17		3.5			
	ASP57		2.1			
	THR58		2.2			
	THR58		1.9			

CONCLUSION

In this investigation, the optimized parameters of title compound structure were found at B3LYP/6-311++G (d,p) level of theory. Comparisons between theoretical and experimental geometrical parameters showed that DFT calculations were in good compatibility with experimental results. The vibrational FT-IR and FT-Raman spectra of the ADHPT molecule were recorded and on the basis of agreement between the calculated and experimental results, the assignments of all fundamental vibrational modes of ADHPT were made unambiguously based on the results of the PED. Low HOMO–LUMO energy gap value indicates that intramolecular charge-transfer takes place within the molecule. Fukui function helps to identify the electrophilic/ nucleophilic nature of a specific site within a molecule. The MEP shows that negative potential sites are on nitrogen and sulfur atoms while the positive potential sites are around the hydrogen atoms. This study shows clearly the inhibitor effect, based on binding affinities and interactions formed between amino acid residues and candidate molecules, of the title compound in front of microbial enzymes. The interactions between the molecule and the antimicrobial enzyme are dominated by van der Waals and hydrogen bond interactions.

The protein-ligand interactions (hydrogen bonds and hydrophobic contacts) and binding energy score enhance the medicinal activity of the ligand. Hence, the title compound may be deemed as an effective and suitable inhibitor of antibacterial diseases.

REFERENCES

1. S. Gunasekaran, S. Kumaresan, R. Arunbalaji, G. Anand, S. Seshadri, S. Muthu, *J. Raman Spectrosc.* **40(11)**, 1675 (2009).
2. I. N. Latosinska, J. Seliger, V. Zagar, D. V. Burchardt, *Journal of Physical Chemistry* **A, 113.30**, 8781 (2009).
3. S. Sahasranaman, D. Howard, S. Roy, *Eur. J. Clin. Pharmacol.*, **64(8)**, 753 (2008).
4. L. Lennard, John S. Lilleyman, *J. Clin. Oncol.* **7(12)**, 1816 (1989).

5. N. Issaeva, *J. Cancer Res.,* **70(15)**, 6268 (2010).
6. D. A. Dougherty, *Science,* **271**, 163 (1996).
7. P. Hohenberg, W. Kohn, *Phys. Rev.,* **136** B, 864 (1964).
8. A. D. Becker, *J. Chem. Phys.,* **98,** 5648 (1993).
9. C. Lee, W. Yang, R. G. Parr, *Phys. Rev.,* **B37**, 785 (1988).
10. A. Frisch, A.B. Nielsen, A. J. Holder, Gauss View User's Manual, Gaussian Inc., Pittsburg, PA, 2000.
11. M. H. Jamroz, Vibrational Energy Distribution Analysis VEDA 4 program, Warsaw, 2004.
12. V. Vetrivelan, *J. Nanosci. Tech*. **4**, 348 (2018).
13. M. J. Frisch, Gaussian 09, Gaussian Inc., Wallingford, CT, USA, 2009.
14. R. Dennington, T. Keith, J. Millam, Gauss View, Version 4.1.2, Semichem Inc., Shawnee mission, KS, 2007.
15. G. Morris, R. Huey, W. Lindstrom, M. Sanner, R. Belew, D. Goodsell, A. Olson, *J. Comput. Chem*., **30** (16), 2785 (2009).
16. G. Keresztury, Raman spectroscopy: Theory in Handbook of vibrational spectroscopy, 2002.
17. Discovery Studio, 'Dassault Systèmes BIOVIA, Discovery Studio Modeling Environment', Release 4.5, San Diego, Dassault Systèmes, 2015.
18. C. E. Bugg, U. Thewalt, *Acta Crystallogr. Sect. A.,* **31(1)**, 121 (1975).
19. S. Bourcier, Y. Hoppilliard, *Int. J. Mass Spectrom.,* **217(1)**, 231 (2002).
20. Y. Yu, L. Ke, X. Zhou, H. Wang, Sh. Liu, X. Ma, *J. Phys. Chem. A*, **111,** 8971 (2007).
21. G. Socrates, Infrared and Raman Characteristics Group Frequencies, Third edn., Wiley, New York, 2001.
22. L. J. Bartolotti, P. W. Ayers, *J. Phys. Chem*. A, **109**, 1146 (2005).
23. P. K. Chattaraj, Chemical Reactivity Theory: A DFT View. CRC Press, (2009).
24. W. Yang, W. J. Mortier, *J. Am. Chem. Soc.,* **108,** 5708 (1986).
25. O. Christiansen, J. Gauss, J. F. Stanton, *J. Chem. Phys. Lett*., **305**, 147 (1999).
26. R. G. Parr, L. Szentpaly, S. Liu, *J. Am. Chem. Soc*., **121**, 1922 (1999).
27. P. K. Chattaraj, B. Maiti, U. Sarkar, *J. Phys. Chem.*, **A107**, 4973 (2003).
28. R. G. Parr, R. A. Donnelly, M. Levy, W. E. Palke, *J. Chem. Phys.,* 6**8**, 3801 (1978).
29. R. G. Parr, R. G. Pearson, *J. Am. Chem. Soc.,* **105,** 7512 (1983).
30. R. G. Parr, P. K. Chattraj, *J. Am. Chem. Soc.,* **113**, 1854 (1991).
31. R. Parthasarathi, J. Padmanabhan, M. Elango, V. Subramanian, P. Chattaraj, *Chem. Phys. Lett.,* **394**, 225 (2004).
32. P. Politzer, J. S. Murray, *Theor. Chem. Acc.*, **108**, 134 (2002).
33. E. Scrocco, J. Tomasi, *Adv. Quantum Chem.,* **11**, 115 (1978).

A bromide-selective PVC membrane potentiometric sensor

Ö. Isildak[1]*, O. Özbek[2]*, K. M. Yigit[3]

[1]*Department of Chemistry, Faculty of Science and Arts, Tokat Gaziosmanpasa University, 60250 Tokat, Turkey*
[2]*Science and Technology, Application and Research Center, Zonguldak Bülent Ecevit University, 67600 Zonguldak, Turkey*
[3]*Department of Molecular Biology and Genetics, Tokat Gaziosmanpasa University, 60250, Tokat, Turkey*

In this study, a novel poly(vinyl chloride) membrane bromide-selective sensor was developed. The best performance was obtained with a membrane composition of 2.0% ionophore, 33.0% poly(vinyl chloride) (PVC), 64.0% *o*-nitrophenyloctylether (*o*-NPOE) and 1.0% potassium tetrakis (*p*-chlorophenyl) borate (KTpClPB). The sensor exhibits linear potentiometric response towards bromide ion in the concentration range of $1.0 \times 10^{-1} - 1.0 \times 10^{-4}$ mol L^{-1} and has a detection limit of 2.2×10^{-5} mol L^{-1}. The bromide-selective sensor has a fast response time of 10 s and displays a highly selective response towards bromide compared to different anions. The sensor can be used in the pH range from 4.0 to 10.0. Finally, the bromide-selective sensor was successfully used for the determination of bromide in purified and commercial drinking water.

Keywords: ion-selective electrode, PVC membrane, all-solid-state, potentiometry, bromide determination

INTRODUCTION

Bromide is a naturally occurring ion that is commonly present in seawater sources and drinking water. Bromide determination is a very important operation in various areas such as pharmaceutical manufacturing, chemistry, food production and in quality control of water. The presence of high amounts of bromide in environmental samples is considered highly dangerous for human health and thus, its measurement is of high importance for environmental scientists [1].

Different analytical methods have been used for the determination of bromide including ion chromatography [2], capillary electrophoresis [3], colorimetry [4], spectrophotometry [5] inductively coupled plasma mass spectrometry (ICP-MS) [6], high performance liquid chromatography (HPLC) [7] and mass spectrometry (MS) [8]. These methods are not ideal due to their high cost, complexity of use, high energy consumption, long measurement time, requirement for trained personnel and necessity of sample pretreatment [9–12]. Since 1950s, ion-selective electrodes (ISEs) have been widely used in industrial, environmental, pharmaceutical and agricultural analysis. Compared to other analytical methods, ISEs are very simple to use, inexpensive, durable, have good reusability, short response time, wide linear working range, low energy consumption and thus can be considered very suitable for the use in environmental analyses [13–15].

The ionophore, the most important component of ISEs is responsible for the selective response to the target ion [16]. In sensor studies reported in the literature, thousands of sensors sensitive to either anions or cations have been developed using different ionophores. In the present study, a cobyrinic acid derivative macrocyclic molecule (Fig. 1) was used as an ionophore and a bromide-selective potentiometric sensor was developed. This sensor was evaluated in terms of some potentiometric properties such as linear working range, reusability, selectivity, pH working range and response time in laboratory conditions.
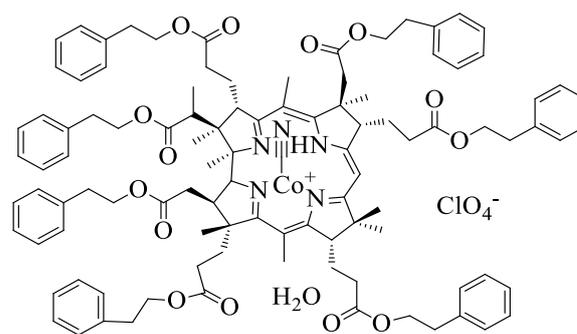
Fig. 1. Structure of the ionophore.

EXPERIMENTAL

Materials

For all-solid-state contact preparation, epoxy (Macroplast Su 2227) and hardener (Desmodur RFE) were obtained from Henkel and Bayer, respectively.

* To whom all correspondence should be sent:
E-mail: omer.isildak@gop.edu.tr
         oguz.ozbek@beun.edu.tr

For bromide-selective sensor preparation, ionophore poly(vinyl)chloride PVC) of high molecular weight, *o*-nitrophenyloctylether (*o*-NPOE), potassium tetrakis (*p*-chlorophenyl) borate (KTpClPB) and tetrahydrofurane (THF) were purchased from Sigma Aldrich, Merck and Fluka chemical companies. Deionized water was obtained using a DI 800 Model deionized water system. Sodium salts of the anions used in selectivity experiments were obtained from Sigma Aldrich and Merck. All anion stock solutions (1.0×10^{-1} mol L^{-1}) were prepared using deionized water.

Apparatus

Potentiometric measurements were performed at room temperature (25 ± 1 °C) using a computer-controlled multichannel potentiometric system. All measurements were performed using a micro-size silver/silver chloride reference electrode (Thermo-Orion). pH measurements were conducted with a digital pH meter (Mettler Toledo Model S220-K).

Method

The preparation of the all-solid-state contact bromide-selective potentiometric sensor was carried out in two steps. We used the same sensor preparation protocol reported in previous studies [17–19]. At the first step, all-solid-state contact was prepared. For this purpose, graphite (50.0%), epoxy (35.0%), and hardener (15.0%) were added to THF in appropriate proportions. After suitable viscosity was obtained, a copper wire was immersed in this mixture 5–6 times and covered with solid-state mixture. Appropriate amounts of ionophore, PVC, *o*-NPOE and KTpClPB were dissolved in 5 mL of

THF. The optimum membrane composition was determined to be 64.0% plasticizer (*o*-NPOE), 33.0% PVC, 2.0% ionophore and 1.0% KTpClPB. This mixture was placed on the all-solid-state electrode surface at a certain thickness and left to dry for 24 h. The schematic diagram for the step-wise preparation of the bromide-selective sensor is shown in Fig. 2. Prior to first use, the prepared sensors were conditioned in a 1.0×10^{-2} mol L^{-1} bromide solution for approximately 3 h. The membranes prepared and the optimum membrane composition are summarized in Table 1.

Potential measurements

Potentials were measured using an Ag/AgCl reference electrode. Potentiometric study of the electrode was carried out by the following cell assembly:

Ag/AgCl; KCl (saturated) $\|$ 10^{-2} mol L^{-1} bromide sample solution $|$ bromide-selective PVC membrane
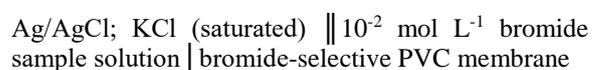
The potentiometric measurement scheme of the bromide-selective sensor is shown in Fig. 2.

RESULTS AND DISCUSSION

Working concentration range and detection limit of the bromide-selective sensor

The PVC membrane bromide-selective sensor was evaluated for its potentiometric performance with optimum membrane composition. Figure 3A shows the calibration curve of the bromide-selective sensor. Figure 3B represents the linear working range of the sensor. Figure 3A shows that the sensitivity of the sensor significantly increases with the increasing concentration.

Table 1. Optimization of the bromide-selective membrane (% w/w) with the use of components at varying ratios.

Membrane	Ionophore	PVC	KTpClPB	*o*-NPOE	Working concentration range
1	1.5	33.0	1.0	64.5	$1.0\times10^{-1} - 1.0\times10^{-3}$
2	**2.0**	**33.0**	**1.0**	**64.0**	**$1.0\times10^{-1} - 1.0\times10^{-4}$**
3	3.0	33.0	1.0	63.0	$1.0\times10^{-1} - 1.0\times10^{-3}$
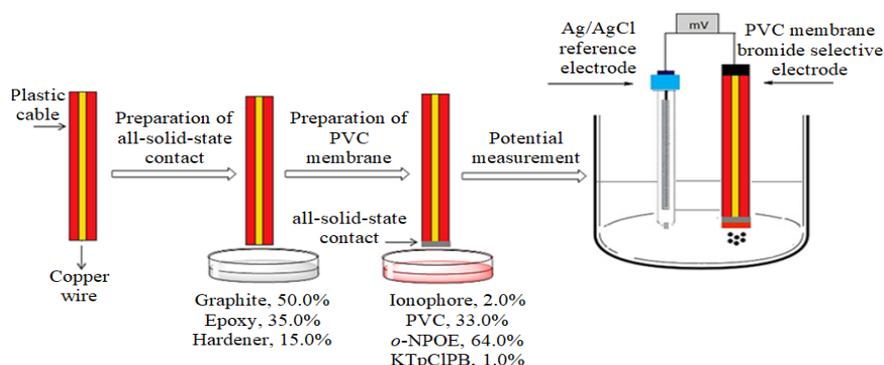
Fig. 2. Schematic diagram for the step-wise preparation of bromide-selective sensors and potential measurement.
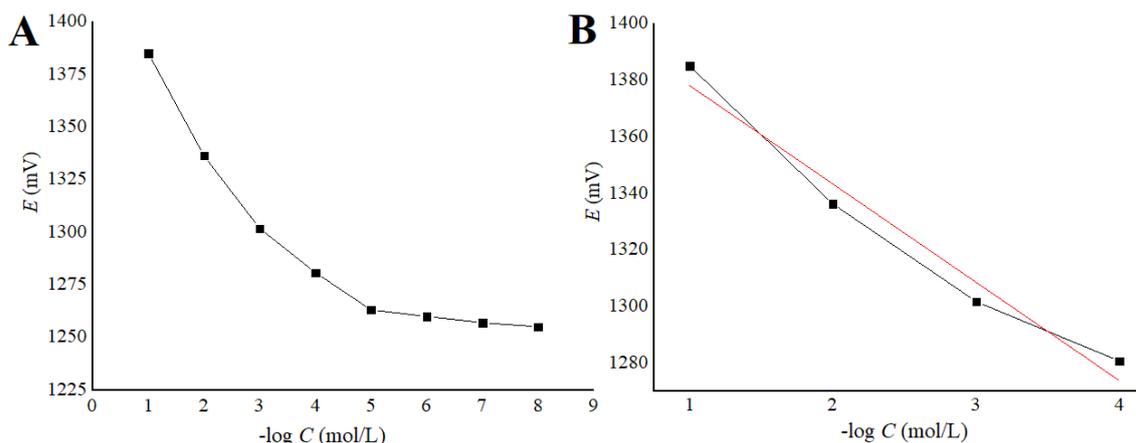
Fig. 3. A) calibration curve; **B)** potential linear response of the bromide-selective sensor.

This observation can be evaluated as a result of the prepared electrode composition. The developed bromide-selective sensor exhibited a linear response to the bromide ions in the concentration range of $1.0 \times 10^{-1} - 1.0 \times 10^{-4}$ mol L^{-1} (Fig 3B). To calculate the detection limit of the bromide-selective sensor, the potential value corresponding to the point where the extrapolations of the two linear regions in the graph intersect was determined (Fig 3A). The resulting value was written in the correct equation ($E = 34.9 \log [Br^-] + 1413$) of the graph. Consequently, the detection limit of the sensor was determined to be 2.2×10^{-5} mol L^{-1}.

Reusability of the bromide-selective sensor

Reusability is considered one of the most important characteristics in evaluating sensor performance [20]. The developed bromide-selective sensor was exposed repetitively to bromide ion solutions at different concentrations ($1.0 \times 10^{-1} - 1.0 \times 10^{-3}$ mol L^{-1}). The results are shown in Fig. 4 and Table 2. Based on these data, it can be seen that the proposed bromide-selective sensor has a good reusability and stability.

Selectivity of the bromide-selective sensor

The selectivity is the behavior of the sensor towards the primary ion in the presence of foreign ions, and it is a highly important parameter for the performance of ion-selective electrodes. Thus, the influence of a number of anions (ClO_3^-, CH_3COO^-, PO_4^{3-}, NO_3^-, SO_4^{2-}, CO_3^{2-}, NO_2^-, Cl^-) on the selectivity behavior of the developed bromide-selective sensor was investigated in the current study. Potentiometric selectivity coefficients of the bromide-selective sensor were calculated according to the IUPAC recommendation by using a separate solution method [21]:

$$log K_{A,B}^{pot} = \frac{(E_B - E_A) Z_A F}{RT ln 10} + (1 - \frac{Z_A}{Z_B}) log a_A$$

where E_A is the potential measured in 1.0×10^{-2} mol L^{-1} bromide solution, E_B the potential measured in 1.0×10^{-2} mol L^{-1} interferent anion solutions, Z_A and Z_B are the charges of bromide and interfering ions, respectively, a_A is the activity of bromide and R, T, and F have the usual meanings. The selectivity coefficients ($log K_{Br^-,X^-}^{pot}$) of the bromide-selective sensor are presented in Table 3. The data show that the sensor is highly selective for bromide ions even in the presence of other anions.
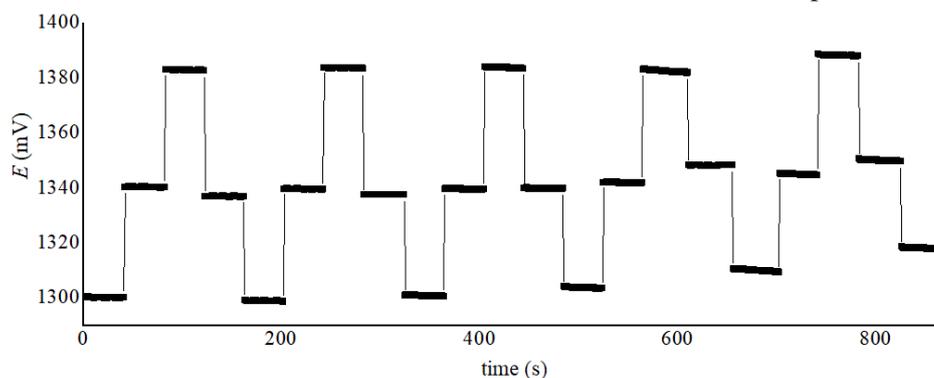
Fig. 4. Reusability of the bromide-selective sensor.

Table 2. Reusability results of the bromide-selective sensor.

Br⁻ solution	Potential (mV)					
	I	II	III	IV	V	Average (± SD) *
1.0×10^{-1}	1383.2	1383.6	1383.8	1383.3	1387.0	1384.2 (± 1.43)
1.0×10^{-2}	1340.2	1339.8	1340.0	1340.6	1343.8	1340.9 (± 1.48)
1.0×10^{-3}	1300.2	1300.2	1301.2	1303.8	1305.0	1302.0 (± 1.97)

*Potential values are given for five separate experimental measurements (I-V) (n = 5)

Table 3. Selectivity coefficient values for the bromide-selective sensor.

Interfering ions	Selectivity coefficient, $logK_{Br^-,X^-}^{pot}$
ClO_3^-	-1.83
CH_3COO^-	-2.32
PO_4^{3-}	-2.34
NO_3^-	-2.37
SO_4^{2-}	-2.46
CO_3^{2-}	-2.53
NO_2^-	-2.67
Cl^-	-2.78

pH dependence of the bromide-selective sensor

The working pH range of the bromide-selective sensor was obtained by using sodium hydroxide (1.0×10^{-2} mol L⁻¹) and hydrochloric acid (1.0×10^{-2} mol L⁻¹) solutions. The bromide solution (1.0×10^{-2} mol L⁻¹) was added to each pH solution (2.0 – 12.0) and measurements were taken for bromide solutions prepared at different pH values. The working pH range measurement results are shown in Fig. 5. Figure 5 shows that the bromide-selective sensor works in the pH range of 4.0 – 10.0, without being affected by the changes in pH.
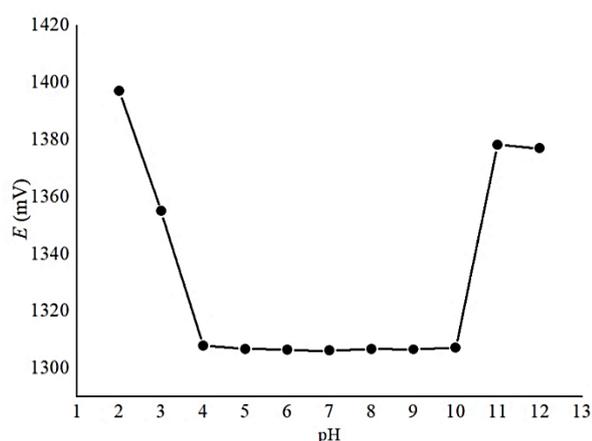
Fig. 5. Effect of pH on the potential of the bromide-selective sensor.

Response time of the bromide-selective sensor

According to the definition made by IUPAC, we determined the response time of the developed sensor [21]. Accordingly, until the sensor reaches 95% of the equilibrium potential, data were obtained after successive immersions of the electrode in a series of bromide ion solutions, each having a ten-fold difference in concentration. The bromide concentration was very rapidly increased from 1.0×10^{-4} to 1.0×10^{-1} mol L⁻¹ and values were measured. The static response time for bromide-selective sensor was observed to be 10 s.

Analytical applications

The developed sensor was successfully used to determine bromide ions in real samples such as purified and commercial drinking water. Known amounts of bromide solution were added to the water samples according to the standard addition method. Bromide analysis was performed in the water samples with the developed sensor. The results are given in Table 4. It can be clearly seen from the table that high recovery is obtained for the determination of bromide in two different water samples.

Table 4. Determination of bromide in water samples.

Real Sample	Added Br⁻ (mol L⁻¹)	Mean (± SD) found with sensor[a] (mol L⁻¹)	% Recovery
commercial drinking water	6.00×10^{-4}	$5.75\ (\pm 0.117) \times 10^{-4}$	95.83
purified drinking water	7.00×10^{-4}	$6.03\ (\pm 0.212) \times 10^{-4}$	86.42

[a]Average value ($n = 3$).

CONCLUSION

In the literature, many potentiometric sensors have been developed for the detection of cations and anions in various samples. In this study, a new bromide-selective sensor was developed and its working conditions were determined. The developed sensor displays a linear concentration range from 1.0×10^{-4} to 1.0×10^{-1} mol L⁻¹ with a detection limit of 2.2×10^{-5} mol L⁻¹. The sensor has a very fast response time, good reusability and good performance over a wide pH range. In addition, we showed that the sensor could be successfully applied to the determination of bromide in water samples.

REFERENCES

1. E. P. Borges, A. F. Lavorante, B. F. Reis, *Anal. Chim. Acta*, **528**, 115 (2005).
2. M. Neal, C. Neal, H. Wickham, S. Harman, *Hydrol. Earth Syst. Sci*., **11**, 294 (2007).
3. G. V. Ram Reddy, A. P. Kumar, B. V. Reddy, J. Sreeramulu, J. H. Park, *J. Liq. Chromatogr. Relat. Technol.*, **32**, 2866 (2009).
4. M. O. Gorbunova, M. S. Garshina, M. S. Kulyaginova, V. V. Apyari, A. A. Furletov, A. V. Garshev, S. G. Dmitrienko,˙ Y. A. Zolotov, *Anal. Methods*, **12**, 587 (2020).
5. K. Uraisin, T. Takayanagi, M. Oshima, D. Nacapricha, S. Motomizu, *Talanta*, **68**, 951 (2006).
6. W. Liu, H. Yang, B. Li, S. Xu, *Geostand. Geoanal. Res.,* **35**, 69 (2009).
7. P. L. Garcıa, F. P. Gomes, M. I. Rocha, M. Santoro, E. R. M. Kedor-Hackmann, *Anal. Lett.*, **41**, 1895 (2008).
8. B. Yuan, J. P. Benskin, C. L. Chen, A. Bergman, *Environ. Sci. Technol. Lett*., **5**, 348 (2018).
9. P. Kumar, S. Kumar, S. Jain, B. Y. Lamba, G. Joshi, S. Arora, *Electroanal*., **26**, 2161 (2014).
10. F. Kardas, C. Topcu, *Pamukkale Univ. Muh. Bilim Derg*., **24**, 1325 (2018).
11. O. Isildak, O. Özbek, M. B. Gürdere, *J. Anal. Test.*, 1 (2020). https://doi.org/10.1007/s41664-020-00147-8
12. O. Özbek, Ö. Isildak, M. B. Gürdere, C. Berkel, *Int. J. Environ. Anal. Chem.,* 1 (2020). https://doi.org/10.1080/03067319.2020.1817427
13. C. Jiang, Y. Yao, Y. Cai, J. Ping, *Sensor Actuat. B-Chem*., **283**, 284 (2019).
14. O. Özbek, C. Berkel, Ö. Isildak, *Crit. Rev. Anal. Chem.,* 1 (2020). https://doi.org/10.1080/10408347.2020.1825065
15. E. Khaled, E. M. Shoukry, M. F. Amin, B. A. M Said, *Electroanal*., **30**, 2878 (2018).
16. O. Özbek, Ö. Isildak, C. Berkel, *J. Incl. Phenom. Macrocycl. Chem.*, **98**, 1 (2020).
17. O. Isildak, N. Deligönül, O. Özbek, *Turk. J. Chem*., **43**, 1149 (2019).
18. O. Isildak, O. Özbek, K. M. Yigit, *Int. J. Environ. Anal. Chem.,* 1 (2019). https://doi.org/10.1080/03067319.2019.1691542
19. O. Isildak, O. Özbek, *J. Chem. Sci.*, **132**, 29 (2020).
20. O. Isildak, O. Özbek, *Crit. Rev. Anal. Chem.,* 1 (2020). https://doi.org/10.1080/10408347.2019.1711013
21. IUPAC, *Pure Appl. Chem*., **72**, 1851 (2000).

Clerodane diterpenoids from *Teucrium scordium* L. subsp. *scordioides* (Shreb.) Maire et Petitmengin

P. I. Bozov[1]*, P. N. Penchev[2], Y. P. Georgieva[3], V. K. Gochev[1]

[1] Department of Biochemistry and Microbiology, Plovdiv University, 24 Tsar Asen Str., 4000, Plovdiv, Bulgaria
[2] Department of Analytical Chemistry, Plovdiv University, 24 Tsar Asen Str., 4000, Plovdiv, Bulgaria
[3] Department of Pharmacognosy and Pharmaceutical Chemistry, Faculty of Pharmacy, Medical University of Plovdiv, 120 Bratya Bukston Blvd., 4000, Plovdiv, Bulgaria

Three clerodane diterpenoids, 6-acetyl teucrin F (**1**), teucrin E acetate (**2**) and 3α-acetoxy-teucvin (**3**) were isolated by the phytochemical investigation of the acetone extract from the aerial parts of *Teucrium scordium* L. subsp. *scordioides* (Shreb.) Maire et Petitmengin, (Lamiaceae). The structure and stereochemistry of the compounds were established by IR spectrum, HR-ESIMS and different ^{1}H NMR and 2D-NMR techniques. Compounds **1** and **2** are isolated for the first time from a natural source while compound **3** is a new natural product.

Keywords: *Teucrium scordium* subsp. *scordioides,* Lamiaceae*, neo*-clerodane diterpenes, *nor*-clerodane diterpenes.

INTRODUCTION

The genus *Teucrium* (Lamiaceae) covers about 360 species spread in different climatic zones. The plants are honey-bearing with medical use. Paws and infusion of the plants have been applied for centuries in open wound healing, treatment of gastrointestinal pains, diabetes, inflammations, rheumatism and other disorders. They are also used as diuretic, antipyretic, tonic, diaphoretic, analgesic [1]. Furanoid clerodane diterpenoids are the main biological active constituents of the plants from *Teucrium* genus [2-5].

The species *T. scordium* L. covers two subspecies, *scordium* and *scordioides* (Shreb.) Maire et Petitmengin. From 1985 to 1988 Papanov and Malakov isolated five new furanoid *neo*-clerodane diterpenoids from *T. scordium* subsp. *scordium*: teuscordinon (**4**) [6], 6-ketoteuscordin (**5**) and 6α-hydroxyteuscordin (**6**) [7], 6β-hydroxyteuscordin (**7**) [8], 2-keto-19-hydroxyteuscordin (**8**) [9], besides the previously known diterpenoids: 2β,6β-dihydroxyteuscordin (= teugin, **9**) [8, 10], teucrin E (**10**) [9, 11] and teucrin H₄ (**11**) [9, 12] (Fig. 1). In 1985 Jakupovic *et al.* [13] reinvestigated this species (collected at the Heidsee, Rosengarten-Raibach, near Schwäbisch-Hall, West Germany) and obtained 13 compounds; the known *neo*-clerodanes **4, 6, 7, 9**, **10**, dihydroteugin (**12**) [14], teucjaponin B acetate (**13**) [15], teucroxide (**14**) [16] and five new furano-clerodanes: 2,3-dehydroteucrin E (**15**), 2β,6α-dihydroxyteuscordin (**16**), 2β-hydroxyteuscordinone (**17**), 6,20-bisdeacetylteupyreinidin (**18**) and 6-deacetyl-teupyreinidin (**19**) (Fig. 1).

The experimental data about chemistry and pharmacology of *T. scordium* L. subsp. *scordioides* are scarce. The previous studies had shown the presence of polyphenols, *β*-sitosterol, tannins and bitter principles compounds [17], and the monoterpene menthofuran (11.9%) predominated in the essential oil of the plant [18]. In the literature there are no data about diterpenoid contents. Cytotoxicity and antimicrobial activity of cyclohexane, dichloromethane and methanol extracts of *T. scordium* subsp. *scordioides* have been studied [19]. Cyclohexane and dichloromethane extracts showed high cytotoxicity against MDA-MB-361 cells (IC$_{50}$ = 130.33 ± 0.1 μg/mL and I$_{C50}$ = 189.89 ± 3.99 μg/mL, respectively). Dichloromethane extract was more effective against MDA-MB-453 cell line with IC$_{50}$ = 130.33 ± 0.1 μg/mL. The methanol extract possessed no cytotoxicity against breast cancer cell lines, MDA-MB-361 and MDA-MB-453. The extracts of the plant had shown weak antibacterial activity on *Pseudomonas aeruginosa*, *Klebsiella pneumoniae*, *Escherichia coli* and *Bacillus subtilis* and didn't possess any activity against *Staphylococcus aureus*, *S. epidermidis*, *Micrococcus luteus*, *Enterococcus faecalis*, and *Candida albicans*.

Continuing our ongoing research of *neo*-clerodane diterpene composition of *Teucrium* species [20] we investigated *T. scordium* L. subsp. *scordioides*. We report herein on the isolation and structure elucidation of three clerodane diterpenes, 6-acetyl teucrin F (**1**), teucrin E acetate (**2**) and 3α-acetoxy-teucvin (**3**) (Fig. 2).

---

* To whom all correspondence should be sent:
E-mail: bozov@uni-plovdiv.bg

	R	R₁	R₂	R₃	Δ
teuscordinone (**4**)	H	= O		H	Δ³
6-ketoteuscordin (**5**)	H	= O		H	-
6α-hydroxyteuscordin (**6**)	H	H	OH	H	Δ³
6β-hydroxyteuscordin (**7**)	H	OH	H	H	Δ³
teugin (**9**)	H	OH	H	OH	Δ³
teucrin E (**10**)	H	H	OH	H	-
dihydroteugin (**12**)	H	OH	H	OH	-
2,3-dehydroteucrin E (**15**)	H	H	OH	H	Δ²
2β,6α-dihydroxyteuscordin (**16**)	H	H	OH	OH	Δ³
2β-hydroxyteuscordinone (**17**)	H	= O		OH	Δ³

2-keto-19-hydroxyteuscordin (**8**)   teucrin H₄ (**11**)

teucjaponin B acetate (**13**)   teucroxide (**14**)

	R
6,20-bisdeacetylteupyreinidin (**18**):	H
6-deacetylteupyreinidin (**19**):	Ac

Fig. 1. Structures of the previously isolated clerodane diterpenoids from *T. scordium* subsp. *scordium*.

	R
6-acetyl teucrin F (**1**):	Ac
teucrin F (**20**):	H

teucrin E acetate (**2**)

	R
3α-acetoxy-teucvin (**3**):	OAc
teucvin (**21**):	H
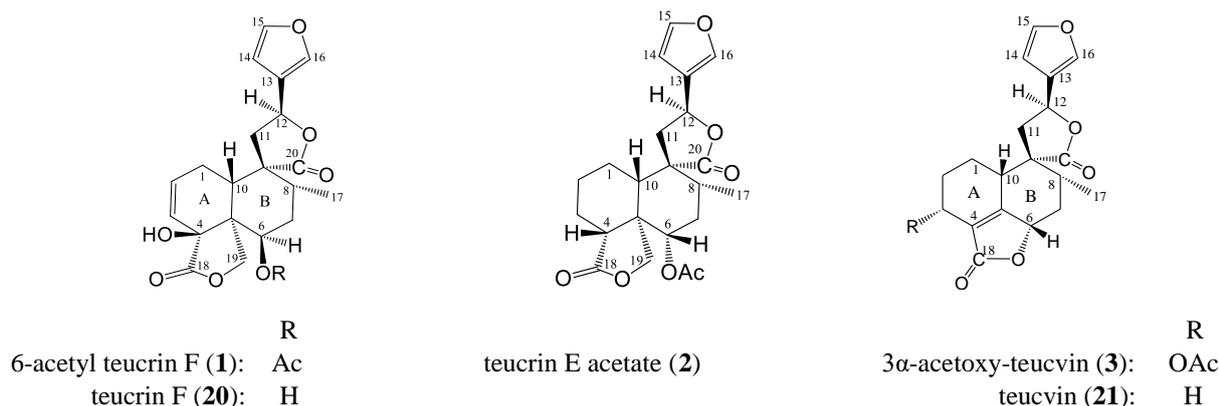
Fig. 2. Structures of the isolated and used in the discussion clerodane diterpenoids.

Although compounds **1** and **2** were previously semi-synthetically prepared by acetylation with acetic anhydride / pyridine of the corresponding hydroxyl derivatives isolated from *Teucrium hamaedris*, in the present study they were isolated for the first time from a plant source. For compound **1** synthesized before by acetylation of teucrin F (**20**), almost all ¹H and ¹³C NMR signals had been

454

assigned [21]. We only interchanged reported values for C-2 and C-3. Compound **2**, synthesized before by acetylation of teucrin E (**10**), had been published with ^{1}H NMR data only [22]. In this study, fully assigned ^{13}C NMR data of compounds **1** and **2** are included in Table 1.

EXPERIMENTAL

Structural data

^{1}H NMR spectra were recorded on Bruker Avance II+ spectrometers, operating at 600.01 MHz. ^{13}C NMR spectra were recorded at 150.89 MHz spectrometer. TMS was used as an internal standard and CDCl$_3$ as solvent (δ_C 76.00, δ_H 7.260). Chemical shifts (δ) are expressed in ppm and coupling constants (J) in Hertz. The IR spectra were registered in KBr pellet on a Bruker Tensor 27 spectrometer from 4000 cm^{-1} to 400 cm^{-1} at resolution 4 cm^{-1} with 70 scans. The mass spectra were measured on Hewlett Packard 6890 GC System Plus/5973 MSD. The melting points were determined by a STUART SMP-10 digital melting point instrument. Specific optical rotation values were measured on Jasco P-2000 polarimeter (Tokyo, Japan) at D line of sodium lamp at 20 ºC by using 0.5 dm quartz cell. The [α]$_D$ are given in deg.cm^3.g^{-1}.dm^{-1}, concentration in g.cm^{-3}.

Plant material

The aerial parts of *Teucrium scordium* L. subsp. *scordioides* (Shreb.) Maire et Petitmengin were collected in Jun 2019 around village Staro Orehovo near Varna, Bulgaria, and voucher specimens (n. 7212) were deposited in the Herbarium of the Higher Institute of Agriculture at Plovdiv, Bulgaria.

Extraction and isolation

Dried and finely powdered material (1.100 kg) were extracted with Me$_2$CO (3 × 5 L) at room temperature for a week. After filtration, the solvent was evaporated to dryness under reduced pressure and low temperature (<40 °C) yielding a gum (20.0 g), which was dissolved in aq. Me$_2$CO (40 % H$_2$O, v/v, 200 mL). This solution was cooled to 4 °C for 24 h and filtered. The filtrate was extracted with CHCl$_3$ (3 × 150 mL) and the organic layer was dried (Na$_2$SO$_4$) and evaporated in vacuum to afford a residue (5.8 g, bitter fraction). This residue was subjected to CC (70 g silica gel Merck n. 7734, deactivated with 10% H$_2$O, w/w). Pure petroleum ether (12 L), followed by a gradient of CH$_2$Cl$_2$ – CH$_3$OH mixtures (10:0 to 9.7:0.3) were used as eluting solvents. Eluting with CH$_2$Cl$_2$ – CH$_3$OH mixtures 9.8:0.23 resulted in the isolation of three diterpenoids, 25 mg of 6-acetyl teucrin F (**1**), 18 mg of teucrin E acetate (**2**) and 25 mg of 3α-acetoxy-teucvin (**3**).

6-Acetyl teucrin F (*1*)

Colorless powder. MP: 207-209 C° (from MeOH), [α]$_D$ + 14 ± 1 (c = 0.77, MeOH), TLC: R$_f$ 0.58 (EtOAc). IR ν$_{max}$ (KBr): 3437, 2963, 2934, 1761, 1505, 1450, 1373, 1239, 1178, 1043, 1023, 875, 754, 603 cm^{-1}. ^{1}H and ^{13}C NMR: see Table 1. Positive ESIMS (70 eV, direct inlet) m/z (rel. int. in %): 439 [M+Na]$^+$ (92.4), 423 (22.3), 399 (9.1), 357 (14.6). HRESIMS m/z 439.1367 [M+Na]$^+$, (calcd. for C$_{22}$H$_{24}$O$_8$Na: 439.1369).

Teucrin E acetate (*2*)

Colorless powder. MP: 201-203 C° (from MeOH), TLC: R$_f$ 0.52 (EtOAc). IR ν$_{max}$ (KBr): 3147, 2965, 2933, 1764, 1506, 1473, 1373, 1240, 1180, 1025, 875, 754, 727, 667, 603 cm^{-1}. ^{1}H and ^{13}C NMR: see Table 1. Positive ESIMS (70 eV, direct inlet) m/z (rel. int. in %): 403 [M+H]$^+$ (95.4), 343 (55.6), 297 (8.5). HRESIMS m/z 403.1757 [M+H]$^+$, (calcd. for C$_{22}$H$_{26}$O$_7$H 403.1753).

3α-Acetoxy-teucvin (*3*)

Colorless powder. MP: 223-224 C° (from MeOH), [α]$_D$ + 201 ± 1 (c = 0.9, MeOH), TLC: Rf 0.49 (EtOAc). IR ν$_{max}$ (KBr): 3146, 2932, 1761, 1506, 1450, 1373, 1239, 1178, 1043, 1022, 974, 875, 753, 603 cm^{-1}. ^{1}H and ^{13}C NMR: see Table 1. Positive ESIMS (70 eV, direct inlet) m/z (rel. int. in %): 409 [M+Na]$^+$ (96.0), 349 (4.2), 327 (14.3), 309 (5.7). HRESIMS m/z 409.1270 [M+Na]$^+$ (calcd. for C$_{21}$H$_{22}$O$_7$Na: 409.1263).

RESULTS AND DISCUSSION

Based on the pseudo-molecular positive ion peak at m/z 439.1367 [M+Na]$^+$ in HR-ESIMS of compound **1** (see supplementary data section) was established molecular formula C$_{22}$H$_{24}$O$_8$ (calcd. for C$_{22}$H$_{24}$O$_8$Na: 439.1369) indicating 11 degrees of unsaturation. In its IR spectrum were observed absorptions consistent with the presence of a furan ring (3147, 1505 and 875 cm^{-1}), lactone and acetate functions (1761 broad, 1178 and 1239 cm^{-1}) and hydroxyl group (3437 cm^{-1}).

The ^{13}C NMR spectrum displayed the presence of twenty-two carbons, and a DEPT experiment identified two methyl (one of them from acetyloxy group), four methylene (one of them oxygenated, CH$_2$-19), nine methine (including three aromatic and two olefinic, five methines are oxidized) and seven quaternary carbon atoms (including two olefinic, one furan, one oxygenated and three for carbonyl groups – one from acetyloxy group and two from γ-lactones) (see Table 1).

Table 1. 6-Acetyl teucrin F (**1**), teucrin E acetate (**2**) and 3α-acetoxy-teucvin (**3**) NMR data [a]

Position	**1**			**2**			**3**		
	δ ^{13}C, nH	δ ^{1}H	m, J (in Hz)	δ ^{13}C, nH	δ ^{1}H	m, J (in Hz)	δ ^{13}C, nH	δ 1H	m, J (in Hz)
1α	25.19, CH$_2$	2.085	m	25.03, CH$_2$	1.57	m^c	19.93, CH$_2$	2.13	ov m^c
1β		2.589	m^c		2.06	ov m^c		1.68	ov m^c
2α	129.85, CH	6.097	ddd, 10.0; 5.2; 2.1	22.5, CH$_2$	2.03	ov m^c	27.92, CH$_2$	2.18	ov m^c
2β					1.51	m^c		1.69	ov m^c
3α	125.56, CH	5.547	m	23.1, CH$_2$	1.45	m^c	60.39, CH	5.601	br s
3β					1.90	m^c		-	-
4	75.85, C	-		46.01, CH	2.165	br s	124.66, C	-	
5	47.84, C	-		45.98, C	-		167.46, C	-	
6α	68.04, CH	5.411	dd, 4.0; 2.0	78.33, CH	-		78.04, CH		
6β		-			4.757	dd, 12.1; 3.8		4.815	dd, 5.5, 3.7
7α	31.84, CH$_2$	2.343	ddd, 14.8, 12.7, 2.0	31.82 CH$_2$	1.81	ov^c	34.76, CH$_2$	2.24	m^c
7β		1.694	dt, 14.8; 4.0		2.21	ov^c		2.37	m^c
8β	32.88, CH	2.179-2.095	m	37.95, CH	1.77	ov^c	35.74, CH	1.938	ddq, 12.6; 3.3; 6.8
9	51.57, C	-		50.89, C	-		53.59, C	-	
10β	37.23, CH	2.653-2.596	m	47.43, CH	1.79	ov^c	42.00, CH	2.70	m^c
11B	42.57, CH$_2$	2.574	dd, 14.3; 8.8	41.72, CH$_2$	2.365	dd, 14.5; 8.9	40.71, CH$_2$	2.584	br d, 8.5
11A		2.474	dd, 14.3; 8.8		2.445	dd, 14.5; 8.9		2.584	br d, 8.5
12α	72.12, CH	5.427	ov	71.88, CH	5.376	t, 8.9	71.76, CH	5.462	t, 8.5
13	124.59, C	-		124.69, C	-		124.08, C	-	
14	107.98, CH	6.406	dd, 1.8; 0.8	107.90, CH	6.376	dd, 1.8; 0.8	107.88, CH	6.392	br s
15	144.33, CH	7.459	t, 1.8	144.30, CH	7.451	br d, 1.8	144.33, CH	7.456	t, 1.6
16	139.62, CH	7.477	dt, 1.8; 0.8	139.62, CH	7.440	m	139.55, CH	7.465	br s
Me-17	16.44, CH$_3$	1.004	d, 6.8	16.40, CH$_3$	1.026	d, 6.6	16.88, CH$_3$	1.096	d, 6.8
18	176.04, C	-		176.54	-		170.72	-	
19B[b]	68.99, CH$_2$	4.536	d, 11.3	68.39, CH$_2$	4.788	d, 11.3	-	-	-
19A		4.118	d, 11.3		4.307	d, 11.3	-	-	-
20 (C=O)	177.51, C	-		178.49, C	-		174.92, C	-	
6^1 (C=O)	170.15, C	-		170.84, C	-		-		
6^2 (Me)	21.48, CH$_3$	2.041	s	20.97, CH$_3$	2.038	s	-		
3^1 (C=O)							170.50, C	-	
3^2 (Me)							21.17, CH$_3$	2.060	s

[a] CDCl$_3$, ^{1}H 600.01 MHz, δ_{ref} 7.26; ^{13}C 150.9 MHz, δ_{ref} 77.0 ppm, TMS as an internal standard; [b] endo hydrogen with respect to ring B; [c] data from HSQC; ov overlapped signal.

The presence of furan ring in the molecule was confirmed by the signals at δ_C 124.59 (C-13), 107.98/δ_H 6.406 (dd, CH-14), 144.33/7.459 (t, CH-15) and 139.62/7.477 (dt, CH-16) in the ^{13}C and ^{1}H NMR spectra. Assignments of the furan protons to the corresponding carbon atoms were in agreement with the data from the HSQC spectrum and the observed HMBC correlations. The presence of two γ-lactone rings, formed between C-20 and C-12, as well as C-18 and C-19, was supported by the

specific signals in the ^{1}H and ^{13}C NMR spectra. For carbonyl groups the signals were at δ_C 177.51 (C-20) and 176.04 (C-18), for oxygenated methine group – at δ_C 72.21/δ_H 5.427 t (CH-12) and for oxygenated methylene group – at δ_C 68.99/δ_H 4.536 d and 4.227 d (CH$_2$-19). These conclusions are in agreement with the correlations observed in the HMBC and COSY spectra.

Attachment of the acetyloxy group at C-6 was established by the HMBC correlations from H-6α

(δ_H 5.411, dd) to 6^1 (δ_C 170.15, C=O) and from 6^2 (δ_H 2.041, 3H) to C-6 (δ_C 68.04). The location of the acetyl ester in β-position and H-6 in α-position was in agreement with the small value of 4.2 Hz and 2.0 Hz for the coupling constants of the δ_H 5.411 dd due to the equatorial methine proton H-6. This conclusion was supported by the observed interaction in the NOESY experiment of H-6 with the downshifted doublet at δ_H 4.536, which was assigned for one of the methylene protons of oxygenated C-19 (δ_C 68.99).

Both olefin carbons, resonated at δ_C 129.85 and 125.56, are methine atoms. This fact determines the double bond to be formed between C-1 – C-2 or between C-2 – C-3. On the ground of the multiplicity and the coupling constants value (Table 1) of the signal for H-3 (dq, J = 10.0, 1.3) we concluded that in compound **1** Δ^2 olefinic bond was present. In case of presence of Δ^1 double bond the signal for H-1, equivalent to H-3 in compound with Δ^2 olefinic bond, would be with a more complicated multiplet structure due to the presence of an additional adjacent proton (H-10).

^{1}H and ^{13}C NMR data of **1** are identical in all respects with those reported by Rodriguez *et al.* [21] for 6-acetyl teucrin F obtained by treatment of teucrin F (**20**) with acetic anhydride/pyridine. Authors have assigned the signals at δ_C 125.56 of C-2 and 129.85 of C-3. Based on the observed HSQC correlations between the signals δ_C 129.85/δ_H 6.097 and δ_C 125.56/δ_H 5.547 we exchanged the signals of these methine carbons: δ_C 129.85 of C-2 and δ_C 125.56 of C-3.

The relative configuration of **1** was determined by the observed NOESY correlations H-1β/H-12α, H-11A/H-12α, H-11B/H-14 and H-11B/H-16. The NOESY correlations Me-17/H-11B, Me-17/H-14 and Me-17/H-16 indicated that the furan ring was in the β-configuration. Moreover, the correlations of H-6 with H-7α, H-19A, H-1α /H-19A and H-7α / H-19B, showed their co-facial relationship and were assigned in α-position. On the ground of all shown above data for **1** a structure of 6-acetyl teucrin F was assigned as depicted in Figure 2.

The HR-ESIMS of compound **2**, with the trivial name teucrin E acetate, showed a pseudo-molecular positive ion peak at m/z 403.1757 [M+H]$^+$, which indicated the molecular formula of $C_{22}H_{26}O_7$, (calcd. for $C_{22}H_{26}O_7H$: 403.1753). Compared to compound **1**, the molecular formula of teucrin E acetate contains two additional hydrogen atoms, and one oxygen atom less, corresponding to 10 degrees of unsaturation

In the IR spectrum of **2** were observed absorption bands consistent with the presence of a furan ring (3147, 1506, 1113 and 875 cm^{-1}), lactone and acetate groups (1764 broad, 1180 and 1240 cm^{-1}).

The ^{13}C NMR spectrum displayed the presence of twenty-two carbons, and a DEPT experiment identified two methyl, six methylene, eight methine (three from furan double bonds, four methines are oxygenated) and six quaternary (two of which were aliphatic, one was for aromatic carbon and the rest three for carbonyl groups at δ_C 176.54 and 178.49 for γ-lactones and 170.84 for acetate) carbon atoms (Table 1).

The ^{1}H and ^{13}C NMR spectral data of **2** revealed very similar structure to that of compound **1**. The only differences in the NMR spectra of **2** were the lack of the characteristic signals in the NMR spectrum of **1** for two olefin methine carbons C-2 and C-3 at δ_C 129.85, CH/δ_H 6.097 ddd and δ_C 125.56, CH/δ_H 5.547 dq, and for quaternary oxygenated carbon atom C-4 at δ_C 75.85, C-4). Instead, characteristic signals for C-4/Hβ methine group appeared at δ_C 46.01, CH /δ_H 2.165 br s.

The acetyloxy substituent was localized at C-6 again, according to the observed HMBC correlations from H-6 to C-6^1 (CO) and from the methyl protons H$_3$-6^2 to C-6, and the COSY correlations of H-6 to H-4, H-7α, H-7β and H-8. This time the acetyloxy group was determined to be α-oriented. This conclusion was based on the large value of the $J_{6,7}$ constant for the signal of the axial H-6β (δ_H 4.757 dd, J = 12.1, 3.8) and from the observed NOESY interaction between H-6β/H-4β, H-6β/8β and H-6β/10β.

The furan ring was placed in β-position according to the observed in the NOESY spectrum correlations of H-12α with H-1β and H-11α, of H-11β with H-14 and H-16 and of Me-17 with H-11β, H-14 and H-16. The interaction of H-6 with H-4, H-8 and H-10 demonstrated their co-facial relationship and β-orientation. On the other hand, the interactions of H-7α with H-19A, H$_3$-6^2 and H$_3$-17, and of H-19B with H-2α revealed their α-positions.

^{1}H NMR data of **2** were the same as those of the derivative obtained by acetylation of teucrin E (**10**) [22]. Therefore, the structure of compound **2** was elucidated as teucrin E acetate, as depicted in Figure 2.

For 3α-acetoxy-teucvin (**3**) the molecular formula $C_{21}H_{22}O_7$ was established by the pseudo-molecular positive ion peak in its HRESIMS at m/z 409.1270 [M+Na]$^+$ (calcd. for $C_{21}H_{22}O_7Na$: 409.1263) indicating 11 degrees of unsaturation. The odd number of C-atoms suggested a structure with a 19-*nor*-clerodane skeleton or a presence of a methoxy group in the molecule.

In the IR spectrum of **3** absorption bands consistent with the presence of a furan ring (3146, 1506, 1069 and 875 cm^{-1}), lactone and acetate groups (1761 broad, 1178 and 1240 cm^{-1}) were observed.

The ^{13}C NMR spectrum displayed the presence of twenty-one carbons, and a DEPT experiment identified two methyl, four methylene, eight methine (three of them aromatic, oxygenated carbons were five) and seven quaternary (including three carbonyl, at δ_C 174.92 from γ-lactone, 170.72 from α,β-unsaturated γ-lactone, 170.50 from acetate; three olefinic at δ_C 124.08, 124.66, 167.46 and one aliphatic at δ_C 53.59) carbon atoms.

No methoxy group signals were observed in the ^{1}H and ^{13}C NMR spectra. Characteristic signals for the methylene protons H$_2$-19 were missing, too. Acetyloxy group signals (δ_C 170.50, C=O; δ_C 21.17/δ_H 2.060 s, CH$_3$) and a signal at δ_H 5.601 br s for its geminal proton were present in the spectra. The aforementioned data define **3** as a diterpenoid with 19-*nor*-furoclerodane dilactone skeleton with an acetyloxy substituent. Spectral data for the C-11 – C-16 substructure were very close to that for diterpenes **1** and **2**. The formation of C-20 – C-12 γ-lactone and β-oriented furan ring at C-12 in **3** was confirmed by the analysis of the 2D experiments, analogous to that described by the structural elucidation of **1.** Thus, the correlations from methylene protons H$_2$-11 to C-12, C-13, C-20, from H-12 to C-13, C-14, C-16, from H-14 to C-13, C-15, C-16, from H-15 to C-16 and from H-16 to C-13, C-14, C-15 are presented in the HMBC spectrum. The β-orientation of the furan ring was confirmed by the NOESY interaction of H$_3$-17 with H-14 and H-16.

The signals at δ_C 124.66 and 167.46, for quaternary olefin carbon atoms, were assigned to C-4 and C-5. They were part of an α,β-unsaturated γ-lactone constructed between C-18 and C-6. This conclusion was supported by the characteristic signal at δ_H 4.815 (dd) for an axial methine proton H-6 geminal to an oxygen atom and by the HMBC correlations from H-7β to C-6 and from methyl protons H$_3$-17 to C-6. The other possible position of the double bond between C-5 and C-10 was excluded due to the observed COSY correlations of H-10 with H-1β and H-1α and NOESY correlations of H-10 with H-1β, H-2β, H-3β and H-11A.

The linkage of the fragment C-18–O– to the C-6 with alpha bond was established by the observed NOESY correlation of the axial H-6β with H-7β, H-8β and H-10β indicating that all these protons were co-facial and β-oriented.

The acetyloxy group was attached to C-3 on the ground of the H^1-H^1 COSY correlation of the geminal to the acetyloxy group proton H-3β (δ_H 5.601) with H-6β (δ_H 4.815) and with H-10β (δ_H 2.685). This conclusion was supported by the HMBC correlation from H-1α (δ_H 2.13) to C-3 (δ_C 60.39) and from H-2α (δ_H 2.18) to the methyl carbon of the acetoxy group C-3^2 (δ_C 21.17). The *a*-orientation of the acetate group was determined by the small value of the *J* constants of the signal (br s) for the pseudo-equatorial H-3 by the coupling with the adjacent protons H-2α and H-2β. This assumption was confirmed by the NOESY interaction of H-3 with H-2α and with H-2β indicating that H-3 was in pseudo-equatorial position and in this case beta-oriented.

Therefore, the new compound **3** was assigned as 3α-acetoxy derivative of teucvin (**21**) isolated by Fujita and Uchida from *Teucrium viscidurn* var. *miquelianum* [23].

CONCLUSION

The 6-acetyl teucrin F (**1**) and teucrin E acetate (**2**) isolated in this study are *neo*-clerodane diterpenoids belonging to a furoclerodane series with 10β-18,19;20,12-diolide functions. It can be noted that compounds from the same series have been previously found in *T. scordium* L. subsp. *scordium*. In contrast, diterpenoids with furoclerodane-10β-18,6α;20,12-diolide structure as that of the new 3α-acetoxy-teucvin (**3**) have not been detected in *T. scordium* L. *subsp. scordium* so far. The accumulation of furoclerodane compounds with 10β-18,19;20,12-diolide functions in *Teucrium scordium* L. subsp. *scordioides* and *T. scordium* L. subsp. *scordium* could be of chemotaxnomic interest.

REFERENCES

1. A. Ulubelen, G. Topcu, U. Sonmez, *Studies in Nat. Prod. Chem.*, **23**, 591 (2000).
2. L. Rodriguez-Hahn, B. Esquivel, J. Cardenas, *Fortschritte der Chemie organischer Naturstoffe / Progress in the Chemistry of Organic Natural Products*, **II** (3), 121 (1994).
3. M. Bruno, F. Piozzi, S. Rosselli, *Nat. Prod. Rep.*, **19**, 357 (2002).
4. F. Piozzi, M. Bruno, S. Rosselli, A. Maggio, *Heterocycles*, **65** (5), 1221 (2005).

5. A. Fiorentino, B. D'Abrosca, S. Pacifico, M. Scognamiglio, G. D'Angelo, M. Gallicchio, A. Chambery, P. Monaco, *Phytochem.*, **72**, 2037 (2011).

6. G. Y. Papanov, P. Y. Malakov, F. Bohlmann, *Phytochem.*, **20**, 170 (1981).

7. G. Y. Papanov, P. Y. Malakov, *Z. Naturforsch.*, **36b**, 112 (1981).

8. G. Y. Papanov, P. Y. Malakov, *Z. Naturforsch.*, **37b**, 519 (1982)

9. G. Y. Papanov, P. Y. Malakov *Phytochem.*, **24** (2), 297 (1985).

10. M. Bruno, G. Savona, C. Pascual, B. Rodriguez, *Phytochem.* **20**, 2259 (1981).

11. D. P. Popa, A. M. Reinbol'd, *Khim. Prirodn. Soedin.*, **67, 27** (1972).

12. E. Gacs-Baitz, L. Radics, G. B. Oganessian, V. A. Mnatsakanian, *Phytochemistry,* **17**, 1967 (1978)

13. J. Jakupovic, R. N. Baruah, F. Bohlmann, W. Quack, *Planta Medica*, **51,** 341 (1985).

14. G. Savona, M. Z.Garcia-Aalvarez, B. Rodriguez, *Phytochem.,* **21**, 721 (1982).

15. J. Fayos, F. Fernandez-Gadea, C. Pascual, A. Perales, F. Piozzi, M. Rico, B. Rodriguez, G. Savona, *J. Org. Chem.* **49**, 1789 (1984).

16. M .C. Garcia-Alvarez, G. Lukacs, A. Neszmelyi, F. Piozzi, B. Rodriguez, G. Savona, *J. Org. Chem.* **48**, 5123 (1983).

17. R. J. Grubešić, D. Kremer, S. Vladimir-Knežević, J. V. Rodríguez, *Cent. Eur. J. Biol.*, **7**, 542 (2012).

18. N. Radulovic, M. Dekic, M. Joksovic, R. Vukicevic, *Chem. & Biodiv.*, 9, 106 (2012).

19. T. Kundakovic, M. Milenkovic, A. Topic, T. Stanojkovic, Z. Juranic, B. Lakušic, *African J. Microbiol. Res.*, **5**, 2950 (2011).

20. P. I. Bozov, P. N. Penchev, *Phytochem. Lett.*, **31**, 237 (2019).

21. M. C. Rodriguez, J. Barluenga, G. Savona, F. Piozzi, O. Servettaz, B. Rodriguez, *Phytochem.*, **23**, 1465 (1984).

22. A. M. Reinbol'd, D. P. Popa, *Chemistry of Natural Compounds*, **10**, 600 (1974).

23. E. Fujita, I. Uchida, *J. C. S. Perk&t,* **I**, 1547 (1974).

Chemical composition, sensory evaluation and antimicrobial activity of Taif rose (*Rosa damascena* Mill.) essential oils

M. Kurkcuoglu[1], K. H. C. Baser[2], S. G. Aкterian[3], H. N. Fidan[4*], A. S. Stoyanova[3]

[1]*Anadolu University, Faculty of Pharmacy, Department of Pharmacognosy, 26470, Eskisehir, Turkey*
[2]*Near East University, Faculty of Pharmacy, Department of Pharmacognosy, Nicosia, Turkish Republic of Northern Cyprus*
[3]*University of Food Technologies, Technological Faculty, Technology of Tobacco, Sugar, Vegetable and Essential oils, 4000, Plovdiv, Bulgaria*
[4]*University of Food Technologies, Faculty of Economics, Department of Nutrition and Tourism, 4000, Plovdiv Bulgaria*

Rosa damascena Mill. is a traditional and promising agricultural plant used for manufacturing essential oil in Saudi Arabia. The present study aims at studying the chemical composition, sensory evaluation and antimicrobial activity of some samples of rose oils (*Rosa damascena* Mill.) from the region of Taif. The chemical composition was determined by GC and GC/MS. Main constituents in the studied essential oils were: citronellol, nerol, geraniol, and nonadecane. The monoterpene alcohols, citronellol, geraniol, and nerol, were the constituents responsible for the odor of the oils analysed. The antimicrobial activity was determined against Gram-positive bacteria (*Listeria monocytogenes* NCTC 11994, *Staphylococcus aureus* ATCC 25093, and *Bacillus cereus* ATCC 11778), Gram-negative bacteria (*Escherichia coli* ATCC 8739 and *Salmonella enterica* subsp. *enterica* serovar Abony NCTC 6017), and a fungal strain - *Aspergillus flavus*. The high antimicrobial effect of these rose oils was confirmed on six types of bacteria and fungi. The strongest antimicrobial effect was against the Gram-positive bacterium *S. aureus*. The specified characteristics of Taif rose oils indicate their potential implementation in perfumery, cosmetic, soap, household and personal care products manufactured in the Kingdom of Saudi Arabia.

Keywords: *Rosa damascena* Mill, Taif rose, chemical composition, sensory evaluation, antibacterial activity

INTRODUCTION

The genus *Rosa*, belonging to the Rosaceae family, contains hundreds of species that form a group of plants with a wide range of usage and application [1]. Bulgaria and Turkey are known as the main producers of *R. damascena* Mill. essential oil in the world. Different commercial products are produced from rose flowers such as rose essential oil, rose water, dried flowers, rose concrete, and rose absolute. Due to the antimicrobial, antioxidant, analgesic, anti-inflammatory, anti-diabetic and anti-depressant properties of *R. damascena,* there is a significant interest in the development of new innovative products with industrial and practical importance [2].

The roses have acquired cultural significance in the societies of Western Saudi Arabia, too. Especially, Taif rose (*R. damascena*) cultivation is a tradition in the Taif region that has contributed to making this city located in the South-west of Saudi Arabia a highly preferred tourist destination. Rose cultivation in the region of Taif started most probably in the 16th century. Today, the rose oil production in Saudi Arabia represents less than 5 % of the global world production. The main regions (fig. 1) for growing oil-bearing roses are Taif, Al Bahah, Abha and Khamis Mushait. The altitude of these regions is between 1800 and 2300 m above sea level. The annual temperature difference is 15-16 °C. Annual rainfalls are between 100 and 150 mm per square m. Therefore, full irrigation is needed for rose growing. The period for harvesting rose flowers is two months - from March to April [3]. Taif rose is used for essential oil and rose water production, having applications in medicine, food industry and perfumery.

A number of authors have conducted agro-bioassays, for example, describing diseases of rose plantations [4], investigating the effect of arbuscular *Mycorrhizal* fungus on the development of rose plantations [5], isolating bacteria, with phytase activity, growing in the soil on which roses have grown [6]. The rose processing in this region is traditionally done by water distillation.

The chemical composition and biological potential of the Taif rose essential oil has been the subject of several studies [7-15]. The content of the major constituents is one of the most important parameters which determine the quality of the rose oil.

* To whom all correspondence should be sent:
E-mail: hfidan@abv.bg

It has been reported that citronellol, geraniol, nonadecane, and nerol were among the main constituents of rose oil obtained from rose blossoms [8-10]. The investigation of the cytotoxic, genotoxic, antimutagenic and anticancer effect of the concrete and absolute rose oils from Taif rose showed that they displayed a cytotoxic effect towards normal human blood lymphocytes in a dose-dependent manner and anticancer activity against HepG2 and MCF7 cells [11].

Rose flower extracts were analyzed for their antioxidant [12-14] and antimicrobial activities [4, 8, 15], while the phytochemical study of the rose flower methanol extract led to isolation and identification of four new compounds [16].

The objective of the present study was to determine the chemical composition, odor evaluation and antimicrobial activity of some industrial samples of Taif rose essential oils.
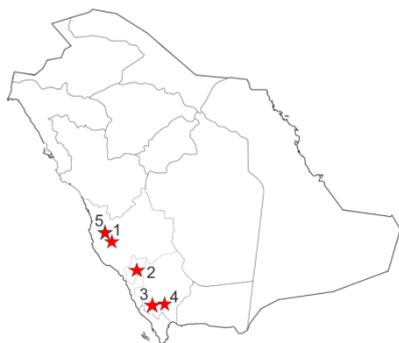
Figure 1. Main regions with favorable conditions for growing oil-bearing roses in the Kingdom of Saudi Arabia: 1- Taif; 2- Al Bahah; 3- Abha; 4- Khamis Mushait; 5- Al Hada.

MATERIALS AND METHODS

Materials

Five samples of industrial essential oils (numbered from 1 to 5) were obtained from distilleries in the Taif region and were used for GC and GC/MS analyses. The oils were kept refrigerated at 4°C before analysis.

GC and GC/MS analyses of essential oils

The GC/MS analysis was carried out with an Agilent 5975 GC-MSD system. (Agilent Technologies Inc., Santa Clara, CA). Innowax FSC column (Hewlett-Packard –HP, U.S.A.) (60 m × 0.25 mm, 0.25 μm film thickness) was used with helium as a carrier gas (0.8 mL/min). GC oven temperature was kept at 60°C for 10 min and programmed to 220°C at a rate of 4°C/min, and kept constant at 220°C for 10 min and then programmed to 240°C at a rate of 1°C/min. Split

ratio was adjusted to 40:1. The injection temperature was 250°C. Electron impact mass spectra were generated at 70 eV with a mass range from *m/z* 35 to 450.

The GC analysis was carried out using an Agilent 6890N GC system. In order to obtain the same elution order with GC/MS, simultaneous injection was done by using the same column and appropriate operational conditions. FID temperature was 300°C.

The chemical constituents of the essential oils were identified by comparison of their mass spectra with those in the Baser Library of Essential Oil Constituents, Wiley GC/MS Library, Adams Library, MassFinder Library and confirmed by comparison of their retention indices. Straight-chain n-alkanes were used as reference points in the calculation of relative retention indices (RRI). Relative percentage amounts of the separated compounds were calculated from FID chromatograms.

Sensory evaluation of rose aroma products

Sensory evaluation of the samples was performed in a sensory laboratory according to ISO 8589 [17] at the University of Food Technologies, Plovdiv, Bulgaria. One professional perfumer and two aroma chemists (each having experience in the field over 10 years; 2 female) participated and independently evaluated the sensory characteristics. At the time of the procedure, each tester was in a normal healthy condition and mood. Three sniffs from the test strip (dipped in the rose product around 1 cm) were performed and fresh air was breathed between each product. The procedure was repeated three times daily within three days. Then, the testers were asked to give their evaluation in a form of descriptive analysis. The results were collected from each tester in a paper ballot. The odor descriptive characteristics of some individual compounds were based on the works of Bauer *et al.* [18], Ohloff *et al.* [19], and Bedoukian [20].

Antimicrobial activity

The antimicrobial activity of the rose oils was tested against test microorganisms provided by the National Bank for Industrial Microorganisms and Cell Cultures in Sofia, Bulgaria: Gram-positive bacteria: *Listeria monocytogenes* NCTC 11994, *Staphylococcus aureus* ATCC 25093, *Bacillus cereus* ATCC 11778; Gram-negative bacteria: *Escherichia coli* ATCC 8739, *Salmonella enterica* subsp. *enterica* serovar Abony NCTC 6017; and fungal strain: *Aspergillus flavus* (clinical isolate). The selective growth media were: Listeria Oxford

Agar Base /Merck/; Baird Parker Agar Base with Egg Yolk Tellurite emulsion supplement /Merck/, Rapid' *E. coli* 2 Agar /BioRad/ and Mac CONKEY Agar /Merck/, Mueller-Hinton agar (MHA) /Oxoid/, Sabouraud Dextrose Agar /Oxoid/, respectively. The media were inoculated with a 24-hour suspension of the bacterial species. The antimicrobial activity was determined by modification of the "agar diffusion" method by measuring the areas of inhibition of pathogen growth [mm] around rings in which a certain amount (0.05, 0.10, and 0.15 mL) of essential oil was applied [21].

RESULTS AND DISCUSSION

Chemical composition of Taif rose essential oils

The samples of essential oils were liquids with pale yellow color, having a low freezing temperature. The chemical composition of the Taif rose oils is shown in Table 1.

Table 1. Composition of Taif rose oils (%)

	RRI	Compound	1	2	3	4	5
1	942	Ethanol	tr	tr	tr	tr	tr
2	1032	α-Pinene	1.0	0.7	2.0	1.6	0.5
3	1118	*β*-Pinene	0.2	0.2	0.4	0.4	0.1
4	1132	Sabinene	0.6	0.1	0.1	0.2	0.4
5	1174	Myrcene	0.1	0.5	1.0	0.9	-
6	1203	Limonene	0.1	0.1	0.1	0.1	0.1
7	1246	(Z)- *β*-Ocimene	-*	-	-	tr	-
8	1255	*γ*-Terpinene	-	-	-	0.1	-
9	1266	(E)- *β*-Ocimene	0.1	tr	0.1	0.1	-
10	1280	*p*-Cymene	0.1	tr	0.1	0.1	-
11	1290	Terpinolene	0.1	-	-	tr	-
12	1362	*cis*-Rose oxide	0.3	0.2	0.3	0.2	0.1
13	1376	*trans*-Rose oxide	0.1	0.1	0.1	0.1	tr
14	1500	Pentadecane	0.3	0.3	0.3	0.3	0.3
15	1535	*β*-Bourbonene	0.1	0.2	0.1	0.1	0.1
16	1553	Linalool	3.5	2.8	5.6	3.7	6.1
17	1596	α-Guaiene	0.5	0.5	0.4	0.4	0.4
18	1611	Terpinen-4-ol	0.7	0.5	0.7	0.7	0.6
19	1612	*β*-Caryophyllene	0.4	0.4	0.4	0.5	0.5
20	1668	Citronellyl acetate	0.4	0.2	0.3	0.4	0.2
21	1687	α-Humulene	0.4	0.4	0.3	0.4	0.4
22	1694	Neral	0.4	0.5	0.5	0.6	0.4
23	1700	Heptadecane	1.2	2.0	1.5	1.3	2.2
24	1706	α-Terpineol	1.0	0.9	1.6	1.0	2.1
25	1726	Germacrene D	0.6	0.9	0.7	1.0	0.7
26	1730	*δ*-Guaiene (=α-Bulnesene)	0.4	0.3	0.3	0.4	0.3
27	1733	Neryl acetate	0.2	0.1	-	0.2	0.1
28	1740	Geranial	0.9	1.0	1.0	1.0	0.6
29	1758	(E,E)-α-Farnesene	-	-	-	-	tr
30	1765	Geranyl acetate	0.7	0.8	1.1	2.2	1.1
31	1772	**Citronellol**	**38.0**	**24.2**	**24.6**	**23.1**	**21.1**
32	1808	**Nerol**	**10.8**	**13.8**	**12.5**	**13.5**	**11.0**
33	1838	2-Phenylethyl acetate	0.1	0.1	0.1	0.2	0.1
34	1857	**Geraniol**	**18.2**	**25.7**	**24.7**	**28.0**	**24.7**
35	1900	**Nonadecane**	**7.2**	**10.8**	**7.4**	**7.0**	**10.7**
36	1915	Nonadecene	2.7	1.4	3.2	1.9	2.4
37	1937	Phenylethyl alcohol	2.3	3.0	2.2	2.4	3.1
38	2000	Eicosane	0.6	0.7	0.5	0.6	0.7
39	2030	Methyl eugenol	1.3	1.0	0.8	1.0	1.0
40	2050	(E)-Nerolidol	-	-	0.1	-	0.1
41	2100	Heneicosane	2.2	2.7	2.0	2.2	2.6
42	2186	Eugenol	0.9	1.1	1.1	0.6	1.8
43	2187	*γ*-Eudesmol	-	-	0.1	-	0.3
44	2250	α-Eudesmol	-	-	-	-	0.1

45	2255	α-Cadinol	-	-	0.1	-	0.4
46	2257	β-Eudesmol	-	-	-	-	tr
47	2300	Tricosane	0.3	0.4	0.3	0.3	0.4
48	2314	(2E,6Z)-Farnesol	0.1	0.1	0.1	tr	0.1
49	2349	Geranic acid	0.1	0.1	0.1	0.1	0.1
50	2369	(2E,6E)-Farnesol	0.7	1.2	1.0	1.1	1.9
51	2500	Pentacosane	-	-	0.1	-	0.1
		Total, %	99.9	100	100	100	100
		Aliphatic hydrocarbons,%	14.2	18.3	15.3	13.6	19.4
		Monoterpene hydrocarbons,%	2.2	1.6	3.7	3.4	1.1
		Oxygenated monoterpenes,%	75.7	70.9	73.2	74.8	68.3
		Sesquiterpene hydrocarbons,%	2.4	2.7	2.2	2.8	2.4
		Oxygenated sesquiterpenes,%	0.8	1.3	1.3	1.1	2.8
		Phenyl propanoids,%	4.7	5.2	4.3	4.3	6.0

RRI: Relative retention indices were calculated against straight-chain n-alkanes; %: calculated from FID data; tr: Trace (< 0.1 %); -: not detected.

Table 2. Comparison between the chemical compositions of Taif rose essential oils of different (%) origins

Component	Saudi Arabia Taif Rose Oil		Bulgaria*		Morocco*		Turkey*		Turkey* peasant type	
	min	max	min	max	min	max	min	max	min	max
Ethanol			-	2.0	-	3.0	-	7.0	-	2.0
Citronellol	21.1	38.0	20.0	34.0	30.0	47.0	34.0	49.0	26.0	40.0
Nerol	10.8	13.8	5.0	12.0	3.0	11.0	3.0	11.0	6.0	12.0
Geraniol	18.2	28.0	15.0	22.0	6.0	23.0	8.0	20.0	12.0	29.0
β-Phenyl-ethanol	2.2	3.1	-	3.5	-	3.0	-	3.0	-	3.0
Heptadecane	1.2	2.2	1.0	2.5	0.6	4.0	0.8	3.0	0.7	3.0
Nonadecane	7.0	10.8	8.0	15.0	7.0	16.0	6.0	13.0	6.0	8.5
Heneicosane	2.0	2.7	3.0	5.5	2.0	5.5	2.0	4.0	1.5	4.0

*ISO 9842 [22]

In sample 1, 41 constituents representing 99.9 % of the total content of the oil were identified. The main compounds were citronellol (38.0 %), geraniol (18.2 %), and nerol (10.8 %). The other compounds characterized were nonadecane (7.2 %), linalool (3.5 %), nonadecene (2.7 %), phenylethyl alcohol (2.3 %), and heneicosane (2.2 %).

Thirty-eight constituents were identified in sample 2, representing 100 % of the total content of the oil. The major compounds were- geraniol (25.7 %), citronellol (24.2 %), nerol (13.8 %), and nonadecane (10.8 %). The third sample contained 43 compounds, representing 100 % of the total content of the essential oil. The main constituents in sample 3 were citronellol (24.6 %) and nerol (12.5 %), geraniol (24.7 %), nonadecane (7.4 %), and linalool (5.6 %).

Sample 4 consisted of 40 constituents representing 100 % of its total content. The main components in the essential oil were geraniol (28.0 %), citronellol (23.1 %), nerol (13.5 %), and nonadecane (7.0 %).

The essential oil obtained from sample 5 was composed of 41 components, representing 100 % of the total essential oil content. Geraniol (24.7 %), citronellol (21.1 %), nerol (11.0 %), nonadecane (10.7 %), and linalool (6.1 %) were the major constituents detected. The distribution of the identified components by groups of compounds is presented in Table 1. Oxygenated monoterpenes (68.3-74.8 %) and aliphatic hydrocarbons (13.6-19.4%) were the dominant groups in the rose oils, followed by phenyl propanoids (4.3-6.0 %), monoterpene hydrocarbons (1.1-3.7 %), sesquiterpene hydrocarbons (2.2-2.8 %), and oxygenated sesquiterpenes (1.1-2.8 %).

According to the requirements of ISO 9842 [22], ethanol content was found to be low and the contents of monoterpene alcohols citronellol, geraniol and nerol determining the rosy odor of the samples comply with the ISO standard. The content of the hydrocarbons, acting as odor fixers and determining the viscosity of the oils at low temperature, are also within the standard limits, while the content of phenylethyl alcohol was found to be higher [22].

The results for the five oil samples do not differ much from the literature data for oils obtained from

this region. The differences in quantities are possibly caused mainly by the time of harvest, and the processing conditions.

The chemical composition of the Taif rose essential oil has been studied by several researchers [1, 7-10]. Table 2 represents the comparison between the content of the main constituents of Taif rose oil and *R. damascena* essential oils growing in different countries, such as Saudi Arabia, Bulgaria, Turkey and Morocco. The differences between the chemical compositions of Taif rose essential oils predominantly depend on the rose genotype but are also influenced by the environmental and climatic conditions, flower processing and oil distillation practices. The differences found in the content of the main constituents with the data in the literature on roses growing in other countries, such as Bulgaria, Turkey, India, China, *etc.,* may be explained by the differences in agrobiological conditions and processing conditions [1, 23-36]. Aliphatic hydrocarbons (alkanes and alkenes) play a significant role in the aroma products as compounds responsible for odor stability. The content of heptadecane and nonadecene/ nonadecane is considered to be of particular importance [37]. Bazaid [7] examined the chemical composition of essential oil obtained from four sites in Taif under laboratory conditions. Essential oils not stored and stored for 12 months were analyzed. According to the author, during the storage, the contents of *α*-pinene, *β*-pinene, limonene, citronellol, and eugenol were reduced, while that of rose oxide increased. Halawani [8] found that the main components of rose oil, obtained by water distillation of rose blossoms, harvested from Al-Hada and Al-Shafa farms were citronellol (14.8-29.0 %), geraniol (11.3-16.2 %), and nerol (11.6 %). According to the author, the differences in the composition of the analyzed oil and that of the literature were due to specific geographical conditions under which they were cultivated.

Kurkcuoglu *et al.* [9] examined the composition of commercial oil samples sourced from retailers in Riyadh, Saudi Arabia. The major components of the oils were citronellol (22.8 and 27.5 %), geraniol (19.9 and 13.5 %), nonadecane (10.9 and 15.7 %), nerol (10.5 and 6.4 %), respectively. The authors compared the results obtained with the data of the ISO standard and according to them the amount of monoterpene compounds was in the range, while that of nonadecane and heneicosane was above the limits.

According to Abdel-Hameed *et al.* [10] citronellol (17.6 %), geraniol (11.4 %), nonadecane (6.5 %), nerol (6.4 %), linalool (5.9 %), *α*-pinene (4.5 %) and phenylethyl alcohol (3.6 %) were the main components of the Taif rose oil. In addition, the *in vitro* cytotoxic, genotoxic and anticancer effects of the oil were investigated toward normal human peripheral blood lymphocytes and two kinds of human cancer cell lines. The essential oil of Taif rose was suggested to be used as an effective therapeutic natural agent after further toxicological *in vitro* and *in vivo* studies.

Sensory evaluation of rose aroma products

According to the sensory characteristics of the investigated Taif rose essential oils, sample 1 was characterized by very intense and typical rose odor with citrus- and balsamic-like undertones. Sample 2 was described with a floral odor reminiscent of rose, while sample 3 had floral odor reminiscent of rose with spice undertones. It was determined that sample 4 had a balsamic odor, with floral and citrus-like undertones, whereas the last sample (sample 5) had an intense and typical rose odor with citrus-like undertones.

The monoterpene alcohols citronellol, geraniol, and nerol are the main constituents responsible for the odor of the oils tested [8-10]. Citronellol is characterized by a pleasant rose-like odor, geraniol with a flowery rose-like odor (different from that of citronellol), and nerol with a pleasant rose-like odor (different from that of geraniol). Other monoterpene alcohols, such as linalool with a flowery-fresh odor; terpinen-4-ol with a spicy, woody-earthy, and also lilac-like odor, and *α*-terpineol with a characteristic lilac aroma are contributing for the denser characteristic odor of rose oil.

The characteristic rose-like odor of the rose oils is due to the phenylethanoid *β*-phenylethyl alcohol, eugenol (with spicy, clove-like odor), methyl eugenol (with mild-spicy, slightly herbal odor), *trans*-rose oxide (with a strong odor reminiscent of geranium oil and carrot leaf odor) regardless of the amount involved in the formation of the bouquet of the smell [2].

Antimicrobial activity

The antimicrobial activity of different Taif rose essential oils against five bacterial strains and one fungus is presented in Table 3.

Table 3. Growth inhibition zones (mm) of Taif rose oils against pathogenic bacteria and a fungus

Test micro-organism	Sample 1			Sample 2			Sample 3			Sample 4			Sample 5		
	Concentration of the essential oil, mL														
	0.15	0.10	0.05	0.15	0.10	0.05	0.15	0.10	0.05	0.15	0.10	0.05	0.15	0.10	0.05
E. coli	18	16	15	16	12	10	6	6	6	20	17	16	16	11	6
S. enterica	6	6	6	25	24	22	15	6	6	10	6	6	16	6	6
L. mono-cytogenes	6	6	6	6	6	6	6	6	6	6	6	6	6	6	6
S. aureus	26	24	20	14	12	11	14	13	11	29	22	20	10	9	8
B. cereus	6	6	6	6	6	6	6	6	6	6	6	6	6	6	6
A. flavus	6	6	6	6	6	6	6	6	6	6	6	6	11	10	6

Results were evaluated according to the diameter of the growth inhibition zone including the diameter of the ring (6 mm). A broad spectrum and variation in the antimicrobial properties of the oils were shown in the study. Sample 1 showed antibacterial activity against *S. aureus* and *E. coli,* as the inhibition zone ranged between 26 to 20 mm for *S. aureus* and 18 to 15 mm for *E. coli* according to the applied amount of essential oil. *S. enterica* is a foodborne pathogenic bacterium with high significance due to the safety of the foods and showed the highest sensitivity on the action of sample 2 with a diameter of zone of inhibition ranged between 25 and 22 mm. Sample 4 showed the strongest antibacterial activity against *S. aureus*, followed by sample 2 which possessed potential against *S. enterica.* Clearly, the *L. monocytogenes* and *B. cereus* were most resistant to the tested essential oils. Sample 3 showed a moderate level of activity only against *S. aureus*, while sample 5 showed the lowest effect against the pathogenic bacterium *S. aureus* and antifungal activity against *A. flavus*.

In terms of antimicrobial activity, the samples tested do not differ from the literature data [8, 25, 28-30].

Taif rose essential oils are complex mixtures comprising many constituents. Each of these constituents contributes to some effects of these oils. Therefore, we suggest that the antibacterial activity of the tested samples could be due to the high amount of monoterpene alcohols and concurrent presence of hydrocarbons.

The higher antibacterial effect of sample 4 was due to the higher content of geraniol. Aridogan *et al*. [38] evaluated the *in vitro* antibacterial activities of *R. damascena* and their components. They found that the antimicrobial activity of *R. damascena* essential oil was determined only against *S. aureus* strains (the inhibition zone was 8 mm), whereas the antimicrobial activity of geraniol and nerol was found against both *S. aureus* and *E. coli* strains (with inhibition zone diameters ranged between 21 mm and 12 mm). They found that citronellol, geraniol and nerol had more potent antimicrobial activity individually than in the oil. Our results are not in agreement with that reported by Aridogan *et al*. [38] and it could probably be related to the synergistic effect between some of the minor components occurring in the essential oils and the major components citronellol, geraniol and nerol. Similar to our results Shohayeb *et al*. [14] reported that rose oil and its different petal extracts exerted a broad spectrum of antimicrobial activities against three fungi and eleven Gram-positive, Gram-negative bacteria. Mahboubi *et al*. [39] also determined the antimicrobial activity of *R. damascena* oil against a large number of microorganisms including Gram-positive and Gram-negative bacteria, and yeast by micro broth dilution assay.

CONCLUSIONS

The results of chemical analysis and sensory evaluation show that Taif rose oils are typical rose oils with their own specific features. Monoterpene alcohols citronellol, geraniol, and nerol were the major constituents and these oils were in compliance with the specifications of ISO 9842 [22]. The variations in chemical composition and odor characteristics of different samples can be explained by specific agro-climatic conditions of sub-regions, the botanical specificity of rose bushes grown and the technological diversities in local distilleries. The antimicrobial studies showed high activity of the rose oils studied, the highest being against the Gram-positive bacterium *S. aureus*. The characteristics of Taif rose oils show that they can be successfully applied not only in perfumery and cosmetic products, but also in soap, household and

personal care products. Presently, these applications are limited in the domestic market due to higher prices of these rose oils.

REFERENCES

1. K. H. C. Baser, *Perfumer and Flavorist,* **17**, 45 (1992).
2. M. Mahboubi, *J. Tradit. Complement Med.,* **6**, 10 (2016).
3. E. De Pauw, *ICARDA,* 2002, p. 77, ISBN 92-9127-119-5.
4. K. El-Den, M. El Awady, M. Said, E. El Hallous, A. El-Tarras, *Life Sci. J.*, **10**(4), 1673 (2013).
5. A. Bahobail, O. Al-Zahrani, M. El-Sharnouby, Y. El Halmouch, *Life Sci. J.,* **11**(1), 83 (2014).
6. A.-E. Farouk, A. Banaja, N. Ahamed, O. AlZahrani, S. Bazaid, *Afr. J. Biotechnol.*, **14**(5), 425 (2015).
7. S. Bazaid, *Am.-Eurasian J. Sustain. Agric.,* **3**(1), 24 (2009).
8. E. Halawani, *Afr. J. Microbiol. Res.,* **8**(24), 2359 (2014).
9. M. Kurkcuoglu, A. Abdel-Megeed, K. H. C. Baser, *J. Essent. Oil Res.*, **25**(5), 364 (2013).
10. E.-S. S. Abdel-Hameed, A. Bazaid, H. A. Hagag, *J. Essent. Oil Res.,* **28**(2), 121 (2016).
11. H. A. Hagag, S.A. Bazaid, E.-S. S. Abdel-Hameed, M. Salman, *Cytotechnology*, **66**, 913 (2014), DOI 10.1007/s10616-013-9644-5.
12. E.-S. Abdel-Hameed, S. Bazaid, M. Shohayeb, *Br. J. Pharm. Res.*, **2**(3), 129 (2012).
13. E.-S. Abdel-Hameed, S. Bazaid, M. Salman, *Biomed. Res. Int.*, e345465 (2013).
14. M. Shohayeb, E.-S. Abdel-Hameed, S. Bazaid, I. Maghrabi, *Global J. Pharmacol.,* **8**(1), 1 (2014).
15. A.E. Farouk, A. Banaja, N. Ahamed, O. AlZahrani, O. Bazaid, *Afr. J. Microbiol. Res.*, **8**(50), 3913 (2014).
16. M. Ali, A. Sultana, M. Jameel, *Int. J. Herb. Med.,* **4**(6), 179 (2016).
17. ISO 8589, Sensory analysis - General guidance for the design of test rooms, 2007.
18. K. Bauer, D. Garbe, H. Surburg, Common fragrance and flavor materials. Preparation, properties and uses, fourth completely revised edition, Weinheim, New York, Chichester, Brisbane, Singapore, Toronto, Wiley – VCH, 2001.
19. G. Ohloff, W. Pickenhagen, P. Kraft, Scent and Chemistry. The molecular world of odors, Verlag Helv. Chim. Acta, Zürich, 2012.
20. Bedoukian Research, Inc. Search technical documents, https://bedoukian.com/flavor/, (Accessed date 05.10.2019).
21. L. L. Zaika, *J. Food Saf.,* **9**(2), 97 (1988).
22. ISO 9842, Oil of rose (*Rosa x damascena* Miller). International standards for business, 2003. Government and Society, Available online: http//www.iso.org.
23. K. H. C. Baser, M. Kurkcuoglu, *Türkisches Rosenöl, Forum für Aromatherapie und Aromapflege*, **20**, 26 (2001).
24. K. Babu, B. Singh, V. Joshi, V. Singh, *Flavour Fragr. J.*, **17**, 136 (2002).
25. L. Jirovetz, G. Buchbauer, M. Shahabi, *J. Essent. Oil-Bear. Plants*, **5**, 111 (2002).
26. K. H. C. Baser, M. Kurkcuoglu, T. Ozek, *Perfumer and Flavourist,* **28**(2), 34 (2003).
27. M. Kurkcuoglu, K. H. C. Baser, *Chem. Nat. Comp.,* **39**(5), 457 (2003).
28. L. Jirovetz, G. Buchbauer, A. Stoyanova, A. Balinova, Z. Guangjiun, M. Xihan, *Flavour Frag. J.*, **20**, 7 (2005).
29. V. Gochev, K. Wlcek, G. Buchbauer, A. Stoyanova, A. Dobreva, E. Schmidt, L. Jirovetz, *Nat. Prod. Commun.*, **7**, 1063 (2008).
30. V. Gochev, L. Jirovetz, K. Wlcek, G. Buchbauer, E. Schmidt, A. Stoyanova, A. Dobreva, *J. Essent. Oil-Bear. Plants*, **1**, 1 (2009).
31. K. H. C. Baser, M. Kurkcuoglu, *Link-Natural Products,* **4**(1), 21 (2008).
32. K. H. C. Baser, A. Altintas, M. Kurkcuoglu, *HerbalGram,* **96**, 40 (2012).
33. F. S. Senol, I. E. Orhan, M. Kurkcuoglu, M. T. H. Khan, A. Altintas, B. Sener, K. H. C. Baser, *Food Res. Int.*, **53**, 502 (2013).
34. M. Berechet, I. Calinescu, M. Stelescu, E. Manaila, G. Craciun, B. Purcareanu, D. Mihalesku, S. Rosca, A. Fudulu, I. Niculescu-Aron, R. Mihai, *Rev. Chim. (Buharest),* **12**, 1986 (2015).
35. K. Rusanov, N. Kovacheva, M. Rusanova, I. Atanasov, *Food Chem.,* **129**, 1851 (2011).
36. R. Verma, R. Padalia, A. Chauhan, A. Singh, A. Yaday, *Nat. Prod. Res.,* 1577 (2011).
37. G. Ohloff, E. Demole, *J. Chromatogr.*, **406**, 181 (1987), doi:10.1016/S0021-9673(00)94029-9.
38. B.nC. Aridogan, H. Baydar, S. Kaya, M. Demirci, D. Ozbasar, E. Mumcu, *Arch. Pharm. Res.,* **6**(25), 860 (2002).
39. M. Mahboubi, N. Kazempour, T. Khamechian, H. Fallah, M. M. Kermani, *J. Biol. Act. Prod. Nat.*, **1**, 1 (2011).

Prediction of the pressure, velocity and axial mass flux profiles within a high-speed rotating cylinder in total reflux condition *via* modified dsmcFoam solver

S. Yousefi-Nasab[1*], J. Safdari[1], J. Karimi-Sabet[1], A. Norouzi[2]

[1] *Materials and Nuclear Fuel Research School, Nuclear Science and Technology Research Institute, Atomic Energy Organization of Iran, P.O. Box:11365-08486, Tehran, Iran*
[2] *Iran Advanced Technologies Company, Atomic Energy Organization of Iran, P.O. Box:1439955931, Tehran, Iran*

A modified version of the dsmcFoam solver was extended for molecular simulation of high-speed rotating geometries. Rotary machines' advantages have made them appealing to various applications such as laboratory centrifuges, analytical ultracentrifuges, haematocrit centrifuges and gas centrifuges. So, simulating the content inside the rotating machines can be important. The dsmcFoam solver has some shortcomings in the rotary machines gas flow modeling. Weakness to model the internal flows with pressure gradient characteristic creating a temperature gradient as a boundary condition and use of Adaptive Mesh Refinement (AMR) are some of them. We selected dsmcFoam as the base solver and tried to troubleshoot all of the above-mentioned faults. Through fixing these shortcomings, the Wide Application Dsmc SIMulation (WADSIM_1) software is introduced that is capable to simulate a wide range of internal flow problems with high-speed rotation. It was used to simulate the gas flow inside the rotating cylinder. Then the pressure, velocity and axial mass flux profiles inside it for light and heavy gases were calculated. Next, the results were compared with the DSMC code for axially symmetric flows. Finally, the compression ratio of a Holweck-type molecular pump (as a complex geometry with the presence of a rotating rotor inside it) obtained from WADSIM_1 was validated with the experimental results. The achieved results illustrated that the WADSIM_1 software has the capability to simulate a wide range of rotating geometries with high precision.

Keywords: dsmcFoam solver; WADSIM_1; Rotating rotor; Helix grooves.

Article Highlights: WADSIM_1 solver is able to simulate all two- and three-dimensional geometries with high-speed rotation; WADSIM_1 solver is able to use Adaptive Mesh Refinement (AMR) and gradient boundary conditions; Inside a rotating cylinder, the amount of light gases present in the cylinder's axis is higher than that of heavy gases.

INTRODUCTION

There are intensive changes in the density of gases within rotating cylinders due to a strong centrifugal force field. The force field causes the formation of different types of flow regimes inside the cylinder, extending from molecular (kn > 0.1) to continuous (kn < 0.1) regime.

In rotating cylinders, the Navier-Stokes equations are used to model the flow in a continuous domain. Generally, analytical solution of these equations is impossible and their numerical solutions require significant amounts of cost and time. Since the mid-1950s, a method has been developed to solve the Navier-Stokes equations based on simplifying and linearizing by appropriate assumptions. In this method, the six governing equations, i.e. conservation of mass, momentum (radial, tangential and axial components), energy and the state equation are combined to form a six-order PDE equation called the Onsager equation [1]. The main reasons for using this method are its high speed comparing to other methods and lack of requirement for high computational facilities. By developing the

computational systems, the Onsager method has been replaced by CFD methods. Other modern methods are Lagrangian methods, especially DSMC, which has the ability to simulate systems with a large number of molecules for all flow regimes by representative particle selection [2, 3]. In recent years, the use of DSMC for simulating the flow inside a rotating cylinder has been widely extended. For instance, Pradhan and Kumaran, in 2011 and 2016, studied and analyzed the axial mass flux based on the dimensionless term in a radial direction using the DSMC method. They compared their results with the generalized Onsager model and achieved similar results [4, 5]. Inside a rotating cylinder, by moving radially forward into the continuous region, and thus, reducing the Knudsen number (Kn), the amount of calculations for the DSMC method increases, causing its implementation for the single core to be time-consuming.

Hence, researchers have recently started using some pieces of software and codes capable to run *via* multiple cores in parallel. In addition to commercial

* To whom all correspondence should be sent:
E-mail: syousefy@aeoi.org.ir

software such as Fluent and CFX for solving the fluid flow by numerical methods, open-source softwares are also provided in this branch, with the most important advantage of having access to code text. As a result, the considered solver and the boundary conditions can be changed according to the problem, and the closest simulation conditions can be achieved for the desired geometry. One of the most important open-source softwares is *OpenFoam*, which is able to solve a wide range of physical phenomena such as compressible and incompressible flows, molecular-based flows, two-phase flows, flows in porous materials, dynamics of gases, combustion, turbo machines, etc. The main strength of *OpenFoam* is its ingenious utilization of C++ programming language abilities, which provides an arranged structure of classes, libraries and objects due to its object-oriented nature [6]. The dsmcFoam solver is usually used for external flows. To our knowledge the gas flows inside a rotating cylinder with a dsmcFoam solver have not been studied so far. In 2013, for the first time, Gutt *et al.* used the internal flow through this solver for a PVD chamber [7]. In 2015, White applied an Adaptive Mesh Refinement (AMR) technique for an arbitrary geometry by modifying its Knudsen number for a modified dsmcFoam solver and achieved good results [8].

John *et al.* investigated in 2015 the high-speed rarefied flow past both stationary and rotating cylinders using the direct simulation Monte Carlo (DSMC) method. The DSMC simulations had been carried out using dsmcFoam solver. They compared various aerodynamic characteristics such as coefficients of lift and drag, pressure, skin friction, and heat transfer for stationary and rotating cylinder [9]. John *et al.* investigated in 2016 the flow past a rotating cylinder over a wide range of flows rarefied from the early slip through to the free molecular regime using dsmcFoam solver. They focused on high-speed flow conditions and considered a wide range of Mach numbers near the high subsonic, transonic, and supersonic regimes [10]. Dongari *et al.* evaluated the effect of curvature on rarefied gas flows between rotating concentric cylinders. They found that non-equilibrium effects were not only dependent on Knudsen number and accommodation coefficient but were also significantly affected by the surface curvature [11]. Kumar *et al.* developed a new multi-species, polyatomic, parallel, three-dimensional Direct Simulation Monte-Carlo (DSMC) solver for external flow problems. The main features of this solver include its ability to

handle multi-species, polyatomic gases for 2D/3D steady and transient nature of flow problems over arbitrary geometries, with a density-based grid adaptation technique. Furthermore, 3D surface refinement (for accurate calculation of surface properties) and 3D gas-surface interaction was implemented in a very efficient manner in the solver [12]. The gas inside the high-speed rotating cylinders has a very high pressure gradient, so the size of each grid can change over time. For this problems the *AMR* technique should be used. The method for modeling the gas inside the rotating cylinder is a hybrid method. The molecular region (near the axis) can be simulated using the DSMC method, and then the results can be transferred as a mass source/sink to the numerical solution of the continuum region equations (the area next to the wall) [13]. Due to the problems of transferring information from one region to another in this method, the DSMC method is chosen as another method to simulate the total gas inside the rotating cylinder. In this paper, the *dsmcFoam* solver has been selected as DSMC molecular-based solver. This solver has previously been rigorously validated for a variety of benchmark cases [14,15]. The dsmcFoam solver, despite having many advantages like the high speed of its execution due to highly optimized codes and the possibility of using parallel runs with unlimited cores, has some defects in modeling the gas inside the rotating cylinders. In the present study, by correcting the temperature and velocity gradient boundary conditions for the dsmcFoam solver as well as applying an internal flow and using the *AMR* technique, a new software called *WADSIM_1* is introduced, which is capable to simulate the different gases inside the high-speed rotating cylinders. Due to the lack of experimental test results for the flow inside the rotating cylinders, simulation of a Holweck-type molecular pump was used to validate the *WADSIM_1* software. Finally, the value of the compression ratio obtained from the simulation was validated by the experimental compression ratio of the molecular pump. Holweck-type molecular pump has a complex geometry where gas molecules move through the grooves to the top of the grooves by hitting the rotating rotor [16].

THEORY

DSMC Method

From the Lagrangian point of view, DSMC is a fluidized simulation method in which a large number of simulated molecules are followed simultaneously, and in addition to colliding the molecules with a surface, the intermolecular collisions are also calculated. DSMC algorithm is shown in Fig. 1.
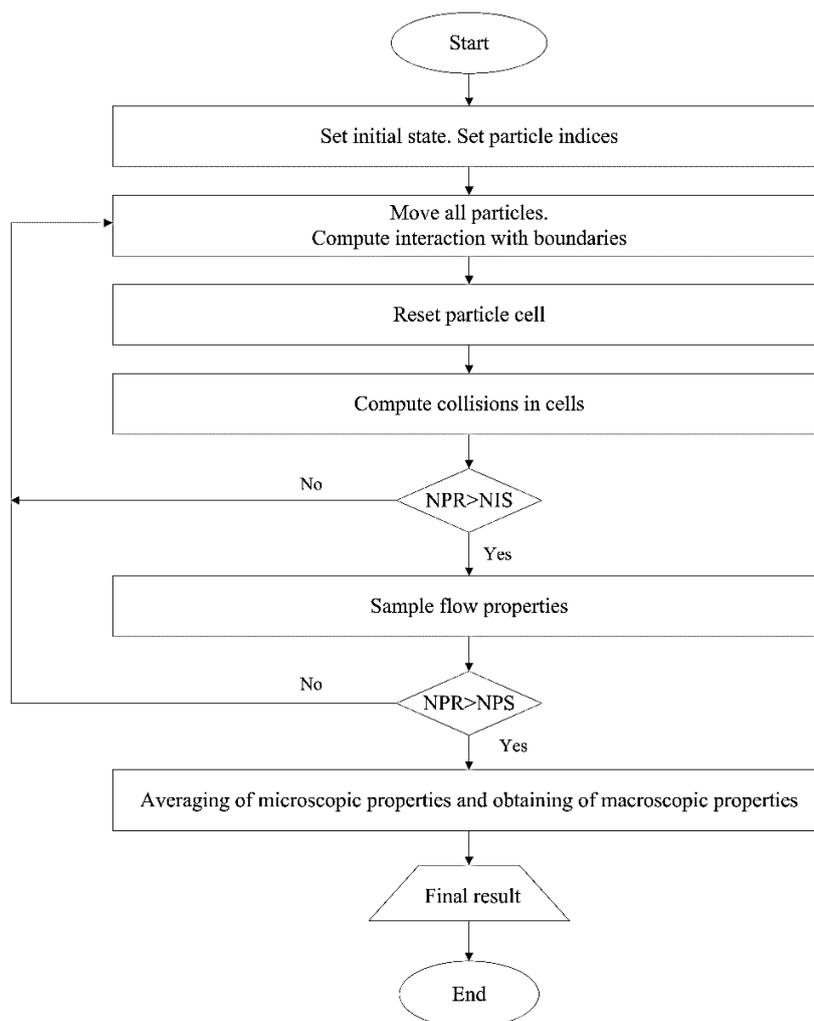
Fig. 1. DSMC algorithm

In this algorithm, the NPR, NIS, and NSP quantities represent the number of repetitions for obtaining the output file, the number of time steps between the samples, and the number of samples between the restart and output file updates, respectively [2].

Different collision models can be used at the collision step of particles. The easiest one is the Hard Sphere (HS) model in which the value of the collision cross-section is constant and does not change with the relative velocity whereas the actual cross-section should be decreased due to increasing the relative velocity.

This model has the advantage of easily calculating the collision mechanics because of the isotropic scattering in the center of the mass frame of reference. However, as its disadvantage, this scattering law is not realistic and the cross-section is independent of the relative translational energy in the collision. In this model, the temperature exponent of the coefficient of viscosity (ω) is equal to 0.5.

The Variable Hard Sphere (VHS) model is a hard sphere model in which the diameter is a function of relative velocity. The cross-section of the VHS model is determined from the viscosity coefficient, but the ratio of momentum to the viscosity cross-section follows the hard sphere value, which is a deficiency in the model. Therefore, the viscosity and the thermal conductivity coefficients are well calculated, but the Schmidt number, which depends on the diffusion coefficient, does not conform to the behavior of a real gas. The Variable Soft Sphere (VSS) model relates the probabilistic relationships to the type of gas used by an exponent in the VSS molecular model (α). As a result, the VSS model involves an empirical modification of the isotropic scattering law and the basic HS collision mechanics.

The Generalized Hard Sphere (GHS) model is an extension of the VHS and VSS models. It bears the same relationship to the Lenard-Jones class of models as the conventional VHS or VSS model bear to the inverse power law model. The Larsen-Borgnakke Variable Hard Sphere model (LBVHS)

469

is also proposed when the objective is to calculate the internal energy of the particles after their inelastic collision. A general Larsen-Borgnakke distribution function for the division of energy between the translational and internal modes between molecules, and between internal modes in each molecule may be defined such that it includes all the distribution functions of the preceding sections as special cases. At the step of the particles' collision with the wall and their reflection (boundary conditions), the five conditions (i.e. periodic, specular, diffusion, Maxwell, and Cercignani-Lampis-Lord) can be used. In fact, at this step, the particles collide with the wall, and then, based on the boundary conditions, the new values of their velocity and positions are set. In the periodic boundary condition, by changing the location of the particles, their location is set to the opposite side of the wall. In the specular boundary condition, the molecular velocity component normal to the surface is reversed, while the velocity components parallel to the surface remain unaffected. In the Diffuse boundary condition, the velocity of each molecule after reflection is independent of its velocity before reflection. However, the velocities of the reflected molecules as a whole are distributed in accordance with the half-range Maxwellian equilibrium for the molecules that are directed away from the surface. The diffuse reflection model is a suitable model for engineering problems and has a good accuracy. In the Maxwell boundary condition, two types of specular and diffuse interactions are considered together so that the specular interaction is reflected with an angle equal to the angle of impact and the interaction of the diffuse with a random angle. Given that the probability of a collision for a pair of molecules is proportional to the product of the cross-section and the relative velocity in the Maxwell's collision model, the collision probability for a particular molecule is independent of velocity. Also, in this model, the viscosity coefficient is linearly related to temperature, which is unrealistic for real gases. In fact, in this model, the collision probability for all molecules is the same. The Cercignani-Lampis-Lord (CLL) boundary condition model, as shown in Fig. 2, is defined based on the coefficients σ_n and σ_t, which represent the accumulation coefficients for the kinetic energy related with the normal and tangential components of the velocity. The model assumes that there is no coupling between the normal and tangential components of the velocity during the reflection process. Set v_r to be the normal component of the molecular velocity normalized to the most probable molecular speed at the surface temperature, and v_θ and v_z to be the

similarly normalized tangential components. Furthermore, the deflection angle is always a function of the incident particle angle [2, 17].
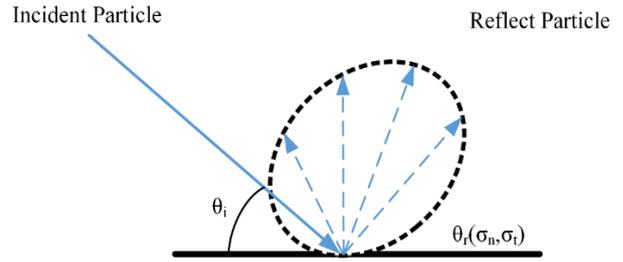
Fig. 2. Incident and reflected particle scheme in the Cercignani-Lampis-Lord model

In geometries with repetitive and symmetric physics, the boundary condition of the periodic can be used instead of the boundary condition of the wall type.

This boundary condition is applied to reduce the computational volume so that when a particle passes through one side of the unit cell of a periodic boundary, it re-appears on the opposite side with the same velocity. The large systems approximated by PBCs consist of an infinite number of unit cells. Consequently, instead of the whole geometry modeling, it is enough to model the repeating element. Fig. 3 illustrates part of a circle sector in which two boundary conditions, PB1 and PB2, have been used.
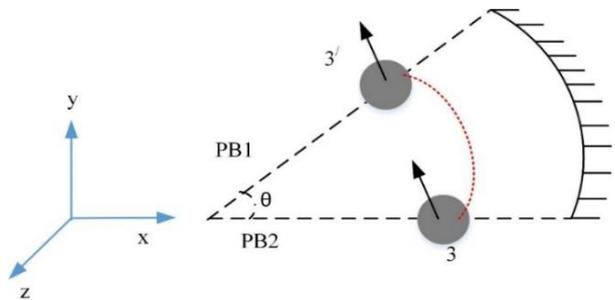
Fig. 3. A schematic of a periodic boundary condition in a rotational transform

Calculation of the position in a rotational transform

The center of a particle (e. g. $3'$ in z_3' y_3' x_3') from the periodic boundary condition of 1 to the periodic boundary condition of 2 can be moved using the following equations:

$$
\begin{aligned}
x &= x' \cos\alpha + y' \sin\alpha \\
y &= -x' \sin\alpha + y' \cos\alpha \\
z &= z'
\end{aligned}
\tag{1}
$$

where, α is the rotation angle, $\alpha = -\theta$ defines the rotation in the clockwise direction, $\alpha = \theta$ defines the

counterclockwise rotation, and θ is the sector angle of the model.

Calculation of the velocity in a rotational transform

When the particle is in its new position, its dynamic characteristics, which may affect the subsequent time step calculations (especially speed), should also be transformed. The velocity of a particle will be kept constant if its value is returned at a rotation angle of α according to the following relations:

$$v_x = v_x' \cos \alpha + v_y' \sin \alpha$$
$$v_y = -v_x' \sin \alpha + v_y' \cos \alpha \quad v_z = v_z' \qquad (2)$$

where, v_x, v_y and v_z are the velocities of the particles in the three directions, x, y and z, respectively.

WADSIM_1 Software

The dsmcFoam solver is one of OpenFOAM's solvers developed under OpenFOAM Version 1.5 by Macpherson and Scanlon at the University of Strathclyde. In spite of its high abilities, it has weaknesses for modeling of the gas inside the rotating cylinder. The WADSIM_1 software is developed to cover a wider range of issues. Table 1 compares the WADSIM_1 software and the dsmcFoam solver. The steps arrangement of the WADSIM_1 software algorithm is similar to the dsmcFoam solver. This implies that it also includes the steps of movement, indexing, collision, reflection from the wall and sampling of the results.

Table 2 shows the types of models of particles collision with each other and the particles collision with the wall used in WADSIM_1 software. In WADSIM_1, the NTC technique is used to calculate the maximum number of collisions in a cell. In the following sections, it will be briefly outlined how to apply Adaptive Mesh Refinement, gradient boundary conditions, and to use the appropriate boundary condition for creating an internal flow in the WADSIM_1.

Applying Adaptive Mesh Refinement (AMR) for WADSIM_1. An intensive change occurs in the radial direction due to the effect of centrifugal force inside a rotating rotor. The criteria for a good DSMC calculation are that, at every location in the flow, the time step should be smaller than the mean collision time and the cell size should be smaller than the mean free path. It is impossible to meet these conditions in the flows involving large changes in the flow properties unless the time step varies across the flow field, and the cell size must also be adapted to the local flow density. Therefore, the cell used in

its geometry simulation should be transformed into a changeable cell over the λ density variations.

Table 1. Comparison of dsmcFoam and WADSIM_1 capabilities

Feature	dsmcFoam	WADSIM-1
Steady / transient solutions	✓	✓
Arbitrary 2D/3D geometries	✓	✓
Arbitrary number of gas species	✓	✓
Rotational energy	✓	✓
Unlimited parallel processing capability	✓	✓
Robust open source solver and utility executables	✓	✓
Periodic boundary condition	✓	✓
Possibility to solve issues with high wall speed	✓	✓
Suitable for the internal flows with strong gradient of variables the characteristic length	×	✓
Suitable for external flow	✓	✓
Gradient boundary conditions	×	✓
Adaptive Mesh Refinement	×	✓

Table 2. WADSIM_1 capability in the models of particle- particle and particle-wall collisions

Interaction Models	WADSIM_1	Reflection Models	WADSIM_1
HS	✓	Periodic	✓
VHS	✓	Diffusion	✓
VSS	×	Specular	✓
GHS	×	Cercignani -Lampis- Lord	✓
LSVHS	✓	Maxwell	✓

In fact, in an AMR, the mean free path in each cell is calculated and compared with the largest cell size, Δx_{max}. The ratio $\lambda / \Delta x_{max}$ should be greater than

471

one; then, the cell size value is smaller than the mean free path [8,18]. The correction of AMR in CFD has been widely used since about 30 years ago. It is practically used to regulate cells in the areas with a high gradient such as shock waves. These areas with a high flow gradient in CFD could have the same concept as a strong difference in the mean free path of DSMC. An AMR for the WADSIM_1 open source solver has been used to provide more accurate results in this research, especially in the areas where changes in the mean free path exist. One of the main advantages of OpenFOAM is its ability to modulation. AMR libraries are available in some continuous flow regime solvers such as multiphase solver (interFoam) that can correct the cell at the connecting point of two fluids and also the rhoCentralDyMFoam solver for compressible gas flows [8]. These solvers use a library called dynamicFvMesh to adapt the cell. The dsmcFoam solver uses the fvMesh cell library, in which the cell does not change over time. In this paper, dsmcFoam connects to a dynamicFvMesh library so that cells could be corrected dynamically and adaptively with the simulation time forward. The steps required to create adaptive cells are mentioned in the following sections. The first step in connecting the library is to create a constructor for the DSMC code with the dynamicFvMesh library instead of fvMesh. The users are supposed to go to the following address at first:

OpenFoam2.1.x/src/lagrangian/dsmc/clouds/
Templates/dsmcCloud

and then find the following commands:

Foam::dsmcCloud::dsmcCloud
(
Time & t,
Const   word& cloudName,
Const   fvMesh& mesh,
bool   readFields
)

and replace them with the following commands:

Foam::dsmcCloud::dsmcCloud
(
Time& t,
Const   word& cloudName,
Const   dynamicFvMesh& mesh,
bool   readFields
)

At the beginning, it should call the proper header file for the dynamicFvMesh library. This is done in three files including dsmcCloud.C, dsmcCloud.H, and dsmcCloudl.C. Then, the dynamicFvMesh folder in the Src file should be inserted at the following directory:

OpenFoam2.1.x/src/lagrangian/dsmc

Next, the user can go to the above-mentioned directory and enter "wclean" followed by "wmake". If the command "is to update" came up at the end of the task, it could be concluded that the applied changes are correct. Afterwards, the following directory should be entered:

OpenFoam2.1.x/applications/solvers/
discreteMethods/dsmc/dsmcFoam

And then, the following changes to the dsmcFoam solver should be applied:

```
# include  "fvCFD.H"
# include  "dynamicFvMesh.H"
# include  "dsmcCloud.H"
Int  main (int arc,char   *argv[])
{
# include  "setRootcaseD.H"
# include  "createTime.H"
# include  "createDynamicFvMesh.H"
While  (runtime.loop())
{
Scalar
timeBeforeMeshUpdate=runtime.elapsedCPUTime();
{
Mesh.update();
}
If (mesh.changing())
{
Info<<"Execution time for mesh.update()="
<< runtime.elapsedCPUTime()-
timeBeforeMeshUpdate
<< "s"  <<endl;
}
```

Afterwards, "wclean" and "wmake" should be entered in the terminal, and finally, the user should see the message "is to update". Now the user can use a dynamic cell in dsmcFoam. The same process could be performed to obtain a variable time step which has not yet been implemented in the dsmcFoam solver.

Creating the internal flow. The definition of geometry is the first step in simulating with the OpenFoam. Given that most open-source softwares define geometry in three dimensions, OpenFOAM is no exception to this. The geometry in this simulation is a wedge from a cylinder with a 5-degree angle, in which one cyclic patch is linked to another through a neighbor Patch keyword in the boundary file.

Due to the symmetry in the geometry, calculations could be made only for the desired wedge greatly reducing the volume of computations. The simulated geometry is shown in Fig. 4.
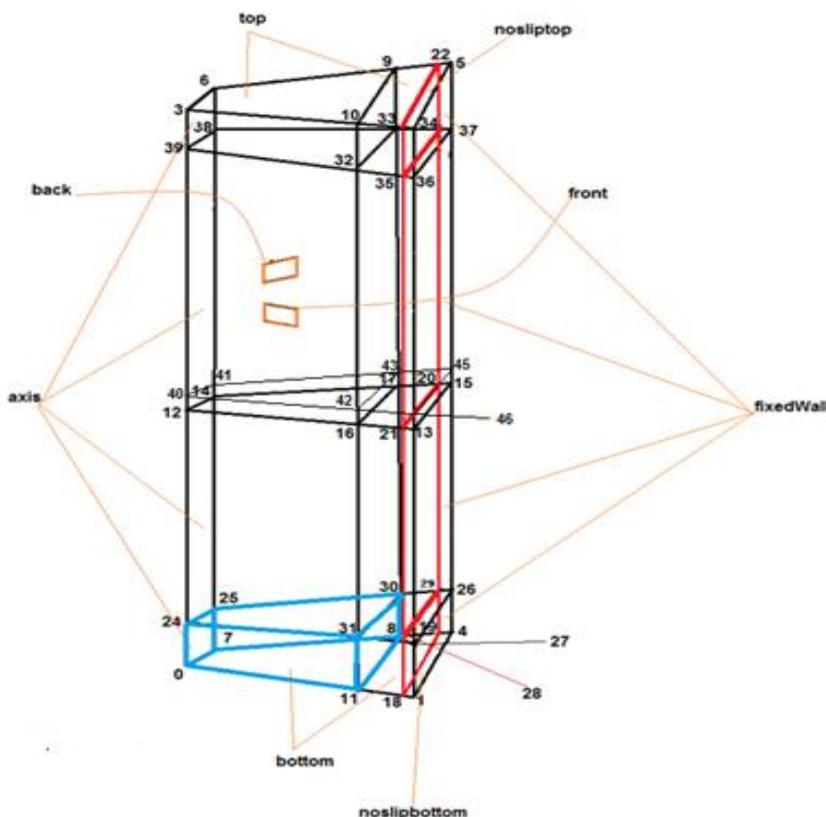
Fig. 4. The simulated geometry and its elements and boundaries

To create an internal flow in the WIDSIM_1 software for rotating cylinder simulation in the total reflux condition, the "Inflow Boundary Model" type should be selected in the "dsmc Properties" folder as "none" meaning that there is no free entrance and exit or free flow in the simulation. In other words, flow is confirmed in the simulation geometry.

Furthermore, in the geometry definition, the type of all boundary conditions must be set to the type "wall". For an internal flow of a geometry with a rotating boundary condition, the following code should be used in the folder "boundary U":

```
rotorWall
    {
Type        rotatingWallVelocity;
axis        (0 0 1);
origin      (0 0 0);
omega       ω;
```

Creating gradient boundary conditions. The GroovyBC library could be used to create gradient boundary conditions in OpenFoam. It is noteworthy that these boundary conditions are not applicable to the dsmcFoam solver because the library is not defined for this solver. Therefore, the user should use the proper coding to create such gradient on the wall.

To create a linear gradient on the wall (points 1-4-5-34), the user can apply the following code in the boundaryT folder:

```
rotorWall
        {
Type        fixedValue;
Value       uniform List<scalar>
Number  Cell
 (
 Temperature Gradient
 )
 }
```

In the above command, the "Temperature Gradient" is equivalent to the temperature corresponding to the cells along the rotor length.

Calculating the initial parameters required by WADSIM_1

The following two conditions should be met in a proper simulation with the DSMC method [19]:

✓ The time step Δt must be smaller than the mean collision time (τ).
✓ The size of each cell (Δx) should be smaller than the mean free path (λ).

The method to calculate the number of cells, the number of simulation particles, the scaling factor

(number of real molecules represented by a single DSMC molecule) and the time step for starting the simulation with the WADSIM_1 solver is described in the following sections.

If the Knudsen number or the pressure of a problem was known, the value of the number density could be calculated as follows:

$$Kn = \frac{\lambda}{L}$$
$$\lambda = \frac{k_B T}{\sqrt{2}\pi d^2 p}$$
$$p = n k_B T \tag{3}$$

where, p is the pressure, λ is the average distance between two collisions of particles with each other, L is the characteristic length of the system, n is the number density of the particles (the number of particles per volume unit), and d is the diameter of the molecule. To determine the local Knudsen number in a field with a strong gradient of variables, the characteristic length should be determined as follows [18]:

$$Kn_{GL} = \max(Kn_{GL-\rho}, Kn_{GL-T}, Kn_{GL-|v|}) \tag{4}$$

where,

$$Kn_{GL-Q} = \frac{\lambda}{|Q_{Local}|}|\nabla Q| \tag{5}$$

In Eq. (5), Q represents fluid density, velocity or temperature. By calculating the mean free path, the length of each cell to change the intensity of the density could be calculated as below:

$$\Delta x, \Delta y, \Delta z \simeq \frac{\lambda}{3-5} \tag{6}$$

Figure 5 shows the simulated geometry and meshing for a rotating cylinder.

By calculating the number density of the simulation environment, the actual number of molecules can be calculated as follows:

$$n = \frac{N}{V} \rightarrow \quad N_{Real} = nV \tag{7}$$

The number of cells in each direction is determined by the following equations:

$$N_x = \frac{L_x}{\Delta x}, N_y = \frac{L_y}{\Delta y}, N_z = \frac{L_z}{\Delta z} \tag{8}$$

As a result, the total number of cells required for simulation is obtained as follows:

$$N = N_x \times N_y \times N_z \tag{9}$$

If the number of simulated particles in each cell was equal to NPPC, then the number of simulated particles N_S will be:

$$N_S = N \times NPPC \tag{10}$$

474

Now, the number of real molecules represented by a single DSMC molecule in WADSIM_1 can be calculated as follows:

$$F_N = \frac{N_{Real}}{N_S} \tag{11}$$

The mean collision time and time step can be obtained as follows:

$$\tau = \frac{\pi\mu}{4nk_B T} \tag{12}$$

At the end, the time step could be calculated by calculating the mean collision time. In any time step, to prevent losing any collision that occurs in the mean collision time, the time step is chosen to be smaller than the time between collisions:

$$\Delta t = \frac{\tau}{3-5} \tag{13}$$

Note that the viscosity coefficient has been given as an input parameter by the user, although it is not in the list of inputs required by the gas properties. In fact, the gas viscosity coefficient is dependent on the gas molecular diameter parameter. The diameter, given by the user as input in this solver, is indeed the reference diameter which must be calculated from the reference temperature and reference viscosity coefficient. The reference diameter and then the effective diameter of each species can be calculated using Eqs. (14) and (15), respectively [2]:

$$d_{ref} = \left(\frac{5(\alpha+1)(\alpha+2)(^{mkTref}/_{\pi})^{1/2}}{4\alpha(5-2\omega)(7-2\omega)\mu_{ref}}\right)^{1/2} \tag{14}$$

$$d_{eff} = d_{pq} = (d_{ref})\left[\frac{\{^{2k(Tref)pq}/_{(m_r c_r^2)}\}^{\omega-1/2}}{\Gamma\left(\frac{5}{2}-\omega_{pq}\right)}\right]^{1/2} \tag{15}$$

As seen in Eq. (15), if the HS model is used to collide two particles together ($\omega = 0.5$), it is observed that by inserting the value $\omega = 0.5$ in Eq. (15), the nominator and denominator of the fraction would be equal to one ($\Gamma(n) = (n-1)!$). This indicates that for the HS model, the effective diameter and reference are equal, in other words, the diameter is independent of the relative velocity in the HS model.

When describing the VHS and VSS models, the diameter of the particles varies with inversing the relative velocity between the two particles. This expression is well seen in Eq. (15) so that the effective diameter has an inverse relation with the relative velocity.

The overall structure of WADSIM_1 software is presented in Fig. 6. The software has three main folders: applications, utilities, and dsmc. The particle' collision and reflection are included in the "submodel" folder.

RESULTS

DSMC code validation for comparison with WADSIM_1 software

The DSMC code is written in FORTRAN programming language in 2-D to validate the results obtained from the WADSIM_1 software, and all the boundary conditions used in the WADSIM_1 software are applied to the DSMC code. The DSMC code for a solid body rotation cylinder with a speed of 500 meters per second was validated with a one-dimensional code written by Bird [3]. The combination of the same percentages of helium, argon, and xenon gases inside the rotating cylinder is simulated by the DSMC method, and at the end, the radial changes of each gas component are shown in Fig. 7. As can be seen, the results obtained from both codes agree with each other.

Simulation of the rotating cylinder in the total reflux mode

In this paper, uranium hexafluoride (as a heavy gas) and air (as a light gas) were separately simulated based on the same input conditions. The purpose was to investigate the effect of the distribution of particles within the rotor based on the molecular mass of the gas. The number of iterations to reach the final results is about 50,000,000, which was executed in a cluster in a parallel mode (MPI) with 31 threads. The physical properties of the studied gases and the required inputs for the open source WADSIM_1 software and DSMC code are presented in Tables 3 and 4.
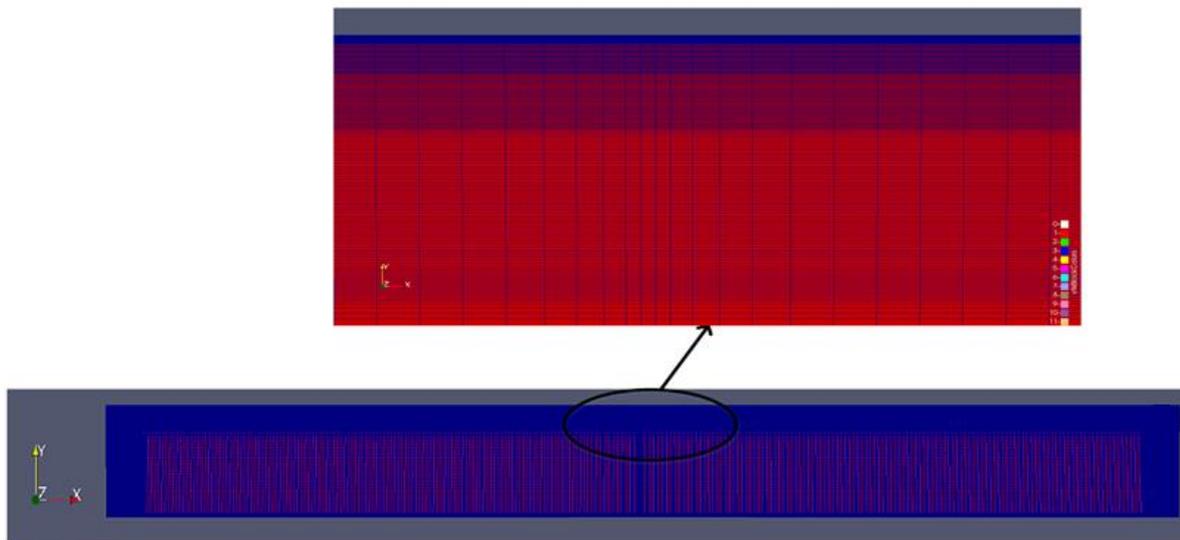
Fig. 5. Example of geometry and meshing of a simulated rotating cylinder.
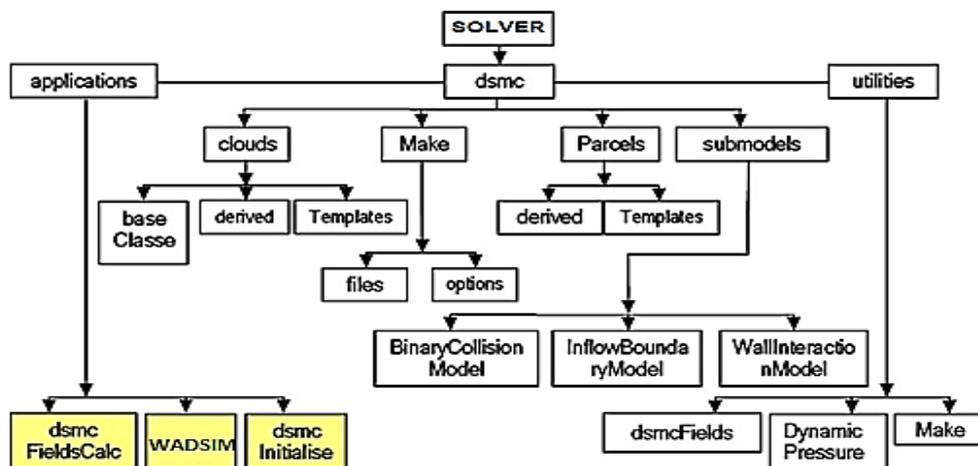
Fig. 6. Directory structure of WADSIM_1
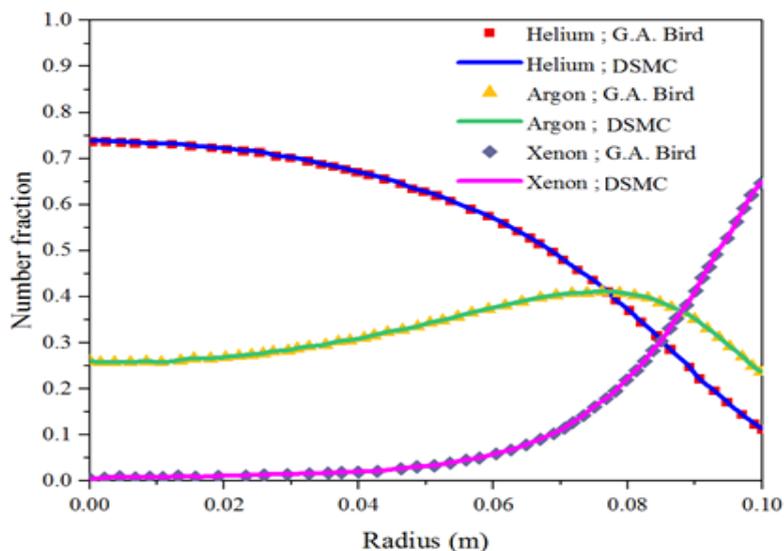
Fig. 7. Comparison of the number density profiles obtained from the two-dimensional DSMC code and the one-dimensional code of Bird [3].

Table 3. The data required to implement the VHS model

Gas	Diameter at 273 K ($\times10^{-10}$ m)	Molecular Mass ($\times10^{-27}$ kg)
UF$_6$	6.0	^{238}UF$_6$ 584.51011 ^{235}UF$_6$ 579.5284
Air	N$_2$ 4.17 O$_2$ 4.07	N$_2$ 46.5 O$_2$ 53.12

Table 4. Characteristics of the hypothetical gas centrifuge

Number density of gases	Azimuthal velocity (m/s)	Number cells
7.729×10^{21}	500	500×1000
Interaction model	Time step	Wall thermal gradient
VHS	1×10^{-7}	20
Gas-Surface interactions	End caps temperature (K)	Dimension of the rotor (m)
Diffuse reflection	300-320	0.1×0.5

The pressure contour resulting from the simulation of air and uranium hexafluoride is shown in Fig. 8.
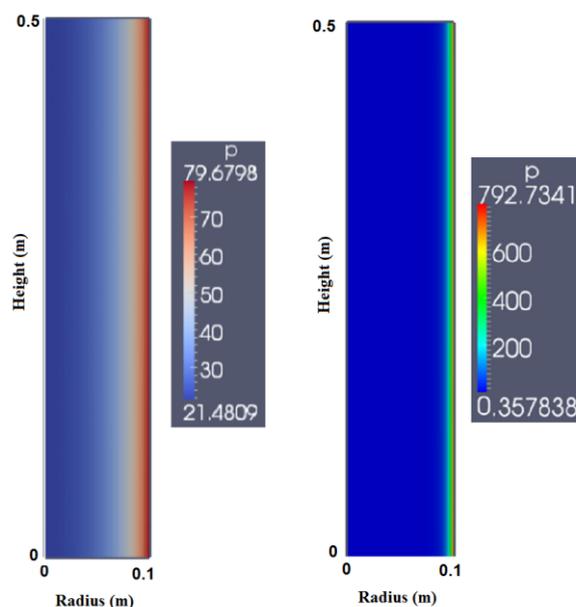
Fig. 8. Contours pressure for air and UF$_6$

As seen, for the light gas, the pressure at the rotor axis is much higher than that for the heavy gas, and on the wall, it is lower than that for the heavy gas, which is due to the low molecular mass of the light gases. This shows that even with the same amount of inputs and the same number density, for the gases with different molecular masses, different pressure contours could be obtained. The pressure changes inside the rotor for light (air) and heavy (uranium hexafluoride) gases are shown in Fig. 9.
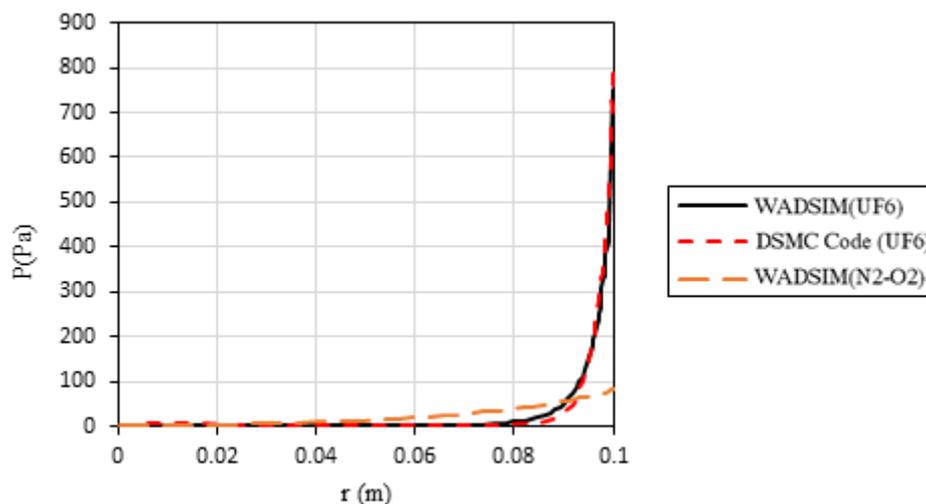
Fig. 9. The radial pressure distribution for air and UF_6 using WADSIM_1 software and DSMC code.

One of the most important contours is the radial velocity. As shown in Fig. 10, the particles take the radial velocity alongside the top and bottom caps due to the collision of the particles with the wall. Thus, the radial velocity in these regions is not equal to zero. It is to be noted that if air is used in the simulation, the maximum radial velocity between the two caps will be lower than when using uranium hexafluoride, because the pressure of light gases is higher than that of heavy gases in the center of the rotor. Hence, the collided particles with the top and bottom caps take the velocity proportional to the radius. In addition, when they want to rebounce from the wall, they collide with the particles on their faces and, in turn, their radial velocity will be reduced; however, in case of using a heavy gas, due to the sharp decrease in pressure within the center of the rotor, the particles would take azimuthal velocity proportional to the radius after colliding with the two caps. As a result, their velocity would be less slowed down due to the very low presence of particles in front of them at the time of return and a low number of molecular collisions between them. The radial velocity drops drastically due to the collision with the background gas. The gas in the total reflux mode is sufficiently compressed to the wall; thus, it does not allow the movement unless in the form of diffusion. Azimuthal velocity graphs are also very important in a machine. The linear behavior of the rotational velocity graph is completely pressure-dependent. As shown in Fig. 11, when uranium hexafluoride is used in the simulation, the azimuthal velocity changes linearly because of the high pressure near the wall; however, with the decrease of pressure in the radial direction, the azimuthal velocity of particles also decreases nonlinearly.
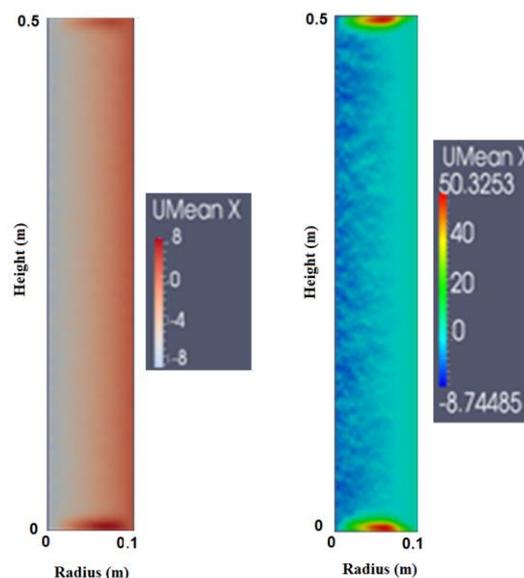
Fig. 10. Radial velocity contour for air and UF_6

Since the pressure variation is roughly uniform along the rotor's radius, if air is used, the change in the azimuthal velocity of the particles also occurs linearly. The steady state of the flow is similar to a "solid body" rotation with azimuthal velocity proportional to the radius.

To convert radial flow to axial one and to increase the gas separation within the rotor, different types of drives can be used in a rotating cylinder. Each driving mechanism drives axial velocity in the rotor. It is possible to use thermal drives of the rotor wall and the caps to create a secondary flow inside the rotor to model and simulate the gas flow in the rotor *via* total reflux mode. Due to the presence of drives, an axial velocity is generated in the entire rotor. The dominant mass lies in the Stwartsons layer (near the rotor wall) due to the centrifugal force effect.
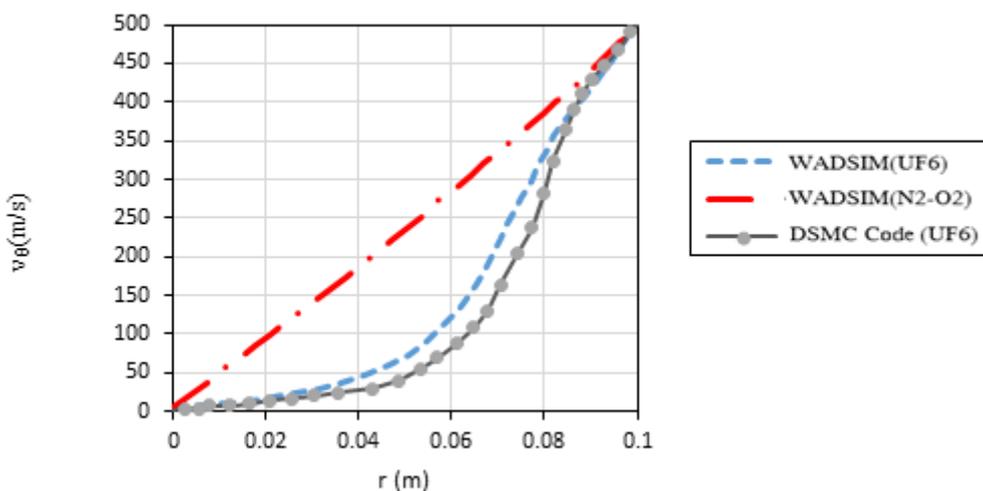
Fig. 11. Azimuthal velocity of air and UF_6 using WADSIM_1 software and DSMC code
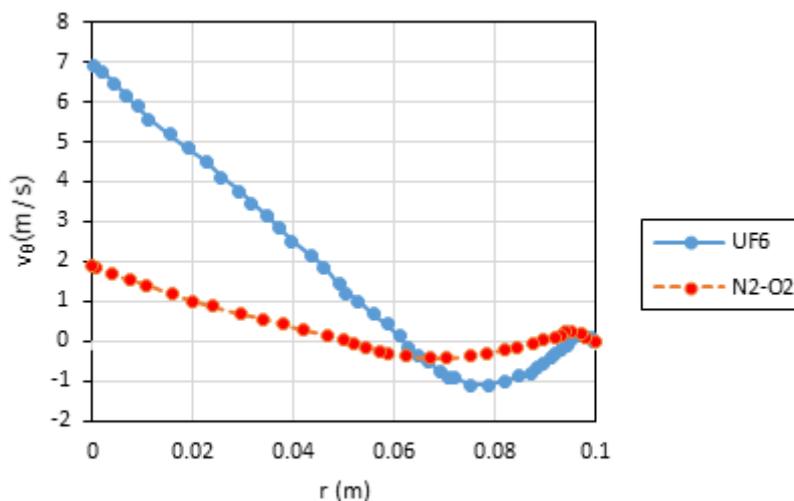
Fig. 12. Axial velocities of air and UF_6
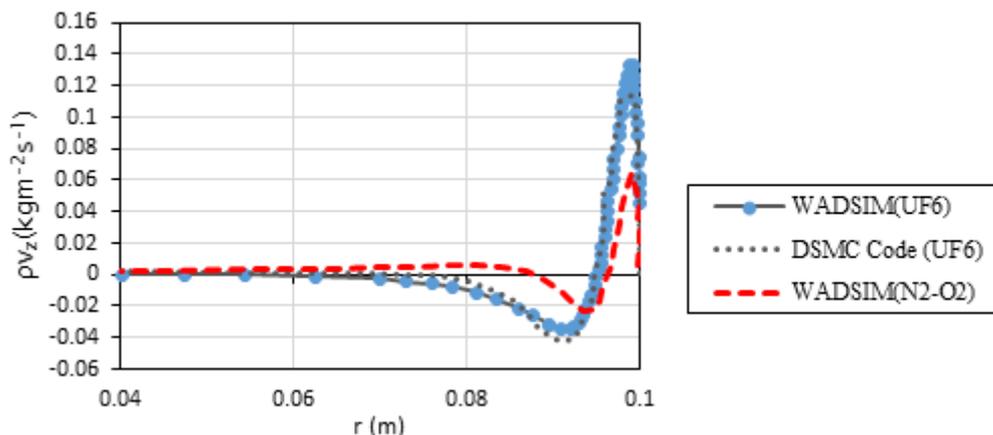
Fig. 13. Axial mass fluxes of air and UF_6 using the WADSIM_1 software and DSMC code

It is worth noting that v_z is created even in the molecular domain of the rotor and has a high value. The axial mass flux (ρv_z) could be calculated by

evaluating the axial velocity inside the rotor. Indeed, due to the secondary flow, it is expected that the resulting axial mass flux has a positive region due to

the upstream flow and a negative region due to the downward flow. The axial velocity diagrams for two different gases are shown in Fig. 12. The axial mass flux diagram in the center of the rotor for uranium hexafluoride gas is plotted in Fig. 13; as shown, it is similar to the results of the DSMC code.

Simulation of the helix groove using the WADSIM_1 software

To demonstrate the ability of the WADSIM_1 software, this section simulates the gas flow within a helix groove as a complex geometry. The molecular pump is located in the upper part of a centrifuge in the space between the rotor and the casing, with the main task of maintaining a vacuum in this region. This pump is made up of a number of grooves, and the wall opposite each groove has a high rotating speed so that the gas molecules collide with this rotating wall and lead to the groove output.

In this simulation, a groove and a periodic boundary condition for it have been used to repeat its geometry to complete the molecular pump's geometry. The pressure gradient with exponential growth will be created along the length of the groove because of the presence of a rotating wall with a high rotation speed. The complex geometry of the mentioned groove was simulated using WADSIM_1 software (see Fig. 14).

The geometrical and operational characteristics of the studied molecular pump, as well as the values of the compression ratio obtained from the simulation and experimental test are given in Table 5.
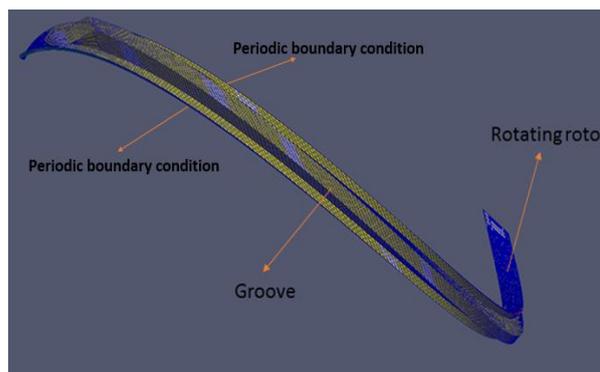
Fig. 14. Geometry and mesh of helix groove

The contour of pressure variations along the groove length is shown in Fig. 15.
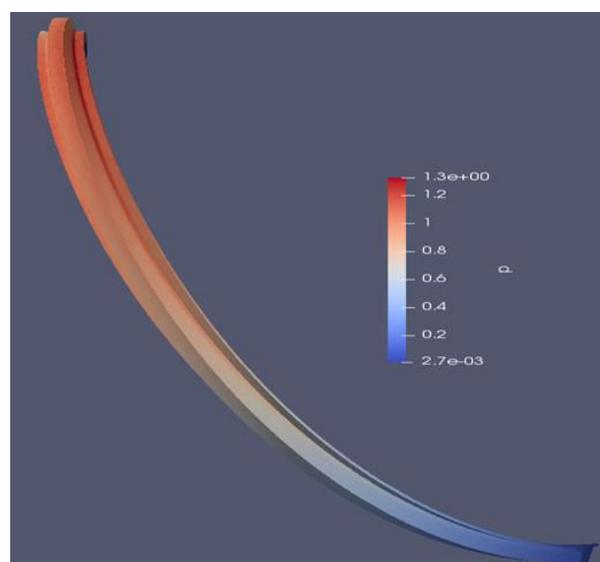
Fig. 15. The contour of pressure variations (Pa) along the groove length using WADSIM_1 software

Table 5. Compression ratio of molecular pump obtained using WADSIM_1 software and experimental test.

Gas	Top width of groove (mm)	Bottom width of groove (mm)	Clearance (mm)	Rotor velocity (m/s)	Length of pump (mm)	Shape of groove
Air	13.8	6.4	1.2	560	170	trapezoidal
Compression ratio of the WADSIM_1 software			Compression ratio of experimental test			
481			470			

CONCLUSION

Since molecular methods have the capability of modeling all flow regimes (molecular and continuous region) and because of the strong pressure stratification, continuous-fluid equations are not valid in the whole cylinder, with or without linearization of the model. In the present work, the molecular-based dsmcFoam solver for investigating the total gas flow in the rotor was chosen from the OpenFoam software. Then it was modified to simulate the gas flow inside a rotating cylinder and introduced as WADSIM_1 software. The capabilities of the software include the possibility of investigating the gas flow inside a rotating cylinder with high-speed rotation, applying a thermal gradient boundary condition for the rotor wall, and

employing the Adaptive Mesh Refinement (AMR) technique due to the strong gradient of flow in the rotor's radial direction.

The simulation results indicated the significant effect of the molecular mass of a gas on the formation of pressure, velocity, and axial mass flux profiles within the rotor after 5 seconds of real time. By changing the gas type, the pressure on the rotor axis was changed significantly so that when a light gas was used in a rotating cylinder, the amount of pressure in the rotor's axis was higher than when a heavy gas was used. As the pressure on the rotor's axis increased, the pressure in the space above the molecular pump increased; as a result, the molecular pump's performance was affected.

Furthermore, comparing the results of DSMC code with the results obtained from the WADSIM_1 software showed that besides having the right precision, the calculation speed was multiplied due to the use of WADSIM_1 software from the MPI parallelization tools with unlimited cores. For example, using a 31-thread cluster, the computing time was ten times lower than with single-core DSMC implementation. At the end, it is concluded that this software, in addition to having the right precision, has a very high speed for simulating the gas flow for all regions (molecular and continuous regimes) within the rotor. In the future works, its development for simulation of the gas inside the rotor under actual conditions is proposed by applying all drives (feed, scoop and baffle drives).

REFERENCES

1. H. G. Wood, J. B. Morton, *J. Fluid Mech.*, **101,** 1 (1980).
2. G. A. Bird, Molecular Gas Dynamics, Oxford University Press, London, 1976.
3. G. A. Bird, The DSMC method, The University of Sydney, 2013.
4. S. Pradhan, V. Kumaran, *J. Fluid Mech*., **686**, 140 (2011).
5. S. Pradhan, The generalized Onsager model for a binary gas mixture with swirling feed, 14th International Energy Conversion Engineering Conference, 2016.
6. www.OpenFoam.org.
7. K. Gott, A. Kulkarni, J. Singh, A Comparison of Continuum, DSMC and Free Molecular Modeling Techniques for Physical Vapor Deposition, in: ASME 2013 International Mechanical Engineering Congress and Exposition, American Society of Mechanical Engineers Digital Collection, 2013.
8. C. White, Adaptive Mesh Refinement for an Open Source DSMC Solver, in: 20th AIAA International Space Planes and Hypersonic Systems and Technologies Conference, 2015.
9. B. John, X.-J. Gu, R.-W. Barber, D.-R. Emerson, High Speed Aerodynamic Characteristics of Rarefied Flow past Stationary and Rotating Cylinders, 20th AIAA International Space Planes and Hypersonic Systems and Technologies Conference, 2015.
10. B. John, X.-J. Gu, R.-W. Barber, D.-R. Emerson, *AIAA Journal*, **54**, 1670 (2016).
11. N. Dongari, C. White, T. J. Scanlon, Y. Zhang, J. M. Reese, *Physics of Fluids*, **25**(5), 052003 (2013).
12. R. Kumar, A.-K. Chinnappan, *Computers & Fluids*, **159**, 204 (2017).
13. M. Khajenoori, J. Safdari, A. H. Asl, *Granular Matter*, **21**(3), 63 (2019).
14. T. J. Scanlon, E. Roohi, C. White, M. Darbandi, *Comput. Fluids*, **39**(10), 2078 (2010).
15. E. Arlemark, G. Markelov, S. Nedea, *Journal of Phys. Conf. Ser.*, **362**, 012040 (2012).
16. S. Yousefi-Nasab, J. Safdari, J. Karimi-Sabet, M. Khajenoori, *Journal of Vacuum,* **172,** 109056 (2020).
17. S. Yousefi-Nasab, J Safdari, J Karimi-Sabet, A. Norouzi, E. Amini, *Journal of Applied Surface Science,* **493**, 766 (2019).
18. Z-X, Sun, Z. Tang, Y.-L. He, W.-Q. Tao, *Journal of Computers & Fluids,* **50**(1), 1 (2011).
19. W. Wagner, *Journal of Stat. Phys*., **66**, 1011 (1992).

Dual functional azo polysiloxane dyes for polyester: synthesis and application

H. K. Sheikh[1,2,3*], T. Arshad[1,4], Z. S. Muhammad[1,5], M. M. Hasan[3], F. Nasir[6], M. H. Kazmi[4]

[1]*Molecular Sciences and Research (SMC-Pvt. Ltd), Pakistan*
[2]*Universidade de Coimbra, Coimbra, Portugal*
[3]*Department of Pharmacognosy, Faculty of Pharmacy, Karachi, Pakistan*
[4]*Department of Applied Chemistry, University of Karachi, Karachi, Pakistan*
[5]*Faculty of Rehabilitation and Allied Health Sciences, Riphah International University, Islamabad, Pakistan*
[6]*Pakistan Air Force-Karachi Institute of Engineering and Technology (PAF-KIET), Karachi, Pakistan*

The purpose of this research was to design and synthesize novel functional polymeric azo dyes that not only dye the polymeric substrates, but also influence their physical handle properties. The synthesis scheme involved azo chromophores synthesis using *tert*-butyl nitrite. Single and dual azo chromophores were bonded with polysiloxane chain using carbonyldiimidazole (CDI). The synthesized molecules were applied to a polymeric polyester substrate. Due to the presence of polysiloxane chains in the molecule, the handle properties of the treated polymeric substrates were modified while the attached chromophore performed its coloration function. Molecules structures of azo polysiloxane products were elucidated by UV-Vis, MALDI-TOF mass spectroscopy, ^{1}H-NMR (500 MHz), elemental analysis. Mass spectroscopy was performed after each synthesis step to check mass difference in peaks of intermediates and products. The coupling components were applied on a polyester substrate and azo coupling reactions were carried out on the polymeric substrate itself carrying the coupling components. Azo molecules were separately synthesized for characterization. The compounds were found to be capable of altering the handle of the substrate and imparting softness even at low concentrations. The subjective evaluation of handle properties confirmed the handle modifying capability of the azo polysiloxane molecule. Two different subjective techniques were used for evaluation, namely, press method and crush method. Crush method turned out to be more reliable, as was judged by the variance among the readings taken by the subjects. Other similar dual-purpose polymeric azo dye molecules can be synthesized on the same pattern for application on other polymeric substrates.

Keywords: Polysiloxane, Synthesis, Azo, Carbonyldiimidazole, Polyester.

INTRODUCTION

Handle of a fabric or any similar material describes the sum of total sensations felt when a fabric is touched by the human hand. Generation of particular handle is one major feature of textile finishing processes [1]. Handle modification refers to imparting a particular "handle or hand" to a fabric or similar material by treatment of the fabric with hand modifier compounds. When the handle of a fabric is changed in such a way that drape is enhanced and material turns silkier, the fabric is referred to have been 'softened'. The inclusion of polysiloxane molecules containing linear siloxane [-Si-O-Si-]$_n$ chains within polymeric chains of fibers accomplishes this softening process. These chains decrease the coefficient of friction between fibers and any surface in contact with them [2] thus imparting softness to the material [3]. Handle is defined by properties such as smoothness, thickness, bulkiness, extensibility, stiffness, draping character, compressibility, surface friction, and elasticity [4-6].

In this research, we evaluated the performance of polysiloxane as a handle modifier when bonded to a chromophore. Terminal functional groups carrying polysiloxane **(4)** and **(8)** were selected to induce handle modifying property in the targeted molecules (Fig. 1). Terminal Lewis basic groups, -OH and bis-NH$_2$ on the polysiloxane chain were responsible for bonding the polysiloxane chain with the coupling component by acyl addition elimination reaction. After synthesis, coupling component compounds **(5)** and **(9)** were applied to the polyester substrate and later *tert*-butyl nitrite-assisted azo synthesis was performed on them. This resulted into mono ester of azo and amide diazo, respectively, connected with the linear polysiloxane chain. Azo synthesis involved formation of stable diazonium through diazotization by *tert*-butyl nitrite in the presence of 1,5-naphthalenedisulfonic acid. It was expected that the handle properties of the treated fabric would be modified due to the presence of polysiloxane chains in the target molecule as they would be providing fiber lubrication, while the bonded chromophore would perform the coloration function. The resulting molecule therefore functions simultaneously as a dye and as a handle modifier.

---

* To whom all correspondence should be sent:
E-mail: Hamdullah.khadim.sheikh@gmail.com
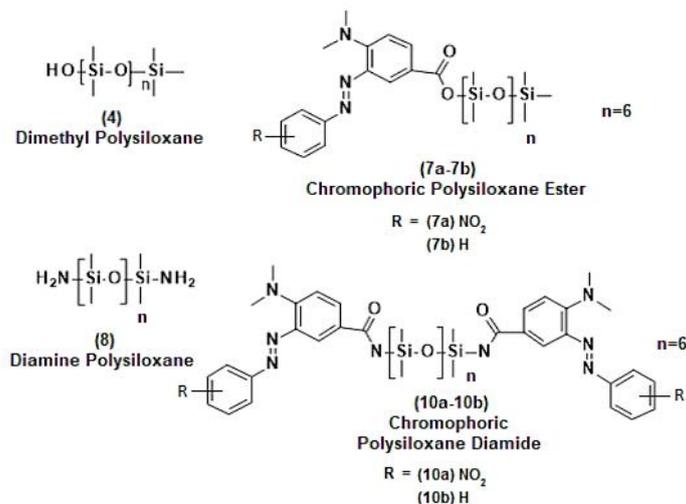
Fig. 1. Core structure of handle-modifying molecules

Subjective evaluation was used for confirming the alteration of the handle properties of the material because of the application of synthesized molecules. This technique transformed psychological perception of touch into an objective parameter by allotting it a single value. Subjective evaluation sets up a parallel between human subjective perception and mechanically measured values. AATCC (American Association of Textile Chemists and Colorists) has defined guidelines for subjective evaluation with standard conditions [7]. Similar to the molecules presented in this research work, other polymeric azo dyes with single or multiple azo chromophores connected to polymeric chains have been reported before. Two kinds of polymeric dyes are included. The first type is when the chromophore is a monomer which is polymerized. The second type has its chromophore connected to a polymeric chain. Examples include polyhdrazone [8], polystyrene azo hybrid [9] polymeric azo containing epoxy reactive group [10] and polyurethanes (PUs) disperse dyes synthesized by epichlorohydrin [11]. Monomeric heterocyclic azo-based polymers have also been reported [12]. Synthesis of these dual functional molecules and subjective evaluation of their effect on handle properties of the substrate is a novel study. It may form the basis for development of functional dyes that can simultaneously perform coloration and functional finishing jobs. Hence, production time and costs may be reduced.

EXPERIMENTAL

Materials

The reagents and solvents used in the reactions and purification steps were acquired from Sigma-Aldrich chemical company, USA. Solvents used were dried before use in reactions and purification steps and were of analytical grade. UV-Vis spectra were recorded on a Thermo Scientific evolution-300 UV-Vis spectrophotometer. ^{1}H-NMR spectra were recorded in CDCl$_3$ with Si(CH$_4$)$_3$ as the internal standard at 500 MHz on a Bruker Avance spectrophotometer. MALDI-TOF was recorded on a Bruker MALDI mass Ultraflex III TOF 200 mass spectrometer. Thin layer chromatography (TLC) was used for monitoring the reaction completion, carried out on Merck silica gel (pre-coated) 60 F$_{254}$ 20 × 20 cm Al sheets. UV light of 254 and 366 nm wavelength was used to identify spots on the TLC. Reagents used in the application process - dispersing agent lycol RDN, stiffening agent arkofil, softening agent sulfosoft polysiloxane and nonionic detergent, were procured from Archroma Pakistan Ltd.

Synthesis

1) Polysiloxane Coupling Components (5) and (9). Carbonyldiimidazole (**2**) (5 mmol) along with 4-N,N-dimethylamine benzoic acid (**1**) (5 mmol) were stirred in tetrahydrofuran THF. Stirring continued for 2 hours and then terminal hydroxypolysiloxane (**4**) (1.25 mmol) or terminal diaminepolysiloxane (**8**) (0.65 mmol) (two separate processes) was dissolved into the reaction solution. In addition, triethylamine (0.52 ml) was also added to the reaction vessel. The stirring was continued for further 48 hours. After the completion of reaction, the solvent was evaporated and the reaction mixture was put into Na$_2$CO$_3$ solution (0.05 M). The precipitate was filtered and then washed with H$_2$O, and extracted with dichloromethane (DCM). Finally, the extracted product was dried over Na$_2$SO$_4$. Subsequently, the solvent was evaporated to obtain the polysiloxane coupling components (**5**) or (**9**) (Schemes 1 and 2).

482
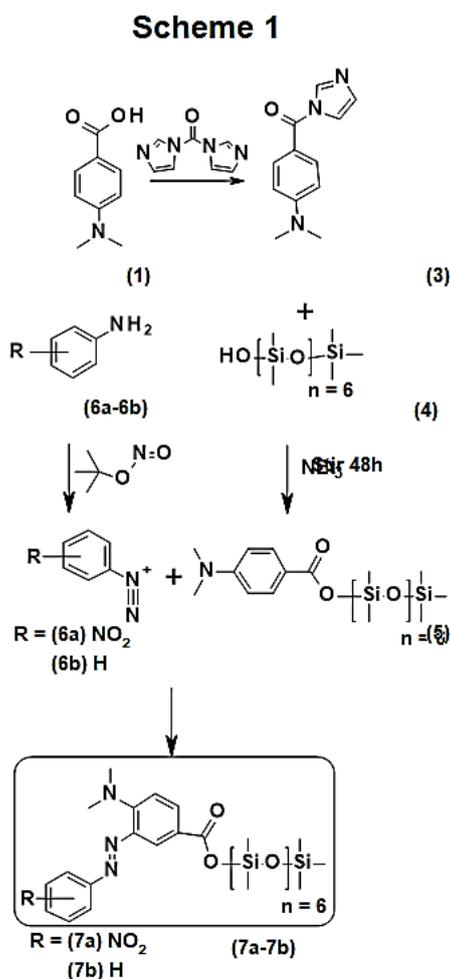
Scheme 1

Scheme 2

Scheme 1. Synthesis of polysiloxane azo dyes (**7a-7b**).

Scheme 2. Synthesis of polysiloxane azo dyes (**10a-10b**).

2) Polysiloxane azo dyes (7a-7b, 10a-10b). In vessel A, aniline derivative (10 mmol) (**6a-6b**) was added to 1,5-naphthalenedisulfonic acid (10 mmol) in 100 ml of ethyl acetate and the solution was brought to 50 °C. Diazonium ion was synthesized by addition of *tert*-butyl nitrite (15 mmol) to the vessel A. Stirring continued for 25 min at 25 ^{0}C. In vessel B, polysiloxane coupling component (**5** or **9**) (10 mmol) was dissolved in ethanol (100 ml) and temperature was brought down to 0-5 ^{0}C. Diazonium derivative (**6a-6b**) from vessel A was transferred to the vessel B containing polysiloxane solution while pH was maintained at 5.5 with 2 % CH$_3$COONa solution. The reaction continued for more 2.5 hours. At this point, an azo precipitate (**7a-7b, 10a-10b**) started to accumulate. This filtered product mass was washed with H$_2$O multiple times and extracted with DCM. Finally, it was dried over Na$_2$SO$_4$. Evaporation of DCM solvent afforded the azo polysiloxane adduct (**7a-7b, 10a-10b**). Spectroscopic details of the synthesized molecules (**7a-7b, 10a-10b**) are given below:

(**7a**) Rust colored viscous mass. Yield: 55 %; UV-Vis (7.27 × 10^{-5} M in CDCl$_3$) [λ$_{max}$, nm (ε$_{max}$, L mol^{-1} cm^{-1})]: 496.0 (42640.9); ^{1}H-NMR (CDCl$_3$, 500 MHz, 25 °C, Si(CH$_3$)$_4$) δ (ppm): 0.08 (s, 9H, C$_1$H$_3$, C$_3$H$_3$, C$_4$H$_3$), 1.14 (s, 36H, C$_{7, 8, 11,12, 15, 16, 19, 20, 23, 24,27, 28}H_3$), 2.91 (s, 3H, C$_{37}H_3$), 2.92 (s, 3H, C$_{38}H_3$), 7.10 (d, 1H, ^3J= 7.5 Hz, C$_{34}$H), 7.86 (m, 3H, C$_{33, 44,48}$H), 8.31 (m, 2H, C$_{45, 47}$H), 8.52 (d, 1H, ^4J= 2.0 Hz, C$_{40}$H); MALDI-TOF *m/z*: 831.2 [M+H]$^+$; Elemental analysis (%) calculated for C$_{30}$H$_{58}$N$_4$O$_{10}$ Si$_7$: C, 34.34; H, 7.03; N, 6.74; O, 19.24; Si, 23.65 %. Found: C, 34.37; H, 7.05; N, 6.71; O, 19.23; Si, 23.64 %.

(**7b**) Yellow colored viscous mass. Yield: 52 %; UV-Vis (7.27 × 10^{-5} M in CDCl$_3$) [λ$_{max}$, nm (ε$_{max}$, L mol^{-1} cm^{-1})]: 380.0 (8093.0); ^{1}H-NMR (CDCl$_3$, 500 MHz, 25 °C, Si(CH$_3$)$_4$) δ (ppm): 0.08 (s, 9H, C$_1$H$_3$, C$_3$H$_3$, C$_4$H$_3$), 1.14 (s, 36H, C$_{7, 8, 11,12, 15, 16, 19, 20, 23, 24,27, 28}H_3$), 2.93 (s, 3H, C$_{37}H_3$), 2.95 (s, 3H, C$_{38}H_3$), 6.90 (d, 1H, ^3J= 7.5 Hz, C$_{34}$H), 7.49 (m, 1H, C$_{46}$H), 7.55 (m, 2H, C$_{45, 47}$H), 7.77 (m, 1H, C$_{44, 48}$H), 7.81 (m, 1H, C$_{33}$H), 8.50 (d, 1H, ^4J= 2.0 Hz, C$_{40}$H); MALDI-TOF *m/z*: 786.1 [M+H]$^+$; Elemental analysis (%) calculated for C$_{30}$H$_{58}$N$_3$O$_8$ Si$_7$: C, 45.82; H, 7.56; N, 5.34; O, 16.28; Si, 25.00 %. Found: C, 45.81; H, 7.57; N, 5.35; O, 16.30; Si,

25.01 %.

(10a) Dark rust colored viscous mass. Yield: 45 %; UV-Vis (7.27×10^{-5} M in CDCl$_3$) [λ_{max}, nm (ε_{max}, L mol^{-1} cm^{-1})]: 496.0 (13755.0); ^{1}H-NMR (CDCl$_3$, 500 MHz, 25 °C, Si(CH$_3$)$_4$) δ (ppm): 0.014 (s, 42H, C$_{5, 6, 9, 10, 13, 14, 17, 18, 21, 22, 25, 26, 29, 30}$ *H$_3$*), 2.98 (s, 12H, C$_{39, 40, 39', 40'}$ *H$_3$*), 7.03 (d, 2H, ^3J = 7.5 Hz, C$_{36, 36'}$*H*), 7.77 (s, 1H, N*H*), 7.99 (dd, 2H, ^3J = 8.0 Hz, ^4J = 2.5 Hz, C$_{35, 35'}$ *H*), 8.13 (m, 4H, C$_{46, 46', 50, 50'}$*H*), 8.31 (m, 4H, C$_{47, 47', 49, 49'}$*H*) 8.72 (d, 2H, ^4J = 2.5 Hz, C$_{42, 42'}$ *H*); MALDI-TOF *m/z*: 1127.3 [M+H]$^+$; Elemental analysis (%) calculated for C$_{44}$H$_{70}$N$_{10}$O$_{12}$ Si$_7$: C, 46.86; H, 6.26; N, 12.42; O, 17.03; Si, 17.43 %. Found: C, 46.88; H, 6.23; N, 12.41; O, 17.06; Si, 17.42 %.

(10b) Yellow colored viscous mass. Yield: 48 %; UV-Vis (7.27×10^{-5} M in CDCl$_3$) [λ_{max}, nm (ε_{max}, L mol^{-1} cm^{-1})]: 380.0 (9); ^{1}H-NMR (CDCl$_3$, 500 MHz, 25 °C, Si(CH$_3$)$_4$) δ (ppm): ^{1}H-NMR (CDCl$_3$, 500 MHz, 25 °C, Si(CH$_3$)$_4$) δ (ppm): 0.014 (s, 42H C$_{5, 6, 9, 10, 13, 14, 17, 18, 21, 22, 25, 26, 29, 30}$ *H$_3$*), 2.98 (s, 12H, C$_{39, 40, 39', 40'}$ *H$_3$*), 7.02 (d, 2H, ^3J = 7.5 Hz, C$_{36, 36'}$*H*), 7.51 (m, 2H, C$_{48, 48'}$*H*) 7.67 (m, 4H, C$_{47, 47', 49, 49'}$*H*) 7.70 (s, 2H, N*H*), 7.89 (m, 4H, C$_{46, 46', 50, 50'}$*H*), 7.99 (dd, 2H, ^3J = 8.0 Hz, ^4J = 2.5 Hz, C$_{35, 35'}$*H*), 8.72 (d, 2H, ^4J = 2.5 Hz, C 42, 42'*H*); MALDI-TOF *m/z*: 1037.3 [M+H]$^+$; Elemental analysis (%) calculated for C$_{44}$H$_{72}$N$_8$O$_8$ Si$_7$: C, 50.93; H, 6.99; N, 10.80; O, 12.33; Si, 18.95 %. Found: C, 50.94; H, 7.01; N, 10.82; O, 12.34; Si, 18.92 %.

3) Application Process of (5) and (9) on Polyester: Exhaust high temperature application method was used for application of **(5)** and **(9)** coupling components on synthetic fiber fabrics. The same application method was used for both **(5)** and **(9)** molecules on polyester fabrics separately. 0.5 % compound o.w.f (on weight of fiber) was used. Before treatment, the fabric (10 g) was prewashed with nonionic detergent (2 g/L) in the presence of Na$_2$CO$_3$ (2 g/L) at 75 °C for 35 min, in a liquor ratio of 1:20. The fabric was then rinsed and dried. The 10 g of polyester fabric was put in water at 65°C, in a liquor ratio of 1:20. pH was stabilized at 5.5 by CH$_3$COOH (10 %). 2 g/L of dispersing agent lycol RDN was dissolved in the water; 0.5 g/L (0.5 % compound o.w.f) azo polysiloxane molecule was transferred to the water. The temperature was increased from 65 to 100 °C at the rate of 5 °C/min and then further from 100 °C to 120 °C at the rate of 3 °C/min. Treatment process continued for 70 min. Temperature of the treatment vessel was reduced to 75 °C at 3 °C/min. The treated sample was rinsed and divided into smaller pieces for evaluation.

4) Polysiloxane azo dyes (7a-7b, 10a-10b) formed inside the polyester fiber. In vessel A, aniline

derivative (10 mmol) **(6a-6b)** was added to 1,5-naphthalenedisulfonic acid (10 mmol) in 100 ml of ethyl acetate and the solution was brought to 50 °C. Diazonium ion was synthesized by addition of *tert*-butyl nitrite (15 mmol) to the vessel A. Stirring continued for 25 min at 25 °C. In vessel B, polysiloxane coupling components (5 or 9)-carrying polyester (from process 3) was put in 100 ml ethanol and the temperature was brought down to 0-5 °C. Diazonium solution of aniline derivative **(6a-6b)** from vessel A was transferred to the vessel B while pH was kept stabilized at 5.5 with 2 % CH$_3$COO Na. Constant conditions were maintained for 2.5 hours, after which an azo compound **(7a-7b, 10a-10b)** started to form on the surface of the polyester fibers. The sample was washed with water.

5) Handle Evaluation Test of (7a-7b, 10a-10b). The treated fabric was divided into samples of 100 × 100 mm size. These samples were put inside a rectangular text box. Subjects were provided with reference fabrics **A**, **B** and **C** before each evaluation and were informed of assigned values. Tests were conducted at 28 °C. The following methods were used:

i.   Press Method

The same method was used for all samples. The subjects placed four fingers on the fabric surface inside the test box. Subjects ran their fingers along the sample linearly while applying pressure. Based upon their perception, the subjects then assigned a value between 1 and 20 (details are provided in Results and Discussion), compared to assigned values of standards **A**, **B** and **C**.

ii.   Crush Method

Subjects were asked to place the treated sample in the palm of their hand and crush it by closing their fist. The subjects assigned a logical value between 1 and 20 (details given in Results and Discussion) compared to values given to the standards **A**, **B** and **C**.

RESULTS AND DISCUSSION

Synthesis

The synthesis consisted of a multiple step scheme (Schemes 1 and 2). The first step was the synthesis of coupling component. In this step, acyl addition elimination was carried out on 4-N,N-dimethylamino benzoic acid (**1**) with the terminal -OH and -NH$_2$ carrying polysiloxane **(4)** and **(8)** by using carbonyldiimidazole (CDI) [13]. The resultant coupling components **(5)** and **(9)** were applied to the polyester fabric substrate and then underwent electrophilic aromatic substitution with diazotised derivatives **(6a-6b)** to form the final polymeric azo dyes **(7a-7b** and **10a-10b)**. Same dyes can be applied

to other polymeric substrates such as polyamide. Polyester fiber is globally the most used fiber, up to 50% of the overall synthetic fibers. Stable diazonium was formed in presence of *tert*-butyl nitrite [14] as a source of nitronium ion Lewis acid in presence of 1,5-naphthalenedisulfonic at room temperature in ethyl acetate. The structure of the azo polysiloxane can be greatly modified. Polysiloxane can be of various types, hence change in handling properties caused by these chains, can be modified as well. This can be achieved by selecting different substituents on the Si atom of the polysiloxane chain. There can be SiH(CH₃), Si(CH₃)₂, etc. The polysiloxane itself can have different chain lengths. Alkyl substitution on the Si atom changes the polarity of the polysiloxane chain which directly relates to its resultant magnitude of softness. Hence, desired softness can be achieved.

Spectroscopic Analysis

We performed MALDI MS of unreacted polysiloxanes and then again after coupling component formation (5) and (9) and azo bond formation (7a, 7b, 10a and 10b). All peaks were detected as the pseudomolecular ion peak [M+H]. MALDI spectra are given in Figs. S1-S8 (See Supplementary Section, A). We checked the difference in the masses of peaks after every reaction to confirm the formation of desired product molecule. Before esterification, the molecular ion peak of polysiloxane (4) was 535.2 m/z (Fig. S1) and a post-esterification compound (5) showed up at 682.3 m/z in MALDI-TOF (Fig. S2). This peak showed a difference of 147.1 m/z between –OH terminated polysiloxane (4) and modified polysiloxane (5). This difference confirms the

bonding of benzoic acid moiety. The difference in molecular ion peaks of compounds (5) and (7a) (Fig. S3) was found to be 148.9 m/z that confirmed the azo coupling of compound (5) with 4-nitroaniline (6b). [M+H]⁺ for (7a) and (7b) appeared at 831.2 and 786.1 m/z, respectively.

For compound (7b) the difference in mass is 104.1 m/z (Fig. S4) that confirmed the azo coupling with aniline (6a). In the spectra of (7a) and (7b) unreacted coupling component (5) appeared at 682.3 m/z.

[M+H]⁺ for (10a) and (10b) appeared at 1127.3 and 1037.3 m/z, respectively. In case of bisamine-terminated polysiloxane (8) (Fig. S5), the chain itself showed a peak at 535.1 m/z and a post-amide bond formation peak showed up at 829.3 m/z which confirmed the synthesis of compound (9) (Fig. S6). The difference of 294.2 m/z confirmed the bonding of two 4-N,N-dimethylamino benzoic s (1) at terminal position of the polysiloxane chain. After azo coupling reactions, molecular ion peaks of (10a) and (10b) showed up at 1127.3 m/z (Fig. S7) and 1037.3 m/z (Fig. S8), respectively. Azo coupled polysiloxane (10a) and (10b) showed differences of 298.0 m/z and 208.0 m/z, respectively, with coupling component (9) (Fig. S6). This confirms the azo formation at both ends of the polysiloxane chain. In the mass spectra of (10b) a peak was detected at 887.2 m/z (Fig. S8). This was attributed to a nitroso product. Mono and dinitroso products were detected at 858.3 m/z and 887.2 m/z in the spectra of (10a) (Fig. S7). This means that a nitroso byproduct was formed at both ends of the molecule, at the ortho position of the N(CH₃)₂ on aryl rings as shown in Fig. 2. No such nitroso product was detected in the (7a) and (7b) azo molecules.
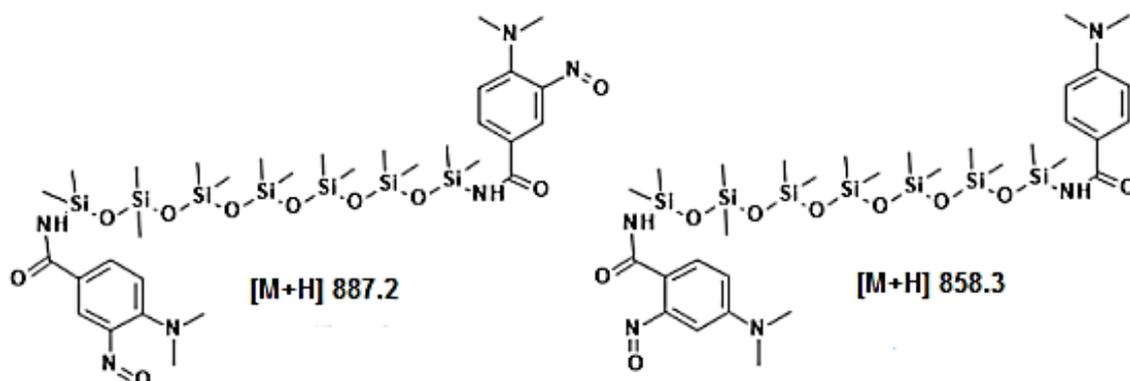
Fig. 2. Mono and dinitroso molecule

^{1}H-NMR details are given in the spectroscopic data in the experimental section. ^{1}H-NMR spectra of **(7a-7b, 10a-10b)** are provided in Figures S9-S12 (see Supplementary Section B).

Handle Properties

Subjective assessment method was used to evaluate the handle properties of the fabric containing **(7a-7b)** and **(10a-10b)**. This method rated the handle-modifier molecule treated fabrics on a grading system which compares it with untreated fabric. Human subjects, designated as **(P-1 to P-10)**, pressed their fingers against the fabric surface or crushed it inside their fists to judge the handle of the fabrics. These two approaches were called as press method and crush method [3]. The subjects gave the fabric a numerical value to the perceived handle between two extremes, i.e. fully stiffened and softener-treated fabrics of the same polymeric substrate. Values given by individual subjects for **(7a-7b)** and **(10a-10b)** are listed in Table 1. Three reference fabrics of the same polymeric structure and construction were used. One of the reference fabrics **A** was treated with a stiffening handle modifier (arkofil; see materials section) and was given the value 1**.** The fabric **B** was untreated, hence was assigned the value 10. The third fabric was designated as **C** and was treated with nonionic silicone softener (sulfosoft; see materials section). Reading for **C** was pre-fixed as 20. If the fabric sample was perceived by the subject to be softer than softened reference fabric **C,** then readings beyond 20 could be recorded. Subjects were provided with reference fabrics before the test samples and the assigned values of the reference fabrics were revealed to them. Hence, the subject now had a reference scale to with two extremities at its end with untreated being the center of the scale. Subjects then assessed the samples by the above defined press method and crush method. Table 1 shows the evaluated readings. All fabrics treated with **(7a-7b)** and **(10a-10b)** showed increased softness compared to the untreated fabric **B**. Less variance was noted in the crush method values, hence it proved to be more reliable.

Table 1. Subjective evaluation data from the crush and the press methods on treated polyester fabric

Judge	Crush method				Press method			
	7a	7b	10a	10b	7a	7b	10a	10b
P-1	14	14	14	14	12	13	16	14
P-2	15	17	17	17	14	16	15	19
P-3	14	15	15	15	12	13	16	17
P-4	17	15	15	16	17	16	18	17
P-5	16	15	16	19	12	12	16	14
P-6	15	16	14	15	16	16	15	16
P-7	16	17	17	17	12	13	17	15
P-8	16	15	15	16	14	16	12	13
P-9	17	15	15	18	12	13	16	12
P-10	18	13	16	16	14	16	18	18
Variance	1.73	1.51	1.15	2.23	3.38	2.93	2.98	5.16

CONCLUSIONS

The synthesis of azo polysiloxane and the study of their impact on the handle properties of treated fabrics provide a foundation for the development of functional textile dyes. We used *tert*-butyl nitrite-based stable diazonium formation method to facilitate fabric azo dye formation. These molecules can simultaneously perform the coloration and finishing functions in textile treatment processes; potentially reducing production time and costs. A series of azo-bonded polysiloxane molecules can be synthesized on a similar pattern. The resultant handle properties were evaluated through a subjective handle evaluation model. Because of the presence of polysiloxane chains on the edge of the molecule, the handle of polymeric substrates treated with azo polysiloxane molecules was altered. This implies that bonded polysiloxane chains are responsible for dire changes in the handle of the substrate.

REFERENCES

1. W. D. Schindler, P. J. Hauser, Chemical finishing of textiles, Woodhead, Cambridge, 2010.

2. D. J. Pu, Q. Zhong, J. P. Wang, *Key Eng. Mater.,* **671**, 186 (2016).
3. Y. Wei, C. Zheng, P. Chen, Q. Yu, T. Mao, J. Lin, L. Liu, *Polyp. Bull.,* **76,** 447 (2019).
4. S. I. Ali, S. Begum, *Ergonomics,* **37,** 801 (1994).
5. J. Hu, X. Ding, R. Wang, *Fibers Polym.,* **8**, 372 (2007).
6. G. D. Kandzhikova, D. S. Germanova-Krasteva, *J. Text. Inst.*, **107**, 355 (2016).
7. M. G. Tadesse, R. Harpa, Y. Chen, L. Wang, V. Nierstrasz, C. Loghin, *J. Ind. Text.,* **48,** 1310 (2019).
8. S. Marquais-Bienewald, C. Cremer, O. Wallquist, X. Z. Zhou, B. Wagner, *US Paten*t 8 221 508 (2012).
9. D. Liu, J. Liu, *J. Mater. Cycles Waste,* **16,** 557 (2014).
10. A. Altomare, F. Ciardelli, G. Faralli, R. Solaro, *Macromol. Mater. Eng.,* **288**, 67 (2003).
11. H. H. Wang, I. S. Tzun, *J. Appl. Polym. Sci.,* **73,** 245 (1999).
12. H. R. Maradiya, V. S. Patel, *Polym. Plast. Technol. Eng.,* **41,** 735 (2002).
13. H. K. Sheikh, M. H. Kazmi, *J. Chil. Chem. Soc.,* **62,** 3496 (2017).
14. J. Qiu, B. Tang, B. Ju, Y. Xu, S. Zhang, *Dyes Pigm.,* **136,** 63 (2017).

New neurotensin analogue with improving effect on some affective symptoms in Parkinson's disease model in rats

A. Popatanasov[1*], S. Abarova[2], L. P. Tancheva[1], T. Pajpanova[3]

[1]*Institute of Neurobiology, Bulgarian Academy of Sciences, Acad. G. Bonchev Str., Bl. 23, Sofia, Bulgaria*
[2] *Department of Medical Physics and Biophysics, Medical University, 2 Zdrave Str., Sofia, Bulgaria*
[3]*Institute of Molecular Biology, Bulgarian Academy of Sciences, Acad. G. Bonchev Str., Bl. 21, Sofia, Bulgaria*

Neurotensin (NT) is a small neuropeptide acting as neurotransmitter and neuromodulator in the nervous system. However, natural neurotensin is rapidly degraded in the body, therefore artificial analogues are needed to prolong its bioavailability and effects. Parkinson's disease (PD) is a neurological disease with specific motor, cognitive and affective disturbances and is associated with high oxidative stress and mitochondrial dysfunction and degeneration of the dopaminergic system. The scope of the study was to evaluate some effects of a new neurotensin analogue (NT2) upon the behavior of rats with a model of PD induced with striatal injection of the neurotoxin 6-hydroxydopamine (6-OHDA). The PD model was produced *via* striatal 6-OHDA (12 µg in 2 µl saline) injection of male Wistar rats. NT2 treatment was with an effective daily dose of 5 mg/kg i.p. for 5 days. NT2 effects were evaluated *via* behavioral tests for locomotor activity and anxiety. Student's t-test was used at $p < 0.05$. The PD model was verified by rotarod tests on the 2nd and 3rd week after the operation and was compared to sham operated animals. There was a significant performance decrease in the mood and affective disturbances. The affective disturbances as anxiety in NT2-treated animals were reduced (both on the 2nd and 3rd week) compared to PD-controls.

Key words: neurotensin, affective disorder, anxiety, Parkinson disease.

INTRODUCTION

Parkinson's disease (PD) is one of the most common neurodegenerative diseases with specific motor, cognitive and affective disturbances and is associated with high oxidative stress and mitochondrial dysfunction and degeneration of the dopaminergic system. Among the non-motor symptoms, some of the most common ones are depression and anxiety [1]. They may seriously impact the wellbeing and performance of the patients and are an additional source of stress for the care givers [2]. However, the current therapies are mostly focused to combat the motor symptoms, while the non-motor ones often remain neglected [3].

One of the first discovered connections between the receptors of the different neurotransmitters and neuromodulators was the one between the DA-receptors and neurotensin (NT) receptors. Such close connection suggests that NT is associated with PD [4]. Additionally, several years after these findings the researchers gradually started to discover that NT can be related to some affective symptoms in the psychiatric disorders [5], which further stimulated such research and the quest for NT-like agents.

Neurotensin is a tridecapeptide acting as neurotransmitter and neuromodulator in the nervous system. It is secreted in both the central nervous system and the gut.

NT exercises its biologic effect from the specific interaction of the peptide with three different cell-surface receptors referred to as NTS1, NTS2 and NTS3/sortilin [6]. However, natural neurotensin is rapidly degraded in the body, therefore artificial analogues are needed to prolong the bioavailability and effects. Therefore, the object of this study is a promising long-lasting NT analogue with code NT2 (Fig. 1) synthesized by Pajpanova *et al*. [7].
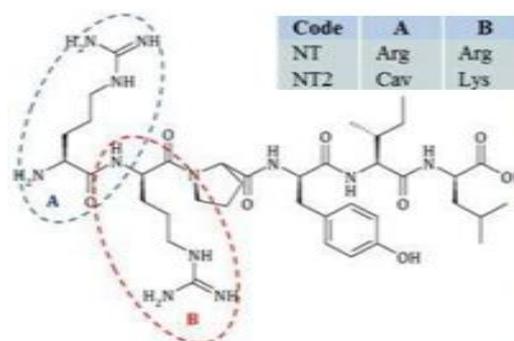
Fig. 1. The amino acid sequence of NT and NT2-analogue.

* To whom all correspondence should be sent:
E-mail: and_atanasov@abv.bg

Our previous research on this NT-analogue showed that it has better permeability of the blood-brain barrier than the native NT and improved hydrolytic stability [8, 9].

Based on all this the goal of our study is to explore the impact of the new NT2-analogue on some affective disturbances in PD.

EXPERIMENTAL

Synthesis of NT analogue

NT-analogue (with code NT2) was synthesized through standard solid-phase method. The peptide chain was assembled on a Wang resin (0.1 mmol scale) with a Fmoc/Boc strategy. The coupling of each amino acid was performed in the presence of 3 mol excess of Fmoc-amino acid, 3 mol excess of HOBt, 3 mol excess of DIC and 5 mol excess of DIPEA. The cleavage step from the resin and the final deprotection of all remained protecting groups was done in a standard cocktail containing TFA, TIPS, thioanisole, and water [7].

Animal experiments and treatment

A total of 24 male Wistar rats (220 – 250 g) were used. Before the beginning of the experiment the rats were adapted to the new conditions in our vivarium. They were housed in groups of four per cage in a temperature-controlled room with a 12 h light-dark cycle, and had free access to food and water.

The animals were treated intraperitoneally (i.p.) for 5 days as follows: SO and 6-OHDA controls with 5 ml/kg saline; 6-OHDA + NT2 group with 5 mg/kg i.p. NT2.

All experiments were performed according to the "Principles of laboratory animal care" (NIH publication No. 85-23), and the rules of the Ethics Committee of the Institute of Neurobiology, Bulgarian Academy of Sciences (registration FWA 00003059 by the US Department of Health and Human Services).

PD experimental model and animal surgical procedures

The rats were anaesthetized with chloralhydrate (420 mg/kg, i.p.), their heads were shaved and skin cleaned with 70 % alcohol. Then the rats were positioned in the stereotaxic apparatus. PD model was induced *via* stereotaxic injection of 2 µl/12 µg 6-hydroxydopamine (6-OHDA, (Sigma-Aldrich, USA)); calculated as free base, dissolved in ice-cold saline with 0.02 % ascorbic acid) in striatum [10]. The target coordinates for striatum were AP=0; ML=3.5; H=-5 from the bregma and dura, according to the stereotaxic atlas [11]. Sham operated (SO) group received only 2 µl of saline. The wound was closed and animals returned to their cages for recovering.

Biochemical assay

At the end of the experiments rats were euthanized by CO_2 and decapitated, the brains were quickly removed and placed on ice until further processing. The dopamine determination followed the method of Jacobowitz *et al.* [12]. In brief, the brain tissue samples were homogenized in N-butanol. Dopamine (DA) was extracted in 0.1 M phosphate buffer. After 20 min DA fluorescence was measured at 320 nm activation/385 nm emission wavelengths. The fluorescence readings were converted into µg DA per g of brain tissue.

Rotarod test

Rotarod test was used for assessment of the motor coordination of the animals. The apparatus consisted of a horizontal rod (6 cm diameter) with discs (40 cm diameter). The rotation speed was set to 8 rotations per minute. During the training and testing sessions the animals were placed on the rotating rod with head pointing against the rotational direction so that they had to walk forward to maintain their equilibrium. The animals were trained one day before the surgery. The number of falls during a period of 180 seconds was recorded [13].

Elevated plus maze

The elevated plus maze consisted of two open arms (length 50 cm and width 11 cm) and two enclosed arms (length 50 cm, width 11 cm, and height 40 cm), arranged in cross formation in such way that two pairs of arms with same construction were opposite to each other surrounding a central platform (11×11 cm). The whole apparatus was positioned 50 cm above ground level. Experiments were performed under dim light conditions. Each animal was placed on the central platform with head facing an open arm. The animal activity was video recorded for 5 min. After each session the apparatus was carefully cleaned. As measures of anxiety the following parameters of the behavior were assessed: 1) percent time spent on the open arms (% open time); 2) percent open arm entries from the total arm entries.

As indicators of locomotor activity of the rats tested on the elevated plus maze test were also assessed: closed arm entries and total arm entries, since anxiety-related effects can be confounded by changes in motor activity [14, 15]. An entry in the

arm was considered when the whole body and four paws were placed on the arm.

Open field test

In order to determine the nonspecific motor effects which may have flustered the assessments in the elevated plus maze test, assessment of the locomotor activity was performed in the same animals following the elevated plus maze test procedures. The assessment of the locomotor activity was done in the same room as the elevated plus maze test.

Additionally, the number of entries from the outer zone into the central zone of the arena was measured which was used to estimate the anti-thigmotactic ratio as an indicator of increased or decreased anxiety of the tested animals. This ratio is calculated by the number of entries into the central arena of the open field to total distance travelled, multiplied by 1000. Initially the rats were placed in the center of the open field arena [16]. The open field apparatus comprised a cylinder (diameter 1 m, height 40 cm) on contrasting background. The arena was divided in two zones – central zone and outer zone equidistantly surrounding it. The testing sessions lasted for 20 min and were video recorded for analysis.

Statistical and data analysis

Results were expressed as means ± SEM. Experimental data were analyzed by Student's t-test. Differences were considered significant at $p < 0.05$.

The video materials from open field and elevated plus maze tests were processed with the specialized neurobehavioral and video analysis software Noldus EthoVision [17]; raw data of the spatiotemporal analysis were imported into Microsoft Excel 2007 (Microsoft Corp., USA) for further processing. The total distance traveled, velocities and entrance and time spent at important areas of the apparatus were calculated with custom-built algorithms.

RESULTS

Dopamine levels

The results from the biochemical assay (Fig. 2) showed decreased levels of DA in the brain tissue in the 6-OHDA intoxicated rats in comparison with the sham operated group. However, the rats treated also with NT2 analogue showed a significant improvement in this parameter (by a factor of 9.37) compared to the non-treated animals. In comparison with the control group the NT2 treated one has lower values by a factor of 0.81. So basically the

DA levels were closer to the ones of the control group than to the ones of the non-treated PD group.

Rotarod test

After the training and the recovery from the surgery the rats' performance on the rotarod test showed gradual decrease in the motor coordination with the progress of the lesion in the 6-OHDA intoxicated animals (Fig. 3).
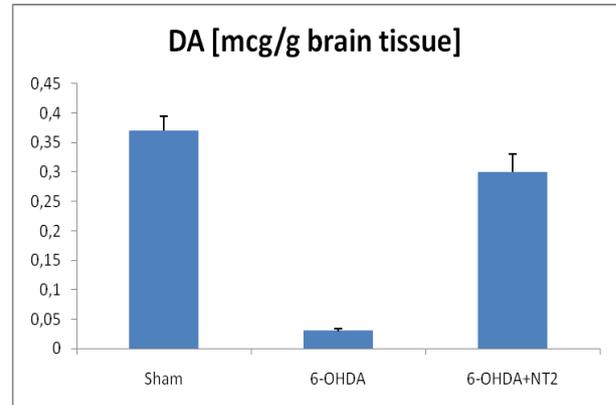
Fig. 2. DA levels in the brain among the groups on the 3rd week after the surgery.
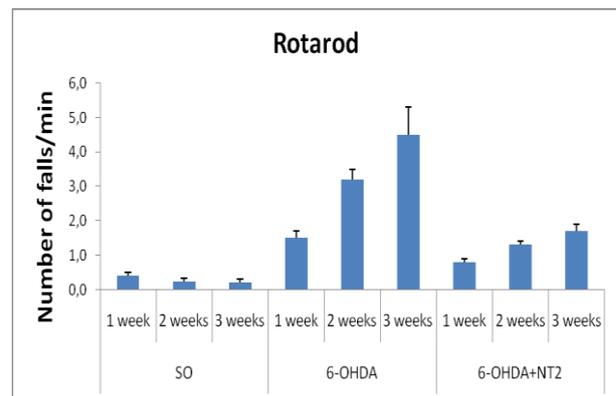
Fig. 3. Rotarod test performance on the 1st, 2nd and 3rd week after the surgery.

The differences in the first week after the lesion were less pronounced: the NT2 treated group showed 30% increase of the number of falls compared to the SO group while this number was increased by 153% in the non-treated 6-OHDA intoxicated group. Two weeks after the lesion the total number of falls in the NT2 treated group was increased by 33% compared to the SO group, while in the non-treated 6-OHDA intoxicated group this number was increased 5 times. On the third week the NT2 treated group showed an increased number of falls by 85% compared to the SO group while in the non-treated 6-OHDA intoxicated group this number was increased by 412%.

Open field test

On the complementary part of the open field test evaluations for possible decrease in the locomotor activity which may confound the results of the other tests, no statistically significant differences were observed among the groups on their respective performance during the first, second and third week after the lesion.

However, on the anxiety related part of the test we see different trends and patterns as shown by the values of the number of entrances in the central area and the anti-thigmotactic ratio (Figs. 4, 5).

Fig. 5. Open field test anxiety related anti-thigmotactic ratios from the 1st, 2nd and 3rd week.

Fig. 4. Open field test number of entrances in the central area from the 1st, 2nd and 3rd week.

In general, these parameters decrease with the longer time from the surgery they were measured. But anti-thigmotactic parameter also differs between the intoxicated groups for the 1st, 2nd and 3rd week by 10.56%, 12.25 and 19.28%, respectively. In comparison with the control group the NT2 treated group has higher values for the different weeks by 22.06%, 37.5% and 42.14%, respectively.

Elevated plus maze

The elevated plus maze test also showed an increase of the measured behavioral parameters related to anxiety in the NT2 treated group, while the trend was opposite in the non-treated 6-OHDA intoxicated group compared to the SO group (Fig. 6).

On the third week the percentage of open arm entries in the NT2 treated group was 12% and in the non-treated 6-OHDA group it was 10%, while in comparison to the SO group the parameter was 21%. The parameters for locomotor activity – closed arm entries and total arm entries showed no statistically significant differences among the groups at p<0.05.

Fig. 6. Elevated plus maze test performance on the 1st, 2nd and 3rd week after the surgery.

DISCUSSION

The worsened locomotor coordination and performance on the Rot-a-rod test verified the chemically induced model of PD. The model was further confirmed by the results of the biochemical assay for the dopamine levels in the brain which show nearly 10-fold decrease in the PD animals. Also, in postmortem histological analysis it was found that the lesions were located in the striatum.

Further, the behavior performance results show that overall, the new NT2 analogue has beneficiary effects on some of the affective symptoms of PD.

Typically, these fearful animals have quite pronounced thigmotaxis when exposed to a new unknown environment especially in open areas without hiding places and objects. Their natural behavioral tendency is to remain as close as possible to the available walls (thigmotaxis) and hiding objects. Although there is little research on these phenomena in relation with DA-ergic neurotransmission, some studies found that some agonists of the D1 and D2 dopamine receptors can have modulatory effects on this parameter, generally by reducing it [18]. Here we see that the damage of DA-ergic system increases it, while treatment with NT2 partly restores it.

In general, the DA-ergic system is less frequently accounted for as engaged in the anxiety and the related disturbances but some studies showed that through D1 and D2 dopamine receptors in mesolimbic circuits the DA-ergic system may also have a modulatory role in this emotional behavior [19]. And here we observe a similar pattern – destruction of a large part of the dopaminergic system leads to affective disturbances as shown in our tests.

The mesolimbic circuits of the dopaminergic system also contain a relatively high level of co-localized NT-receptors as some neuroanatomical studies show [20]. In behavioral concordance with this is the observed significant improvement in the NT2 treated group performance in all the anxiety tests, which can be related to stimulation of compensatory mechanisms by the NT2 in this pathway, such as the fact that NT elicits evoked DA release in the striatum and prefrontal cortex [21]. A clinic research by Ruiz *et al.* from 1992 [22] showed that plasma levels of some neuropeptides are significantly reduced in patients with depression or anxiety disorder, which get restored after recovery. With our study we go further by confirming that there is a functional connection between the NT associated part of the dopaminergic system and some affective disturbances, since by introducing the NT2 analogue into the plasma we partially mitigate some of the affective symptoms incurred by the massive selective neurotoxin destruction of the dopaminergic system.

In our previous studies [9, 10] we showed the beneficiary effects of NT2 on the behavior related to the damaged DA-ergic circuits in PD in charge for the motor and cognitive behavior. In this study it was shown that NT2 impacts positively other DA-ergic neural circuits related to the emotional behavior.

CONCLUSION

The new NT-analogue is a promising agent for the management of some of the non-motor symptoms of PD as anxiety, and deserves further exploration and development.

REFERENCES

1. R. F. Pfeiffer, *Parkinsonism Relat. Disord.*, **22**, S119 (2016).
2. O. B. Leiknes, I. Tysnes, D. Aarsland, J. P. Larsen, *Acta Neurol. Scand.*, **122**(6), 418 (2010).
3. A. Todorova, P. Jenner, K. R. Chaudhuri, *Practical Neurology*, **14**(5), 310 (2014).
4. F. St-Gelais, C. Jomphe, L. É. Trudeau, *J. Psychiatr. Neurosci.*, **31**, 229 (2006).
5. R. Cáceda, B. Kinkead, C. B. Nemeroff, *Peptides*, **27**(10), 2385 (2006).
6. J. P. Vincent, J. Mazella, P. Kitabgi, *Trends Pharmacol. Sci.*, **20**, 302 (1999).
7. T. Dzimbova, S. Stoeva, L. Tancheva, A. Georgieva, R. Kalfin, T. Pajpanova, in: Peptides 2014, (Proc. 33rd European Peptide Symp., Sofia, 2014), E. Naydenova, T. Pajpanova, D. Danalev (eds.), European Peptide Society, Sofia, 2014, p. 260.
8. S. Michailova, T. Dzimbova, K. Kalíkova, E. Tesařová, T. Pajpanova, *Bulg. Chem. Commun.*, **49**(E), 113 (2017).
9. M., Lazarova, A., Popatanasov, R., Klissurov, S., Stoeva, T., Pajpanova, R., Kalfin, L. Tancheva. *J. Mol. Neurosci.*, **66**(4), 552 (2018).
10. A. Popatanasov, S. Stoeva, M. Lazarova, L. Traikov, T. Pajpanova, R. Kalfin, L. Tancheva. *Bulg. Chem. Commun.,* **49**(E), 146 (2017).
11. G. Paxinos, C. Watson, The Rat Brain in Stereotaxic Coordinates, Elsevier Acad. Press, San Diego, 2005.
12. D. M. Jacobowitz, J. S. Richardson, *Pharmacol. Biochem. Behav.*, **8**(5), 515 (1978).
13. D. M. Pechlivanova, P. P. Markova, D. Popov, A. G. Stoynev, *Peptides*, **39**, 152 (2013).
14. R. D. Porsolt, G. Anton, N. Blavet, M. Jalfre, *Eur. J. Pharmacol.*, **47**(4), 379 (1978).
15. G. R. Dawson, M. D. Tricklebank, *Trends Pharmacol. Sci.*, **16**(2), 33 (1995).
16. A. Skórzewska, M. Lehner, A. Wisłowska-Stanek, P. Krząścik, A. Ziemba, A. Płaźnik, *Hormones and Behavior*, **65**(1), 6 (2014).
17. P. Escudero, V. Hinz, A. de Polavieja, *Nat. Methods*, **11**(7),743 (2014).
18. P. Simon, R. Dupuis, J. Costentin, *Behav. Brain Res.*, **61**(1), 59 (1994).
19. R. J. Rodgers, E. M. Nikulina, J. C. Cole, *Pharmacol. Biochem. Behav.*, **49**(4), 985 (1994).
20. R. Quirion, C. C. Chiueh, H. D. Everist, A. Pert, *Brain Res.*, **327**(1-2), 385 (1985).
21. E. Hetier, A. Boireau, P. Dubedat, J. C. Blanchard, *Naunyn Schmiedebergs Arch. Pharmacol.*, **337**(1), 13 (1988).
22. J. P. Saiz, J. R. Carrasco, A. Hernanz, *Archivos de Neurobiologia*, **55**(1), 1 (1992).

Studies on FeP/TiO$_2$ catalysts in the ammoxidation of 2-methyl pyrazine to 2-cyano pyrazine

N. Pasupulety*, M. Daous, A. A. Al-Zahrani, H. Driss, L. A. Petrov

Chemical and Materials Engineering Department, Faculty of Engineering, King Abdulaziz University, P.O. Box 80204, Jeddah 21589, Saudi Arabia

Nominal loadings of iron phosphate (FeP) from 5 to 25 wt% were deposited on TiO$_2$ (anatase) through a wet impregnation method. Vapor phase ammoxidation of 2-methyl pyrazine (2-MP) to 2-cyano pyrazine (2-CP) was carried out on these catalysts in the reaction temperature range of 633 to 693K at W/F= 2 g/(ml/h). Characterization of FeP/TiO$_2$ samples was done by using XRD, FTIR, laser Raman and potentiometric titration techniques. XRD analysis showed quartz type FePO$_4$ at 15 wt% of iron phosphate loading. Essentially, the quartz phase was intensified and new phases such as TiPO$_4$ and TiP$_2$O$_7$ were observed for 20 and 25FeP/TiO$_2$ samples. At lower FeP loadings (5 and 10 wt%) the quartz phase was inadequate and resulted in decreased ammoxidation activity. On the other hand, at higher FeP loadings (20 and 25 wt%) aggregation of FePO$_4$ and titanium phosphate phases reduced the ammoxidation activity. Among the catalysts studied, 15FeP/TiO$_2$ showed 2-CP selectivity of 91% with 75.5% of 2-MP conversion at 653K. It is associated with (i) its higher acid strength and (ii) adequate active quartz phase dispersed on TiO$_2$.

Keywords: Iron phosphate; titanium dioxide; ammoxidation; 2-methylpyrazine; 2-cyano pyrazine

INTRODUCTION

Heterocyclic nitriles are valuable intermediates and reactants in the fine chemical sector. These nitriles are used for the synthesis of several pharmaceuticals, dyestuffs, pesticides, etc. [1, 2]. Alkyl heterocyclic compounds can be converted into their corresponding nitriles in a single step *via* ammoxidation process. Through this process one can achieve high yields of nitriles over direct vapor phase oxidation [3]. Essentially, V$_2$O$_5$ deposited on TiO$_2$, Nb$_2$O$_5$ and Al$_2$O$_3$ catalysts was investigated in the ammoxidation process [4-7]. The studies revealed that nitrile formation was influenced by the nature of support through metal-support interactions [8, 9]. However, usage of V$_2$O$_5$ supported catalysts in the ammoxidation process was limited by high temperature activity and over oxidation (led to undesired products). Further, vanadium phosphate deposited TiO$_2$ catalysts were investigated in the ammoxidation of 2,6-dichloro toluene [10]. Bulk lanthanum vanadate and iron phosphate catalysts were studied for 2-methyl pyrazine ammoxidation reaction [11-13]. However, these catalysts showed either lower selectivity or lower yield of 2-cyano pyrazine. In this regard, very few reports are available on supported iron phosphate catalysts for oxidation and ammoxidation reactions. McCormick *et al.* [14] have studied the methane oxidation process by employing iron phosphate deposited metal oxide (Al$_2$O$_3$, SiO$_2$, TiO$_2$ and ZrO$_2$) catalysts.

In the present study, the catalytic behavior of FeP/TiO$_2$ catalysts was investigated in the ammoxidation of 2-MP in the temperature range of 633-693K with W/F=2 g/(ml/h). The detailed catalyst characterization was carried out by using XRD, FTIR, FT-Raman and potentiometric titration techniques. The possible structure-activity correlations will be discussed further. To the best of our knowledge, this is the first report on FeP/TiO$_2$ catalysts for the vapor phase ammoxidation of 2-MP to 2-CP.

Scheme 1. Generalized 2-methyl pyrazine ammoxidation scheme.

EXPERIMENTAL

Catalyst preparation

Nominal loadings of iron phosphate (5 to 25 wt%) were deposited on TiO$_2$ (anatase, $\geq$ 99.8%, Sigma-Aldrich) by using a wet impregnation method. For example, 1.071 g of iron nitrate (Fe(NO$_3$)$_3$.9H$_2$O, $\geq$ 98%, Sigma-Aldrich) and 0.381 g of ammonium dihydrogen phosphate ((NH$_4$)H$_2$PO$_4$, Sigma-Aldrich) were used for 10 g of 5FeP/TiO$_2$ catalyst with P-to-Fe atomic ratio of 1.2.

---

* To whom all correspondence should be sent:
E-mail: nsampathra@kau.edu.sa

The precursor salts were dissolved each in 25 ml of deionized water. These solutions were mixed together under continuous stirring at room temperature. TiO$_2$ powder was added to the above mixed solution and aged for 1 h. The excess water from the resultant slurry was removed on a preheated hot plate at 383 K. The obtained solid crystals were dried for 12 h in a preheated oven at 393 K. Finally, the dried mass was calcined in an oven at 823 K for 4 h in static air. These catalysts were denoted as 5FeP/TiO$_2$ for 5 wt.% of iron phosphate loading and so on so forth. Furthermore, 15FeP/CeO$_2$ and 15FeP/ZrO$_2$ catalysts were also synthesized by a wet impregnation method and used for comparison studies.

Catalysts characterization studies

N$_2$-physisorption studies of calcined TiO$_2$ and FeP/TiO$_2$ samples were carried out using a Micromeritics (Auto Chem-2910) instrument at liquid nitrogen temperature (77 K).

Powder X-ray diffraction analysis of calcined TiO$_2$ and FeP/TiO$_2$ samples was performed using a Rigaku Miniflex diffractometer at Cu K$_\alpha$ radiation (λ =1.5405 Å). FTIR spectra of spent catalysts were recorded on a DIGILAB (USA) spectrometer at a resolution of 4 cm^{-1} by the KBr disc method.

Fourier transform laser Raman spectroscopic measurements were carried out using a Bruker RFS 100/S spectrometer equipped with Nd:YAG laser (1.064 μm) and InGaAs detector. A laser power of 50 mW was employed.

The acid strength of calcined TiO$_2$ and FeP/TiO$_2$ samples was measured by the potentiometric titration method [15]. Each, 50 mg of sample was suspended in acetonitrile and kept under continuous stirring for 3 h. The resultant suspension was titrated with 0.05 N n-butyl amine acetonitrile solution at a flow rate of 0.05 ml/min. The variation in the electrode potential (E, mV) was measured with a digital pH meter (Automatic titrator, Schott GmbH, Germany), having a standard calomel electrode. The potentiometric titration was performed with a glass electrode. The instrument was calibrated using standard buffer solutions.

Catalytic reaction

Ammoxidation of 2-MP was carried out in a fixed-bed glass reactor in the temperature range of 633 to 673 K. In a typical experimental procedure, about 4 g of each FeP/TiO$_2$ sample was loaded in the reactor in between two quartz plugs. The feed composition ratio employed in this reaction was about 2-MP/water/ammonia/air = 1/13/17/38. The 2-MP solution was fed into the reactor by using a Braun pump at a flow rate of 2 ml/h. After attaining the steady state for 30 min, at each reaction temperature, the liquid product was collected for 10 min. The collected liquid sample was analyzed by GC equipped with FID connected to SE-30 column. Pyrazine was the major byproduct in this reaction. The CO$_x$ selectivity (TCD, Restek Plot Q column) was found to be about 2 to 5 % under the studied reaction conditions.

$$\% \ X_{\text{2-MP}} = \frac{(\text{Moles of 2-MP, \textbf{in}} - \text{Moles of 2-MP, \textbf{out}})}{\text{Moles of 2-MP, \textbf{in}}} \ \text{x} \ 100$$

$$\% \ S_i = \frac{\text{Moles of product } i \ \textbf{out}}{(\text{Moles of 2-MP, \textbf{in}} - \text{Moles of 2-MP, \textbf{out}})} \ \text{x} \ 100$$

$$\% \ \text{Yield} = \frac{\text{Moles of product } i \ \textbf{out}}{\text{Moles of 2-MP, \textbf{in}}} \ \text{x} \ 100$$

RESULTS AND DISCUSSION

N$_2$-physisorption studies

BET surface area results of TiO$_2$ and FeP/TiO$_2$ samples are presented in Table 1. Among the samples studied, TiO$_2$ showed the greatest surface area of 55 m^2/g. Deposition of FeP on TiO$_2$ decreased the BET surface area of the resultant sample. It is associated with the pore blockage of

TiO$_2$ by FeP. Similar results were reported by McCormic *et al.* [13] for FePO$_4$/Al$_2$O$_3$ catalysts.

XRD analysis

Powder X-ray diffraction analysis results of FeP and FeP/TiO$_2$ samples are presented in Fig. 1. The bulk FeP primarily exhibited quartz type FePO$_4$ with a small amount of tridymite phase [16]. FeP/TiO$_2$ samples principally exhibited X-ray reflections related to TiO$_2$ anatase phase (ICDD

PDF 21-1272) up to 10 wt% of FeP loading. Essentially, X-ray reflections related to quartz type of FePO$_4$ phase was observed at 15 wt.% of FeP loading on TiO$_2$. After this loading, X-ray reflections of quartz type of FePO$_4$ was intensified and also new phases were observed for 20 and 25FeP/TiO$_2$ samples. X-ray reflections exhibited at 2θ = 20.2 and 25.8º correspond to quartz type of FePO$_4$ phase [16]. Further, the new X-ray reflections appeared at 2θ = 22.4, 34.8, 40.9, 54.6, 58.0, 71.0 and 78.2º correspond to crystalline TiPO$_4$ phase [ICDD No. 81-1334] and those at 28.6 and 67.6º correspond to TiP$_2$O$_7$ phase [ICDD No. 03-0300]. It is noteworthy that the titanium phosphate phases were not detected up to 15 wt% of FeP loading in FeP/TiO$_2$ samples. The formation of TiPO$_4$ and TiP$_2$O$_7$ phases in 20 and 25FeP/TiO$_2$ samples suggest that the stiochiometric excess of phosphate [17] interacts with TiO$_2$ during the calcination process. Glaum *et al.* [18] have reported that the TiPO$_4$ phase formation was due to the combination of TiO$_2$ and TiP$_2$O$_7$. McCormick *et al.* [13] pointed out that monolayer coverage of TiO$_2$ (anatase) can be achieved at 16 wt% of FeP loading. The XRD analysis results obtained in the present study are in agreement with the literature reports.
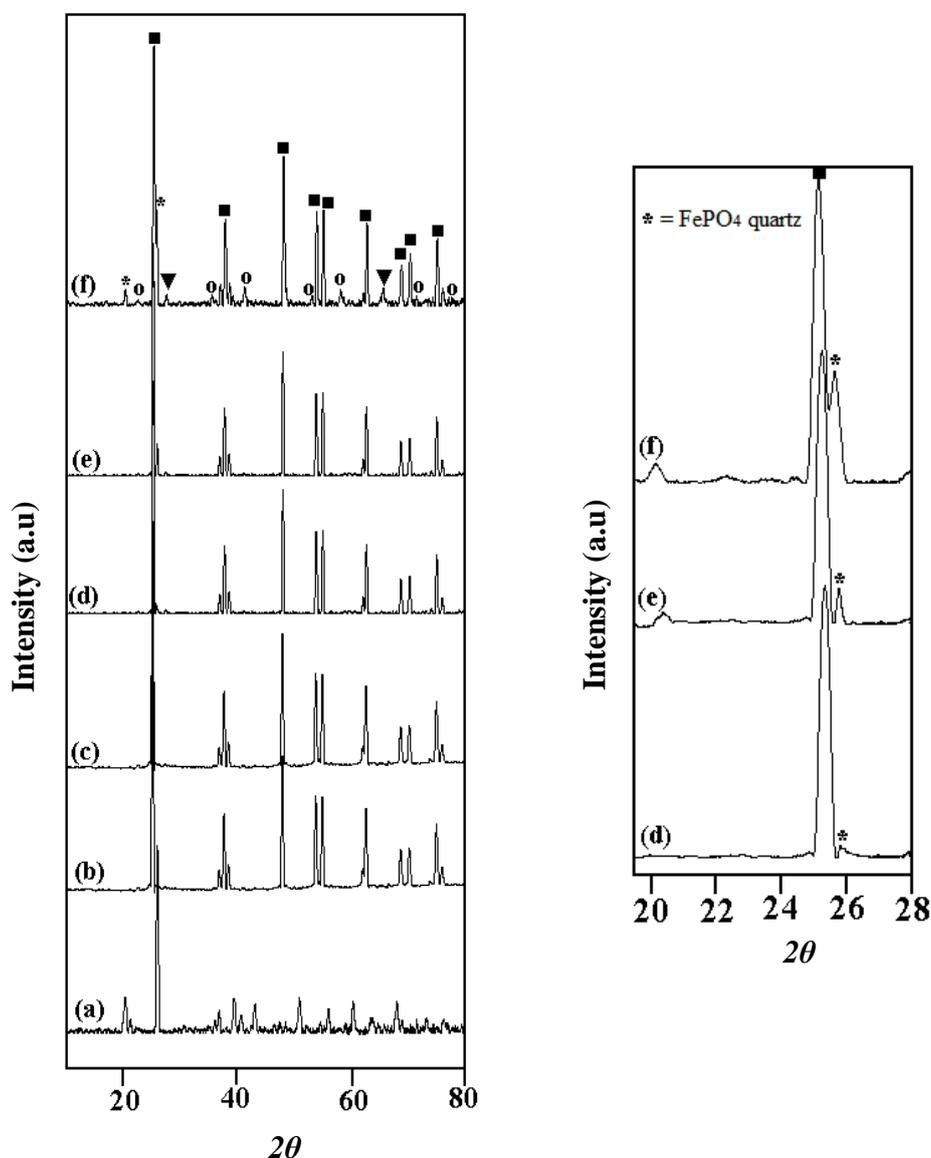
Fig. 1. XRD patterns of calcined iron phosphate catalysts supported on TiO$_2$. (a) Bulk FeP (b) 5FeP/TiO$_2$ (c) 10FeP/TiO$_2$ (d) 15FeP/TiO$_2$ (e) 20FeP/TiO$_2$ (f) 25FeP/ TiO$_2$ (∗) FePO$_4$ quartz phase (■) TiO$_2$ anatase (o) TiPO$_4$ (▼) TiP$_2$O$_7$

Laser Raman studies

FT-Raman spectral analysis results of TiO_2, FeP and FeP/TiO_2 samples are presented in Fig. 2. Bulk FeP exhibits the Raman vibrations in the region of 1000-1200 cm^{-1} due to the stretching and bending modes of phosphate groups [19]. Very strong Raman vibrations were observed for bulk TiO_2 in the region of 350-700 cm^{-1}. The Raman bands at 395, 510 and 635 cm^{-1} are assigned to the B1g, A1g and B2g modes of the TiO_2 anatase phase, respectively [20]. However, only TiO_2 vibrations were observed upbto 15 wt% of FeP loading on TiO_2. After this loading, the vibrations related to TiO_2 were reduced and new vibrations appeared at 280, 420, 1050 and 1180 cm^{-1} in the 20 and 25FeP/TiO_2 samples. The band appeared at 280 cm^{-1} is attributed to PO$_4$ tetrahedra units of TiPO$_4$ and the bands at 420 and 1180 cm^{-1} are characteristic bands for TiP$_2$O$_7$ [21]. The broad band appeared at 1050 cm^{-1} might be due to the asymmetric coupled vibration of phosphate groups of FePO$_4$. It is clear from the Raman data that titanium phosphate formation is taking place at higher loadings of FeP on TiO_2. These results are in good agreement with XRD data.

Acidity measurements by potentiometric titration

The potentiometric titration profiles of TiO_2 and FeP/TiO_2 samples are presented in Fig. 3 and the obtained acid strength values (E (mV)) are presented in Table 1. Linear butyl amine was used as a base component in the potentiometric titrations. Among the samples studied, pure TiO_2 showed lower acidity. A gradual increase in the acidity was observed upon a gradual increase in the FeP loading up to 15 wt% on TiO_2. After this loading, the acidity of the 20 and 25FeP/TiO_2 samples slightly decreased. It might be associated with the aggregated FePO$_4$ particles and/or surface phosphorus interaction with TiO_2 to form titanium phosphates. The decreasing order of acidity is as follows: 15FeP/TiO_2 > 20FeP/TiO_2 > 25FeP/TiO_2 >10FeP/TiO_2 > 5FeP/TiO_2 > TiO_2. At lower FeP loadings (5 and 10 wt%) the active FePO$_4$ phase was inadequate and resulted in lower acid strength.
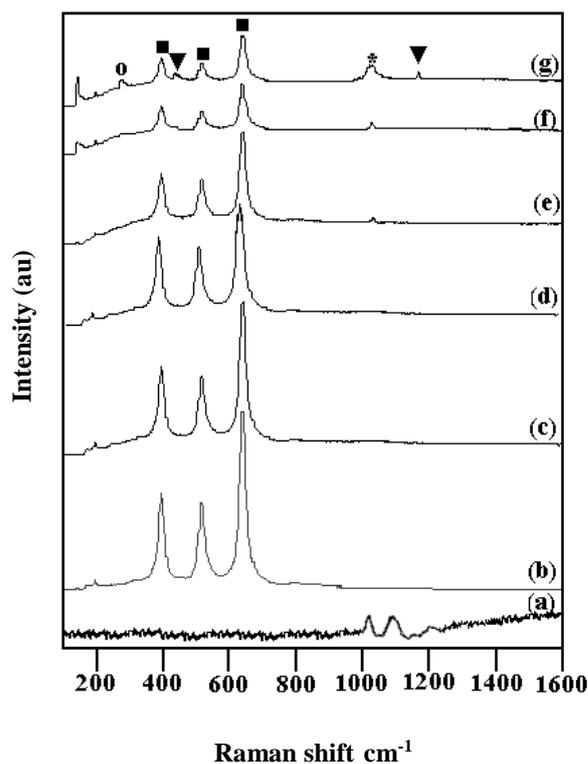
Fig. 2. FT-Raman spectra of calcined samples. (a) Bulk FeP (b) TiO_2 (c) 5FeP/TiO_2 (d) 10FeP/TiO_2 (e) 15FeP/TiO_2 (f) 20FeP/TiO_2 (g) 25FeP/TiO_2 (∗) FePO$_4$ (■) TiO_2 anatase (o) TiPO$_4$ (▼) TiP$_2$O$_7$

Table 1. BET surface area, SEM/EDX, acid strength and 2-CP selectivity results of TiO_2 and FeP/TiO_2 catalysts.

Catalyst	*SEM/EDX %	BET surface area (m²/g)	Acid strength **E (mV)	(%) Selectivity 2-CP at 653 K
TiO_2 (anatase)	-	55	190	66
5FeP/TiO_2	4.65	45	340	71
10FeP/TiO_2	9.8	33	378	78
15FeP/TiO_2	14.5	21	438	91
20FeP/TiO_2	18.9	12	419	82
25FeP/TiO_2	24.6	8	390	75

* Analysis done using LEO-1530- Pegasus EDX system; ** Electrode potential values
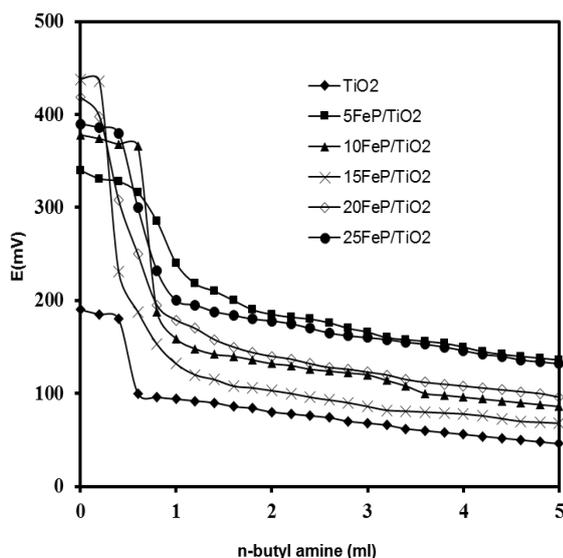
Fig. 3. Potentiometric titration curves of TiO_2 and FeP/TiO_2 catalysts.

Catalytic activity results

Catalytic activity results of TiO_2 and FeP/TiO_2 catalysts are shown in Fig. 4. Fig. 4(A) presents the conversion of 2-MP in the reaction temperature range of 633 to 693K. Among the studied catalysts, lowest conversion of 35% was obtained on pure TiO_2. The conversion of 2-MP increased with an increase in iron phosphate loading up to 15 wt% on TiO_2 and also increased with an increase in the reaction temperature from 633K to 693K. At 693K, about 80% of 2-MP conversion was obtained on the 15FeP/TiO_2 catalyst. At higher loadings (20 and 25 wt%) the conversion of 2-MP leveled off under the studied reaction conditions. It is associated with titanium phosphate formation in 20 and 25FeP/TiO_2 catalysts. These phosphates were active above 723 K in the ammoxidation of propylene to acrylonitrile [22]. Hence, titanium phosphates are either less active or high reactions temperatures are required for the ammoxidation of 2-MP. The order of 2-MP conversion at 693 K is as follows: 25FeP/TiO_2 (81%) ≈ 20FeP/TiO_2 (80%) ≈ 15FeP/TiO_2 (79%) > 10FeP/TiO_2 (68%) > 5FeP/TiO_2 (60%) > TiO_2 (33%).

Fig. 4(B) presents the 2-CP selectivity results on TiO_2 and FeP/TiO_2 catalysts. Pyrazine (major byproduct) formation was found high at 673 and 693K. It might be associated with methyl group dissociation from 2-MP at higher reaction temperatures. On the other hand, higher 2-CP selectivity was found at lower reaction temperatures (633-653K). The maximum 2-CP selectivity of 92.5% was obtained on 15FeP/TiO_2 at 633K. Further, the 2-CP selectivity decreased at higher FeP loadings (20 and 25 wt%). It is

noteworthy that the acid strength increased up to 15 wt% of FeP loading and after this it slightly decreased. The results suggest that high acid strength was necessary for 2-CP formation during the ammoxidation reaction. In order to understand the influence of acid strength on 2-CP selectivity we examined the spent catalysts by FTIR technique and the resultant spectra are presented in Fig. 5A. The major band observed at 760 cm⁻¹ is attributed to the Ti-O or Ti-O-Ti stretching vibration of TiO_2 in an octahedral coordination [23]. The band at 1040 cm⁻¹ is ascribed to phosphate group vibrations of $FePO_4$ and $TiPO_4$ [24]. Further, the FTIR band observed at 565 cm⁻¹ in 15, 20 and 25FeP/TiO_2 is assigned to asymmetric stretching mode of the phosphate group of $FePO_4$. Apart from support and phosphate bands a new shoulder was observed at 1402 cm⁻¹ in spent 15, 20 and 25FeP/TiO_2 catalysts (for comparison purposes fresh FeP/TiO_2 FTIR spectra were added in Fig. 5B). It is associated with asymmetric stretching mode of ammonium ion of an ammonium complex of $FePO_4$ [19]. Further, it should be noted that the formation of ammonium complex is facile on catalysts with higher acid strength. Martin *et al*. [25] pointed out that the ammonium complex of the metal ion (V or Fe) can act as a source of N atoms to form the nitrile compound in the ammoxidation reaction. Hence, the observed high 2-CP selectivity on 15FeP/TiO_2 is associated with its higher acid strength. Fig. 4(C) presents the major byproduct pyrazine formation on FeP/TiO_2 catalysts. About 29% of pyrazine formation was observed on support TiO_2 at 653K whereas pyrazine formation decreased with the increase in FeP loading on TiO_2. Only 7% of pyrazine formation was observed on 15FeP/TiO_2. Further, pyrazine formation was improved on 20 and 25FeP/TiO_2 catalysts.

It was reported that TiO_2 lattice oxygen participation in the thermally induced catalytic reaction of organic compounds results in the formation of a surface vacancy [28]. These defects in TiO_2 can improve the formation of pyrazine aldehyde intermediate from 2-MP and thereby influence the nitrile formation (2-CP).

CONCLUSIONS

Iron phosphate deposited TiO_2 (anatase) catalysts demonstrated good catalytic activity in the ammoxidation of 2-MP to 2-CP in the reaction temperature range of 633-693K. Essentially, at lower FeP loadings (5 & 10 wt%) the active $FePO_4$ phase was inadequate and resulted in low 2-MP conversion.

Fig. 5. FTIR spectra of (A) spent and (B) fresh FeP/TiO₂ catalysts. (a) 5FeP/TiO₂; (b) 10FeP/TiO₂; (c) 15FeP/TiO₂; (d) 20FeP/TiO₂; (e) 25FeP/ TiO₂.

Fig. 4. (A) 2-MP conversion (B) 2-CP selectivity on FeP/TiO₂ catalysts (C) Pyrazine selectivity on FeP/TiO₂ catalysts at 653 K.

Table-2. Catalytic activity results obtained at 653 K with 2-MP/water/ammonia/air ratio = 1/13/ 17/38.

Catalyst	% Conversion 2-MP	% Yield 2-CP	Reference
Pure TiO₂	25	16.5	Present study
15FeP/CeO₂	59	44	Present study
15FeP/ZrO₂	80	48	Present study
15FeP/TiO₂	75.5	69	Present study
Bulk FePO₄	45	43	[19]
15AMPV/SiO₂	66	40	[26]
Bulk 3Mo/FePO₄	70	63	[27]

AMPV= vanadium incorporated ammonium salt of molybdophosphoric acid

On the other hand, at higher FeP loadings (20 and 25 wt%) aggregation of FePO$_4$ and titanium phosphate formation decreased the catalytic activity. Hence, to obtain the maximum 2-CP yield of 69% at least 15 wt% of FeP loading was necessary on TiO$_2$. FTIR analysis of spent 15FeP/TiO$_2$ showed facile ironammonium complex formation at higher acidity.

REFERENCES

1. G. Ertl, H. Knozinger, J. Weitkamp, in: Handbook of Heterogeneous Catalysis, vol. 5, Wiley-VCH, 1997, p. 2322.
2. B. Lucke, A. Martin, in: Fine Chemicals through Heterogeneous Catalysis, R. Sheldon, H. van Bekkum (eds.), Wiley-VCH, Weinheim, 2001, p. 527.
3. Ger. Pat. 1940320 (1972).
4. G. C. Bond, P. Konig, *J. Catal.,* **77,** 309 (1982).
5. I. E. Wachs, R.Y. Saleh, S. S. Chart, C. C. Chersich, *Appl. Catal.,* **15,** 339 (1985).
6. F. Cavani, E. Foresti, F. Trifiro, G. Busca, *J. Catal.,* **106,** 251 (1987).
7. V. M Bondareva, T. V Andrushkevich, O. B Lapina, *Catal. Today,* **61,** 173 (2000).
8. K. V. R. Chary, K. Rajender Reddy, Ch. Praveen Kumar, D. Naresh, V. Venkat Rao, G. Mestl, *J. Mol. Catal. A.,* **223,** 363 (2004)
9. K. V. R. Chary, K. Rajender Reddy, Ch. Praveen Kumar, *Catal. Commun.,* **2,** 277 (2001).
10. K. V. Narayana, A. Martin, *Catal. Today,* **157,** 275 (2010).
11. D. Naresh, K. V. Narayana Kalevaru, A. Martin, *Catalysts,* **10,** 1 (2016).
12. P. Nagaraju, N. Lingaiah, M. Balaraju, P. S. Sai Prasad, *Appl. Catal. A: Gen.,* **339,** 99 (2008).
13. P. Nagaraju, Ch. Srilakshmi, N. Pasha, N. Lingaiah, I. Suryanarayana, P. S. Sai Prasad, *Catal. Today,* **131,** 393 (2008).
14. R. L. McCormick, G. O. Alptekin, *Catal. Today,* **55,** 269 (2000).
15. P. Villabrille, P. Vazquez, M. Blanco, C. Caceres, *J. Colloid. Interface.,* **251,** 151 (2002).
16. X. Wang, Y. Wang, Q. Tang, Q. Guo, *J. Catal.,* **217,** 457 (2003).
17. M. Ai, E. Muneyama, A. Kunishige, K. Ohdan, *J. Catal.,* **144,** 632 (1993).
18. R. Glaum, M. Reehuis, N. Stuber, U. Kaiser, F. Reinauer, *J. Sol. Chem.,* **126,** 15 (1996).
19. P. Nagaraju, Ch. Srilakshmi, Nayeem Pasha, N. Lingaiah, I. Suryanarayana, P. S. Sai Prasad, *Appl. Catal. A.,* **334,** 10 (2008).
20. K. Mallick, M. J. Witcomb, M. S. Scurrell, *Appl. Catal. A.,* **259** 163 (2004).
21. S. del Val, M. L. Granados, J. L. G. Fierro, J. S. Gonzalez, A. J. Lopez, *J. Catal.,* **188,** 203 (1999).
22. K. Schwarzer, A. Hausweiler, US3280167A (1966).
23. S. X. Liu, X. Y. Chen, X. Chen, *J. Hazard. Mat.,* **143,** 257 (2007)
24. Ch. Pan, S. Yuan, W. Zhang, *Appl. Catal. A.,* **312,** 186 (2006).
25. A. Martin, Y. Zhang, H. W. Zanthoff, M. Meisel, M. Baerns, *Appl. Catal. A.,* **139,** L11 (1996).
26. K. Mohan Reddy, N. Lingaiah, P. Nagaraju, P. S. Sai Prasad, *Catal. Lett.,* **122,** 314 (2008).
27. P. Nagaraju, H. Driss, Y. A. Alhamed, A. A. Alzahrani, M. A Daous, L. Petrov, N. Lingaiah, P. S. Sai Prasad, *J. Chem. Sci.,* **128,** 227 (2016).
28. D. A. Panayotov, J. R. Morris, *J. Phys. Chem. C.,* **113,** 15684 (2009).

Optimization of osmotic dehydration parameters for sweet cherries (*Prunus avium*) using response surface methodology

S. Zhelyazkov[1*], S. Aleksandrov[1], M. Ruskova[1], T.Petrova[1], V. Gotcheva[2], N. Penov[3]

[1]Institute of Food Preservation and Quality, Plovdiv, Bulgaria
[2]Department of Biotechnology, University of Food Technologies, Plovdiv, Bulgaria
[3]Department of Canning and Refrigeration Technology, University of Food Technologies, Plovdiv, Bulgaria

Osmotic dehydration of foods has recently gained attention as a processing method for obtaining better quality fruit products. The objective of this study was to investigate the effect of temperature of osmotic treatment (43, 50, 60, 70, and 77°C), concentration of osmotic solution (47, 50, 55, 60, and 63°Brix) and fruit-to-solution ratio (1:2, 1:3, 1:4, 1:5, and 1:6 w/w) on water loss (WL), solid gain (SG), and total antioxidant capacity (TAC) of osmotically dehydrated sweet cherries and to perform optimization of technological parameters by response surface methodology (RSM). The optimized criteria yielded high values of water loss, solid gain, and total antioxidant capacity.

Keywords: optimization, osmotic dehydration, sweet cherries, response surface methodology

Abbreviations:

OD – osmotic dehydration
WL – water loss
SG – solid gain
TAC – total antioxidant capacity
RSM – response surface methodology

INTRODUCTION

Cherries are one of the most popular early summer fruits. They comprise about 30 species, of which the most popular edible types are sweet cherry (*Prunus avium*), tart (sour) cherry (*Prunus cerasus*), and duke cherry. Cherries could be yellow, red, or yellow-red colored and are consumed fresh, dried, or processed. Sweet cherry fruits contain carbohydrates (12 – 26%), organic acids (0.3 – 0.8%), water-soluble vitamins (vitamin C, B vitamins) and fat-soluble vitamins (vitamins A, E and K), and some carotenoids [1, 2]. They are a good source of polyphenols (44 – 87 mg gallic acid equivalents/ 100 g) [1], anthocyanins (70 – 100 mg cyanidin 3-glucoside equivalents /100 g) [3], and flavonols (3 – 5 mg /100 g) [4]. The listed phytochemicals have been shown to exhibit high antioxidant capacity and to play a pivotal role in cell protection from reactive oxygen species (ROS) produced in the human body. Therefore, consumption of these fruits can reduce the risk of diseases such as cancer [5], arthritis, inflammation [6], and neurodegenerative diseases [7]. In the last few decades, sweet cherries are used for manufacturing health-promoting juices, syrups, jams, dried, and dietary foods, where preservation of antioxidants during cherry processing is of key importance.

Osmotic dehydration (OD) is one of the perspective pre-treatments for manufacturing dried fruit products, since it offers a number of benefits such as reducing the heat degradation of biologically active phytochemicals, color retention, reduction of fruit browning and decrease of the energy costs [8]. Osmotic dehydration often precedes processes such as air drying, freeze drying, or vacuum drying.

Osmotic dehydration is based on partial removal of water from plant tissues by immersion of foodstuff in a hypertonic water solution. It involves three simultaneous mass transfer flows (Fig. 1). The first one is water removal from the plant tissues into the osmotic solution, the second is the diffusion of osmotic agent from the osmotic solution into the plant cells and the third mass transfer flow is excretion of plant compounds (organic acids, mineral salts and vitamins) from the tissues to the osmotic solution. Although this third flow is not significant in the mass exchange, it is essential for the chemical composition and organoleptic qualities of the products [9].

Several factors are responsible for osmotic process efficiency, including type and concentration of the osmotic agent, temperature of the osmotic treatment, fruit : osmotic solution ratio and process duration.

* To whom all correspondence should be sent:
E-mail: s.zhelyazkov@canri.org
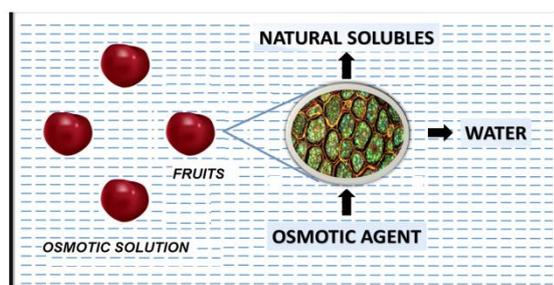
Figure 1. Mass transfer in fruit tissue during osmotic dehydration

Improvement of the dehydration rate is very important, since osmotic drying is a rather slow process. The type of the osmotic agent is a very important factor that determines the rate of diffusion. The most commonly used osmotic agents for the preparation of osmotic solutions are sucrose, glucose, fructose, sorbitol, corn syrup, and fructo-oligosaccharides. A number of scientists have concluded that osmotic agents with low molecular weight pass easier into the fruit cells membrane compared to osmotic agents with high molecular weight [10, 11]. In osmotic treatments, the increase of the osmotic agent concentration leads to an increased rate of dehydration. The study of Falade *et al.* (2007) [12] on the osmotic dehydration of watermelon in solutions with 40 – 60°Brix confirmed that the increase in the concentration of the osmotic agent (sucrose) resulted in higher water loss and solid gain throughout the osmotic period. The temperature of osmotic dehydration is one of the most significant variables affecting the kinetics of mass transfer [13]. According to the concept of osmotic dehydration, the increase of the solution temperature results in increased water loss, weight reduction and uptake of solids. The effect of osmotic treatment temperature on the osmotic process efficiency is proved by a number of scientists [14, 15]. It was also found that the increase of fruit : osmotic solution ratio results in an increase in water loss, solid gain and rate of dehydration [16].

Response surface methodology (RSM) is a statistical tool used to compose experiments for evaluation of the effects of independent process variables on dependent variables, as well as to determine optimal process conditions. The advantages of RSM are: reduced number of experiments, evaluation of the relative significance of several affecting factors even in the presence of complex interactions, and improved statistical interpretation. Several reported studies on optimization of plant products dehydration by the RSM method show its efficacy [17].

Therefore, the objective of this study was to investigate the effect of independent process variables (temperature of osmotic treatment, concentration of osmotic solution, and fruit-to-solution ratio on dependent variables (water loss, solid gain, and total antioxidant capacity) of osmotically dehydrated sweet cherries and to perform optimization of the technological parameters by response surface methodology.

MATERIALS AND METHODS

Raw materials

Sweet cherry (*Prunus avium*) fruits with soluble solids of 15.40% were purchased from Degustos Ltd. (Bulgaria). The fresh fruits were sorted and stored in a refrigerator at 3°C until used. Osmotic agents - concentrated sour cherry juice, concentrated apple juice, and inulin (oligo-fructose - 87%; average degree of polymerization - 8; sum of sucrose, glucose, and fructose - 12%) were purchased from Krichimfrukt Ltd. (Bulgaria), Agrobiotech Ltd. (Bulgaria), and Food Consulting Ltd. (Bulgaria), respectively. The concentrated sour cherry juice and apple juice were stored in a refrigerator at 3°C until used.

Chemicals

1,1-Diphenyl-2-picrylhydrazyl radical (DPPH), (±)-6-hydroxy-2,5,7,8-tetramethyl-chromane-2-carboxylic acid (Trolox), Folin-Ciocalteu phenol reagent, and gallic acid Sigma-Aldrich (St. Louis, MO, USA) were used as analytical standards. Methanol, ethanol, concentrated hydrochloric acid (HCl) and sodium carbonate monohydrate ($Na_2CO_3 \cdot H_2O$) of analytical grade were purchased from Rai-Him, Bulgaria.

Methods

Sample preparation and osmotic process. The sweet cherries were washed with tap water and the stones were removed.

Osmotic solutions were prepared in five concentrations (47, 50, 55, 60 and 63°Brix) (Table 1) using concentrated sour cherry juice with 63°Brix (60% w:w), concentrated apple juice with 72°Brix (20% w:w), and inulin (20% w:w). The concentration of the osmotic solutions was monitored by an Abbe refractometer (VEB Carl Zeiss Jena, Germany).

Osmotic dehydration of cherries was performed in a water bath (VEB MLW Prüfgerätewerk, Medingen, Sitz Freital, Germany). The choice of the process conditions was based on a literature survey on osmotic dehydration. The fruits were kept in an osmotic solution with concentration from 47 to 63°Brix and temperature from 43 to 77°C for 4 hours according to the experimental design (Table 1). The

501

fruit : solution ratio was 1:2, 1:3, 1:4, 1:5, and 1:6 (w:w) (Table 1). Further, the osmotically dehydrated cherries were removed from the solutions, quickly rinsed with hot water (40°C) and gently dried with paper towel to remove surface moisture. Total dry matter and drained weight (final sample weight) of the osmotically dehydrated fruits were determined. The fruits were also analyzed for the mass transfer indicators (water loss, solid gain) and total antioxidant capacity.

Water loss (WL) is defined as the net loss of water from the fresh fruits after osmotic dehydration based on the initial sample.

Solid gain (SG) is defined as the net uptake of sugar by the osmotically dehydrated fruits based on the initial sample weight.

WL and *SG* were calculated according to the following equations [18]:

$$WL = \frac{x_o^w M_o^o - x_f^w M_f^o}{M_o^o} \, 100 \,, \% \quad + \quad (1)$$

$$SG = \frac{x_f^{st} M_f^o - x_o^{st} M_o^o}{M_o^o} \, 100, \% \quad (2)$$

where: x_o^w – initial moisture content (%), x_f^w – final moisture content (%), M_o^o – initial sample weight (kg), M_f^o – final sample weight (kg), x_o^{st} – initial solids content (%), x_f^{st} – final solids content (%).

The moisture content in the fruits and the concentrated juices was determined according to BCS EN 12143:2000 and BCS EN 12145:2000.

Extract preparation. The osmotically dehydrated sweet cherries (5.00 g) were mixed with acidified methanol HCl (1000 ml MeOH with 2.3 ml conc. HCl) in a 50 ml volumetric flask. After 12 hours in a refrigerator at 3°C, the extracts were filtered through filter paper and transferred into flasks.

Total antioxidant capacity (*TAC*) was determined by the DPPH assay (free radical scavenging activity).

The ability of the fruit extract to interact with free radicals (scavenger again DPPH•) was determined by the colorimetric method of Brand-Williams *et al.* (1995) [19]. A 2250 µl aliquot of DPPH - ethanol solution (2.4 mg DPPH in 100 cm^3 ethanol) was mixed with 250 µL of methanol extract. The samples were incubated in a dark cabinet at room temperature. The change in absorbance after 15 minutes was measured at 515 nm by a spectrophotometer (UV-Vis Thermo Fisher Scientific, Madison, WI, USA). The standard curve for the method was created with ethanol solutions of Trolox in a concentration range between 100 and 1000 µmol per 100 ml. The total antioxidant capacity (TAC) was expressed as µmol Trolox equivalent per 100 g of samples on dry weight basis (dw). All determinations were performed in triplicate (n = 3).

Experimental design and statistical analysis. Response surface methodology (RSM) was used to investigate the main effects of the process variables (osmotic treatment temperature, solution concentration and fruit : solution ratio) on WL, SG, and TAC during osmotic dehydration of sweet cherries and to find the optimum parameters of dehydration. The experimental design adopted was a central composite rotatable design with three factors and five levels for each factor [20]. Selection of the actual factor values was based on the literature. The independent variable values and their corresponding levels are presented in Table 1.

The complete design consisted of 17 experimental runs with three replications of the central point. The generalized second-order polynomial model used in the response surface analysis was the following:

$$Y = b_o + \sum_{i=1}^{n} b_i x_i + \sum_{i=1}^{n} b_{ii} x_i^2 + \sum_{i=1}^{n} \sum_{j=1}^{n} b_{ij} x_i x_j \quad (3)$$

where: *Y* is the dependent variable (response), x_i and x_j are the independent variables (factors), β_o, β_i, β_{ii}, β_{ij} are the regression coefficients for intercept, linear, quadratic, and interaction terms. Experimental design data were analysed through the analysis of variance (Anova) and the *F*-test at $P < 0.1$, using the statistical software SYSTAT (SPSS Inc., Chicago, USA, version 7.1) and Excel (Microsoft Office, 97, 2003).

RESULTS AND DISCUSSION

The average values for WL, SG, and TAC of the osmotic dehydrated sweet cherries are presented in Table 2.

Regression analyses of the water loss, solid gain, and total antioxidant capacity of osmotically dehydrated sweet cherries indicated that all second-order polynomial models correlated well with the measured data and were statistically significant (p < 0.05).

Table 1. Central composite rotatable design in coded form and natural units of independent variables

Run №	Osmotic treatment temperature - X_1 (°C)	Solution concentration X_2 (°Brix)	Fruit : solution ratio X_3 (w/w)
1.	50 (-)	50 (-)	1:3 (-)
2.	70 (+)	50 (-)	1:3 (-)
3.	50 (-)	60 (+)	1:3 (-)
4.	70 (+)	60 (+)	1:3 (-)
5.	50 (-)	50 (-)	1:5 (+)
6.	70 (+)	50 (-)	1:5 (+)
7.	50 (-)	60 (+)	1:5 (+)
8.	70 (+)	60 (+)	1:5 (+)
9.	43 (-1.68)	55 (0)	1:4 (0)
10.	77 (+1.68)	55 (0)	1:4 (0)
11.	60 (0)	47 (-1.68)	1:4 (0)
12.	60 (0)	63 (+1.68)	1:4 (0)
13.	60 (0)	55 (0)	1:2 (-1.68)
14.	60 (0)	55 (0)	1:6 (+1.68)
15.	60 (0)	55 (0)	1:4 (0)
16.	60 (0)	55 (0)	1:4 (0)
17.	60 (0)	55 (0)	**1:4 (0)

The resulting models, after removing the non-significant terms, were evaluated in terms of uncoded factors and are presented below:

$WL = 564.81 - 6.74X_1 - 16.33X_2 + 0.07X_1^2 + 0.18X_2^2 - 0.64X_2X_3$, % ($R^2 = 0.97$)   (4)

$SG = 20.13 - 1.38X_1 + 0.87X_2 + 0.02X_1X_2 + 1.03X_3^2$, % ($R^2 = 0.93$)   (5)

$TAC = 74452.7 + 2313.57X_1 - 4089.52X_2 - 15.94X_1^2$, µmol TE/100g ($R^2 = 0.93$)   (6)

It was found that the osmotic treatment temperature and solution concentration were the most significant factors affecting the water loss, solids gain, and total antioxidant capacity. The effects of the independent variables (osmotic treatment temperature, solution concentration and fruit: solution ratio) on the dependent variables (WL, SG, and TAC) are indicated by the response surfaces plots (Figs. 2, 3, and 4) developed from the equation models shown above.

The criterion for estimation of the optimal osmotic dehydration conditions of sweet cherries was the achievement of high values of water loss (WL > 35%), solid gain (SG > 7.5%), and total antioxidant capacity (TAC > 21000 µmol TE/100 g).

Optimization was carried out by the superposition of several contour surfaces of competing responses. The response surface plots were generated for interaction of two independent variables (osmotic treatment temperature and solution concentration), while the value of the third variable (fruit : solution ratio) remained constant (at the central value). The best conditions that correspond to the shaded area obtained by superimposing contour plots of water loss, solid gain and total antioxidant capacity, are shown in Figure 5.

Table 2. Water loss, solids gain, and total antioxidant capacity of osmotically dehydrated sweet cherries

№	Water loss Y_1 (%)	Solids gain Y_2 (%)	Total antioxidant capacity Y_3 (µmol TE / 100 g dw)
1	28.35	6.84	18982.5
2	58.89	8.83	16804.5
3	44.48	7.14	24304.6
4	74.25	15.62	19832.2
5	31.55	6.16	18540.1
6	56.79	9.54	18201.2
7	33.37	6.57	26811.5
8	60.89	12.63	23750.2
9	30.29	7.28	19198.6
10	72.49	12.07	14894.2
11	37.33	6.34	23773.3
12	51.66	9.11	25325.3
13	35.06	12.19	19417.4
14	35.63	11.25	23890.1
15	34.23	8.47	23174.7
16	35.11	8.32	21470.8
17	34.47	8.43	19723.7
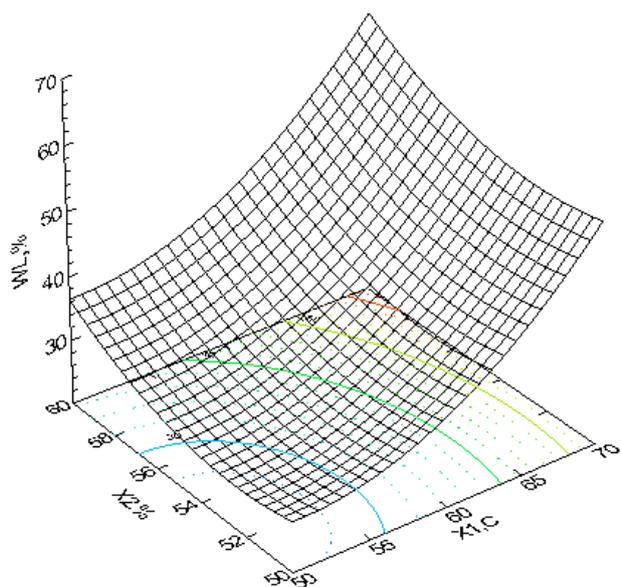
Figure 2. WL (%) depending on X_1 (ºC) and X_2 (°Brix) at fruit : solution ratio 1:4 (w:w).
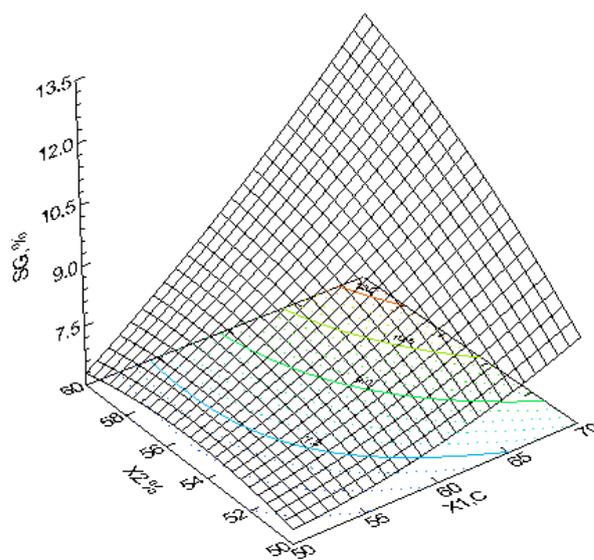
Figure 3. SG (%) depending on X_1 (ºC) and X_2 (°Brix) at fruit : solution ratio 1:4 (w:w).
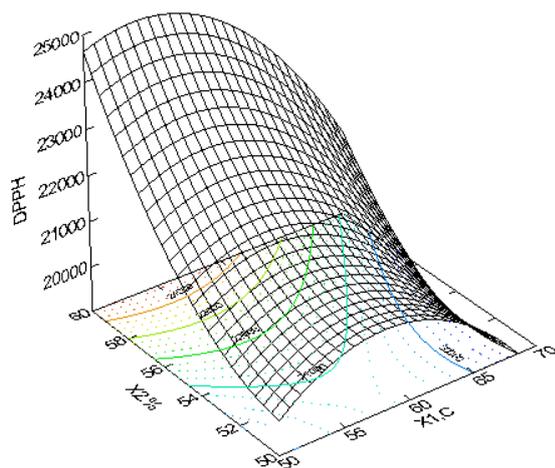
Figure 4. TAC (µmol TE/100 g) depending on X_1 (ºC) and X_2 (°Brix) at fruit : solution ratio 1:4 (w:w).
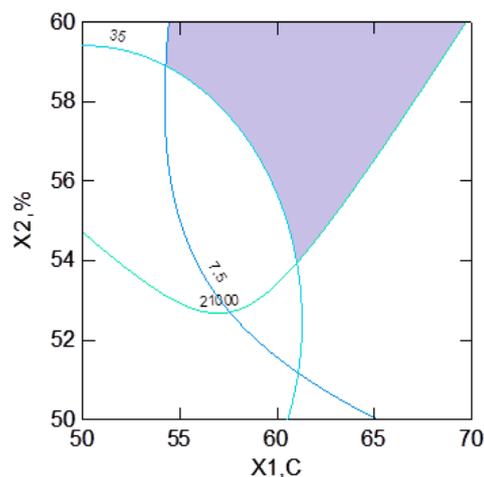
Figure 5. Superposition area of the responses as an effect of the treatment temperature (X_1) and solution concentration (X_2) on the osmotic dehydration of sweet chokeberry.

CONCLUSION

Response surface methodology was used for a quantitative study on the effects of process variables on water loss, solid gain, and total antioxidant capacity of osmotic-dehydrated cherry fruits. Optimization was carried out by the superposition of several contour surfaces of competing responses. The criterion to determine the optimal osmotic dehydration conditions of sweet cherries was the achievement of high values of water loss (WL > 35%), solid gain (SG > 7.5%), and total antioxidant capacity (TAC > 21000 µmol TE/100 g). Results from the present study showed that the osmotic treatment temperature and solution concentration had a significant effect on the mass transfer (water loss and solid gain) and the total antioxidant capacity. The increase of the osmotic treatment temperature resulted in degradation of the biologically active components and, respectively, in decreased total antioxidant capacity. The application of response surface methodology proved to be very efficient for the optimization of osmotic dehydration of sweet cherries.

REFERENCES
1. V. Usenik, J. Fabčič, F. Štampar, *Food Chemistry*, **107**, 185 (2008).
2. G. Ferretti, T. Bacchetti, A. Belleggia, D. Neri, *Molecules*, **15**, 6993 (2010).
3. V. Usenik, N. Fajt, M. Mikulic-Petkovsek, A. Slatnar, F. Stampar, R. Veberic, *J. Agric. Food Chem.*, **58**, 4928 (2010).
4. H. Kelebek, S. Selli, *Int. J. Food Sci.Technol.*, **46**, 2530 (2011).
5. S.-Y. Kang, N. Seeram, M. Nair, L. Bourquin, *J. Crohn's Colitis*, **7**, 202 (2003).
6. R. Jacob, G. M. Spinozzi, V. A. Simon, D. S. Kelley, R. Prior, B. Hess-Pierce, *J. Nutrition*, **133**, 1826 (2003).
7. D.-O. Kim, H. Heo, Y. Kim, H. Yang, C. Lee, *J. Agric. Food Chem.*, **53**, 9921 (2005).
8. J. Alakali, C. Ariahu, N. Nkpa, *J. Food Process. Preservation*, **30**, 597 (2006).
9. H. Lazarides, K. Petrotos, *J. Food Eng.*, **49**, 201 (2001).
10. Â. El-Aouar, P. Azoubel, F. Murr, *J. Food Eng.*, **75**, 267 (2006).
11. A. İspir, İ. Toğrul, *Chem. Eng. Research Design*, **87**, 166 (2009).
12. K. Falade, J. Igbeka, F. Ayanwuyi, *J. Food Eng.*, **80**, 979 (2007).
13. C. Tortoe, *African J. Food Sci.*, **4**, 303 (2010).
14. E. Devic, S. Guyot, J.-D. Daudin, C. Bonazzi, *J. Agric. Food Chem.*, **58**, 606 (2010).
15. M. Khan, *Pakistan J. Food Sci.*, **22**, 71 (2012).
16. J. Ponting, G. Walters, R. Forrey, R. Jackson, W. Stanley, *Food Technol.*, **20**, 125 (1966).
17. İ. Eren, F. Kaymak-Ertekin, *J. Food Eng.,* **79**, 344 (2007).
18. F. Kaymak-Ertekin, M. Sultanoğlu, *J. Food Eng.*, **46**, 243 (2000).
19. W. Brand-Williams, M. Cuvelier, C. Berset, *LWT – Food Sci. Technol.*, **28**, 25 (1995).
20. P. Haaland, Experimental Design in Biotechnology. CRC Press, 1989, ISBN 9780824778811.

Integrated membrane processes for green technologies

Selected papers presented on the workshop "Method for assessment the transfer efficiency of integrated processes in bioreactor with membrane separation" , 10-11.09.2019, Sofia, Bulgaria

On the potential of integrating extraction with nanofiltration for separating and concentrating polyphenols from plant materials

I. Tsibranska[1*], E. Simeonov[2]

[1]*Institute of Chemical Engineering, Bulgarian Academy of Sciences, Acad. G. Bonchev Str. Bl. 103, 1113 Sofia, Bulgaria*
[2]*Dept. of Chemical Engineering, University of Chemical Technology and Metallurgy, 8 Kl. Ohridski Blvd., 1756 Sofia, Bulgaria*

A green integrated process of solid–liquid extraction and nanofiltration is modeled and numerically investigated considering the separation and concentration of polyphenols from plant extracts. The integrated operation is studied in view of solvent reuse, processing time and degree of concentration. A considerable shortening of the total processing time and reducing of the organic solvent volume is predicted together with high yield and favorable permeate flux. The study is based on extraction kinetics and nanofiltration data for three systems: *Sideritis scardica × Sideritis syriaca* – 80% EtOH; *Geranium sanguineum L* – 70% EtOH; and *Cotinus coggygria L.* – 50% EtOH. Over 97% of extractable solute is reached within up to 2 times shorter extraction time; a degree of concentration above 3.7 times in the final product is achieved at 74% solvent recovery.

Keywords: Process integration, modelling, green solid-liquid extraction, polyphenols, nanofiltration.

INTRODUCTION

Plant-derived polyphenols are strong antioxidants with numerous health benefit effects. Their practical utilization implies extraction and further separation/concentration of the phenolic content, the nanolfiltration being recognized as an effective method for the latter. Each one of the processes – solid-liquid extraction (SLE) and membrane filtration – has been investigated in view of optimal operating conditions. Possibilities for intensification of the polyphenols extraction from the solid material are discussed [1] including ultrasound/microwave-assisted extraction [2-4] or supercritical fluid extraction [5]. For a number of industrially important applications integrated membrane processes are proposed [6, 7], because they allow both improved and low-energy separation solvent-extract. In particular, nanofiltration has been intensively investigated for concentration and fractionation of bioactive compounds such as soluble phenolics by selecting a sequence of membranes with suitable molecular weight cut-off (MWCO) in the range of 150–1000 Da [8]. Regarding the composition of the extract, neither extraction nor nanofiltration is selective enough on their own. Their joint use gives satisfactory results when the composition of the extract is valuable and the solvent used is favorable for high value-added molecules, such as polyphenols antioxidants [9-11]. Over the years, the interest in the successive use of the two unit operations is shown in a great number of publications, including optimizing the extraction-nanofiltration process as a whole [3, 4, 12, 13]. The advantages of the latter are demonstrated in terms of green methodology, avoiding high temperatures and toxic solvents, and providing polyphenols recovery from the plant material together with solvent amount reduction. In the search of the final goal to obtain small volumes, concentrated and rich in polyphenols, and to restore an essential part of the solvent for reuse in a subsequent extraction, an integrated extraction-nanofiltration process is expected to reveal a greater potential while preserving the high quality of the extracts [12, 14]. The estimation of the integrated process as possible comprises information about the solvent, the extraction kinetics and the process of transfer across the membrane.

Solvent

The appropriate solvent for both steps of the integrated process is determined by the yield and selectivity to a compound or a group of target compounds, as well as sufficient solubility for the dissolved components over the entire range of concentrations (to prevent precipitation) and non-disruptive effect on the membrane structure. The problem may be significant in extracts containing compounds with a high molecular weight distribution profile and very different solubility. It may lead to uncontrollable flux decline, related to

---

* To whom all correspondence should be sent:
E-mail: tsibranska@yahoo.com

increased viscosity and oversaturation of higher molecular weight polyphenols at high concentration factors.

Extraction kinetics

Kinetic investigations give essential information about the required time of extraction, as well as on the governing mass transfer mechanism. The appropriate extraction time to approach equilibrium, resp. the range of low variability of the TP yield (the plateau of the kinetic curve) has to be comparable with the time for nanofiltration (needed to achieve a certain degree of concentration) in order to facilitate the integration of the two processes into a single system. In fact, the combination between extraction time and different intensification approaches (temperature, ultrasound- or microwave assistance) is important for the composition and quality of the extract, as well as for the economic feasibility of the process [12]. In general, extraction under agitation is an effective technique for polyphenols extraction because of better hydrodynamic conditions in the extraction vessel and reduced external mass transfer. The mechanisms of mass transfer have been investigated in detail, including the effect of variable rate parameters, particle size evolution and polydispersity [15-18]. Extraction time increases with particle size and, in the presence of large particle size distribution, the larger particles act in the direction of extended both kinetic curve and extraction time [12]. The solute concentration, leaving the extractor vessel, has to be reliably predicted by the kinetic model in order to facilitate the calculations in the NF step, where the value and composition of the feed are very important.

Transport mechanisms across the membrane

High rejections, reasonable values and stability of the permeate flux are required within a predetermined range of feed concentrations, the fouling behavior and mass transfer coefficients being an important source of information [12, 19, 21]. Typical values in the order of 10 l/(m² s) are reported for permeate fluxes when concentrating polyphenols containing natural extracts. Rejections over 90% are required in view of the quality of solvent recovery and its possible multiple reuse. Based on the statistical adequacy of the experimental flux *vs* time data regarding the four basic fouling models, the cake layer formation is found as the predominant mechanism, usually followed by the intermediary, standard or complete pore blocking. Mass transfer coefficients in the order of 10^{-5} to 10^{-6} m.s^{-1} are reported for natural

antioxidants such as polyphenols extracted from different natural sources [19, 20, 22, 23].

Potential of the integrated SLE-NF separation process

The integration is viewed as a coupling of two unit processes (extraction and nanofiltration, extraction and adsorption, etc.) into a single system (ex. within a common recirculation loop), Fig. 1.
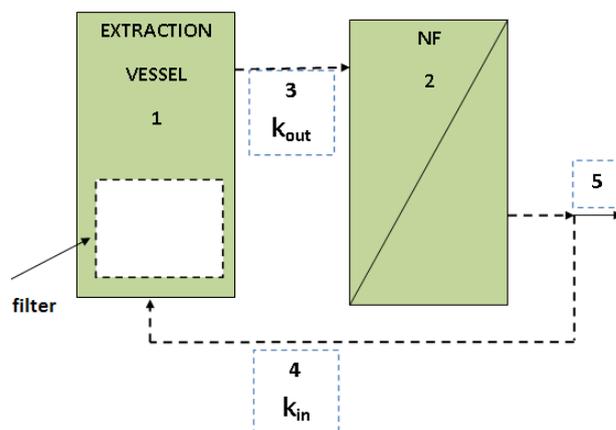
Fig. 1. Schematic representation of the integrated process.

Positive results for integration of solid-liquid extraction with adsorption are recently reported aimed at selective recovery of antioxidant phenolics from chicory grounds [24]. In this case the integration enables simultaneous extraction of phenolics and their purification in a single operation. The comparison with a conventional process of successive extraction and adsorption is in favor of the integrated one because of the higher TP recovery obtained at lower energy consumption [24]. The main purpose of the integration is to achieve better performance than any of the component parts, as weaknesses in certain processes can be reduced by other processes in the integrated system [25]. Though examples for integrated extraction-membrane filtration processes can be found in literature [26, 27], there is little existing experience regarding the principles for integration of the two separation processes, i.e. the simultaneous extraction of phenolics and separation from the solvent in a single system.

The integration of two batch processes is strongly dependent on time, which has to be optimized within the requirements for maximum polyphenols recovery; the latter comprises almost full extraction from the raw material and high solute concentrations in the obtained retentate. The total processing time has to enable high values of extracted polyphenols to be achieved, reuse of the

solvent and full utilization of the raw material, as well as concentrated phenolic content in the final product. For the NF cell operation, it is important to maintain a limited range of variations of the entering (feed) concentrations. The number of recirculated volumes during the integrated extraction-nanofiltration process has to assure values of extracted polyphenols per gram of solid, near the maximum available in the solid to be obtained. The last step (concentration mode) is relevant for the quality and bioactive properties of the final product.

The present study is focused on the potential of integrating solid-liquid extraction with nanofiltration for separating and concentrating polyphenols from plant extracts. The integrated process is investigated in view of three important characteristics - solvent reuse, processing time and degree of concentration.

EXPERIMENTAL

Successive extraction and nanofiltration

The investigation is based on own data for three experimental systems, for which optimal solvent and extraction conditions were found and reported previously [9, 10, 17, 33]. They represent differently fast extraction kinetics, as well as different phenolic contents. The batch kinetic curves shown in Fig. 2 are calculated with the parameter values from Table 1, where data for the

three systems, obtained from successive extraction and nanofiltration, are presented.
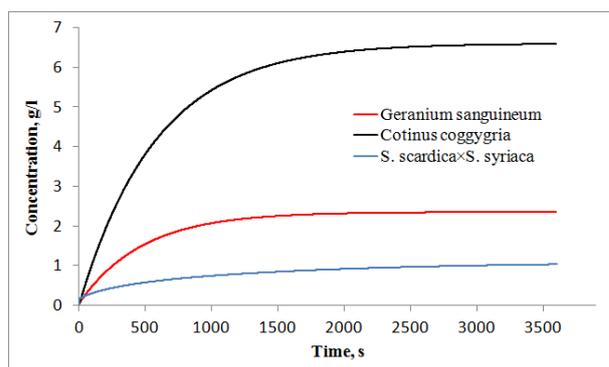
Fig. 2. Batch extraction kinetic curves calculated with the data in Table 1.

System 1 - The genus *Sideritis* L. comprises more than 150 species occurring mainly in the Mediterranean area and the Balkan Peninsula, the selected hybrids *S. scardica×S. syriaca* being cultivated since 20 years [28]. The valuable phytochemical content of the plant is utilized either as the traditional remedy tea, or as alcoholic extract with high antioxidant, anti-inflammatory and anti-rheumatic properties. The antioxidant activity is mainly attributed to the flavonoids and phenylpropanoid glycosides content of the plant. Under conventional batch extraction with EtOH 16.4 mg TP/g (solid) were obtained after 2.5 h of extraction, the maximum obtainable after 24 h being 17.5 mg/g solid [17].

Table 1. − Extraction and nanofiltration conditions

EXTRACTION					
No	Solute	Extraction system,	Extraction conditions	Extraction kinetics	Method of analysis
1	TP	*Sideritis scardica× Sideritis syriaca* – 80% EtOH [10,17]	LSR 15:1 $2r_0$ $4 \cdot 10^{-5}$ m T 20 °C	Time 2.5 h D_e $2.5 \cdot 10^{-14}$ m²/s $C_l=1.13$ mg/l	Spectrophotometric [32] Gallic acid equivalent Calibration curve [10,17]
2	TP	*Geranium sanguineum L.-* 70% EtOH [33]	LSR 30:1 $2r_0$ $4\text{-}8 \cdot 10^{-4}$ m T 20 °C	Time 2 h D_e $1.17 \cdot 10^{-10}$ m²/s $C_l=2.37$ mg/l	Spectrophotometric [34] Gallic acid equivalent Calibration curve [35]
3	TT	*Cotinus coggygria L.-* 50% EtOH [9]	LSR 30:1 $2r_0$ $3 \cdot 10^{-4}$ m T 40 °C	Time 2 h D_e $1.90 \cdot 10^{-11}$ m²/s $C_l=6.86$ mg/l	Titrimetric [16]
NANOFILTRATION					
No	TMP bar	MWCO Da	J l/(m².h)	R_{obs} -	V_p/V_f -
1	20	300	7.3	0.98	0.77
2	30	200	10.0	0.997	0.27
3	20	300	9.0	0.91	0.25

Using ultrasound-assisted extraction (UAE) and cross-flow filtration the total processing time for system 1 in sequential operation mode was reduced to 2.5 h, including 1 h for each of the extraction and NF steps and 0.5 h between them for separation of the solid phase [12]. UAE enabled the maximum amount extracted for 24 h to be obtained within 1 h.

System 2 - The phenol compounds, especially the flavonoids from *Geranium* spp. were reported to exhibit antiviral, antitumor, hepatoprotective, anti-inflammatory, anticancer and immune-stimulant effects. The content of flavonol and flavone glycosides and aglycones in the extracts of *Geranium sanguineum* L. was studied in detail by HPLC [29]. The phytochemical screening of the water extracts (initial, after MF, UF and NF process) showed the presence of flavonoids, reducing sugars, terpenoids, saponins and aminoacids [30]. A potential for concentrating by membrane filtration of the polyphenolic content was demonstrated.

System 3 - Cotinus coggygria is a well-known medicinal plant source of high-quality polyphenolic compounds with rich biological activity - antiatherogenic, antioxidant, anti-inflammatory, cardioprotective, antimicrobial, anticarcinogenic and neuroprotective [31]. Ethanolic extracts of *Cotinus coggygria* dry leaves are rich in total phenols, total flavonoids, rutin and tannins. Concentration by NF allows retaining the majority of valuable compounds, the dead-end filtration runs being subject to significant fouling and flux decrease. The data given in Table 1 correspond to the average permeate flux after 4 h of filtration.

Nanomembranes Duramem with low MWCO (200-300 Da) were chosen in view of high rejections and solvent recovery. The filtration data in Table 1 refer to a stirred laboratory NF cell (METcell, Evonic MET LTD, UK) with bottom-placed membrane (effective surface area A=54 cm^2), working volume up to 200 ml, magnetic stirrer close to the membrane surface in order to minimize the concentration polarization effect and stirring speed of 300 rpm.

Integrated extraction-nanofiltration process

The best processing time obtained from the sequential SLE-NF operation (ex. 2.5 h) [12] was used as a time frame for the integrated process, including solvent reuse. Recirculation of the recovered solvent is expected to give shorter extraction time and more complete extraction of the solute for the same initial solvent volume. The three systems in Table 1 have different extraction kinetics, but due to the appropriate choice of solid

512

size and respective intraparticle resistance, the extraction time was reduced to a 2-2.5 h interval. Low concentrations and a narrow range of variation in both the extraction and NF vessels were searched for as favorable in view of higher concentration gradient during extraction and lower susceptibility to fouling during nanofiltration. The criterion for maximum recovery of polyphenols from the plant materials was followed together with high degree of concentration in the final retentate. The latter was achieved by a NF step alone (within the same total processing time), when only concentrating of the solution proceeds.

The model of the integrated extraction-nanofiltration process follows the schematic representation of Fig. 1, where extraction and nanofiltration are carried out separately and are connected in a recirculation loop (lines 3 and 4). When the final step for separating the solvent and concentrating the valuable compounds proceeds, line 4 is excluded and the operation follows lines 3 and 5.

Extraction model

The solid phase extraction is described as a diffusion process with constant effective diffusivity D_e in the particles:

$$\frac{\partial C}{\partial t} = D_e \frac{1}{r^\alpha} \frac{\partial}{\partial r}(r^\alpha \cdot \frac{\partial C}{\partial r}) \qquad (1)$$

For spherical particles the form factor α=2 and the boundary condition at r=0 accounts for the central symmetry of the concentration profile $C(r,t)$ in the particle:

$$t>0, r=0, \quad \frac{\partial C}{\partial r}\bigg|_{r=0} = 0 \qquad (1.1)$$

The second boundary condition at the solid/liquid interface includes the external mass transfer in the fluid film around the particle, k_f being the rate coefficient.

$$t>0, r=R, \quad D_e \frac{\partial C}{\partial r}\bigg|_R = k_f(C|_R - C_l) \qquad (1.2)$$

Usually conditions for eliminating the external mass transfer are searched for and experimentally proven for stirrer speeds above 320 min^{-1} (system 3) [9].

The liquid phase concentration $C_l(t)$ is calculated from the mass balance in the extraction vessel:

$$\frac{\partial C_l}{\partial t} = -\frac{V_s}{V_l} \frac{d\langle C \rangle}{dt} - k_{out}\dot{V}C_l + k_{in}v_y AC_p \qquad (2)$$

The latter runs under intensive agitation, so perfect mixing conditions are supposed in the model and homogeneous concentration $C_l(t)$ within the liquid volume V_l. The volume-averaged solid phase concentration is derived from eq. (1) as follows:

$$\frac{d\langle C\rangle}{dt} = \frac{3}{R^3}\int_0^R \frac{dC}{dt}r^2 dr = \frac{3}{R^3}\int_0^R D_e \frac{1}{r^2}\frac{\partial}{\partial r}\left(r^2\frac{\partial C}{\partial r}\right)r^2 dr \quad (3)$$

$$= \frac{3}{R^3}D_e\left(r^2\frac{\partial C}{\partial r}\right)\Big|_0^R = \frac{3}{R}D_e\frac{\partial C}{\partial r}\Big|_R$$

According to the boundary condition (1.2), it is calculated as:

$$\frac{d\langle C\rangle}{dt} = \frac{3}{R}k_f\left(C\big|_R - C_l\right) \quad (4)$$

Eq. (2) includes the outlet and inlet lines 3 and 4 (Fig. 1), described by the switch on/off keys k_{out} and k_{in}, which take the values of "1" and "0", respectively. Further calculations use the presumption of constant volume V_l, so the outgoing flow rate $\dot{V}$ is set equal to the permeate flow rate $v_y A$. As the permeate flux is a characteristic of the membrane separation, higher flow rate during the simultaneous extraction-nanofiltration operation can be realized by increasing the membrane area (A). The solute concentration in the permeate C_p, appearing in the last term of eq. (2), is calculated from the mass balance of the NF cell.

The initial conditions for solving eqs. (1) and (2) suppose a pure solvent and known initial solute concentration in the solid:

$$t=0, \quad 0 \leq r \leq R \quad C = C_0, \ C_l = 0. \quad (5)$$

Nanofiltration model

The model of the stirred NF cell supposes perfect mixing conditions in the bulk and concentration polarization in the boundary layer to the membrane, accounting for the true rejections and flux decline. When observed, the latter is used as an experimentally defined function of the time of filtration or the volume-averaged retentate concentration. The effect of the permeate concentration and its increase during repeated permeate reuse as solvent is also considered.

The mass transfer in the boundary layer adjacent to the membrane in a dead-end stirred filtration cell is viewed as unsteady one-dimensional problem with a convective flow $v_y C$ directed normal to the membrane and diffusion flow $D_{AB}\frac{\partial c}{\partial y}$ back to the bulk:

$$\frac{\partial c}{\partial t} = D_{AB}\frac{\partial^2 c}{\partial y^2} - v_y\frac{\partial c}{\partial y} \quad (6)$$

The boundary condition at the membrane surface ($y=0$) accounts for both convective and diffusional mass transfer:

$$0 = D_{AB}\frac{\partial c}{\partial y}\Big|_{y=0} + v_y\left(c_{y=0} - C_p\right) \quad (6a)$$

The true rejection coefficient is used to express the permeate concentration:

$$R_i = 1 - \frac{C_p}{C_m} = 1 - \frac{C_p}{c_{y=0}} \text{ or } C_p = C_{y=0}(1-R_i). \quad (6b)$$

Inserted in equation (6a), the boundary condition at the membrane surface becomes:

$$0 = D_{AB}\frac{\partial c}{\partial y}\Big|_{y=0} + v_y c_{y=0} R_i \quad (7)$$

In the second boundary condition the bulk concentration in the filtration cell was used:

$$c_{y=\delta} = C_r \quad (8)$$

The latter is calculated from the mass balance of the filtration cell:

$$\frac{d(VC_r)}{dt} = -v_y A C_p + k_{out}\dot{V}C_l = -v_y Ac|_{y=0}(1-R_i) + k_{out}\dot{V}C_l \quad (9a)$$

$\frac{dV}{dt} = -v_y A + k_{out}\dot{V}$ being the change in the liquid volume, eq. (9a) is transformed to:

$$\frac{dC_r}{dt} = \frac{k_{out}\dot{V}(C_l - C_r) + v_y A(C_r - c|_{y=0}(1-R_j))}{V} \quad (9)$$

thus allowing the retentate concentration C_r in the NF cell to be calculated.

When a variable flux case is observed, the experimentally obtained $v_y(t)$ is directly used in eqs. (6) to (9), or after recalculation, in the function of the bulk fluid concentration $v_y(C_r)$.

RESULTS AND DISCUSSION

Effect of the number of recirculated volumes

Fig. 3 illustrates the effect of the multiple solvent recycling on the amount extracted within 2.5 h as compared to the conventional batch extraction.

The initial liquid/solid ratio 15:1 was recommended from previous results (system 1, Table 1). When results for different recycling volumes are compared with batch extraction, the latter is calculated using liquid volume equal to the sum of the recycled volumes plus the initial one. The TP concentration in the recirculating flow is low, equal to the permeate concentration C_p (see

Table 1), while pure solvent was used in the case of conventional extraction.
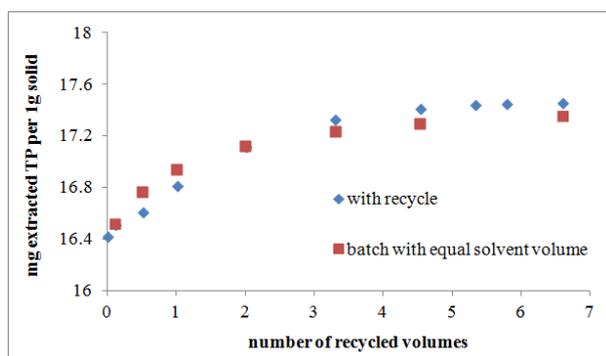
Fig. 3. Effect of the number of recycled volumes of solvent on the amount extracted – calculated results.

Despite this difference, increasing the number of permeate volumes reused, the maximum of extractable TP is approached, the results being comparable or even better than the respective conventional extraction with a larger solvent volume. Experimental confirmation for the suitability of the permeate as a solvent for multiple use is reported for rosmarinic acid from lemon balm [5], where threefold extraction with pure solvent and with NF permeate were compared; similar results are obtained, the difference being in favor of the permeate as solvent. In the presence of over 99% TP rejection (R_i=0.99) the model supposes almost pure solvent, which is not necessarily true in practice, considering the multicomponent composition of the natural extracts. In the particular case of system 1, Table 1, 99.7% of the TP are extracted, the latter being achievable by batch extraction with 6.6 times greater volume of solvent.
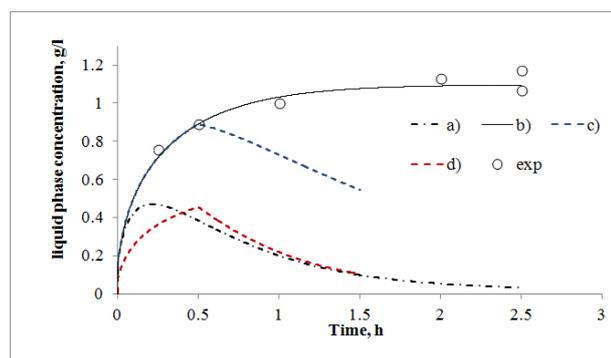
Fig. 4. Calculated bulk TP concentration evolution in the extractor (system 1, LSR 15:1): case a) with recycle; case b) without recycle; case c) without recycle until 80% of the batch plateau, then recycle switched on; case d) 30 min batch extraction (LSR 30:1) + 1 h with recycle (LSR 15:1).

System 1 used powdered solid and the gain of over 6.7% as compared to the batch extraction is

not impressive, but it is expected to be higher in cases of slower kinetics (ex. larger particle size) and stronger influence of the liquid to solid ratio.

The evolution of the liquid phase concentration in the extraction vessel is illustrated in Fig. 4, where also the batch extraction curve and the agreement with the experimental points can be seen (Fig. 4, case b). The same kinetic data were used for the rest of the calculations. The corresponding liquid phase profile for extraction with solvent recycle is given in Fig. 4, line a). The latter illustrates also the feed concentration input to the NF vessel. The recirculation case provides operation under lower concentrations and narrower range of their variation for both the extraction and the NF units. The recycle can be used to increase the degree of extraction and to reduce the overall time of the process. Results shown in Fig. 5 illustrate the comparison of different extraction-nanofiltration modes. First conventional extraction was coupled to nanofiltration at different moments of the extraction (C_l=70, 80, 90% of the batch curve plateau) and performed until overall time of 2.5 h. The resulting amounts extracted are shown in Fig. 5 and the concentration evolution in the extraction vessel looks like line c) and d) in Fig. 4.
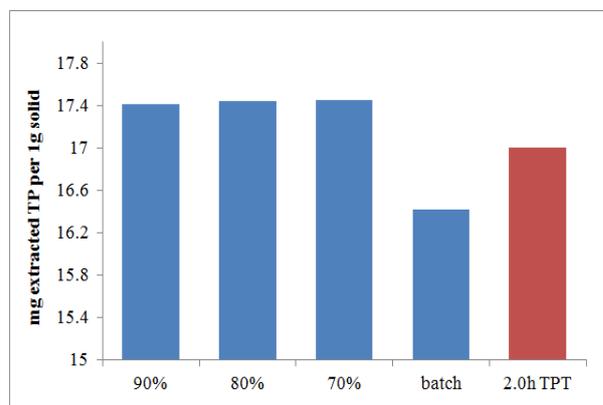
Fig. 5. Calculated amount extracted for different extraction-nanofiltration modes: recycle switched on at C_l=70, 80, 90% of the batch curve plateau; batch; conditions corresponding to Fig. 4, case d, total processing time 2 h.

These two examples are chosen among several numerical calculations investigating the potential for shortening the time of the process. The last one - line d) in Fig. 4 – corresponds to a concentration profile close to the one with maximum TP yield (Fig. 4, line a), but the total processing time (including the concentration step by NF) is reduced to 2 h. Thus over 97% of the extractable TP is reached (the last column in Fig. 5) under 1.7-fold reduction of the extraction time. The experimental procedure comprised 30 min extraction with double

LSR to assure higher concentration gradient in the extraction vessel, followed by 1 h of integrated SLE-NF operation with LSR 15:1 (the rest of the volume being transferred to the NF cell). Then a final step of 30 min for concentrating the TP is provided. The initial concentration for this step is 1.2 mg/ml, at the end $C_r/C_f=3.72$ of TP concentration degree is achieved together with 74% solvent volume recovery.

Effect of the recirculation flow rate and concentration

In all experiments so far the recirculating flow rate was equal to the one leaving the NF cell. Variation of the latter is practically achievable by increasing the membrane area and/or choosing another membrane. The evolution of the liquid phase concentration under two different recirculation flow rates is shown in Fig. 6. They were calculated based on the measured permeate fluxes (Table 1) and the membrane area. As can be seen, within a twofold increase of the recirculation flow rate, the range of variation of the liquid phase concentration is essentially reduced, which is favorable for the NF cell operation. The degrees of extraction for the experiments shown in Fig. 6 are compared with the batch extraction ones (Fig. 7a).

Except for the slowest kinetics case of system (1), the recirculation flow allowed to increase the degree of extraction over the batch one within 1 h of integrated operation, thus revealing potential for further reduction of the total processing time. For these systems extraction over 99% and threefold concentrating by NF could be achieved in less than 1.5 h total processing time (based on 100 ml initial volume). The calculations were performed both with constant and variable concentration in the recirculation flow. In the first case the measured average permeate concentration in the NF cell were used – 0.023 mg/ml, 0.008 mg/ml and 0.617 mg/ml for systems 1, 2 and 3, respectively.
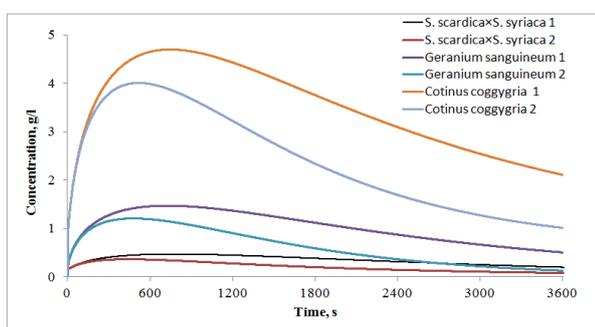
Fig. 6. Effect of the recirculation flow rate on $C_l(t)$: case 1 - permeate fluxes and membrane area according to Table 1; case 2 - twofold increased recirculation flow rate.
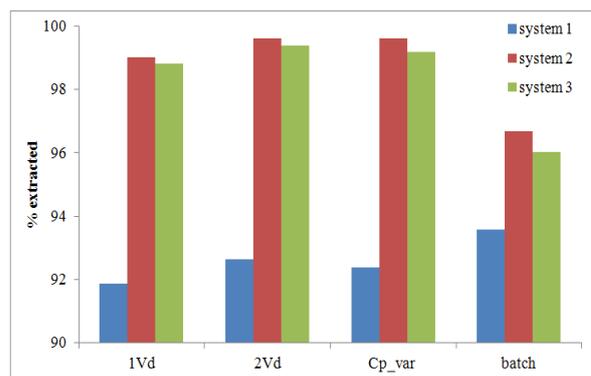
Fig. 7a. Effect of the recirculation flow rate and concentration on the percentage extracted from the solid: 1Vd – permeate fluxes and membrane area according to Table 1 (C_p=const); 2Vd - twofold increased recirculation flow rate (C_p=const); Cp_var – the change in the permeate concentration (line 4, Fig. 1) accounted for; batch results.
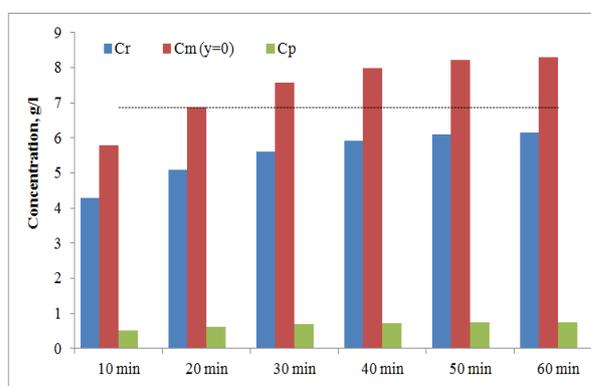
Fig. 7b. Concentration evolution in the NF cell during integrated operation (system 3): columns - calculated retentate, permeate and membrane surface concentrations; dashed line – experimental TP feed concentration in the NF cell, obtained from successive extraction – nanofiltration operation runs.

In the second case variable $C_p(t)$ was used as calculated by the model accounting for the concentration polarization, eqs. (6) to (9). The results are shown as C_{pvar} in Fig. 7a. Due to the narrow concentration range during the integrated operation, no essential effect of the variable concentration is observed. The calculated extracted amount is only slightly less than that with constant C_p and higher recirculation flow rate.

Effect of variable flux and rejection

By selecting the appropriate conditions for narrow concentration variation one can rely on constant permeate flux during the integrated process. For example, in the case referring to line d) in Fig. 4, the TP concentration in the NF cell varied within 0.891 to 0.989 mg/ml during the integrated operation; for comparison, 16.92 mg/g were

515

extracted for 1.5 h *versus* 16.42 mg/g for 2.5 h batch extraction. The experiments shown in Fig. 6 refer to a wider concentration change in the NF cell, also illustrated in Fig. 7b) for system 3; but the permeate flux should not be less than the one corresponding to the feed concentration in the successive extraction – NF operation. The respective flux values for the three investigated systems and membranes Duramem with different MWCO are shown in Fig. 8a.
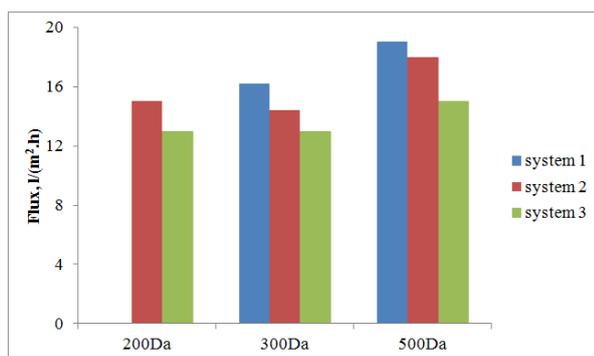
Fig. 8a. Initial permeate flux for different MWCO of the membrane, obtained from experiments with system 1, 2 and 3 in a successive SLE-NF operation.
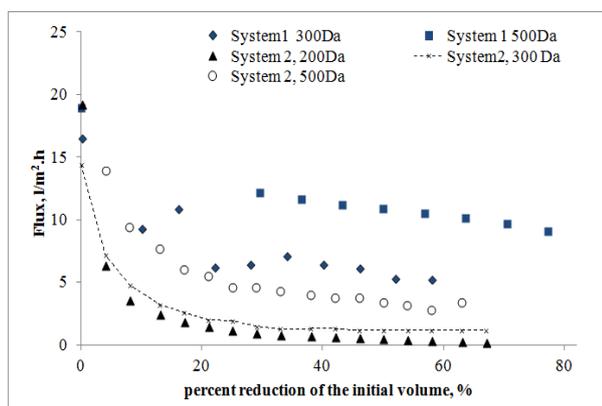
Fig. 8b. Permeate flux *vs* percent reduction of the initial volume for different MWCO (experimental data for systems 1 and 2).

In Fig. 7b concentrations in the NF cell are given (C_p, C_r and C_m) as calculated by the model for integrated SLE-NF operation. The input concentrations for the NF cell are shown in Fig. 6 (*Cotinus coggygria* 2), the output ones being the calculated permeate concentrations (C_p) in Fig. 7b. The averaged permeate concentration agrees with the experimentally measured one (0.618 mg/ml calculated *vs* 0.617mg/ml experimental). The bulk concentration C_r after 1 h of integrated operation does not exceed the feed one (see the dashed line in Fig. 7b) for which NF was initiated with 13 l/(m².h) permeate flux. The latter is illustrated in Fig. 8a, according to the data referred for system 3 [9].

The effect of variable flux and rejection is most pronounced during the last step of concentrating the TP content and depends on the composition of the extract and the required degree of concentration (C_r/C_f). Fig. 8b presents the experimentally observed permeate flux decrease for the three systems.

Low but stable permeate flux is reached for system 2 with Duramem 300 until over 60% reduction of the initial volume. For the rest of the cases a gradual flux decrease is observed under dead-end NF operation, thus limiting the achievable degree of concentration.

In case of important flux variation, the latter was included in the model after a mathematical processing of the experimentally observed one. The calculated flux variation has to assure the same average value as the measured one. Example for system 1 is given in Fig. 9a, where the permeated volume *vs* time is shown – experimental and calculated. The average flux for this experiment was 7.34 l/(m².h) *vs* 7.13 l/(m².h) predicted by the model.
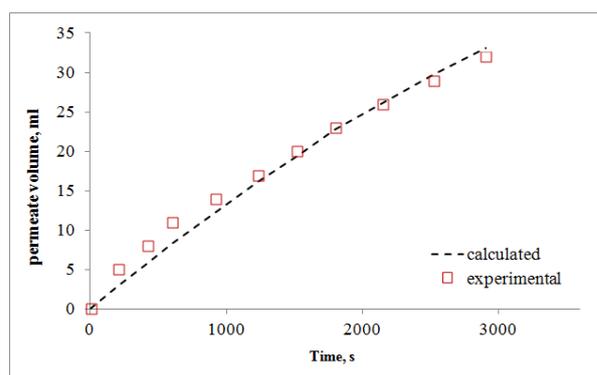
Fig. 9a. Permeate volume *vs* time (system 1).

Rejection was set as constant intrinsic R_i=0.98 according to eq. (6b). Within threefold concentration of the extract an increase in the permeate concentration is expected, due to the concentration polarization (0.023 to 0.086 mg/ml), which results in decreasing observed rejections $R_{obs} = \left(1 - \frac{C_p}{C_f}\right)$ from 0.98 to 0.926. Concentration polarization was accounted for using approximate values of 100 μm boundary layer thickness (δ) and 10^{-9} m²/s molecular diffusion coefficient (D_{AB}); the order of 10^{-9} m²/s was chosen as typical for polyphenols in water and ethanol extracts [36]. For these values the evolution of the TP concentrations in the bulk and at the membrane surface (mg/ml), are shown in Fig. 9b.
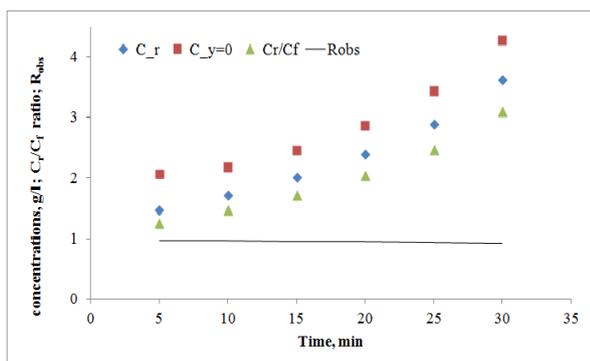
Fig. 9b. Calculated parameters evolution with the time of filtration: retentate side concentrations (g/l), degree of concentration and observed rejections.

CONCLUSIONS

This study is set in the plan of the contemporary environmental trends for exploring natural sources rich in valuable bioactive phenolics. In the same context lies the industrial aspect of the process, including the need to recycle, recover and reuse the solvent. The potential of the latter is investigated in an integrated extraction-nanofiltration process using an appropriate mathematical model and experimental data obtained from the extraction and nanofiltration steps with three different systems. Considerable shortening of the extraction time and reducing of the organic solvent volume is predicted, thus reducing the potential environmental pollution. The integrated process provides higher yield, shorter total processing time, favorable permeate flux. Two solutions were illustrated where the concentrations in the NF cell are maintained at a narrow variation range and/or the permeate flow does not fall below the highest (initial) value recorded for the NF concentration step.

In the first case one can rely on a constant permeate flux during the integrated process. For example, over 97% of the extractable TP was reached with system 1 under 1.7-fold reduction of the extraction time and 20% reduction of the overall processing time by combining three steps: batch extraction, integrated extraction-nanofiltration, final concentrating by NF. At the end a 3.72 fold concentrating of the TP was achieved and 74% of the solvent volume was recovered.

In the second case the integrated extraction-nanofiltration process alone led to reduced extraction time of 1 h (i. e. 2 times shorter). The total processing time including the final concentration step was 1.5 h. The appropriate choice of recirculating flow allows to reduce the range of concentration variation to some extent, the permeate flux being not constant, but also not less

than the initial one in the successive extraction – NF operation. High extraction yield is obtained, the advantages over the batch process being more pronounced for faster extraction kinetics, ex. systems 2 and 3.

In fact, the last step of concentrating by nanofiltration offers the main drawbacks, related to considerable flux decrease with increasing retentate concentrations, which also limits the achievable degree of concentration of the final product. Here the experimental observations and the model predictions including variable permeate flux and rejection can help calculating the appropriate final degree of concentration and percent of solvent recovery.

List of Symbols			R_{obs}	observed rejection (-)
A	membrane area (m²)		R_j	intrinsic rejection (-)
C	concentration in the solid (kg/m³)		$2R$	particle size (m)
C_f	feed concentration (kg/m³)		t	time (s)
			T	temperature (°C)
C_l	liquid phase concentration (kg/m³)		TMP	transmembrane pressure (bar)
C_0	initial solid phase concentration (kg/m³)		TP	total polyphenols
			TT	total tannins
c	concentration in the boundary layer of the NF cell (kg/m³)		V	volume liquid in the NF cell (m³)
C_p	permeate concentration (kg/m³)		V_p/V_f	volume permeate/feed ratio (-)
C_r	retentate concentration (kg/m³)		V_s	solid phase volume (m³)
D_{AB}	molecular diffusion coefficient (m²/s)		V_l	liquid phase volume (m³)
D_e	effective diffusion coefficient (m²/s)		$\dot{V}$	volumetric flow rate (m³/s)
J	permeate flux l/ (m² h)		v_y	permeate flux linear velocity (m/s)
k_f	external mass transfer coefficient (m/s)		y	coordinate normal to the membrane (m)
LSR	liquid/solid ratio (l/kg)		α	form factor (-)
MWCO	molecular weight cut-off (Da)		δ	boundary layer thickness (m)
NF	nanofiltration			
r	radial coordinate (m)			

REFERENCES

1. A. Oreopoulou, D. Tsimogiannis, V. Oreopoulou, in: Polyphenols in Plants, R. R. Watson (ed.), Academic Press, 2019, p 243.
2. K. Kaderides, L. Papaoikonomou, M. Serafim, A. M. Goula, *Chem. Eng. Process.*, **137**, 1 (2019).
3. R. S. Rabelo, M. T. C. Machado, J. Martínez, M. D. Hubinger, *J. Food Eng.*, **178**, 170 (2016).
4. J. A. A. Meija, G. P. Parpinello, A. Versari, A., C. Conidi, A. Cassano, *Food Bioprod. Process.*, **117**, 74 (2019).

5. G. Peev, P. Penchev, D. Peshev, G. Angelov, *Chem. Eng. Res. Des*., **89**(11), 2236 (2011).
6. I. Tsibranska, B. Tylkowski, in: Integrated membrane operations in the food production, A. Cassano, E. Drioli, (eds.), De Gruyter, 2013, p. 269.
7. C. Conidi, E. Drioli, A. Cassano, *Curr. Opin. Food Sci.,* **23**, 149 (2018).
8. B. Tylkowski, M. Nowak, I. Tsibranska, A. Trojanowska, L. Marciniak, R. Garcia Valls, T. Gumi, M. Giamberini, *Curr. Pharm. Design.,* **23**(2), 231 (2017).
9. V. Koleva, E. Simeonov, *Chem. Biochem. Eng. Q.,* **28**(4), 545 (2015).
10. B. Tylkowski, I. Tsibranska, R. Kochanov, G. Peev, M. Giamberini, *Food Bioprod. Process.,* **89**(4), 307 (2011).
11. B. Tylkowski, B. Trusheva, V. Bankova, M. Giamberini, G. Peev, A. Nikolova, *J. Memb. Sci.,* **348**(1-2), 124 (2010).
12. A. Trojanowska, I. Tsibranska, D. Dzhonova, M. Wroblewska, M. Haponska, P. Jovancic, V. Marturano, B. Tylkowski, *Chem. Eng. Res. Des.,* **147**, 378 (2019).
13. M. A. Nunes, S. Pawlowski, A. S. Costa, R. C. Alves, M. B. P. Oliveira, S. Velizarov, *Sci. Total Environ.,* **652**, 40 (2019).
14. I. Tzibranska, I. Seikova, R. Kochanov, V. Kancheva, G. Peev, in: Nanoscience & Nanotechnology, vol. 9, E. Balabanova, I. Dragieva, (eds.), BAS-NCCNT, Sofia, 2009, p. 210.
15. E. Simeonov, Z. Yaneva, C. Chilev, *Green Process. Synth.,* **7**(1), 68 (2018).
16. C. Chilev, V. Koleva, E. Simeonov, *Ind. Eng. Chem. Res.,* **53**(15), 6288 (2014).
17. I. Tsibranska, B. Tylkowski, R. Kochanov, K. Alipieva, *Food Bioprod. Process.,* **89**(4), 273 (2011).
18. I. Tsibranska, B. Tylkowski, *J. Chem. Technol. Metall.,* **51**(5), 489 (2016).
19. I. Dammak, M. A. Neves, H. Nabetani, H. Isoda, S. Sayadi, M. Nakajima, *Food Bioprod. Process.,* 94, 342 (2015).
20. A. Giacobbo, A. Moura Bernardes, M. Filipe Rosa, M., de Pinho, *Membranes,* **8**(3), 46 (2018).
21. I. Tsibranska, B. Tylkowski, *Food Bioprod. Process.,* **91**(2), 169 (2013).
22. S. Todisco, P. Tallarico, B. Gupta, *Innov. Food Sci. Emerg. Technol.,* **3**(3), 255 (2002).
23. C. Li, Y. Ma, H. Li, G. Peng, *Food Sci. Nutr.,* **7**, 1884 (2019).
24. D. Pradal, P. Vauchel, S. Decossin, P. Dhulster, K. Dimitrov, *Chem. Eng. Process.,* **127**, 83 (2018).
25. W. L. Ang, A. W. Mohammad, N. Hilal, C. P. Leo, *Desalination,* **363**, 2 (2015).
26. I. X. Cerón, R. T. L. Ng, M. El-Halwagi, C. A. Cardona, *J. Food Eng.,* **134**, 5 (2014).
27. M. Cissé, F. Vaillant, D. Pallet, M. Dornier, *Food Res. Int.,* **44**(9), 2607 (2011).
28. L. Evstatieva, *Annuaire de l'Université de Sofia "St. Kl. Ohridski" Faculté, de Biologie, Livre 2 Botanique,* **97**, 45 (2006).
29. S. Leucuta, L. Vlase, S. Gocan, L. Radu, C. Fodorea, *J. Liq. Chromatogr. Relat. Technol.* **28**(19), 3109 (2005).
30. G. Paun, E. Neagu, A. Tache, G. L. Radu, V. Parvulescu, *Chem. Biochem. Eng. Q.,* **25**(4), 453 (2011).
31. V. L. Christova-Bagdassarian, M. S. Atanassova, V. K. Hristova, M. A. Ahmad, *Int. J. Sci. Eng. Res.,* **7**(2), 1466 (2016).
32. V. L. Singleton, R. Orthofer, R. M. Lamuela-Raventós, *Method Enzymol.,* **299**, 152 (1999).
33. E. Simeonov, V. Koleva, *Chem. Biochem. Eng. Q.,* **26**(3), 249 (2012).
34. D. Marinova, F. Ribarova, M. Atanassova, *J. Univ. Chem. Technol. Metall.,* **40**(3), 255 (2005).
35. E. Simeonov, V. Koleva, G. Nedeva, *J. Univ. Chem. Technol. Metall.,* **46**(1), 41 (2011).
36. M. S. Guerrero, J. S. Torres, M. J. Nuñez, *Bioresource Technol.,* **99**(5), 1311 2008.

Extraction of biologically active compounds from Ñora pepper and their successive concentration by membrane processes

B. Tylkowski[1]*, M. Haponska[1,2], E. Aguilar Rodríguez[3], K. Fierro Troncoso[3], R. Jastrzab[2]

[1] Departament d'Enginyeria Química, Universitat Rovira i Virgili, Av. Països Catalans, 26, Campus Sescelades, 43007 Tarragona, Spain

[2] Faculty of Chemistry, Adam Mickiewicz University, Uniwersytetu Poznańskiego 8, 61-614 Poznań, Poland

[3] Departament de Química Analítica i Química Orgànica, Universitat Rovira i Virgili, Carrer Marcel·lí Domingo s/n, Campus Sescelades, 43007 Tarragona, Spain

In this study extraction of polyphenols and flavonoids from Ñora pepper, a variety of sweet pepper that is widely cultivated in Spain, was investigated. Solid-liquid extraction assisted with ultrasound was carried out using ethanol and isopropanol as a solvent. High equilibrium values of the extracted species were obtained - 52.35 mg/(g solid) total phenolics and 46.2 mg/(g solid) total flavonoids with isopropanol. Furthermore, collected extracts containing these biologically active compounds were concentrated using a cross-flow filtration process equipped with a home-made polyvinylidene fluoride (PVDF) membrane. The PVDF membrane was prepared by a phase-inversion precipitation method in a water coagulation bath set up at 60°C. Permeate flux and rejection were monitored during the filtration process.

Keywords: Ultrasound-assisted extraction, Polyphenols, Flavonoids, Ñora pepper, polyvinylidene fluoride (PVDF) membrane

INTRODUCTION

Phytochemicals are chemical compounds generated by plants that are typically involved in plant growth or in the process of protecting them from predators or pathogens [1]. They are secondary metabolites created by plants and they can be divided into the following classes: flavonoids, phenolic acids, phenyl alcohols, secoiridoids, lignans, stilbenes and glycosides, all with somewhat different activities and health benefiting effects (antioxidant, anti-inflammatory, anti-cancer, cardio-protective, antimicrobial, antifungal, chemo-preventive, cardio-protective) [2]. Flavonoids (60 %) and phenolic acids (30 %) constitute the most abundant classes of polyphenols and are characterized by a great diversity of the compounds [3–6]. Nowadays, the use of phytochemicals, especially polyphenols, as alternative anticancer drugs is a promising alternative since they diminish or suppress the adverse effects of the usually more aggressive conventional therapies [2]. The leading sources of polyphenols involve berries, grapes, olive oil, cocoa, nuts, peanuts, propolis and other fruits and vegetables, which contain up to 200–300 mg of polyphenols per 100 g of fresh weight. Furthermore, products manufactured from these fruits such as tea, wine, or beer also include polyphenols in considerable quantities [7].

Ñora pepper is a variety native to the East coast of Spain and is very popular in Mediterranean cuisine. Ñora peppers are small, round and sweet-fleshed red bell peppers. They are dried in strips and used as a spice. Thanks to their sweetness and intense aroma, they are perfect for adding flavour to casseroles and sauces.

Conventional techniques, i. e. extractions using organic solvents, have been thoroughly used to extract antioxidant compounds from plants and vegetables [8]. However, they rely on high temperatures and long incubation times, which usually lead to a low yield in antioxidant activity, while requiring a high energy input [9]. Ultrasound-assisted extraction (UAE) of polyphenols and flavonoids from plant material possesses many advantages over conventional solid–liquid extractions [6]. The use of ultrasound as pretreatment, in general, offers significant advantages in terms of improvement in the yield of biologically active compounds extraction with effects in preserving antioxidant and antimicrobial activities, reduction in the thermal degradation of compounds, reduction in time to extract the products, making the extraction cheaper and environmentally friendly. The beneficial effects of ultrasound on extraction are determined by (i) biomass fragmentation attributed to the collisions between particles and ultrasonic waves, which causes a reduction in the particle size, thereby facilitating mass transfer; (ii) erosion which helps to improve the accessibility of the solvent by imploding the bubbles on the surface of the plant matrix; (iii) sonocapillarity and sonoporation which improve the penetration of liquid through the chan-

by the bubble implosion and the alteration of the permeability of the cell membranes, respectively; (iv) the sheer stress mechanism produces the collapse of the cavitation bubble into the fluid, due to the oscillation phenomenon [6]. During the UAE process the solutes are in contact with the solvent, so the extraction efficiency is greatly influenced by the interaction time between the two phases resulting in rapid extraction rate so that up to 90% of the polyphenols can be extracted during the first 10-20 min [10]. The traditional approaches used for concentrating of biologically active compounds, extracted from natural products, involve simple steam distillation and vacuum distillation, which commonly require an increased temperature and high energy consumption [5, 11]. The former is inappropriate for heat-sensitive products. These methods may also result in a loss of compounds of low molecular weight, which can be removed together with the solvent during evaporation. Another method described in the literature, particularly for vegetable extract concentration is the lyophilization process [11]. Nevertheless, this method demonstrates some of the disadvantages of the previously mentioned processes, e. g. involves a large amount of energy, comprises incubation at about 70 °C, etc. [11, 12]. A membrane separation process can be utilized as an alternative of the approaches mentioned above. Membrane processes have received a great attention as processes with reduced operation cost, carried out at ordinary temperature. The latter is very crucial because most of the species extracted from natural products are very unstable at elevated temperatures. A possible use of the permeate as an extraction solvent allows to decrease the required rejection of the membranes [3, 5, 13]. For this reason, the aim of the present work is to investigate the amount of polyphenols and flavonoids in Ñora pepper and their possible concentration by employing a PVDF membrane.

Materials

Ñora pepper was purchased from Hacendado, Mercadona brand, Spain. Ethanol (99.2%), isopropanol (99%) and aluminium chloride anhydrous, sodium carbonate, N-methyl-2-pyrrolidone (NMP), gallic acid and quercetin, Folin–Ciocalteu's phenolic reagent were supplied by Merck. Polyvinylidene fluoride membranes (PVDF) used for polyphenols and flavonoids concentration were prepared using a phase inversion precipitation method described in [14], using Solef 6020 polymer supplied by Solvay Specialty Polymers (Bollate, Italy).

Extraction

Before the extraction processes Ñora pepper samples were first dried for 72 h in a Memmert brand oven at 40°C and then they were ground using a Braun MQ 745 Aperitif Multiquick 7 grinder. Successively, solid-liquid extractions of biologically active compounds were conducted in an ultrasonic bath Ultrasounds Selecta 3000683 (50/60 kHz, 100 W) following a protocol described in [6]. Then, the ground material was extracted with liquid–solid ratio 15:1 (ml/g) using ethanol and isopropanol, determined as optimal and kept constant throughout the experiments. The total quantity of extracted material (g extract/g dry solid) was determined gravimetrically after evaporation of the solvent. In order to control the extraction conditions, the temperature changes in the bath caused by the ultrasound were monitored with a thermometer during all UAE experiments.

TP and TF content determination

The total phenolic content (TP) was determined spectrophotometrically according to the procedure reported in [15]. A volume of 0.5 ml of Folin–Ciocalteu's reagent was added to a flask containing 0.5 ml of the sample and 10 ml of H_2O. After 5 min 8 ml of 7.5% aqueous Na_2CO_3 solution was added to the mixture. The prepared samples were kept in dark for two hours at room temperature 22 ± 2 °C and then the absorbance was measured at 765 nm with UV-1800 Shimadzu spectrophotometer (Kyoto, Japan). Three parallel measurements were performed. The results were calculated as gallic acid equivalents, using a standard curve: Abs = 2.578 × C + 0.026, R^2 = 0.982, where C [gGAE/ml]. Calibration curve was prepared using standard solution of gallic acid (0.03–0.25 mg/ml).

Total flavonoids content (TF) was determined using a spectrophotometric method based on the formation of aluminium-flavonoid complexes and calculated as quercetin equivalents, following the calibration curve: Abs = 27.555 × C + 0.089, R^2 = 0.995, where C is the concentration in µgQE/mL (concentration range 5–26 µg/mL). The following procedure was applied: 0.5 ml of $AlCl_3$ was added to 0.5 ml of diluted sample. The samples were kept in darkness for 1 hour at room temperature 22 ± 2 °C and then the absorbance was measured at 765 nm with UV-1800 Shimadzu spectrophotometer. Three parallel measurements were performed.

Preparation of PVDF membranes

PVDF membrane was prepared by an immersion precipitation method. In summary, PVDF pellets were dissolved in NMP at 80 °C, with vigorous stirring for 48 h, to form a 15 wt % homogeneous casting solution. After air bubbles were removed completely, the resulting solution was cooled to room temperature, 20 ± 2 °C, and spread uniformly onto a glass plate with a non-woven support (15 cm × 20 cm) attached, using a casting knife with a 250-µm gate opening (K Paint Applicator, R K Print Coat Instruments, Ltd., Litlington, UK) and the coating speed set up at 2 m/min. The membrane was immediately immersed (approximately 10 s after coating) into a precipitation bath of deionized water (DW, 3 L) set up at 60 ± 2 °C. Next, the formed solid membrane was thoroughly washed with deionized water to remove residual NMP and dried at about 40 °C for 24 h under vacuum before further application.

Membrane filtration

Concentration of extracted polyphenols and flavonoids was carried out using a self-made stainless steel cross-flow filtration apparatus containing a disk membrane module applying a filtration protocol described in [16]. The effective membrane area in the module was 12.6 cm². Figure 1 provides the scheme of the cross-flow filtration equipment. The extract (feed) to the filtration cells was supplied by a piston pump and damped by a pulsation dampener before the membrane cell. During the experiments, the temperature of feed/retentate and permeate, as well as pressure in the membrane cells were controlled and kept constant (22 ± 2 °C, and 5 bar) during all experiments.
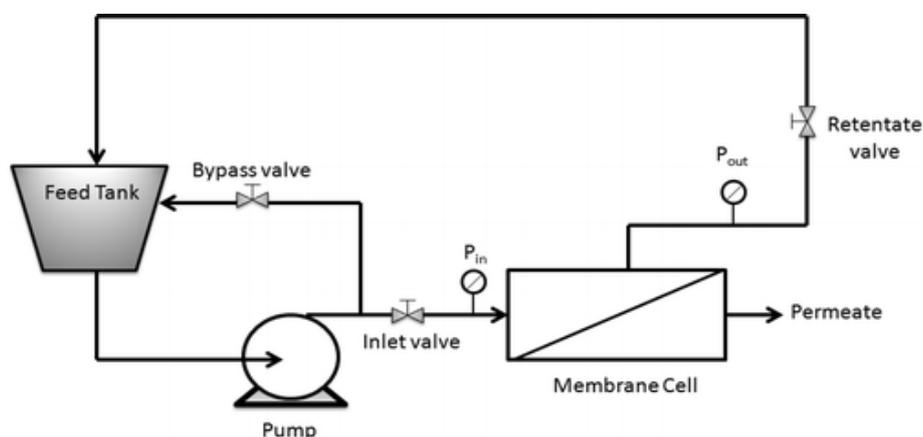
Figure 1. Flow diagram of the cross-flow filtration apparatus.

The flux and rejection experiments were performed using the following procedure: after the initial insertion of the membrane films in the cells, the plant was run first for 15 min without feed pressure in order to condition the system and, hence, for 15 min with a feed pressure of 5 bar, to reach a steady-state permeate flux and to complete the initial membrane compaction. As far as experiments at a pressure of 5 bar are concerned, whenever the solution in the feed tank was changed, the entire apparatus was washed three times with the new solvent before continuing the experiments. In addition, the system was run with a feed pressure of 5 bar for at least 15 min in order to facilitate the removal of the former solvent. Then, compaction at 5 bar feed pressure was done again until steady-state conditions were reached. Membrane performance was assessed on the basis of the solvent flux and rejection experiments. The flux (J) through the membrane can be described by the following equation:

$$J = \left(\frac{V}{A * \Delta t}\right)$$

where V is the permeate volume, A is the membrane area, and Δt is the permeation time. The biologically active compounds rejection rate was calculated using the following equation:

$$R = \frac{Cf - Cp}{Cf} * 100\%$$

where Cp and Cf (mg/mL) are the concentrations of permeate and feed solutions, respectively. The cross-section morphology of the PVDF membrane and the particle size of ground Ñora pepper were characterized by environmental scanning electron microscopy [ESEM (Quanta 600, FEI)] [17, 18]. The cross-sections of the membranes were prepared by fracturing the membranes in liquid nitrogen. The details of this method can be found elsewhere. The real thickness of the membranes (10 measures) and the diameter of the Ñora pepper on the membrane

surfaces (30 measures) were calculated using Image-ProPlus 5® software and the ESEM micrographs.

RESULTS AND DISCUSSION

Figure 2a shows an illustration of the Ñora pepper pieces before extractions, while Figure 2b shows the same sample after 1 h of extraction carried out with ethanol in ultrasound bath.
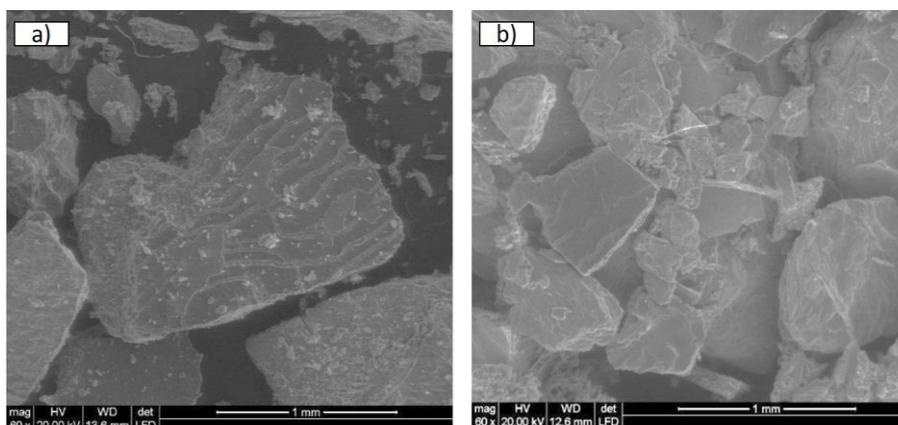
Figure 2. ESEM micrographs of Ñora pepper ground pieces before (a) and after (b) 1 h of ultrasound-assisted extraction with ethanol.

By means of Image-ProPlus 5® software, we analyzed the ESEM micrographs and we found that the pieces used for extraction had diameter fluctuating between 500 μm and 600 μm, while after extraction their size decreased and was in a range of 50 -150 μm. The maximum absolute error of these measurements was 2 μm. It is well known that ultrasound technique helps in the disruption of plant cell walls, improving the solvent permeation and enhancing mass transport across the cell membrane, which leads to higher extract yields. In our opinion, these advantages of using ultrasound energy for extraction not only include more effective mixing and micro-mixing but also could have a significant influence on the mechanical properties of the plant material. The decrease of the particle size and appearance of new small pieces suggest that the ultrasound makes the plant material more fragile and breakable. Indeed, Petigny and co-authors reported that after 2 h of ultrasound-assisted extraction of boldo leaves, the sample was heavily damaged [19]. As we reported in the previous paper, increased temperature of extraction positively affects solubility and enhances the mass transfer both to and into the solid, thus leading to faster kinetics and higher amounts extracted [6]. Ultrasound-assisted extraction experiments were performed in a Selecta 3000683 bath for 1 h. During the experiments the temperature of the ultrasound bath increased from 25 ±2 °C up to 60 ±2 °C. The obtained yield of extrac-

tion with ethanol as solvent was 0.0456 g/(g dry solid) while with isopropanol it was by 16% higher. Moreover, 52.36 mg/g of solid for total polyphenols and 46.2 mg/g solid for total flavonoids were achieved during extraction with isopropanol while with ethanol 45.3 mg/g of solid for total polyphenols and 20.7 mg/g solid for total flavonoids were collected. El-Malah *et al.* also reported that extraction performed with isopropanol provides a higher amount of biologically active compounds than that carried out with ethanol as a solvent [20].

In order to concentrate the extracted biologically active compounds we decided to apply the previously investigated PVDF membrane the surface of which is mainly formed by a mixture of TGTG' chains in α phase crystalline domains. This membrane was deeply investigated and reported in [14].

Figure 3 shows the ESEM image of cross-section morphology of the PVDF membrane. From the micrograph can be observed that the selected membrane possesses a compact structure. Moreover, based on the ESEM images, we were able to measure the membrane thickness by means of Image-ProPlus 5® software. The thickness of the employed membrane for TP and TF concentration was 106 ±2 μm. In order to evaluate the rejection of TP and TF extracted from Ñora pepper, their concentrations in the feed and permeate were analyzed. The results are given in Table 1.

B. Tylkowski et al.: Extraction of biologically active compounds from Ñora pepper and their successive ...

Table 1. Content of biologically active compounds in the investigated extracts

	TP content in ethanol solution*(µg/ml)	TP content in isopropanol solution* (µg/ml)	TF content in ethanol solution** (µg/ml)	TF content in ethanol solution** (µg/ml)
Feed	3.02 ± 0.02	1.38 ± 0.01	3.49 ± 0.01	3.08 ± 0.01
Permeate	1.41± 0.02	0.72 ± 0.01	1.16 ± 0.02	1.34 ± 0.02

*TP expressed as the gallic acid equivalent; **TF expressed as the quercetin equivalent.
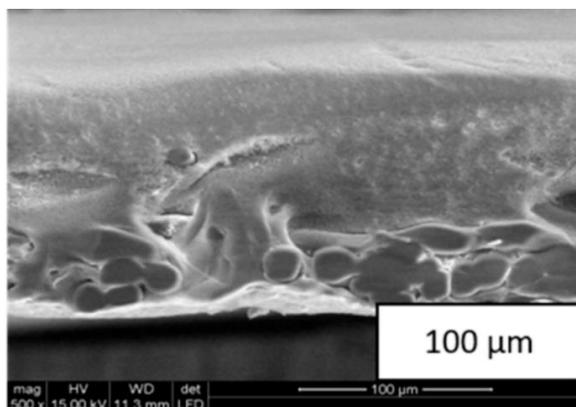
Figure 3. ESEM micrographs of the cross-section of PVDF membrane

Obtained results indicate that only 53% of TP and 48% of TF dissolved in ethanol were rejected by the PVDF membrane. Better results were achieved with isopropanol: 67% of TP and 56% of TF. Permeability flux through the polymeric membrane is strongly influenced by the structures and properties of the solvents. It has been reported that the membrane–solvent interactions can be expected to vary depending on the solvent properties, such as viscosity, dielectric constant, molecular size, dipole moment, solubility parameter, and surface tension [21]. Comparing the flux values for the extracts with isopropanol and ethanol, it can be observed that the flux of ethanol (36 L/m^2×h) with solvent relative polarity of 0.654 is higher than that of the less polar isopropanol (26 L/m^2×h) with solvent relative polarity of 0.546. Moreover, it has been reported that the flux values decrease with increasing molecular length, i. e., by lengthening the alcohol structure with additional CH$_2$ groups, irrespective of the transport mechanism.

CONCLUSIONS

Ultrasound-assisted extraction of biologically active compounds from Ñora pepper was performed. Obtained results indicated that higher amounts of polyphenols and flavonoids were extracted with isopropanol than with ethanol. PVDF membrane with a thickness of 106 µm were obtained by the phase inversion precipitation method at 60° C. By applying this membrane in a cross-flow filtration apparatus we were able to concentrate the BACs.

REFERENCES

1. O. S. Arvaniti, Y. Samaras, G. Gatidou, N. S. Thomaidis, A. S. Stasinakis, *Food Res. Int.* **119,** 244 (2019).
2. X. Montané, O. Kowalczyk, B. Reig-Vano, A. Bajek, K. Roszkowski, R. Tomczyk, W. Pawliszak, M. Giamberini, A. Mocek-Płóciniak, B. Tylkowski, *Molecules*, **25,** 3342 (2020).
3. B. Tylkowski, I. Tsibranska, R. Kochanov, G. Peev, M. Giamberini, *Food Bioprod. Process.,* **89** 307 (2011).
4. B. Tylkowski, I. Tsibranska, Physical Sciences Reviews, Volume 2: Issue 6, 2017.*
5. .H. Tsibranska, B. Tylkowski, *Food Bioprod. Process.*, **91,** 579 (2013).
6. A. Trojanowska, I. Tsibranska, D. Dzhonova, M. Wroblewska, M. Haponska, P. Jovancic, V. Marturano, B. Tylkowski, *Chem. Eng. Res. Des.*, **147,** 378 (2019).
7. K. B. Pandey, S. I. Rizvi, *Oxid. Med. Cell. Longev.* **2,** 270 (2009).
8. I. Tsibranska, B. Tylkowski, *J. Chem. Technol. Metall.*, **51**, 489 (2016).
9. I. Cabezudo, M.-R. Meini, C. C. Di Ponte, N. Melnichuk, C. E. Boschetti, D. Romanini, *Food Chem.*, **338,** 128131 (2020).
10. A. Nayak, B. Bhushan, A. Rosales, L. R. Turienzo, J. L. Cortina, *Food Bioprod. Process.,* **109,** 74 (2018).
11. B. Tylkowski, B. Trusheva, V. Bankova, M. Giamberini, G. Peev, A. Nikolova, *J. Membr. Sci.*, **348,** 124 (2010).
12. I. Gülçin, E. Bursal, M. H. Şehitoĝlu, M. Bilsel, A. C. Gören, *Food Chem. Toxicol.*, **48,** 2227 (2010).
13. B. Tylkowski, M. Nowak, I. Tsibranska, A. Trojanowska, Ł. Marciniak, R. G. Valls, T. Gumi, M. Giamberini, R. Jastrz̨ab, *Curr. Pharm. Des.*, **23,** 231 (2017).
14. M. Haponska, A. Trojanowska, A. Nogalska, R. Jastrzab, T. Gumi, B. Tylkowski, *Polymers (Basel,* **9,** 718 (2017).
15. M. Ammendola, M. Haponska, K. Balik, P. Modrakowska, K. Matulewicz, L. Kazmierski, A. Lis, J. Kozlowska, R. Garcia-Valls, M. Giamberini,

A. Bajek, B. Tylkowski, *Sci. Rep*., **10,** 1 (2020).

16. B. Tylkowski, F. Carosio, J. Castañeda, J. Alongi, R. García-Valls, G. Malucelli, M. Giamberini, *Ind. Eng. Chem. Res*., **52,** 14606 (2013).

17. B. Tylkowski, I. Tsibranska, *J. Chem. Technol. Metall.,* **50,** 3 (2015).

18. B. Tylkowski, M. Giamberini, T. Underiner, S.F. Prieto, J. Smets, *Macromol. Symp*., 360 (2016).

19. L. Petigny, S. Périno-Issartier, J. Wajsman, F. Chemat, *Int. J. Mol. Sci.*, **14,** 5750 (2013).

20. M. H. El-Malah, M. M. M. Hassanein, M. H. Areif, E. F. Al-Amrousi, *Am. J. Food Technol.*, **10,** 14 (2015).

21. I. Tsibranska, B. Tylkowski, Concentration of polyphenols by integrated membrane operations, In: Cassano A, Drioli E, editors. Integrated membrane operations in the food production. De Gruyter, 2014:269–294.

Organic solvent nanofiltration of extracts from *Hypericum Perforatum L.*: effect of variable feed composition on rejection and flux decline

I. Saykova[1]*, I. Trayanov[1,2] M. Bojkova[1], N. Stoilova[3], M. Funeva-Peycheva[3]

[1]*Department of Chemical Engineering, Faculty of Chemical and System Engineering, University of Chemical Technology and Metallurgy, Sofia, Bulgaria*
[2]*Institute of Chemical Engineering, Bulgarian Academy of Sciences, Sofia, Bulgaria*
[3]*Central Laboratory for Veterinary-Sanitary Expertise and Ecology, Sofia, Bulgaria*

The medicinal plant *Hipericum Perforatum* is traditionally used as a herbal remedy and food supplement because of its versatile bioactive properties, in particular the anxiolytic and antidepressant activities. The extraction and separation of the specific active compounds hypericins is still problematic because of their very low and variable content (standardized to 0.3% in the extract), poor solubility in water, and extreme sensitivity to light, pH, and heat. In this context, this work evaluates the potentiality of using a direct nanofiltration process to promote the enrichment of extracts in hypericins relatively to other largely present compounds as polyphenol and flavonoids. By using ethanolic extracts obtained by different methods and different raw materials, the effect of variation in feed composition on permeate flux, concentration and content of effective components were investigated in dead-end mode at a fixed pressure (5-20 bar) and stirring speed (350 rpm). The set of the four commercial flat-sheet membranes (DuraMem™ 200, 500, and 900 and StarMem™240) displayed very distinct permeation patterns in terms of rejections and fluxes. Hermia's fouling models were considered to explain the flux decline and fouling phenomena during concentration of extracts. According to the experiments, the membrane with a larger pore size (900 Da) had the highest average flux of 26.5 $Lm^{-2}h^{-1}$ and a higher propensity to fouling. The membrane with a lower cut-off (200 Da) having rejections above 95%, could be selected for concentration of the extracts, but also some other high-value small molecules, such as gamma aminobutyric acid (GABA) identified and quantified, using HPLC/MS, can be simultaneously recovered only in the permeate stream with 200 Da membrane.

Keywords: nanofiltration, *Hipericum Perforatum,* extract enrichment

INTRODUCTION

Considering the increased recognition of health benefits of plant extracts and their utilization in the food, pharmaceutical and cosmetic industries, it is of interest investigating into efficient and cost-effective separation processes for better control of the properties of the final products [1]. Nowadays, membrane-based technologies, e.g. microfiltration (MF), ultrafiltration (UF), nanofiltration (NF), membrane distillation, and pervaporation, have demonstrated meeting the requirements and are involved in different food and byproduct processes owing to the technology's advantages as high selectivity, mild processing conditions, and low energy consumption over other (in many cases thermally driven) separation processes. Polymer membranes, as well the newer class of organic solvent-resistant NF membranes (100-1000 Da) and tight UF membranes (1-3 kDa) and their combinations have been recognized for their capability to recover valuable compounds from various natural and processed products [2-4]. Several successful OSN applications have been reported for increasing the concentration of dilute species from lower molecular-weight solvents, and providing recycling of organic solvents, recovery of aromas, fractionation of bioactive compounds as phenolic compounds and other antioxidants, as the most popular ones.

Fouling represents a real limitation in any membrane separation, but for NF it might be even more complex because of the interactions between membrane-solvent-solutes taking place at nanoscale and being difficult to understand and to predict [5]. Membrane fouling is a complex multi-scale (occurring both on the membrane surface and in the membrane pores) and multi-physical phenomenon depending on many inter-related factors, including the operating conditions, membrane properties and feed characteristics. Membrane fouling formed during treatment of plant extracts could be especially prevalent as often more than 80% of the components present in the extracts are non-active macromolecules that can easily block the membrane pores. Regarding the therapeutic effect, typically the whole herbal extracts are considered as active compounds because of the synergy among the various secondary and primary metabolites, so their

---

* To whom all correspondence should be sent:
E-mail: i.seikova@uctm.edu

preservation and as minor as possible change in their properties during processing is very important.

The objectives of this work are to evaluate the combination of extraction followed by Organic Solvent Nanofiltration (OSN) for the concentration of ethanolic (96%) extracts from *Hypericum perforatum* and to provide a prediction of the fouling mechanisms responsible for the flux decline involved in dead-end mode.

EXPERIMENTAL

Solvent extraction and analysis

The plant extracts were prepared by using commercial samples of fractionated and non-fractionated dry material. Batch solid-liquid extraction was carried out at room temperature 20±2°C, liquid-to-solid ratio of 10 ml liquid/g solid, for 120 min under shaking, using 96% ethanol as solvent. Three different extracts were prepared, using the fraction of 1.25 mm (E1), non-fractionated material (E2), and the fraction of 0.9 mm (E3). To quantify the content of extractable compounds present in the plant, the extraction was carried out repeatedly with fresh solvent, until there were no significant differences from additional extractions (minimum 3 steps). The extracts were filtered through 0.2 μm PVDF syringe filters for removing suspended solids.

Plant extracts and OSN products (retantate, permeate, washing solutions) were characterized using standard spectrometric procedures with subsequent confirmation by HPLC/MS identification and quantification of some key components. The total hypericins content (THC) was measured by direct UV-Vis analysis at 590 nm. The total phenolic content (TPC) was determined colorimetrically according to the Folin-Ciocalteu method, and expressed as mg gallic acid equivalent (mg GAE g^{-1} plant material). The content of flavonoids was determined by the aluminium chloride method and expressed as mg quercetin equivalent (mg QE g^{-1}). The total solids content (TSC) was obtained by drying in an oven at $70 \pm 1°C$ until constant weight.

Dead-end filtration experiments

Nanofiltration trials were carried out in a stirred dead-end cell (METCell, Membrane Extraction Technology, UK) with an effective membrane area of 54 cm². The cell was operated at a constant transmembrane pressure (TMP) up to 40 bar, regulated with high purity nitrogen gas, and stirred at 350 rpm by a magnetic stirrer plate. Four flat sheet OSN membranes from Evonik MET Ltd. with different molecular weight cut-off (MWCO), made of different materials, were used in this study (Table 1).

Table 1. OSN membranes employed and their characteristics (manufacturer's data)[b]

Membrane	M_w g mol^{-1}	Membrane type and material	Pressure bar	Nature	δ_{HSP}[c] MPa$^{1/2}$
StarMem™ 240	400[a]	Polyimide-based top layer (pore size <5 nm)	20	Hydrophobic	23.2
DuraMem™ series	200[b] 500[b] 900[b]	Crosslinked polyamide	20 20 5-10	Amphiphilic	26.8

[a] based on rejection of n-alkanes in toluene; [b] based on rejection of styrene oligomers in acetone; [c] total Hansen solubility parameter

The membrane conditioning was performed following the guidelines provided by the suppliers [5]. After filtration, the membrane was rinsed with ethanol, and the pure solvent was permeated at the operating pressure. All filtration experiments were conducted at room temperature, using a volume reduction factor (VRF) up to 6. The permeate volume was recorded at regular time intervals, and the volumetric flux was calculated according to:

$$J_v = \frac{1}{A} \frac{dV_p}{dt} \qquad (1)$$

where V_p is the volume of permeate (L) collected in a certain time t (h) through the membrane filtration area A (m²). The evolution of flux *vs* time was fitted

by polynomial equation of second or third order and the average permeate flux was calculated by integration of J(t) function:

$$<J> = \frac{1}{t_n} \int_{t_1}^{t_n} J(t)dt \qquad (2)$$

The observed rejection values (R_i) for a specific component group were defined as:

$$R_i(\%) = \left(1 - \frac{C_{p,i}}{C_{f,i}}\right) \cdot 100 \qquad (3)$$

where $C_{f,i}$ and $C_{p,i}$ denote the feed and permeate (averaged over the time) concentration.

Fouling modeling

The mathematical analysis of the permeate flux behavior was performed based on Hermia's model that is a common approach employed in microfiltration, ultrafiltration and reverse osmosis to nanofiltration systems as well [7, 8]. The governing equation associates the "rate of blocking" of the membrane (d^2t/dV^2) with the instantaneous resistance (reciprocal of the flux rate dt/dV):

$$\frac{d^2t}{dV^2} = K\left(\frac{dt}{dV}\right)^n \qquad (4)$$

where K is a rate constant and n is the blocking index equal to 2, 1.5, 1 or 0 for complete pore blocking, standard pore blocking, intermediate pore blocking and cake filtration, respectively.

On the basis of many studies on membrane fouling, it was determined that these mechanisms may occur individually or in some cases the relative importance of individual mechanisms can change with time. Many researchers have derived combined models such as the cake-complete blocking, cake-intermediate blocking, cake-standard blocking, and others, for the more complete coverage of fouling stages and the more realistic handling of complex fouling caused by multiple foulants [9, 10].

Table 2. Blocking models during constant-pressure dead-end operation

Model	V/A=f(t)	Physical concept
Cake layer formation (CLM)	$\frac{V}{A} = \frac{1}{K_{CL}J_0}\sqrt{1+2K_{CL}J_0^2 t} - 1)$	$d_{solute} \gg d_{pore}$
Intermediate blocking (IBM)	$\frac{V}{A} = \frac{J_0}{K_{IB}}\ln(1+K_{IB}\cdot t)$	$d_{solute} \approx d_{pore}$
Standard blocking (SBM)	$\frac{V}{A} = t\,(\frac{K_{SB}}{2} + \frac{1}{J_0})^{-1}$	$d_{solute} \ll d_{pore}$
Complete blocking (CBM)	$\frac{V}{A} = \frac{J_0}{K_{CB}}(1-\exp^{-K_{CB}\cdot t})$	$d_{solute} \approx d_{pore}$
Complete blocking - Cake layer (Combined)	$\frac{V}{A} = \frac{J_0}{K_B}(1-\exp(\frac{-K_B}{K_C J_0^2}\sqrt{1+2K_c J_0^2 t} - 1)))$	Loss of active area plus rise in cake resistance

Table 2 presents the analytical expressions for the kinetic models used. More precisely, the relation between the cumulative permeate volume per unit area (V/A) and the filtration time (t) is considered, where J_0 is the initial permeate flux and K is the constant with the subscript indicating the blocking mechanism.

RESULTS AND DISCUSSION

Membrane selection

Hypericum perforatum is one of the most widely used and researched medicinal plants, and to date, at least 900 molecules with unique structure have been isolated and characterized [11]. Most relevant for the pharmacological activity are the characteristic naphthodianthrone pigments (hypericin, pseudohypericin) and the phloroglucinols (hyperforin, adhyperforin), along with the more common flavonoids, as glycosides of quercetin-like hyperoside, rutin, isoquercitrin, quercitrin, various flavonols; phenolic acids, oligomeric procyanidins, and tannins, among others.

The choice of a suitable membrane is mainly governed by the MWCO characteristics of the membranes, taking into account the size of the organic molecules relative to the membrane pore size, and the intended use. It is well accepted that the value of nominal MWCO provided by the manufacturer is an initial indication of the membrane operating range since it is dependent on the solvent-solute system used for testing. For polymeric membranes, the solvent used can interact with the membrane, resulting in compaction, solvation and differential swelling with enough impact to significantly alter separation/ fractionation properties in some systems [5].

Table 3 gives the range of variation of several physico-chemical properties of secondary metabolites of the plant affecting the transport across the membrane. In order to better account for the molecular size instead of its weight, the Stokes diameter (d_s) and diffusion coefficients (D_0) were calculated by using the Stokes-Einstein equation. Hansen solubility parameters (δ_{HSP}), including dispersion, polar and hydrogen bonding forces, that have proved to be a good first estimate for selecting membrane materials for specific organic-organic separations, were also calculated using group contribution methods [12].

Table 3. Physicochemical characteristics of the main constituents of *Hypericum perforatum*

Chemical class	Molar mass gmol^{-1}	d_s nm	D_0 10^{-9} m^{2}s^{-1}	Nature	δ_{HSP} MPa$^{1/2}$
Hypericins	504-522	0.9-1.0	2.2-2.1	Amphiphilic	42-42.8
Flavonoids	286-610	0.7-1.1	2.8-2.0	Lipophilic/hydrophilic	34-35.3
Phenolic acids	200- 578	0.6-1.0	3.3-2.1	Hydrophilic	17-32.6
Procyanidins	500-3000	0.9-2.2	2.2-1.1	Hydrophilic	25-33.2
Ethanol			1.58	Protic-polar	26.5
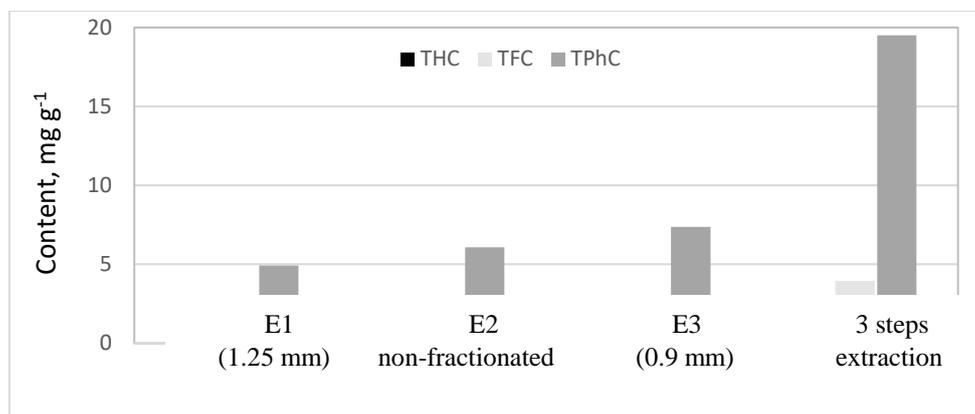
Figure 1. Contents of total hypericins (THC), flavonoids (TFC) and phenolics (TPC) in the feed extracts

Because of a broad size distribution (as seen in most natural extracts), *Hypericum perforatum* has both small molecules with high diffusivities and bigger molecules with low diffusivities. Most of the secondary metabolites, however, are low- to moderate-size species that correspond to an equivalent of Stokes diameter up to 1 nm. OSN membranes can reject molecules within the range 100-1000 Da, a reason why they could be used in concentrating natural extracts obtained with organic solvents. Given the reported amphiphilic character of DuraMem™ series (δ_{HSP}=26.8 MPa$^{1/2}$) and hydrophobic for StarMem™240 (δ_{HSP}=26.8 MPa$^{1/2}$), some specific interactions with the solvents and solutes would be expected [5, 6]. Taking these points into account, several OSN membranes were tested, covering almost the whole NF range, and the choice of membrane was based on the requirement of high rejection and minimum losses in the permeate for the key secondary metabolites.

Membrane performance under different process conditions

The content of classes of substances obtained by different extraction procedures, both one-step and sequential, are given in Fig. 1. They present high levels of polyphenols (up to 7.37 mg GAEg^{-1}), less amounts of flavonoids (up to 1.47 mg QE g^{-1}) and comparatively very low contents of hypericins (up to 0.15 mg HYPg^{-1}). In spite of using 96% ethanol instead of ethanol-water mixtures and low temperature of 20°C, yet significant TSC were obtained, varying between 0.05 and 0.1 g g^{-1}. The extraction yields after the single extraction were only 20-30% of the exhaustive 3-step extraction values used as a reference. The extraction from the fraction with low particle size (E3) allowed more complete recovery of all soluble compounds but the relative proportions of the minor THC and TFC in relation to the to TPC and TSC decreased.

A summary of the average permeate fluxes and rejections for the key compounds and total soluble solids is presented in Table 4. The values of pure solvent flux before ($J_{s,in}$) and after the extract filtration ($J_{s,f}$) are also presented.

Results demonstrate considerable variations in permeability, extending up to a factor over 45 for pure solvent (0.55 - 24.8 Lm^{-2}bar^{-1}h^{-1}) and 2-3 for feed extracts (0.11-0.96 Lm^{-2}bar^{-1}h^{-1}). No recovery of ethanol permeability was obtained after the physical cleaning performed, for all membranes. The rejection of particular fractions was revealed to depend on the used membrane and feed characteristics to much lower extent, all membranes having rejections of at least 80%, in addition to a high pigment retention capacity. These results are consistent with those of several studies that also reported retention from > 85 up to 100% for the concentration of phenolic compounds from the hydroethanolic extracts with the same membranes providing permeate fluxes in the same low range [1-4].

Table 4. Permeate fluxes and rejection values during OSN

Membrane	Extract	Fluxes, L.m^{-2}h^{-1}			Rejection, %			
		$J_{s,in}$	$< J >$	$J_{s,f}$	TSC	THC	TPC	TFC
DuraMem^{TM}900	E2	124.1	4.8	3.3	86.3	> 99	86.5	89.4
DuraMem^{TM}500	E1	11.2	4.4	4.3	94.3	> 99	91.2	93.9
	E2		2.4	3.5	95.1	> 99	94.1	97.7
	E3		1.7	2.1	91.2	> 99	95.3	93.1
StarMem^{TM}240	E1	30.1	6.5	8.1	86.1	> 99	84.4	90.8
	E2		4.9	6.3	85.2	> 99	83.3	84.9
DuraMem^{TM}200	E1	11	6.5	8.4	96.7	> 99	97.9	98.1

Nevertheless, the membrane with apparent cut-off of 900 Da has distinguished itself by providing a very high ethanol flux and permeating more solutes. That is, the retentions varied between 86% and 100%, more than 10% of TSC being found in the permeate. The membrane StarMem^{TM}240, also showing a large flux decline, presented comparable rejections (83-100%) to that of DuraMem^{TM}900 and lower ones compared to DuraMem^{TM}500, in spite of having a lower nominal cut-off of 400 Da. The disparities observed cannot be explained simply by the differences of ethanol permeability and initial cut-off of the membranes. In this case, the dead-end operation probably misrepresented the selectivity that could be expected. The ingredients in the neighborhood of the membrane carried by the high initial flux toward the membrane surface, probably blocked highly permeable outer membrane pores, causing a change in nominal MWCOs.

For the DuraMem^{TM}500 the rejections remained at high levels of 90-95%, without sensible losses in the permeate, but this was at the expense of lower permeate flux. The modification of the initial feed concentration resulted in a slight tendency to increase or decrease in rejection of solutes - the 2.5-fold increase in feed TSC reduced by approximately 5% the rejection of hypericins and up to 35% the permeate flux.

The DuraMem^{TM}200 showed the best efficiency for concentrating the extracts combined with sufficient fluxes and degree of recovery of permeability. The small amount of the permeating molecules was confirmed by the high rejection of total extract (~ 97%). Spectrophotometrically analyzed hypericins consistently showed almost complete rejection (> 99%), though the HPLC/MS detected some traces in the permeate, advisable for the lack of high sensitivity of a spectrophotometer at low-level concentrations (data not shown). Still it is interesting to note that some other valuable compounds were detected, as gamma-aminobutyric acid (GABA, 103.12 gmol^{-1}) that plays a role in regulating neuronal excitability in the brain.

Basically, the rejection towards the analyzed compounds decreased by decreasing the MWCOs of the membranes of the same type, and agreed with the size exclusion mechanism. However, despite the high rejection values, the concentration factor obtained for TPC and TFC was lower than the VRF used. This behavior may have been observed due to the establishment of fouling.

Modeling of permeate flux decline

Membrane fouling was characterized by the permeation curves, i.e. cumulative permeate volume per membrane area *versus* time V/A=f(t) in order to discriminate low-fouling conditions (slow-rate reduction) where the intrinsic membrane resistance is predominant and there are strong-fouling conditions with additional resistance to the filtration. The experimental data were fitted using the selected models (Table 2) and examples of curve-fits with the parameters identified after non-linear regression are presented in Figs. 2 and 3.

To address the impact of the membrane structure and properties, the flux decline through the membranes StarMem^{TM}240 and DuraMem^{TM}500 was compared during the treatment of extract E3 (Fig. 2). While the soluble solids increased from 1 to about 2 g L^{-1}, the fluxes decreased by 70% at very different rates. The experiments were carried out at the same TPM (20 bar) and not at the same initial flux. For the StarMem^{TM}240 (starting with high $J_{s,in}$ of 30 Lm^{-2}h^{-1}) the flux decreased very fast (0.6 h) while for the DuraMem^{TM}500 the flux gradually decreased, comparable reduction of the $J_{s,in}$ (11 L m^{-2}h^{-1}) was obtained after 6 hours of operation.

The analysis of Fig. 2 indicates that the combined pore blocking/cake formation model, having 3 fitting parameters (J_0, K_b, K_c) instead of 2 (J_0, K) for the classic models, had the best fits (R^2 > 0.95) to the non-linear increase of V/A for both membranes over the entire permeation run. There is a time interval in which the three kinetic models describing the surface fouling (complete, intermediate blocking and cake layer) also provided good data fits; the gap widens for longer durations.
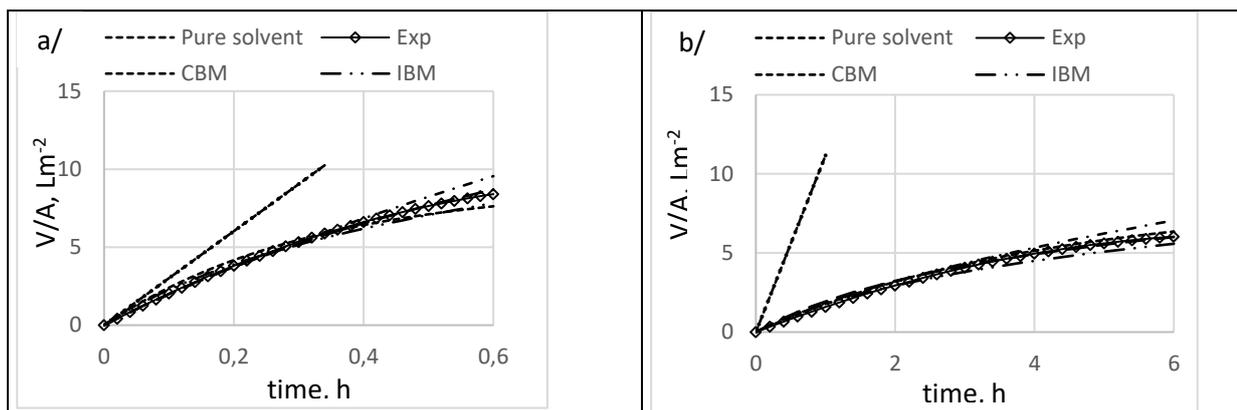
Figure 2. Experimental and calculated evolution of permeate volume *vs* time for the StarMem™240 (a) and DuraMem™500 (b) membranes in the presence of strong flux decline (extract E3; 20 bar)
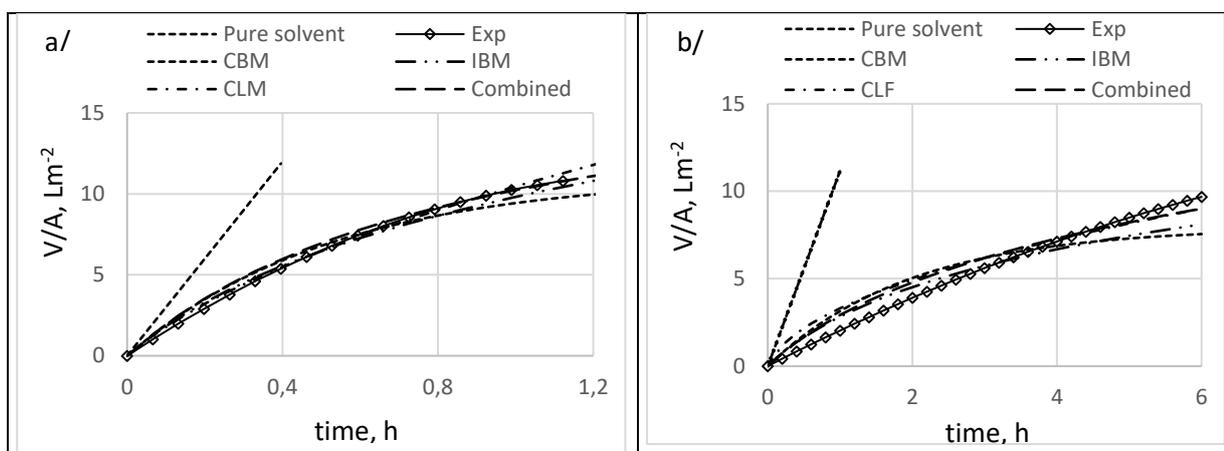
Figure 3. Fouling analysis for the StarMem™240 (a) and DuraMem™500 (b) membranes in the presence of slow flux decline (extract E1; 20 bar)

Given the polydispersity in solute size distribution and pore sizes of the membrane, at this early stage several pore-blocking mechanisms may take place simultaneously, producing a synergistic effect, followed by a transition to the cake layer at the latter stages [8, 10].

The higher values for the kinetic coefficients identified for the StarMem™240 compared to the DuraMem™500 specify a greater fouling tendency. The hydrophobic Starmem™240, not cross-linked, characterized by a small difference between the HSP values (Table 1 and 3) for ethanol and for polymer ($\Delta\delta_{HSP} \approx 3.3$ MPa$^{1/2}$), would have higher degree of swelling and behave elastically under pressure [5]. Consequently, the pore size enlargement may cause an increase in the initial fluxes and a negative effect on the rejection, as observed in the present study (Table 4). On the other side, the higher rejection and lower flux of DuraMem™500 can be attributed to its cross-linking rather to its slightly higher hydrophilicity, giving them a superior stability when exposed to ethanol solution.

The combined effects of the three hypothesized mechanisms: solute adsorption, hindered back

diffusion, and increased resistance of the fouling layer can explain not only the increase of the total resistance to the permeation but also the variation in the separation efficiency. According to *Cassano et al.*, polyphenols have been shown to be the predominant cause of adsorptive fouling in the initial stage owing to the ability to form larger aggregates or complexes with other ingredients [13]. Consequently, the back-diffusion of smaller solutes is hindered and they can be also retained forming a variable cake layer. In this study, this was confirmed by analysis of the washing solvent after desorption of the fouled surface; phenolic compounds were predominant in the fouling layer, followed by hypericins and flavonoids, respectively, 22% TPC, 18% THC, and 10% TFC of the feed extract.

According to the results obtained, the process operating at lower TSC or VRF was less liable to be fouled. Fig. 3 shows the analysis during treatment of the extract E1 where the contents of TFC and TSC are by nearly 70% lower than in E3.].

For both membranes, there was again a quite rapid flux reduction at the beginning of the operation. A slow-rate reduction in the first 1.2 h was

observed for the StarMem™240 while no obvious flux decline was observed for the DuraMem™500 where the relation V/A=f(t) starts to deviate from linearity after 6 h. The low values obtained for the kinetic parameters incapable of satisfactory fits to the experimental data would reflect that there was a small development of the pore blocking and cake layer, the concentration by polarization was a major contributor to the observed flux decline. Apparently, in these favorable conditions, larger solutes tend to be swept away in the bulk volume rather than deposited; a loose reversible layer formed (concentration polarization) prevented initial pore blockage, so the transition to an irreversible packed structure (gel or deposit layer) could occur at the latter stages under severe concentration polarization.

At this point of the process, the main resistance can be reversible, so that the process had to be stopped for cleaning, before strong irreversible fouling happens. In fact, after the interruption of process and intermediate rinsing of the DuraMem™200 membrane, it was possible to further concentrate the E1 extracts and to reach contents for minor compounds hypericins comparable to that in the 3 steps sequential extraction. The dry solids content in the permeate was sufficiently low to permit direct reuse as extracting agent or washing solvent.

CONCLUSION

Among the membranes tested, all of them showed equally good high rejection towards hypericins, but the natural ratio hypericins: polyphenols: flavanoids is important for the biological susceptibility (of humans, bacteria and other plants), so the membrane with the highest rejection DuraMem™200 is predominantly preferred. Meanwhile the MWCO value does not play an important role, because the non-crosslinked StarMem™240 has much smaller rejections than the crosslinked DuraMem series even than the DuraMem™900 with the largest cut-off. DuraMem™200 membrane appeared to be suitable for the concentration of ethanolic extracts from *Hypericum perforatum*, but with relatively low permeance of 0.33 $Lm^{-2}bar^{-1}h^{-1}$, requiring frequent cleaning. Optimizing solid-liquid extraction by using emerging and more efficient techniques regarding extraction time, type and amount of solvent, and desorption kinetics, could help to reduce the flux decline and to make the combination of extraction and membrane processing more competitive.

REFERENCES

1. V. M. de Moraes, R. Rabelo, A. de L. Pereira, M. Hubinger, *Clean. Prod.,* **174** (2018).
2. R. Castro-Muñoz, V. l Fíla, *Trends Food Sci. Technol.*, **82**, 8 (2018).
3. A. Cassano, C. Conidi, R. Ruby-Figueroa, R. Castro-Muñoz, *Int. J. Mol. Sci.*, **351**, 19 (2018).
4. B. Tylkowski, I. Tsibranska, *Physical Sciences Reviews*, **2** (2017).
5. A. Bocking, V. Koleva, J. Wind, Y. Thiermeyer, S. Blumenschein, R. Goebel, M. Skiborowski, M. Wessling, *J. Membr. Sci.*, **217**, 575 (2019).
6. DuraMem Membrane Flat Sheet - Instructions for use, Evonik Industries, 2011.
7. J. Hermia, *Chem. Eng. Trans.,* **60**, 83 (1982).
8. G. Arend, S. Castoldi, M. Rezzadori, *BJFT*, **1**, 22 (2019).
9. G. Bolton; D. LaCasse, R. Kuriyel, *J. Membr. Sci.*, **277**, 75 (2006).
10. N. Amin, A. Mohammad, *J. Applied Membr. Science & Technology,* **22**, 85 (2018).
11. R. Zhang, Y. Ji, X. Zhang, E. J. Kennelly, C. Long, *J. Ethnopharmacol.*, **254** (2020).
12. M. Boykova, I. Saykova, I. Trayanov, *Scientific Works of UFT-Plovdiv,* **1**, 66 (2019).
13. A. Cassano, G. De Luca, C. Conidi, E. Drioli, *Coord. Chem. Rev.,* **35**, 45 (2017).

Theoretical assessment of the use of nanofiltration for fractionation of waste aqueous fractions from the essential oil industry

D. Peshev

University of Chemical Technology and Metallurgy, Department of Chemical Engineering, 8 Kl. Ohridsky Blvd., 1756 Sofia, Bulgaria

The possibility to fractionate hydrosols and extracts (residual waters) from the distillation of representative essential oil plants using nanofiltration was investigated. The rejections of five commercial nanofiltration membranes with respect to key bioactive components were predicted based on regression models. Membranes of different Molecular Weight Cut-Off (MWCO), structure and composition were analyzed. Descriptors in the models were the membrane MWCO and zeta potential, as well as the molecular weight (Mw), octanol-water partition coefficient (log P) and acidity constant (pKa) of the solutes. For consistency, log P and pKa of all studied components were calculated according to the COSMO-RS method, which has the quantum-chemical basis of the Conductor-like Screening Model (COSMO). The distribution of the key components in the two types of effluents under the process conditions was also predicted using COSMO-RS for modelling of the solid-liquid, liquid-liquid and vapor-liquid equilibrium. The calculations were performed using the BIOVIA COSMOsuite software package. The results showed that independently of the membrane material, the polymeric membranes exhibit high retention capability against charged solutes such as the phenolic acids contained in the residual waters. Since the pKa of the phenolic compounds, representatives of the flavonoid family, is within the range of pH of the aqueous extracts, their retention or permeation could be controlled by slight variations of the pH. The essential oil components dissolved in the aqueous fractions are easily permeating through the membranes.

Keywords: nanofiltration, membrane, fractionation, hydrosol, residual water, COSMO-RS

INTRODUCTION

The intensively changing lifestyle and technological developments in recent decades have led to the significant presence of synthetic and semi-synthetic functional ingredients in food and cosmetics, leading to adverse effects on human health and quality of life. As a result, the demand for organic foods and beverages, as well as cosmetics and pharmaceuticals with a high content of natural ingredients, has been significantly increased in recent years as an alternative to synthetic ones. Crude and refined plant extracts rich in phenolic compounds are increasingly applied as natural colorants, antioxidants, preservatives and nutritional supplements. At the same time, plants rich in valuable essential oils are also the main sources of natural antioxidants, but according to market forecasts, annual consumption of essential oils on the world market is growing steadily, reaching 403 thousand tons in 2025 [1]. Since essential oils make up a very small fraction of the mass of the respective plants, from a few percent for typical representatives of the *Lamiaceae* family [2,3] to as little as 0.03% for *Rosa × damascena* [4], this means that tens of millions of tons of waste fractions are generated each year, that is becoming an environmental problem in areas with traditions in the production of essential oils. At the same time, valuable substances with biological activity are being lost.

The steam distillation remains a major technology, ensuring a high and sustainable quality of the extracted oils [5]. Depending on the mode of contact between the plant material and the steam and/or water three types of process are distinguished - dry steam distillation, direct steam distillation and hydrodistillation [5]. In all the three cases, besides the waste vegetable mass and the essential oil, there are two more liquid fractions - aqueous condensate (hydrolat, hydrosol) and extract (residual water). The hydrosol is obtained by the separation of the distillate into an oil fraction and an aqueous fraction. It contains small amounts of volatile aromatic substances, which in the case of some plant species makes it an end product for aromatherapy, ingredient into cosmetic compositions or raw material for further distillation in order to increase the yield of essential oils. In many cases, however, it is discarded into the environment without further processing. The residual water is generally considered waste and disposed of in the environment. The amount varies depending on the steam distillation mode and the operating parameters. Typical values per kilogram

---

of essential oil produced can be stated as 100 kg in dry steam distillation [6] and 12000 kg in the hydrodistillation of *Rosa × damascena* petals [7]. These waste fractions have traditionally been underestimated as a source of high value-added substances due to their low concentration and the susceptibility of the contained biologically active substances to oxidation and degradation at high temperature. Hence, traditional thermal separation methods, such as distillation and evaporation, are considered economically unprofitable and often lead to reduced product quality. Therefore, alternative separation methods are required to allow for softer conditions during concentration or fractionation, so as to increase the quality of the products obtained and at the same time reduce the cost of their recovery.

Separation processes at the molecular level, and in particular nanofiltration have in recent years been the subject of intense research regarding their application for the utilization of by-products of the food- and agro-industries [8, 9]. Up-to-date report on the trends in nanofiltration and nanofiltration membrane research in the last decade highlights their application to wastewater treatment and clean water production as main topics [10]. The factors determining the selectivity and permeate flux of nano- and ultra-filtration membranes for isolation, fractionation and concentration of phenolic compounds with biological activity, extracted from products of the agricultural and food industry have been studied [9]. Significant discrepancies between the retention capacity of commercial membranes and their nominal MWCO were established during separation of aqueous solutions of polyphenolic compounds [9], which is explained by specific interactions between the membrane and the components of the separated mixtures. These interactions consist of components adsorption on the membrane surface, hydrophobic or electrostatic interactions with the membrane, which cannot be influenced by the process parameters. Some physicochemical and structural characteristics of water-soluble organic substances and membranes have been used as descriptors in empirical quantitative models to predict membrane rejection and permeate flux during nanofiltration, taking into account the effects of membrane fouling [11, 12]. Nevertheless, studies on the capability of typical commercial nanofiltration membranes for fractionation or concentration of hydrosols and aqueous extracts from the steam distillation of essential oils, with regard to their specific composition, have not been carried out.

The aim of the present study was to assess the separation performance of typical commercial nanofiltration membranes aiming at their application for fractionation or concentration of effluents from the essential oil industry using available models for the membrane rejection. To achieve this aim, subject of theoretical analysis was a set of plant materials, which are emblematic and of economic interest for Bulgaria, as well as representative for a wide range of aromatic plants in terms of their phytochemical composition and technological parameters of the steam distillation of their essential oils. The distribution of key components in the waste fractions under the process conditions was predicted using universal models of statistical thermodynamics (Conductor-like Screening Model Real Solvents, COSMO RS) [13-15] for modelling of the solid-liquid, liquid-liquid and vapor-liquid equilibrium.

METHODS

Prediction of physico-chemical properties using COSMO-RS

Analysis of the distribution of the most significant valuable substances and essential oil components in the waste aqueous streams was carried out using quantum chemistry and statistical thermodynamics methods to optimize the molecular structures of interest and predict the required physicochemical properties of the multicomponent mixtures, as well as to describe the phase equilibrium. The components solubility, Vapour-Liquid Equilibrium (VLE) diagrams, pKa and logP were predicted using the COSMO-RS method, which is available in many commercial molecular simulation software packages. Some of them (e.g. Turbomole, Gaussian, DMOL3, GAMESS-US, PQS, Molpro, Columbus, ORCA, Q-Chem) can be used to calculate a discrete surface around a pre-optimized at the required level molecular structure surrounded by an imaginary conducting medium with an infinite dielectric constant. Each element of this surface is characterized by the size of its surface and the so-called Screening Charge Density (SCD). The liquid is regarded as a set of closely situated ("packed") molecules, whereby macroscopic thermodynamic and physical properties are predicted based on the statistical averaging of possible electrostatic interactions between segments with different SCD [13-15]. To implement the last step, specialized software, COSMOtherm [14], is available, which uses the SCD distribution data for the studied structure and its total energy obtained as a result of quantum-chemical simulations. In this work, the BP-TZVP-

parameterized BIOVIA COSMObase 2020 Golden database supplied with the BIOVIA COSMOtherm 2020 Golden software (Dassault Systèmes SE, France) was used for all databank components. So as to parameterize all non-databank compounds at the same computational level, a simulation sequence was developed using the Turbomole Version 7.4 software (Dassault Systèmes SE, France). The initial structure was generated from the compounds SMILES *via* the software graphical user interface TmoleX 4.3. The initial structure was pre-optimized at a semi-empirical AM1 (MOPAC 7) level with the SVP basis set in vacuum. The resulting structure was further optimized at DFT level using the BP86 density functional and TZVP basis set and subjected to COSMO calculation in order to obtain the charge screening on the molecular surface and the respective .cosmo file, considering solvent effects through the conductor-like polarizable continuum model. In this way the compound structure was parameterized at a computational level compatible with the BP-TZVP-parameterized COSMObase 2020 database. The new component was added to the COSMObase 2020 by importing from the obtained .cosmo file. Component solubilities and VLE were analyzed by means of the COSMOtherm application. LogP partition coefficients and pKa for all components were predicted using the COSMO-RS theory *via* the COSMOquick (Dassault Systèmes SE, France) program and COSMO*frag* approach [16]. The COSMO-RS theory allowed for prediction of logP at user-defined temperature as opposed to commonly used QSAR (quantitative structure activity relationship) methods.

Regression models for membrane rejection

A limited number of studies reported QSAR models for prediction of the rejection and permeate flux of commercial nanofiltration membranes during filtration of aqueous solutions of organic solutes that account for the solute-solvent-membrane molecular interactions [11, 12]. In a study covering a range of organic solutes and variety of nanofiltration membranes empirical models for prediction of the amount of solute adsorbed by the membranes, the permeate flux and the solute rejection are derived [12]. In this study five commercial nanofiltration membranes with different MWCO, structure and composition were

used: Desal51HL and Desal5DL (GE Osmonics, USA), N30F and NFPES10 (MICRODYN-NADIR, Germany), NTR7450 (Nitto-Denko, Japan). Desal51HL and Desal5DL have a polyamide top layer while in N30F, NFPES10 and NTR7450 the selective layer is made of (in the case of NTR7450, sulfonated) polyethersulfone (PES). MWCO, porosity of the surface layer (represented as the volume fraction of the pores with small and large size), roughness of the active surface, water contact angle, water permeability and membrane charge (expressed as zeta potential of the membrane at three pH values) were used as membrane descriptors. Independent models were obtained for the cases of nanofiltration of uncharged and charged organic solutes dissolved in water. In this work the membrane rejection coefficients for the key components of the extracts and hydrosols were predicted using the regressions reported in [12] for uncharged, Eq. (1), and charged, Eq. (2), solutes:

$$Rejection = (5.73 - 0.71 LogP - 0.002 MWCO)^2 \quad (1)$$

$$Rejection = -82.75 + 26.13 \ln(Mw) + 5052.63/MWCO - 18.54/Membrane\ charge \quad (2)$$

The membrane rejection coefficient is defined based on the ratio of the concentration in the permeate, C_P, and retentate, C_R, streams as follows [13]:

$$Rejection = 1 - C_P/C_R \quad (3)$$

Membrane-related model parameters in Eqs. (1) and (2) are the MWCO and *Membrane charge* expressed as zeta potential at a specific pH. Their values for the studied membranes are summarized in Table 1. Solute-related descriptors are the M_W in the case of charged and LogP in the case of uncharged organic compounds. The charge of the solutes in the present work was estimated at the respective pH based on their pKa value. The compounds containing either carboxyl (-COOH) or hydroxyl (-OH) functional groups at pH higher than their pKa are preferably deprotonated and thus negatively charged. At pH lower than pKa these compounds are assumed to be neutral as none of them contains basic groups as also confirmed by our simulations. Some of the components contain neither acidic nor basic groups and are considered as neutral independently of the pH.

Table 1. Summary of the membrane-related parameters in the models for membrane rejection
at different pH values [12].

Membrane	pH 3		pH 6		pH 10	
	MWCO, Da	*Mambrane charge (Zeta potential), mV*	MWCO, Da	*Mambrane charge (Zeta potential), mV*	MWCO, Da	*Mambrane charge (Zeta potential), mV*
Deasal51HL	220	4	190	-13	220	-17
Desal 5DL	290	7	260	-17	270	-21
NTR 7450	310	1	310	-15	310	-19
N30F	590	1	680	-14	630	-18
NFPES10	1300	1	1200	-10	1300	-15

RESULTS AND DISCUSSION

Biologically active constituents of the essential oil cultures and their distribution amongst the aqueous extracts and hydrosols

This study focusses on the water-soluble biologically active components of the essential oil cultures, as well as on the major constituents of their essential oils. Due to their relatively high solubility in warm water, phenolic compounds in plants are also the major bioactive components in aqueous decoctions or infusions from medicinal plants. Often the total phenolic fraction from the plant (anti-inflammatory agents [4, 7, 17]), purified and standardized polyphenolic fractions (venoactive drugs [18], phytoestrogens [19], hepatoprotective drugs [20]) or individual phenolic compounds (medications for acute and chronic liver diseases, cancer and haematological diseases [21], drugs and materials for dental medicine [22]), are the active component of medicines and medical materials. In Table 2 are summarized the key polyphenolic and essential oil components of crops that are highly popular, cultured and processed in high volumes due to their formidable benefits to human health - *Rosa × damascena*, aromatic plants of the *Lamiaceae* family (lavender, lemon balm) and cloves. Bulgaria is a leading country in the world for lavender cultivation and processing and in 2017 accounts for 52% of world essential oil production. Rosa Damascena's cultivation and processing is an emblematic sector for Bulgaria.

Studies on the phytochemical profile of the aqueous extract from hydrodistillation of *Rosa × damascena* petals showed that it contains phenolic compounds, representatives of different subclasses of the flavonoid family (flavan-3-ols, flavanones, flavonols and flavones) [7]. The quantitative analysis proved that predominant phenolic compounds in both the waste water and the residual biomass [4] are flavonol glycosides containing campherol and quercetin in their structure, as well as flavonol, ellagic acid, flavone, quercetin and kaempferol. The molecular weights of the phenolic

components in the water extract range from about 280 g/mol for kaempferol to about 637 g/mol for multiflorin A [7], thus covering a significant part of the selectivity spectrum of nanofiltration membranes (200-1000 g/mol). Under conditions of boiling in water, a high content of high molecular weight pectic polysaccharides can be expected in the water extract [23]. Depending on the source and method of extraction, the molecular weight of recovered pectic polysaccharides varies in a wide range from about 30,000 to about 250,000 g/mol, fall outside of the nanofiltration membranes range of selectivity and were not considered in the present work. Major constituents of the essential oil from *Rosa × damascena* are monoterpenes (geraniol, citronellol, nerol), phenethyl alcohol and hydrocarbons (nonadecane) with molecular weights mostly below the nanofiltration range [24-26].

Lavender and lemon balm are aromatic herbs belonging to the *Lamiaceae* family, which are characterized by a high content of polyphenolic compounds. In extracts with polar organic solvent from plant waste remaining after steam distillation of lavender [3, 27, 28] and in aqueous extracts from lemon balm [29, 30] flavonoid glycosides, similar to those in the *Rosa × damascena* hydrodistillation waste streams, have been identified. Their structures contain luteolin and apigenin in the case of lavender or myricetin and quercitin in the case of lemon balm. In addition to the content of flavonoids, these fractions are rich in polyphenolic acids, such as caffeic, gallic, chlorogenic and rosmarinic acids. Dominant with respect to all phenolic constituents in both herbs is the rosmarinic acid, which is also a major contributor to the antioxidant capacity of the aqueous extracts. Despite the variations in the composition of the essential oils, primary components are linalool and citral in the case of lavender and lemon balm, respectively. Other common constituents of lavender essential oil are linalyl acetate, trans-β-ocimene, terpinen-4-ol and borneol [24, 31, 32]. In

Table 2. Key polyphenolic (PF) and essential oil (EO) components, their thermodynamic properties and distribution amongst aqueous extracts and hydrosols.

Plant	Fraction	Key component	COSMO parametrization	Mw, Da	$m_{100} \times 10^6$	$m_{30} \times 10^6$	y* at 100 °C × 10^6	K_{AW} at 100 °C
Rosa × damascena	PF	2-Phenylethyl-O-β-D-glucopyranoside	User	284.3	3588.0	361.3	0	0
		Kaempferol	User	286.2	1300.7	178.2	0	0
		Quercetin	User	302.2	1522.0	305.0	0	0
		Ellagic acid	User	302.2	6720.1	1546.1	0	0
		Kaempferol-3-O-glucoside (Astragalin)	User	448.4	163.1	4.871	0	0
		Kaempferol-3-O-glucosylrhamnoside (Multiflorin B)	User	594.5	8.4	0.1	0	0
		Quercetin-3-O-rhamnosylglucoside (Rutin)	User	610.5	3.4	0	0	0
		Kaempferol-3-O-acetylglucosylrhamnoside (Multiflorin A)	User	636.6	3.3	0.1	0	0
	EO	Geraniol	BIOVIA	154,3	974.4	592.8	8381.1	73.77
		Citronellol	BIOVIA	156,3	578.1	310.2	8405.1	126.4
		Nerol	BIOVIA	154,3	1188.0	709.0	15032.2	108.5
		Phenethyl alcohol	BIOVIA	122,2	37570.0	24261.7	15930.7	2.79
		Nonadecane	BIOVIA	268,5	0	0	NA	NA
Lavandula angustifolia	PF	Rosmarinic acid	User	360.3	12900.1	1806.2	0	0
		Luteolin	User	286.2	740.5	25.3	0	0
		Caffeic acid	User	180.2	135479.9	23161.1	0	0
	EO	Linalool	BIOVIA	154.3	607.8	322.6	22449.1	316.1
		Linalyl acetate	BIOVIA	196.3	93.5	43.0	4741.0	553.3
		Trans-β-ocimene	User	136.2	65.8	15.9	164681.6	19240
		Terpinen-4-ol	BIOVIA	154.3	529.3	61.5	7347.9	119.2
		Borneol	BIOVIA	154.3	759.3	67.7	4888.5	55.27
Melissa officinalis	PF	Rosmarinic acid	User	360.3	12900.1	1806.2	0	0
		Caffeic acid	User	180.2	135479.9	23161.1	0	0
		Rutin	User	610.5	3.4	0	0	0
	EO	Citral (Neral and Geranial)	BIOVIA	152,2	2261.1	3082.2	12588.7	47.49
		Germacrene D	BIOVIA	204.4	4.8	0.1	1420.9	3379
		β-Caryophyllene	BIOVIA	204.4	13.6	2.5	2878.3	2400
		Citronellal	BIOVIA	154.3	417.6	246.0	33679.5	695.7
		D-Limonene	BIOVIA	136.2	93.4	23.7	86305.1	7051
Syzygium aromaticum (Cloves)	PF	Eugenol	BIOVIA	164.2	1479.9	677.3	4569.4	28.33
		Gallic acid	BIOVIA	170.1	278190.0	89312.9	0	0
		Kaempferol	User	286.2	1300.7	178.2	0	0
		Quercetin	User	302.2	1522.0	305.0	0	0
		Tamarixetin 3-O-β-D-glucopyranoside	User	478.4	81.5	2.0	0	0
	EO	Eugenol	BIOVIA	164.2	1479.9	677.3	4569.4	28.33
		Eugenyl acetate	BIOVIA	206.2	533.5	179.1	152.441	3.275
		β-Caryophyllene	BIOVIA	204.4	13.6	2.5	2878.3	2400
		3-(1-Methylethyl)-benzoic acid	BIOVIA	164.2	3017.5	344.8	657.0	2.002
		α-Humulene	BIOVIA	204.4	6.0	0.2	851.1	1604

m_{100} - solubility in water at 100 °C (maximum concentration in aqueous extracts), mass fraction; m_{30} - solubility in water at 30 °C (concentration in hydrosols), mass fraction; K_{AW} - air–water partitioning coefficient (y* /x_{sat}); x_{sat} – mole fraction of component in saturated solution; y* - concentration of vapor phase at equilibrium with saturated solution in mole fraction.

addition to citral, the oil from lemon balm contains germacrene D, β-caryophyllene, citronellal and D-limonene [24, 33-35].

The aromatic flower buds of the tree *Syzygium aromaticum* (cloves), in addition to being widely used as a spice, food preservative and in medicine, are also one of the popular raw materials for the preparation of essential oil by steam distillation [36-38]. This is due to their high content of biologically active polyphenolic and aromatic substances. Eugenol is the main constituent of the essential oil [36-38] and also the biologically active component with the highest content per unit mass of plant material - up to approximately 10 wt. % [37]. In a systematic study on methanolic extracts of 26 aromatic plants belonging to 12 botanical families with pronounced antioxidant activity, the flower buds of *Syzygium aromaticum* were found to have the highest total phenolic content [37]. A key representative of the polyphenolic compounds is gallic acid (783.5 mg/100 g dry plant mass) and its derivatives (2375.8 mg/100 g dry plant mass), flavonoids (caempferol, 23.8 mg/100 g and quercetin, 28.4 mg/100 g dry plant mass) [37] and their glycosides (tamarixetin 3-O-β-D-glucopyranoside [38]). Apart from eugenol, the essential oil contains also significant amounts of eugenyl acetate, β-caryophyllene, 3-(1-methylethyl)-benzoic acid and α-humulene [36, 39, 40].

To be able to discuss the effects from nanofiltration of the extracts and hydrosols from the distillation, a preliminary appraisal of their composition is required. As an estimate for the magnitude of a component concentration in the extracts is assumed its predicted solubility in water at 100 °C shown in Table 2. This approximation is justified since the operating pressure is usually close to atmospheric one while the plant material is in contact with boiling water during hydrodistillation or eventually in contact with aqueous condensate leading to the formation of extract during steam distillation. The plant materials have to contain required amount from the respective component to achieve the equilibrium concentration in water at the said temperature as an additional prerequisite. However, the solubility at 100 °C is not a sufficient criterion for presence of the respective compound in the extract. In the course of a typical process for the studied essential oil plants (duration is in the range from 40 min to 4 hours [68]), highly volatile compounds would be stripped from the extract and quantitatively transferred in the distillate. For this reason, the isobaric VLE was also simulated and the results are

illustrated in Table 2. The VLE diagram y=f(x) was a linear relationship (coefficient of linear correlation more than 0.9996 in all cases) for all studied volatile components within the ranges for x with a slope equal to y*/x$_{sat}$ (Table 2). The latter represents the air–water partitioning coefficient, K$_{AW}$, and indicates that Henry's law for dilute systems holds in the range of essential oils components solubility at 100 °C and 1013.25 mBar. A smaller value of K$_{AW}$ implies high reflux ratio and multiple stages, thus inefficient separation of the essential oil components *via* distillation. In the case of simple distillation, which depicts the process of hydrodistillation of essential oil cultures and can be used as an approximation for the case where steam distillation of the biomass is accompanied by formation of aqueous condensate (extract), small K$_{AW}$ would require distillation of large fractions of the feed solution in order to achieve sufficient yield of the essential oil components in the distillate. As a result, components with the highest partitioning coefficients are expected to be quantitatively transferred in the distillate and consequently distributed between the hydrosols and essential oil fraction, while these with extremely low partition coefficient may also be present in the aqueous extracts. Hence, in Table 3 as constituents of the extracts are listed only components that have solubility at 100 °C and K$_{AW}$ values permitting theoretical concentration in the extracts higher than 100 ppm.

The hydrosols will contain dissolved components of the respective essential oils in concentrations corresponding to their solubility at the emulsion decantation temperature (28-35 °C) [16, 41]. The solubility of essential oil components in this work was predicted at a reference temperature of 30 °C (Table 2) and only compounds with solubility higher than 40 ppm were considered in the model mixtures representing the hydrosols from the distillation of the essential oil cultures (Table 3).

Parameters of the membrane rejection models

The values for the membrane MWCO and zeta potential at different pH were taken from the literature and listed in Table 1. The only solute specific model parameter is LogP. For each of the suggested key components of the extracts and hydrosols, the COSMO-RS predicted value is included in Table 3. In contrary with the generally accepted simplified approach of the so-called "sieve" mechanism of membrane separation, in which the ability of the membrane to separate

certain substances is determined by its MWCO, Eq. (1) reveals that for the range of LogP values in this work, the hydrophobicity of the organic solutes expressed as LogP has an impact on the membrane rejection in an order of magnitude equal to that of the MWCO.

Even though not explicitly present in the model equations, pKa is another physicochemical property of the organic solutes predetermining their membrane rejection. A quick observation of the theoretical predictions demonstrated that only polyphenolic acids are negatively charged at neutral pH. In a moderately basic environment of pH 10, all polyphenolic constituents except phenylethyl-glucopyranoside will exist in a deprotonated form and behave as negatively charged solutes permeating the membranes. The components of the hydrosols are either aprotic or have a pKa higher than 14 (except phenethyl alcohol and 3-(1-methylethyl)-benzoic acid) that make them practically uncharged within a feasible range of pH.

Membrane fractionation of the waste aqueous fractions from the steam distillation

The predicted membrane rejection coefficients against all individual components of the aqueous fractions are plotted in Figs. 1 - 4. An overview of the results reveals that none of the nanofiltration membranes is capable to retain the uncharged organic compounds to a level permitting their practical implementation for component concentration. An exception is phenethyl alcohol in *Rosa × damascena* hydrosols where a suitable process configuration may render nanomembrane concentration feasible. In contrast, the negatively charged components at certain pH were as a rule highly rejected by all studied commercial membranes independently of their MWCO, morphology or composition of the selective layer.

Table 3. Suggested composition of extracts and hydrosols from the investigated cultures and summary of the solute-related parameters in the models for membrane rejection at different pH values.

Plant	Fraction	Component	pKa	LogP	Component charge		
					pH3	pH6	pH10
Rosa × damascena	Extract	2-Phenylethyl-O-β-D-glucopyranoside	11.8	2.39	0	0	0
		Kaempferol	6.74	3.66	0	0	-1
		Quercetin	6.27	3.96	0	0	-1
		Ellagic acid	7.65	2.48	0	0	-1
		Kaempferol-3-O-glucoside (Astragalin)	6.74	3.89	0	0	-1
		Phenethyl alcohol	13.9	1.51	0	0	0
	Hydrosol	Geraniol	15.5	3.55	0	0	0
		Citronellol	15.7	3.63	0	0	0
		Nerol	15.5	3.55	0	0	0
		Phenethyl alcohol	13.9	1.51	0	0	0
Lavandula angustifolia	Extract	Rosmarinic acid	3.22	2.98	0	-1	-1
		Luteolin	6.27	2.76	0	0	-1
		Caffeic acid	4.4	1.36	0	-1	-1
	Hydrosol	Linalool	19.2	3.71	0	0	0
		Linalyl acetate	NA	4.23	0	0	0
		Terpinene-4-ol	19.2	3.44	0	0	0
		Borneol	17.7	2.95	0	0	0
Melissa officinalis	Extract	Rosmarinic acid	3.22	2.98	0	-1	-1
		Caffeic acid	4.4	1.36	0	-1	-1
		Citral (Neral and Geranial)	NA	3.06	0	0	0
	Hydrosol	Citral (Neral and Geranial)	NA	3.06	0	0	0
		Citronellal	NA	3.54	0	0	0
Syzygium aromaticum (Cloves)	Extract	Eugenol	7.4	3.34	0	0	-1
		Eugenyl acetate	NA	3.27	0	0	0
		3-(1-Methylethyl)-benzoic acid	4.27	2.86	0	-1	-1
		Gallic acid	4.21	1.40	0	-1	-1
		Kaempferol	6.74	3.66	0	0	-1
		Quercetin	6.27	3.96	0	0	-1
	Hydrosol	Eugenol	7.4	3.34	0	0	0
		Eugenyl acetate	NA	3.27	0	0	0
		3-(1-Methylethyl)-benzoic acid	4.27	2.86	0	-1	-1

This phenomenon can be explained only if a mechanism of membrane retention controlled by intermolecular solute-membrane, solute-solvent and solvent-membrane interactions rather than sieving is assumed. As expected, the rejection for uncharged solutes in both extracts and hydrosols is consistently decreasing with increasing the membrane MWCO. Due to their relatively low hydrophobicity (based on their low LogP values), phenethyl alcohol, caffeic acid and gallic acid are the most highly rejected uncharged components with predicted rejection coefficients of up to about 20% for polyamide composite membranes.

The results on extracts from *Rosa × damascena* (Fig. 1) illustrate the potential of nanofiltration for both isolation and concentration of the contained flavonoid polyphenols and ellagic acid from their mixture with other phenolic compounds and phenethyl alcohol when the process is held at elevated pH of 10. The pH susceptibility of the nanomembranes performance may be further exploited to claim that a single set-up and membrane can be used for purification of the phenolic fraction *via* removal of high molecular weight compounds such as pectin at neutral pH, followed by further fractionation of the phenolic fraction at basic pH. Despite the relatively low rejection for phenethyl alcohol, its concentration in hydrosols can be practically achieved *via* design of multistage nanofiltration operation [42] with membranes such as Desal51HL or Desal5DL. In

lavender extracts, the negligible rejection at normal pH and high rejection at pH 10 for luteolin along with the high rejection for the two phenolic acids in both cases reveals the opportunity to separate the phenolic acids from the flavonoid components and concentrate them (Fig. 2). Rosmarinic and caffeic acids are also key components of the extracts from lemon balm and the data in Fig. 3 demonstrate the possibility for their direct purification and concentration at normal pH of the environment using preferably Desal membranes. Due to the negligible rejection for essential oil components in the hydrosols from both lavender and lemon balm (Figs. 2, 3), the nanofiltration of their hydrosols would not bring any benefits. Predicted performances of the nanofiltration membranes are favorable for efficient fractionation of the biologically active constituents of both clove extracts and hydrosols (Fig. 4). At pH 6 nanofiltration can selectively remove organic acids from the extracts. If the permeates are subjected to nanofiltration with the same membranes at pH 10, this would allow for isolation of the flavonoids fraction together with eugenol in the retentates. Since eugenol is the target bioactive component of cloves and at the same time due to its high water solubility is contained in high concentrations in the hydrosols, nanofiltration appears as a feasible technology to recycling eugenol from this waste stream from the steam distillation of cloves. As is
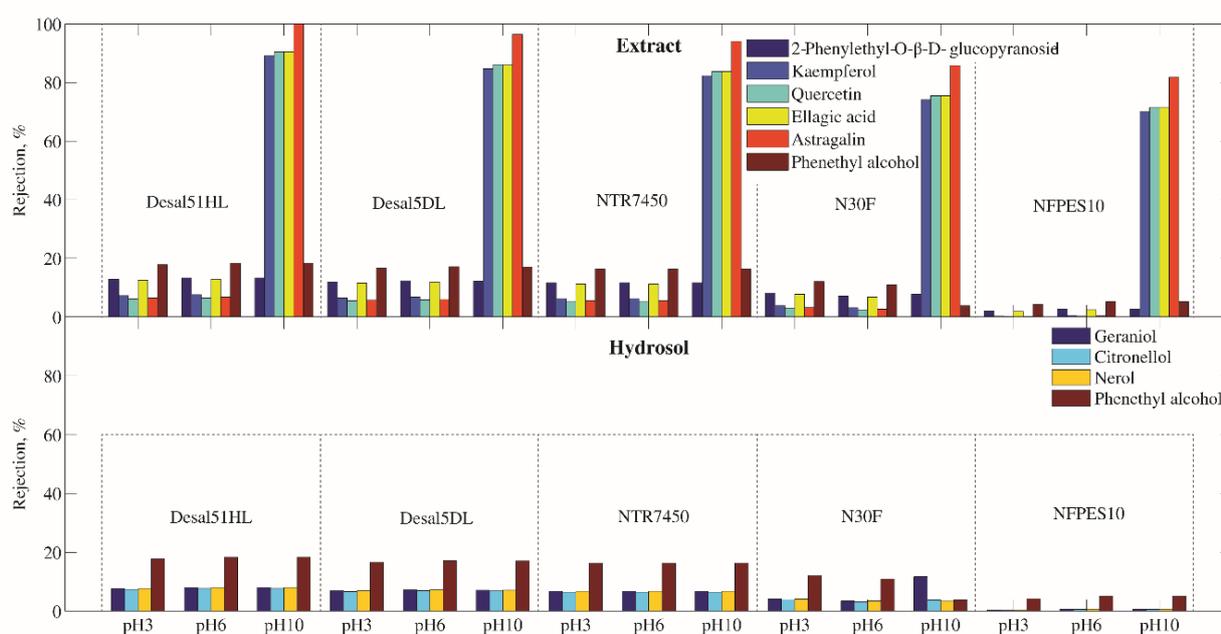
Fig. 1. Nanomembrane selectivity against key components of extracts and hydrosols from hydrodistillation of *Rosa × damascena* petals
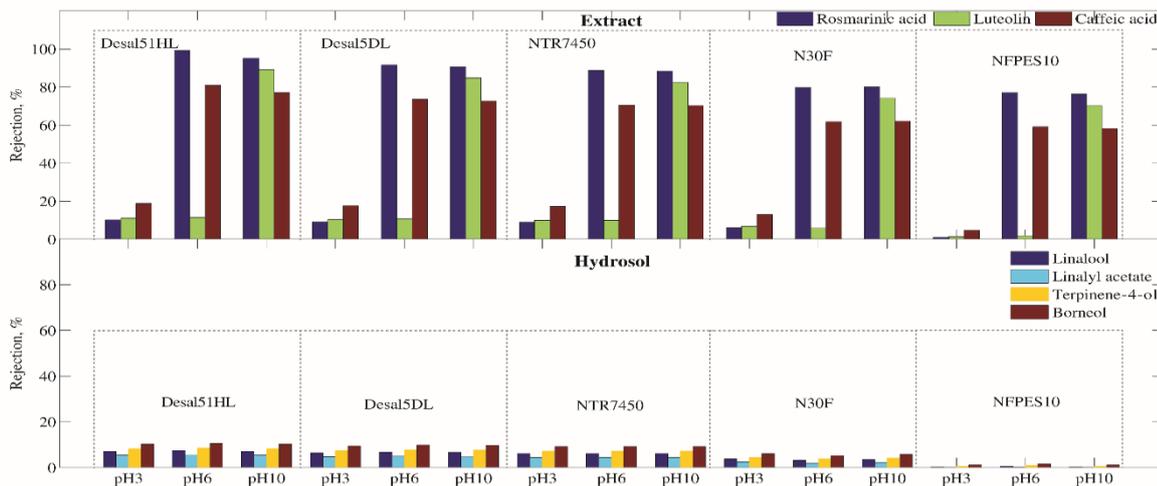
Fig. 2. Nanomembrane selectivity against key components of extracts and hydrosols from steam distillation of *Lavandula angustifolia*
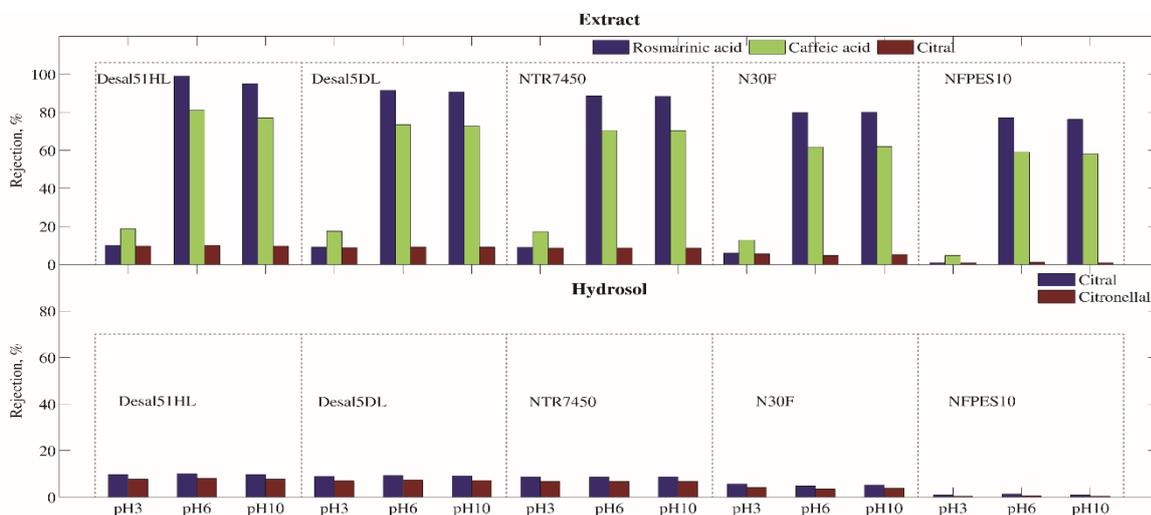
Fig. 3. Nanomembrane selectivity against key components of extracts and hydrosols from steam distillation of *Melissa officinalis*
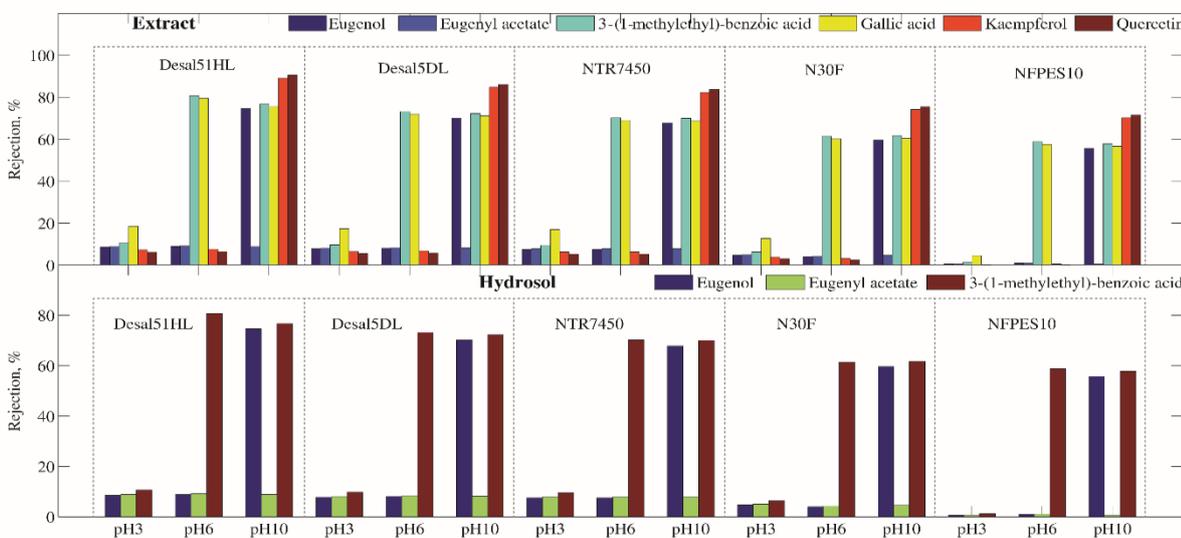
Fig. 4 Nanomembrane selectivity against key components of extracts and hydrosols from steam or hydrodistillation of *Syzygium aromaticum* (Cloves)

obvious from Figure 4, eugenol in hydrosols can be isolated by their nanofiltration at neutral pH aiming to purify it in the permeates. The obtained permeates can be concentrated by nanofiltration at pH 10 using the same membranes.

CONCLUSIONS

The selectivity with respect to key biologically active constituents of effluents from the essential oil industry of five representative commercial nanofiltration membranes with different MWCO, structure and composition was predicted based on empirical models. The theoretical analysis was performed on a set of emblematic and of economic interest for Bulgaria essential oil cultures such as *Rosa × damascena*, *Lavandula angustifolia* and *Melissa officinalis*. Flower buds from *Syzygium aromaticum* (Cloves) has also been selected due to encouraging in the scope of the present research specifics in its phytochemical composition and technological parameters of the steam distillation of its essential oil. The key biologically active constituents of the selected plants were summarized based on literature review. Their presence in the waste aqueous fractions from the steam distillation was assessed *via* prediction of the components solubility, VLE diagrams, pKa and LogP using the COSMO-RS universal models of statistical thermodynamics. The membrane selectivity was expressed in terms of membrane rejection coefficient. The most significant parameters affecting the membrane rejection were the hydrophobicity of the solutes and pH of the nanofiltered aqueous mixtures. The results clearly demonstrated the viability of nanofiltration for isolation of refined polyphenolic fractions from the extracts effluents and for recovery of phenethyl alcohol and eugenol from hydrosols of *Rosa × damascena* and cloves, respectively.

REFERENCES

1. https://www.grandviewresearch.com/press-release/global-essential-oil-market (accessed 18.08.2019).
2. N. Gavaric, N. Kladar, A. Misan, A. Nikolic, I. Samojlik, N. Mimic-Dukic, B. Bozin, *Ind. Crop Prod.*, **74**, 457 (2015).
3. L. Lesage-Meessen, M. Bou, C. Ginies, D. Chevret, D. Navarro, E. Drula, E. Bonnin, J. C. Del Río, E. Odinot, A. Bisotto, J.-G. Berrin, J.-C. Sigoillot, C. B. Faulds, A. Lomascolo, *Biotechnol. Biofuels*, **11**, art. 217 (2018).
4. A. Schieber, K. Mihalev, N. Berardini, P. Mollov, R. Carle, *Z. Naturforsch.*, **60c**, 379 (2005).
5. C. M. Galanakis, Food Waste Recovery: Processing Technologies and Industrial Techniques, Elsevier Inc., 2015.
6. Bul Phyto Oils Ltd., Bulgaria, private communication.
7. K. Rusanov, E. Garo, M. Rusanova, O. Fertig, M. Hamburger, I. Atanassov, V. Butterweck, *Planta Med.*, **80**, 1657 (2014).
8. C. Brazinha, J. G. Crespo, Valorization of food processing streams for obtaining extracts enriched in biologically active compounds, in: Integrated Membrane Operations in the Food Production, A. Cassano, E. Drioli (eds.), De Gruyter, 2014, p. 295.
9. A. Cassano, C. Conidi, R. Ruby-Figueroa, R. Castro-Muñoz, *Int. J. Mol. Sci.*, **19**, 351 (2018).
10. I. Tsibranska, B. Tylkowski, Concentration of polyphenols by integrated membrane operations, in: Integrated Membrane Operations in the Food Production, A. Cassano, E. Drioli (eds.), De Gruyter, 2014, p. 269.
11. M. Cai, W. Hou, Y. Lv, P. Sun, *J. Food Eng.*, **195**, 97 (2017).
12. K. Boussu, C. Vandecasteele, B. Van der Bruggen, *J. Mem. Sci.*, **310**, 51 (2009).
13. D. Peshev, A. Livingston, *Chem. Eng. Sci.*, **104**, 975 (2013).
14. Dassault Systèmes, COSMOlogic, http://www.cosmologic.de/home.html (accessed 19.08.2019).
15. F. Eckert, A. Klamt, AIChEJ. **48**, 369 (2002).
16. M. Hornig, A. Klamt, *J. Chem. Inf. Model.*, **45**, 1169 (2005).
17. J. Wedler, A. Weston, J. Rausenberger, V. Butterweck, *Fitoterapia*, **114**, 56 (2016).
18. R. Russo, D. Chandradhara, N. De Tommasi, *Molecules*, **23**, 2174 (2018).
19. J. V. Turner, S. Agatonovic-Kustrin, B. D. Glass, *J. Pharm. Sci.*, **96** (8), 1879 (2007).
20. A. Kalantari, A. Salimi, H. Kalantari, J. E. Broojeni, I. Rashidi, A. R. Vanani, I. Bácskay, *Toxicology Reports*, **6**, 444 (2019).
21. H. Zou, X.-X. Zhu, G.-B. Zhang, Y. Ma, Y. Wu, D. S. Huang, *Oncotarget*, **8** (51), 89307 (2017).
22. B. K. Jadhav, K. R. Khandelwal, A. R. Ketkar, S. S. Pisal, *Drug Dev. Ind. Pharm.*, **30** (2), 195 (2004).
23. A. Slavov, I. Panchev, D. Kovacheva, I. Vasileva, *Food Hydrocoll.*, **61**, 469 (2016).
24. Galen-N Ltd., https://galen-n.com/category/products/essential-oils/ (accessed on 01.09.2020).
25. T. Atanasova, M. Kakalova, L. Stefanof, M. Petkova, A. Stoyanova, S. Damyanova, M. Desyk, *Ukr. Food J.*, **5**(3), 492 (2016).
26. R. S. Verma, R. C. Padalia, A. Chauhan, A. Singh, A. K. Yadav, *Nat. Prod. Res.*, **25** (7), 1577 (2011).
27. L. Torras-Claveria, O. Jauregui, J. Bastida, C. Codina, F. Viladomat, *J. Agric. Food Chem.*, **55**, 8436 (2007).

28. I. Mendez-Tovar, B. Herrero, S. Perez-Magarino, J. A. Pereira, M. C. Asensio-S.-Manzanera, *J. Food Drug Anal.*, **23**, 225 (2015).
29. A. Sentkowska, M. Biesaga, K. Pyrzynska, *Int. J. Food Prop.*, **18**, 2009 (2015).
30. M. Jacotet-Navarro, M. Laguerre, A. S. Fabiano-Tixier, M. Tenon, N. Feuillere, A. Bily, F. Chemat, *Electrophoresis*, **1** (2018).
31. M. Biało, T. Krzysko-Łupicka, E. Nowakowska-Bogdan, P. P. Wieczorek, *Molecules*, **24**, 3270 (2019).
32. K. Smigielski, A. Raj, K. Krosowiak, R. Gruska, *Jeobp*, **12** (3), 338 (2009).
33. A. G. Pirbaloutia, M. Nekoei, M. Rahimmalek, F. Malekpoor, *Biocatal. Agric. Biotechnol.*, **19**, 101144 (2019).
34. F. Abdellatif, H. Boudjella, A. Zitouni, A. Hassani, *EXCLI J.*, **13**, 772 (2014).
35. F. S. Sharopov, M. Wink, D. R. Khalifaev, H. Zhang, N. S. Dosoky, W. N. Setzer, *Int. J. Trad. Nat. Med.*, **2**(2), 86 (2013).
36. D. F. Cortés-Rojas, C. R. F. de Souza, W. P. Oliveira, *Asian Pac. J. Trop. Biomed.*, **4**(2), 90 (2014).
37. B. Shan, Y. Z. Cai, M. Sun, H. Corke, *J. Agric. Food Chem.* **53**, 7749 (2013).
38. M. I. Nassar, A. H. Gaara, A. H. El-Ghorab, A.-R. H. Farrag, H. Shen, E. Huq, T. J. Mabry, *Rev. Latinoamer. Quím.*, **35** (3), 47 (2007).
39. M. N. I. Bhuiyan, J. Begum, N. C. Nandi, F. Akter, *African Journal of Plant Science*, **4** (11), 451 (2010).
40. M. Mahboubi, M. Mahboubi, *TEOP*, **18** (4), 967 (2015).
41. I. I. Sidorov, N. A. Turysheva, L. P. Faleeva, E. I. M. Yasyukevich, Technology of natural essential oils and synthetic fragrances, Light and Food Industry, 1984, (in Russian).
42. N. M. Mazlan, D. Peshev, A. Livingston, *Desalination*, **377**, 138 (2016).

Extraction of bioactive compounds from conifers growing in the Windsor Great Park and other arboretums

D. I. Ivanova[1]*, R. P. Adams[2], J. Anderson[3], A. N. Tashev[4], P. T. Nedialkov[5], Z. K. Kokanova-Nedialkova[5], Y. E. Ilieva[6], T. N. Atanassova[5], G. I. Kalotova[1], G. Angelov[1], H. M. Najdenski[6]

[1] Institute of Chemical Engineering, Bulgarian Academy of Sciences, 1113 Sofia, Bulgaria
[2] Biology Department, Baylor University, Waco, TX 76798, USA
[3] Crown Estate Office, Windsor Great Park, SL4 2HT Windsor, UK
[4] University of Forestry, Department of Dendrology, 1756 Sofia, Bulgaria
[5] Faculty of Pharmacy, Medical University, 1000 Sofia, Bulgaria
[6] The Stephan Angeloff Institute of Microbiology, Bulgarian Academy of Sciences, 1113 Sofia, Bulgaria

The present study is aimed at identification of antioxidant and antiproliferative compounds in extracts of conifers originating from the Windsor Great Park (WGP), UK, and other arboretums. Species of the genera *Juniperus, Cupressus*, *Chamaecyparis* and *Taxus* were studied. Rare representatives of *J. indica, J. squamata, J. pingii, J. recurva, J. davurica* etc., as well as widely distributed species and cultivars were analyzed. Antioxidant activities were evaluated by total polyphenol content (TPC) and half-maximum DPPH-radical scavenging concentrations (DPPH-SC$_{50}$) of the extracts. Antiproliferative activities were determined by half-maximum growth-inhibitory concentrations (IC$_{50}$) obtained after MTT-assay of NB4 acute promyelocytic leukemia cells treated with the corresponding extracts. In this group of studied conifers, *J. indica* leaves extract was determined as the best antioxidant agent with DPPH-SC$_{50}$ 52 μg/ml and TPC 320±10 GAE mg/g extract. The best antiproliferative properties were demonstrated by the leaves extracts of *J. virginiana* cultivars with NB4-IC$_{50}$ in the range of 0.27-0.31 μg/ml. Remarkable cytotoxic activity was found also for *J. × pfitzeriana, J. pingii* var. *wilsonii* and *T. baccata* leaves extracts. Rare species, such as *J. indica* and *J. recurva* "Embley Park", also showed high antiproliferative activity. Podophyllotoxin was identified in the best cytotoxic extracts obtained from *J. virginiana* and *J. × pfitzeriana* cultivars. Identification of other metabolites in the efficient bioactive extracts is in progress. The present results revealed various conifers as potential sources of cytotoxic and antioxidant lead compounds for prevention of the living organisms from oncogenic, degenerative or other radical-induced diseases.

Keywords: Antioxidants, Antiproliferative activity, *Chamaecyparis* Spach., *Cupressus* L., *Juniperus* L., *Taxus* L.

INTRODUCTION

Conifers belong to the Pinophyta (Coniferophyta) division of the Plantae kingdom. They are cone-bearing gymnosperm plants, growing as magnificent trees or small shrubs. Various conifers are natural sources of highly efficient bioactive molecules. The essential oils from various conifers have been used from ancient times and nowadays, due to their efficient antioxidant, antimicrobial, cytotoxic and other bioactive properties. Cedar oil is obtained from conifers belonging to Cupressaceae (*Juniperus, Cryptomeria, Cupressus, Calocedrus, Chamaecyparis, Austrocedrus* and *Thuja* species) and Pinaceae (*Cedrus* and *Pinus* species) families [1]. In the present study, extraction of antioxidant and antiproliferative compounds as potential pharmaceutical agents from representatives of the genera *Juniperus, Cupressus*, *Chamaecyparis* and *Taxus*, growing in the Windsor Great Park and other arboretums, were investigated.

The genus *Juniperus* L. (Cupressaceae) includes about 50-67 species and more than 220 cultivars [2, 3]. About 580 juniper secondary metabolites have been identified – cytotoxic podophyllotoxin (PPT) and other lignans, sesquiterpenes, diterpenes, flavonoids, etc. [4]. The present sources of PPT [*Sinopodophyllum hexandrum* (Royle) T. S. Ying, *Podophyllum peltatum* L.] are already considered as endangered species because of their intensive industrial exploitation in the synthesis of efficient anticancer drugs Etoposide, Teniposide, etc. That is why, new sources of PPT are necessary.

In the context of the conquest of cancer, new sources of antioxidant compounds are also required as active agents against excessive accumulation of deleterious free radicals in the cells. We have found recently that *J. sibirica* Burgsd. and *J. excelsa* M. Bieb. leaves extracts have demonstrated the best antioxidant activity among plenty of juniper species from the Balkan region [5].

In this study, more efficient antioxidant properties were found for other conifer representatives – *J. indica* Bertol., *J. recurva* "Embley Park", *C. arizonica* Greene, *J. squamata* Buch.-Ham. ex D. Don, etc.

The genus *Cupressus* includes about 16-25 species and a wide variety of cultivars. *Cupressus sempervirens* L. leaves extract and essential oil have demonstrated remarkable radical scavenging activity [6]. Quercetin, rutin, caffeic acid, and *p*-coumaric acid have been isolated from *C. sempervirens* leaves [7]. The bark extract of *Cupressus lusitanica* Mill. (Mexican white cedar) has shown high cytotoxicity on MCF-7 (estrogen receptor positive breast carcinoma) cells [8].

Chamaecyparis Spach is a small genus with about 5-7 species. *Chamaecyparis nootkatensis* D. Don (Alaskan yellow cedar, disputed now to be classified back in the genus *Cupressus*), containing diterpene constituents termed nootkastatins, has demonstrated efficient cytotoxic effects [9]. Thujaplicins (tropolone-related compounds) were identified in the woods of *Chamaecyparis obtusa* (Siebold & Zucc.) Endl. (Japanese cypress) and are known for their antioxidant and other bioactive properties [10]. The lignan chamaecypanone C is a novel microtubule inhibitor from the heartwood of *Chamaecyparis obtusa* var. *formosana* (Taiwan hinoki) that has shown high cytotoxic activity in nanomolar ranges on various cancer cells [11]. In addition, hot-water leaves extract of this Taiwan endemic conifer has exhibited high radical scavenging activity, attributed to several constituents (catechin, quercetin, quercetin-3-O-α-rhamnoyranoside, myricetin-3-O-α-rhamnoyranoside, vanillic acid, and 4-hydroxybenzoic acid). Extracts from the bark of this cypress have also shown efficient antioxidant activity [12].

Representatives of genus *Taxus* L. (Taxaceae), such as *T. baccata* L., *T. brevifolia* Nutt., *T. cuspidata* Siebold & Zucc., etc., are sources of taxine alkaloids, which are precursors for the synthesis of powerful anticancer drugs like Paclitaxel [13], Docetaxel [14], etc. Cytotoxic lignans have been isolated from the heartwood of *T. baccata* (common yew) and have shown antioxidant and other activities [15]. The comparison of the bioactivity of extracts of *Taxus baccata* bark and *Juniperus sabina* fruits have revealed their similar cytotoxicity on different cancer cells [16]. These findings showed that junipers are also perspective sources of efficient cytotoxic and antioxidant agents for treatment of various malignances and other diseases.

In response to the requirements of the pharmacy in invention of new efficient bioactive agents, the present study is aimed at extraction and identification of antioxidant and antiproliferative substances as potential pharmaceutical agents from species of the genera *Juniperus* L.*,* *Cupressus* L.*,* *Chamaecyparis* Spach and *Taxus* L., growing in the Windsor Great Park, UK, and other arboretums.

EXPERIMENTAL

Materials

Chemicals and reagents. Podophyllotoxin, DPPH (2,2-diphenyl-1-picrylhydrazyl), MTT [3-(4,5-dimethylthiazol-2-yl)-2,5-diphenyltetrazo-lium bromide], Folin-Ciocalteu's reagent (2N), gallic acid, formic acid, RPMI 1640 medium were purchased from Sigma-Aldrich Co. (Saint Louis, MO, USA). Fetal calf serum for cell culture was delivered by Biochrom GmbH (Berlin, Germany), DMSO was from Fluka Chemie AG (Buchs, Switzerland). LC-MS grade solvents were purchased from Fisher Scientific (USA) and Sigma-Aldrich (USA).

Plant material. Juniperus representatives and *Cuprocyparis notabilis* were delivered in June 2018 from the Windsor Great Park, London, UK. Their specimen numbers are given in Table 1. *Taxus baccata*, *Cupressus arizonica*, *Chamaecyparis lawsoniana* and *Chamaecyparis pisifera* were obtained in February 2018 from the Arboretum of the University of Forestry, Sofia, Bulgaria. Voucher specimen of the plants of Bulgarian origin were deposited in the Herbarium (SOM) of the Institute of Biodiversity and Ecosystem Research, Bulgarian Academy of Sciences. The plant species were authenticated by R. P. Adams and A. N. Tashev (Table 1).

Experimental procedures

Experimental procedures were carried out as it has been described previously (Ivanova *et al.* [5]) and are described here in brief.

Determination of total polyphenol content (TPC). The TPC of the extracts was determined by Folin-Ciocalteu method with minor modifications [17] and was expressed in Gallic Acid Equivalents (GAE) according to the formula:

$$C = c.V/m,$$

where C is concentration of phenolic compounds in mg GAE per gram dry extract; c – gallic acid concentration [mg/ml], calculated from the calibration curve; m – weight of the dry plant extract [g]; V – plant extract volume [ml].

Table 1. Summary of the specimens of conifers of different origin, total polyphenol content, antioxidant and antiproliferative activity of their leaves extracts.

№	Specimen number	Conifer species	Arboretum	TPC [GAE mg/g DE]	DPPH-SC$_{50}$ [µg/ml]	NB4-IC$_{50}$±SD [µg/ml]
1	1999-6149	*Juniperus virginiana* "Glauca" × "Grey Owl"	WGP	107 ±6	190	0.27±0.03
2	1999-6045	*Juniperus virginiana* "Canaertii"	WGP	134±4	151	0.31±0.03
3	2001-2555	*Juniperus × pfitzeriana* "Saybrook Gold"	WGP	86±1	282	2.3±0.2
4	2000-1308	*Juniperus pingii* var. *Wilsonii*	WGP	151±4	112	2.6±0.2
5	2000-1308	*Juniperus indica* Bertol.	WGP	320±10	52	43±2
6	1999-2968	*Juniperus recurva* "Embley Park"	WGP	213±3	71	25±1
7	1999-5914	*Juniperus davurica* "Expansa Aurea"	WGP	84±2	250	85±11
8	1999-6163	*Juniperus squamata* Buch.-Ham. ex D.Don	WGP	209±9	78	139±14
9	1999-5996	*Juniperus sargentii* "Glauca"	WGP	97±12	191	184±17
10	SOM 177 249	*Taxus baccata* L.	UFA	127±16	141	9±1
11	SOM 177 250	*Cupressus arizonica* Greene	UFA	196±4	76	62±7
12	SOM 177 251	*Chamaecyparis lawsoniana* Parl.	UFA	152±1	106	87±11
13	SOM 177 252	*Chamaecyparis pisifera* (Siebold & Zucc.) Endl.	UFA	134±4	134	145±22
14	1999-3346	*Cuprocyparis notabilis* (A. F. Mitchell.) Farjon	WGP	174±6	118	111±12

Abbreviations: WGP – Windsor Great Park, London, UK; BAS – Bulgarian Academy of Sciences; UFA – University of Forestry Arboretum, Sofia, Bulgaria; TPC – total polyphenol content; DE – dry extract; GAE – milligrams gallic acid equivalents per gram DE. Lower IC$_{50}$ and SC$_{50}$ values denote higher activity.

The TPC of each extract was determined by two independent analyses and was given as an average value ± SD (standard deviation).

Determination of antioxidant activity. The radical scavenging activity of the extracts was determined by the DPPH-method [18]. The percentage of the DPPH-inhibition by the corresponding extract was calculated according to the formula:

$$\% \ inhibition \ = \ [(Ac - As)/Ac] \times 100,$$

where *Ac* is the absorbance of the DPPH solution in the control sample without extract and *As* is the absorbance of the DPPH in the sample containing the corresponding plant extract.

The antioxidant activity of the plant extracts was analyzed by their DPPH-SC$_{50}$ (half-maximum DPPH-scavenging concentration of the extracts) – concentration of the extract that decreased the initial DPPH concentration by 50%.

An UV-1600PC spectrophotometer (VWR int.) was used for Folin-Ciocalteu and DPPH-assays.

Cell culture and MTT-test for antiproliferative activity of the plant extracts. NB-4 cells were purchased from the DSMZ (Germany). MTT-tests were carried out using a microplate reader Labexim

545

LMR1s. The antiproliferative activity of the corresponding extract was determined by analysis of its NB4-IC$_{50}$ (half-maximum growth-inhibitory concentration in NB4 cells) – concentration of the extract that decreased the initial NB4 cells growth by 50%. Positive control for MTT-test was podophyllotoxin standard with NB4-IC$_{50}$ 0.005±0.001 µg/ml. Cell proliferation was determined by MTT-assay as it was described elsewhere [19].

Data processing and statistics. The MTT data were fitted to sigmoidal concentration–response curves and the NB4-IC$_{50}$ values were calculated using non-linear regression analysis (GraphPad Prism software). Statistical processing exploited Student's t-test with p≤0.05 set as the lowest level of statistical significance. TPC and DPPH-SC$_{50}$ statistics were calculated using 'Excel 2013' software.

UHPLC/HRMS for podophyllotoxin identification. Ultra high-performance liquid chromatography (UHPLC) coupled to high-resolution mass spectrometry (HRMS) was performed on a Thermo Scientific Dionex Ultimate 3000 RSLC system connected to Thermo Scientific Q Exactive Plus mass spectrometer (Bremen, Germany), equipped with a heated electrospray ionization (HESI-II) probe (Thermo Scientific). The tune parameters in positive mode were as follows: spray voltage 3.5 kV; sheath gas flow rate 38; auxiliary gas flow rate 12; spare gas flow rate 0; capillary temperature 320 °C; probe heater temperature 320 °C and S-lens RF level 50. Acquisition was acquired at Full-scan MS and Data Dependent-MS^2 modes (ddMS^2). Full-scan spectra were obtained over the *m/z* range 100-1500 at a resolution of 70000, authomatic gain control (AGC) target and maximum ion injection time (IT) were set to 3e^6 and 100 ms, respectively. The instrument parameter settings for ddMS^2 mode were as follows: resolution 17500, AGC target 1e^5, maximum IT 50 ms, loop count 5 (TOP5), isolation window 2.0 m/z, stepped normalized collision energy (NCE) 10, 30, 60 eV. Data acquisition and processing were carried out with Xcalibur 4.0 software (Thermo Scientific). Fragmentation pathways were simulated with Mass Frontier 7.0 (Thermo Fisher Scientific). Prior to injection, samples were subjected to solid-phase purification by Sep-Pak C$_{18}$ cartridges (Waters, Ireland), using 80% (v/v) methanol. Chromatographic separation was achieved on AkzoNobel Kromasil Externity XT-1.8-C18 (Bohus, Sweden) narrow-bore column (2.1×100 mm, 1.8 µm) with Phenomenex Security Guard ULTRA UHPLC EVO C18 (Torrance, USA) at 40°C. The mobile phase consisted of systems A (0.1% formic acid in water) and B (0.1%

formic acid in acetonitrile). The following gradient was used: the mobile phase was held at 5% B for 0.5 min, gradually turned to 60% B over 22.5 min, kept at 60% B for 2 min, followed by a gradual increase to 85% B over 2.5 min, kept at 85% B over 2 min and the system was turned to the initial condition of 5% B in 0.5 min. The system was conditioned at 5% B for 4.5 min before injection. The flow rate and injection volume were 300 µL/min and 2 µL, respectively.

RESULTS AND DISCUSSION

Correlation of the total polyphenol content with the antioxidant activity of various conifers – determination of J. indica extract as superior antioxidant agent

According to the requirements of the pharmacy for identification of new efficient antioxidant agents, the present work studied the activity of extracts of widely distributed species, as well as rare representatives of *J. indica* Bertol. (black juniper), *J. squamata* Buch.-Ham. ex D. Don (Himalayan juniper, flaky juniper), *J. pingii* W. C. Cheng (Chinese juniper), *J. recurva* Buch.-Ham. ex D. Don (Himalayan juniper, drooping juniper), *J. davurica* Pall., etc., growing in the Windsor Great Park and other arboretums. The Windsor Great Park has been created in the 13th century. At present, it covers about 2020 hectares of lands, in which a large part is a conservation area with recognized value of biodiversity.

Conifers of different origin, total polyphenol content, antioxidant and antiproliferative activity of their leaves extracts are presented in Table 1. As it could be seen from the examined specimens, lowest DPPH-SC$_{50}$ values were determined for *J. indica* Bertol. (52 µg/ml), followed by *J. recurva* "Embley Park" (71 µg/ml), *C. arizonica* Greene (76 µg/ml) and *J. squamata* Buch.-Ham. ex D. Don (78 µg/ml) extracts. These findings corresponded to the highest values of their TPC. Data about the total polyphenol content of the studied juniper leaves extracts are presented in Figure 1.

A polynomial function was derived in order to describe the correlation between the TPC and half-maximum DPPH-radical scavenging concentrations of the corresponding extracts (Figure 2). Lower DPPH-SC$_{50}$ values denote higher activity and correspond to higher TPC values. In summary, the comparison of the polyphenol content and radical-scavenging activities of the extracts revealed *J. indica* (the black juniper) leaves extract as a superior antioxidant agent, exhibiting best TPC and DPPH-SC$_{50}$ values among the studied species.

Moderate radical scavenging activity and cytotoxicity have been observed previously for *J. recurva* Buch.-Ham. ex D. Don extracts [20].
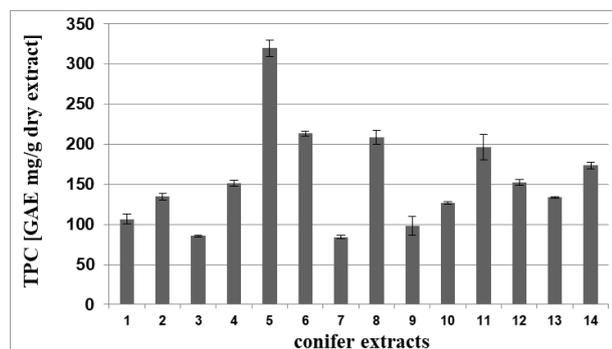
Figure 1. Comparison of the total polyphenol content of the studied conifer leaves extracts. Conifer extracts (**1-14**) correspond to the numbers in Table 1.
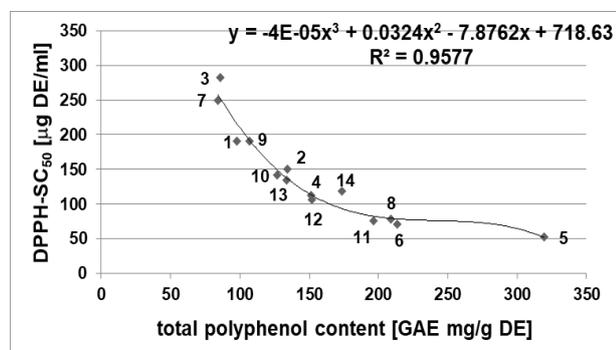
Figure 2. Graphical presentation of the polynomial function derived as a correlation of the total polyphenol content of the studied conifer leaves extracts with their DPPH-radical scavenging half-maximum concentrations. Conifer extracts (**1-14**) correspond to the numbers in Table 1.

The fruit oil of *Cupressus arizonica* Greene and extracts from the bark of *Chamaecyparis lawsoniana* (A. Murray) Parl. (Lawson cypress) have shown also remarkable antioxidant activity [21, 22]. To our knowledge, this study is the first observation about the remarkable antioxidant activity of *J. indica*. The black juniper is a rare plant, grown in the Windsor Great Park, but it exists naturally at high-altitudes of the Himalayas (as high as 5200 m a.s.l.) and the Tibetan Plateau.

Identification of conifers with efficient antiproliferative activity in NB4 APL cells.

The anticancer drug precursor podophyllotoxin (PPT) with efficient antiproliferative properties has been detected in many *Juniperus* species, such as *J. virginiana* L. [23], *J. × media* Pfitzeriana (Spath) Schmidt [24], *J. horizontalis* Moench, *J. scopulorum* Sarg. [25], etc. In this study, the antiproliferative activity of the studied conifer extracts was analyzed by MTT tests after treatment of NB4 APL (acute

promyelocytic leukemia) cells, bearing t(15;17) PML-RARA fusion gene with oncogenic properties. The comparative analysis of the NB4-IC_{50} values of the studied leaves extracts revealed the best antiproliferative activity of *J. virginiana* cultivars ('Canaertii', 'Glauca × Grey Owl') with NB4-IC_{50} values in the range of 0.27-0.31 μg/ml. In addition, high activity in NB4 cells was found also for the extracts of *J. × pfitzeriana, J. pingii* var. *wilsonii* and *T. baccata* representatives with IC_{50} values in the range of 2-9 μg/ml. This study revealed that the leaves extracts of *J. virginiana, J. × pfitzeriana* cultivars and *J. pingii* var. *wilsonii*, distinguished here as the best cytotoxic agents among the studied species, showed even higher antiproliferative activity in comparison with the *T. baccata* leaves extract (Table 1). Rare species of the Windsor Great Park, such as *J. indica* and *J. recurva* "Embley Park" also showed remarkable antiproliferative activity.

Podophyllotoxin was identified in the extracts of *J. virginiana* and *J. × pfitzeriana* cultivars, which demonstrated the best antiproliferative activity in this study. Using UHPLC- HRMS, the exact mass of the protonated molecule $[M+H]^+$ of PPT was detected in the full scan spectrum at *m/z* 415.1385 (the calculated *m/z* for $C_{22}H_{23}O_8$ is 415.1387), while its characteristic ion fragments at *m/z* 397.1267, 313.1068, 282.089 and 247.0603 appeared in the MS^2 spectrum [26]. Taxine alkaloids were identified in the *T. baccata* leaves extract in correspondence with literature data [27]. Identification of other bioactive metabolites in the most efficient antioxidant and cytotoxic extracts is in progress.

CONCLUSIONS

The Windsor Great Park is an area of recognized value of biodiversity, making it a perspective source of rare species and cultivars of scientific interest. To our knowledge, this research is the first study of the bioactivity of conifers growing in the Windsor Great Park. Their activity and bioactive metabolites were analyzed in comparison with conifers from other arboretums.

This study outlined for the first time *J. indica* leaves extract as a natural agent with superior total polyphenol content and antioxidant properties.

Highly efficient antiproliferative activity was observed for the first time in NB4 acute promyelocytic leukemia cells for the leaves extracts of *J. virginiana* ('Canaertii', 'Glauca x Grey Owl'), *J. × pfitzeriana* cultivars and *J. pingii* var. *wilsonii*. These agents showed excellent cytotoxic activity that was even at higher values in comparison with the activity of the *T. baccata* leaves extract containing taxine alkaloids. Rare species of the

WGP, such as *J. indica* and *J. recurva* "Embley Park", also showed remarkable antiproliferative activity. Podophyllotoxin was identified in the extracts of *J. virginiana* and *J. × pfitzeriana* cultivars. Identification of other metabolites and quantitative analysis of the bioactive substances, identified in the best cytotoxic and antioxidant extracts, are in progress. The conifer extracts, selected in this study as efficient antioxidant and antiproliferative agents, are potential natural sources of lead compounds for the drug industry.

REFERENCES

1. M. Ramadass, P. Thiagarajan, *Research J. Pharm. and Tech.*, **8**, 1714 (2015).
2. a. R.P. Adams, Junipers of the World: The Genus *Juniperus*, 4th edn., Trafford Publishing Co., Bloomington, Indiana, USA, 2014. b. A. Farjon, World checklist and bibliography of conifers, 2nd edn., Royal Botanic Gardens, Kew, London, UK, 2001.
3. G. Krüssmann, Manual of cultivated conifers, Timber Press, Portland, Oregon, USA, 1991.
4. A.M.L. Seca, A.M.S. Silva, in: Recent progress in medicinal plants, J.N. Govil, V.K. Singh (eds.), Studium Press LLC, Texas, Houston, USA, 2006, vol. 16, p. 401.
5. D. I. Ivanova, A. N. Tashev, P. T. Nedialkov, Y. E. Ilieva, T. N. Atanassova, M. Olech, R. Nowak, G. Angelov, F. V. Tsvetanova, I. A. Iliev, Z. K. Kokanova-Nedialkova, G. H. Yotov, *Bulg. Chem. Commun.,* **50C**, 144 (2018).
6. a. R. Mothana,, R. Gruenert, P. J. Bednarski, U. Lindequist, *Pharmazie*, **64,** 260 (2009); b. S. Rguez, R. Essid, A. Papetti, K. Msaada, M. Hammami, K. Mkadmini, N. Fares, O. Tabbene, S. Elkahoui, D. Portelli, R. Ksouri, I. H. Sellami, *Ind. Crops Prod.,* **131,** 194 (2019); c. S. Aazza, B. Lyoussi, M. G. Miguel, *Molecules,* **16**, 7672 (2011).
7. N. A. Ibrahim, H. R. El-Seedi, M. M. D. Mohammed, *Nat. Prod. Res.,* **21**, 857 (2007).
8. A. T. Mbaveng, V. Kuete, B. M. Mapunya, V. P. Beng, A. E. Nkengfack, J. J. M. Meyer, N. Lall, *Environ. Toxicol. Pharmacol.,* **32**, 162 (2011).
9. G. R. Pettit, R. Tan, J. S. Northen, D. L. Herald, J.-C. Chapuis, R. K. Pettit, *J. Nat. Prod.,* **67**, 1476 (2004).
10. Y. Arima, A. Hatanaka, S. Tsukihara, K. Fujimoto, K. Fukuda, H. Sakurai, *Chem. Pharm. Bull.,* **45**, 1881 (1997).
11. a. C.-C. Hsieh, Y.-H. Kuo, C.-C. Kuo, L.-T. Chen, C.-H.A. Cheung, T.-Y. Chao, C.-H. Lin, W.-Y. Pan, C.-Y. Chang, S.-C. Chien, T.-W. Chen, C.-C. Lung, J.-Y. Chang, *Biochem. Pharmacol.,* **79**, 1261 (2010); b. Y.-H. Kuo, C.-H. Chen, Y.-M. Chiang, *Tetrahedron Lett.,* **42**, 6731 (2001).
12. P. Marimuthu, C.-L. Wu, H.-T. Chang, S.-T. Chang, *J. Sci. Food Agric.,* **88**, 1400 (2008).
13. V. D. Nikolic, I. M. Savic, I. M. Savic, L. B. Nikolic, M. Z. Stankovic, V. D. Marinkovic, *Cent. Eur. J. Med.*, **6**, 527 (2011).
14. a. V. Georgoulias, *Curr. Med. Chem.,* **9**, 869 (2002); b. P. Fumoleau, A.D. Seidman, M.E. Trudeau, B. Chevallier, W. W. Ten Bokkel Huinink, *Expert Opin. Investig. Drugs,* **6,** 1853 (1997).
15. N. Kucukboyaci, I. E. Orhan, B. Şener, S. A. Nawaz, M. I. Choudhary, *Z. Naturforsch., C, Biosci.*, **65**, 187 (2010).
16. M. Shokrzadeh, M. Azadbakht, N. Ahangar, H. Naderi, S. S. Saeedi Saravi, *Pharmacogn. Mag.,* **6,** 102 (2010).
17. a. O. Folin, V. Ciocalteu, *J. Biol. Chem.,* **27**, 627 (1927); b. V. L. Singleton, R. Orthofer, R. M. Lamuela-Raventos, *Meth. Enzymol.,* **299**, 152 (1999); c. A. L. Waterhouse, in: Current Protocols in Food Analytical Chemistry, R. E. Wrolstad, (ed.), vol. 1, Wiley, New York, 2001.
18. a. C. Sanchez-Moreno, *Food Sci. Technol. Int.,* **8**, 121 (2002); b. J. Perez-Jimenez, S. Arranz, M. Tabernero, M. Diaz-Rubio, J. Serrano, I. Gono, F. Saura-Calixto, *Food Res. Int.,* **41**, 274 (2008).
19. a. T. Mosmann, *J Immunol Methods*, **65**, 55 (1983); b. S. M. Konstantinov, H. Eibl, M. R. Berger, *Br. J. Haematol.,* **107,** 365 (1999).
20. J. Bhandari, A. Naqvi, P. Niraula, P. Thapa, N. Thapa, N. Shrestha, B. G. Shrestha, *Int. J. Pharm. Biol. Sci.,* **6**, B1134 (2015).
21. S. A. Emami, M. Fakhrjafary, M. Tafaghodi, M. K. Hassanzadeh, *J. Essent. Oil Res.,* **22**, 193 (2010).
22. H. Gao, T. F. Shupe, C. Y. Hse, T. L. Eberhardt, *Holzforschung*, **60**, 459 (2006).
23. a. K. E. Cushman, M. Maqbool, P. D. Gerard, E. Bedir, H. Lata, R. M. Moraes, *Planta Med.,* **69**, 477 (2003); b. A. J. Gawde, C. L. Cantrell, V. D. Zheljazkov, *Ind. Crops Prod.,* **30,** 276 (2009).
24. S. Kusari, S. Zühlke, M. Spiteller, *Phytochem. Anal.,* **22,** 128 (2011).
25. V. D. Zheljazkov, C. L. Cantrell, M. A. Donega, T. Astatkie, B. Heidel, *HortScience*, **47**, 1696 (2012).
26. T. J. Schmidt, S. Hemmati, E. Fuss, A. W. Alfermann, *Phytochem. Anal.,* **17,** 299 (2006).
27. L. H. D. Jenniskens, E. L. M. van Rozendaal, T. A. van Beek, P. H. G. Wiegerinck, H. W. Scheeren, *J. Nat. Prod.,* **59,** 117 (1996).

Influence of amphotericin B on the physicochemical properties of model lipid membranes

M. Dencheva-Zarkova*, J. Genova

Institute of Solid State Physics, Bulgarian Academy of Sciences, 72 Tzarigradsko Chaussee Blvd., 1784 Sofia, Bulgaria

Amphotericin B (AmB) is a widely used antifungal antibiotic and has been extensively studied over the last decades due to its superior properties. However, the mechanism of action of AmB on the biological cell is still not completely understood. It is well known that the interaction of the antibiotic with the lipid membrane induces formation of anion-selective pores thus significantly increasing the permeability for ions through lipid cell membrane. The aim of the present work is to study the influence of AmB antibiotic on the phase behavior and the channel formation activity of the synthetic lipid membrane. The ability of AmB to form ion channels in lipid bilayers is studied by tip-dip patch clamp technique. We observed that AmB reduces the electrical resistance of the lipid membrane. The phase transition temperatures and corresponding enthalpies are obtained *via* differential scanning calorimetry. The obtained results show that the presence of AmB has a significant influence on the phase behavior of the lipid system.

Keywords: Amphotericin B, lipid membrane, phase behavior, enthalpy, ion channel.

INTRODUCTION

Amphotericin B (AmB) is one of the main polyene antibiotics widely used to treat deep-seated fungal infections [1]. The antibiotic is designated chemically as (1R,3S,5R,6R,9R,11R,15S,16R, 17R,18S,19E,21E,23E,25E,27E,29E,31E,33R,35S, 6R,37S)-33-[(3-amino-3,6-dideoxy-β-D-manno pyranosyl)oxy]-1,3,5,6,9,11,17,37-octahydroxy-15, 16, 18-trimethyl-13-oxo- 14,39-dioxabicyclo [33.3.1] nonatriaconta- 19,21,23,25,27,29,31-heptaene-36-carboxylic acid.

AmB was originally extracted in 1955 from *Streptomyces nodosus*, a filamentous bacterium, at the Squibb Institute for Medical Research from cultures of an undescribed streptomycete isolated from the soil collected in the Orinoco River region of Venezuela. Infections as a consequence of weakened immunity defense, such as from AIDS or from many cancer therapies, have renewed the scientific studies on the polyene antibiotic amphotericin B (AmB). The mechanism of biological action of AmB is most probably directly related to the ability of the drug to form hydrophilic pores in the hydrophobic membrane core, where it increases the permeability of the cells to ions and small molecules [2].

However, the detailed molecular mechanisms of the interaction of AmB with the membrane, as well as the formation of a transmembrane pore structure, are still imperfectly understood. The molecular structure of AmB used in the study is shown in Fig. 1.
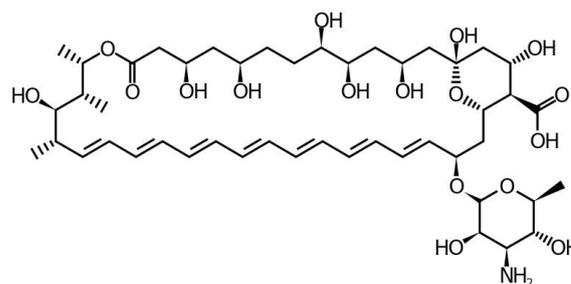
Fig. 1. Structure of the antibiotic amphotericin B

The molecule features a lactone ring containing conjugated double bonds, a chain of hydrophilic groups, and two ionizable groups - a carboxyl and a mycosamine.

The antibiotic forms channels in lipid membranes and has conducting and nonconducting states, with frequent transitions between them. One can induce a rise in conductance with amphotericin B on one or both sides of the planar bilayer membranes [3]. When the antibiotic is added to both sides, the electrical conductance is much higher and the permeability of univalent anions is larger than that of the cations [4]. When the antibiotic is added to only one side, it is selective to univalent cations.

Amphotericin B forms two types of channels that are structurally very similar but differ in length. It is assumed that the channels are formed by one or two "barrels" consisting of antibiotics and incorporated lipid molecules, with the long axes oriented perpendicularly to the membrane surface [5].

* To whom all correspondence should be sent:
E-mail: *biolayer@issp.bas.bg*

The hydrophilic, charged, and hydrophobic sides of the antibiotic molecules are turned toward the water pore, water, and lipid phase, respectively. The one-sided action is attributable to channels having essentially the same structure as those formed by the two-sided action, except that only one "barrel" (half-pore) spanned the bilayer to form a functional channel. The two-sided channels are formed by two barrels bound end to end in the membranes [3, 6, 7].

The open channel does not undergo overall rearrangements, such as a change in the number of molecules in the pore or channel from the open to the closed state, it is probably not the result of such rearrangements, but may be caused by shrinking of the pores [8], those formed by the two-sided action, except that only one "barrel" (half-pore) spanned the bilayer to form a functional channel [5, 6].

Artificially created lipid vesicles mimic the cell membrane. They present a simple model for investigation of membrane properties and can be formed from various lipids with controlled composition in controlled environment. With a better understanding of AmB mechanism of action on model lipid membranes we will have a clearer image on how this antibiotic interacts with living cells.

The aim of the present study is to investigate the effect of amphotericin B (AmB) on the physicochemical properties of model lipid membranes formed from synthetic lipids.

MATERIALS AND METHODS

L-α-lecithin from soybean (choline content 20%), and amphotericin B were obtained from Sigma, HEPES. KCl (p.a.), n-propanol (p.a.) and n-hexane (p.a.) were purchased from Valerus Co. The synthetic lipid 1-stearoyl-2-oleoyl-sn-glycero-3-phosphocholine (SOPC) 18:0/18:1 was purchased from Avanti Polar Lipids Inc. (Alabaster, Alabama, USA). The solvents, chloroform (purity 99%) and methanol (purity 99:8%), were purchased from Sigma-Aldrich Corporation, part of Merck & Co., Inc. (Kenilworth, USA). All the chemicals were used without any further purification.

Patch-clamp technique

Lipid bilayers were self-assembled at the tips of patch pipettes, using the tip-dip patch clamp technique, from monolayers formed by spreading L-α-lecithin from soybean in n-hexane (10 mg ml^{-1}) onto the surface of electrolyte solutions contained in Petri dishes (Fig. 2).
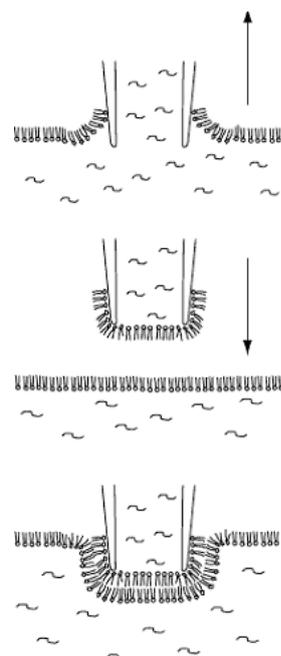
Fig. 2. Scheme of lipid bilayer formation at the tip of a patch pipette

Patch pipettes (tip diameter 1-2 μm) and Petri dishes (10 cm^2 area) were filled with aqueous solutions of KCl (0.1M) buffered with HEPES (0.01M) at pH 7. Only bilayers with seal resistances >1 GΩ were used. AmB dissolved in n-propanol:distilled water (4:6, v/v), was added to the Petri dish after bilayer formation to a final concentration of 5×10^{-6} M and 8×10^{-4}M.

Single AmB channel currents were monitored using a patch clamp amplifier Model 2400 (A-M Systems, Inc.) and patch clamp software. The currents were stored on a PC hard disc with 1 ms time resolution. All measurements were performed at room temperature (~20°C).

Differential scanning calorimetry

Differential scanning calorimetry (DSC) was used to study the influence of amphotericin B on the phase behavior of the SOPC lipid system. DSC is an experimental method that determines the difference in heat required to increase the temperature of an examined sample and a reference as a function of temperature. When the sample under consideration experiences a phase transition, a certain amount of heat flows to the reference sample in order to maintain both samples at the same temperature [10, 11]. Comparing the heat flows during a phase transformation identifies the process as being exothermic (heat is generated) or endothermic (heat is absorbed). The output from the DSC measurements consists of the heat required to maintain both cells containing the samples, at the

same temperature converted into heat flow, or equivalently heat capacity. The values of the changes in the thermodynamic quantities, such as enthalpy, entropy, and heat capacity at any transition might be deduced from the ensuing calorimetric data.

SOPC was dissolved in chloroform, while AmB antibiotic was dissolved in methanol. The final lipid–cholesterol solution was prepared by mixing SOPC and AmB in the desired molar proportion for every AmB concentration. The investigated quantity of the final lipid/antibiotic solution was placed in a flask that was places under vacuum for about 4 – 5 h until the entire solvent evaporation. Then, the appropriate amount of double-distilled water was added to the dry lipid/AmB film and the samples were positioned in a warm (40 – 45°C) ultrasonic bath for at least 2 h to hydrate the lipid film and achieve homogeneity of the lipid-water mixture. For all AmB concentrations, the samples were prepared to contain 20 wt.% of water (80 wt.% of the lipid/AmB mixture).

RESULTS AND DISCUSSION

Patch clamp technique

Lecithin bilayers were used to study the effect of AmB channels formed by several molecules self-assembled into a "bundle" structure which traverses the lipid bilayer. Incorporation of AmB molecules into the hydrophobic core of the membrane results in the formation of molecular aggregates, which probably take the form of hydrophilic pores composed of six to nine molecules.

Fig. 3. Record showing two types (A, B) of amphotericin B channels in a lecithin bilayer. Transmembrane potential 100 mV. A - AmB concentration 5×10^{-6} M; B - AmB concentration 8×10^{-4}M.

Differential scanning calorimetry

For the investigation of the influence of amphotericin B antibiotic on the thermal behavior of the synthetic SOPC lipid system DSC measurements at three different molar

concentrations of AmB in the lipid system were performed - 10^{-5} M, 10^{-3} M and 10^{-1} M, respectively. Special attention was paid to the heating rate and incubation procedure. The amount of AmB in the membrane was chosen to match the conditions of the channel formation experiments, performed by patch-clamp technique. The influence of water content on the thermograms of pure SOPC was studied in detail [12]. It was shown that the optimal water content in the lipid-water samples is from 10 to 20 wt.%. We used 20 wt.% of water in all the experiments with all three molar concentrations of AmB. The used DSC equipment was Discovery 250 (TA Instruments, USA). The optimal quantity of the investigated sample, typically 20-30 mg, was inserted in the special DSC pan. The pan containing SOPC sample was closed with a hermetic cover and matched with the reference pan. The incubation procedure for all the performed experiments consisted of inserting the sample at room temperature in the DSC oven and heating from 30°C to 50°C then the sample was cooled at a rate of 5 °C min^{-1} from 50 to −10° C. The sample was further heated up at a rate of 5 °C min^{-1} from −10 °C to 70 °C.

On Fig. 4 the obtained thermograms at heating for 10^{-5} M, 10^{-3} M and 10^{-1} M AmB in the lipid matrix, respectively, are shown in the temperature range where the phase transition peaks are seen (from 3 to 40 °C).

On Fig. 5 the thermogram for pure SOPC lipid system, obtained at identical conditions (water content, heating rate, etc.) as those in presence of AmB, is shown for comparison [12]. As it can be seen from the obtained thermogram, even at the least amount of amphotericin B in the lipid matrix, (10^{-5} M AmB in the SOPC system, down left picture on Fig. 4) the phase behavior of the system substantially changes. The sharp shape of the transition observed for pure SOPC (Fig. 5) is smeared out and split into several less pronounced peaks.

As the concentration of AmB within the lipid membrane increases, the behavior of the phase transition curve does not change significantly. The peaks remain 2-3 with a slight change in the locations of their maxima and their relative intensities. In Table 1 the obtained main transition temperatures of the most pronounced peaks for all studied systems and the corresponding enthalpies are presented.
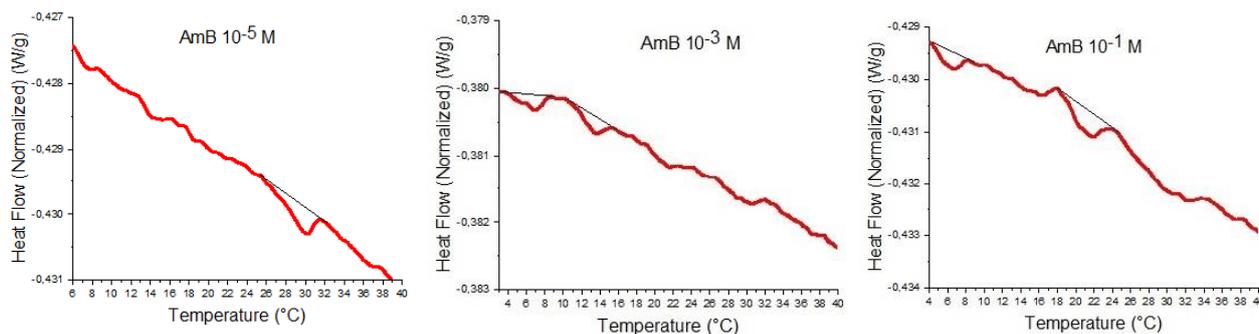
Fig. 4. DSC thermograms for SOPC with various molar concentrations of AmB at heating.
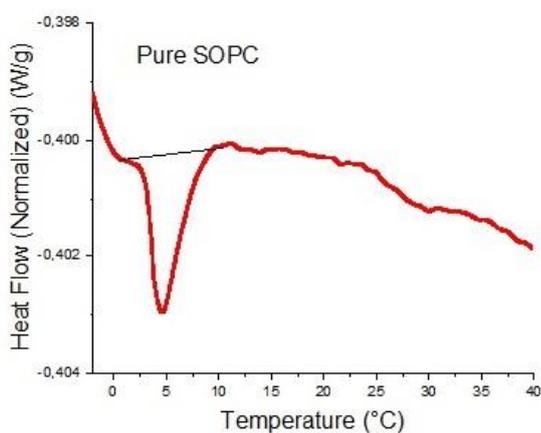
Fig. 5. DSC thermogram for pure SOPC at heating for comparison.

Table 1. Thermodynamic quantities (phase transition temperatures and associated enthalpies) derived from DSC measurements for SOPC lipid–AmB antibiotic samples. All the samples contain 20 wt. % double distilled water.

Sample	Temperature [°C]	Enthalpy [J.g^{-1}]
Pure lipid	4.6	0.147
10^{-5} AmB	30	0.012
10^{-3} AmB	6.9; 13.5	0.007; 0.03
10^{-1} AmB	6.6; 21.5	0.01; 0.017

The values for pure SOPC lipid are given for comparison [12]. Analyzing the obtained values for the peak positions and enthalpies it is seen that with the addition of AmB in the lipid matrix the typical peak of the phase transition from L$_\beta$ to L$_\alpha$ phase at around 5°C for SOPC lipid is not only split into several peaks, but also slightly shifted towards higher temperatures, resulting with at least one order of magnitude lower enthalpies. Similar phase transition temperature shift, but in the opposite direction is observed with addition of cholesterol in the lipid membrane [13]. It was reported in the literature [14] that the addition of hydrophobic gold nanoparticles in the lipid membrane results in a comparable smearing of the transition thermograms.

CONCLUSIONS

Patch-clamp technique measurements showed that amphotericin B reduces the electrical resistance of the lipid membrane. AmB forms ion channels in the lipid membrane with millisecond dwell times in the lipid membrane. The obtained volt-ampere characteristics were linear over a range of ± 100 mV.

The rate of rise of the membrane conductance for small times is proportional to the rise in the antibiotic concentration. The addition of a higher concentration of AmB drastically reduced the membrane resistance.

The experiment provided further evidence in support of the widely held view that at high concentrations of the antibiotic AmB will drive the membranes into a state of instability. It is possible that at these large concentrations, large pores are formed, perhaps by confluence of the small pores.

By means of differential scanning calorimetry aiming to investigate the influence of amphotericin B on the thermal properties of SOPC phospholipid, we have found that even a very small amount of AmB, inserted in the phospholipid SOPC, is enough to substantially modify the structural and dynamical properties of the phosphatidylcholine bilayer system. It was shown that AmB antibiotic, when added to the SOPC lipid system, smears out the phase transition curve and splits it into several less pronounced peaks, slightly shifts the main phase transition temperature and significantly reduces the transition enthalpy.

REFERENCES

1. J. Brajtburg, W. G. Powderly, G. S. Kobayashi, G. Medoff, *Antimicrobial Agents and Chemotherapy,* **34**,183 (1990).

2. L. N. Ermishkin, K. M. Kasumov, V. M. Potseluyev, *Biochim. Biophys. Acta,* **470**, 357 (1977).
3. J. Bolard, *Biochim. Biophys. Acta,* **864** 257 (1986).
4. M. P. Borisova, R. A. Brutyan, L. N. Ermishkin, *J. Membrane Biol.,* **90**, 13 (1986).
5. A. Finkelstein, R. Holz, in: Membranes: Lipid Bilayers and Antibiotics, G. Eisenman (ed.), vol. 2, New York, Marcel Dekker, Inc., 1973. p. 377.
6. R. A. Brutyan, P. McPhie, *J. Gen. Physiol.,* **107**, 69 (1996).
7. B. E. Cohen, *J. Membrane Biol.,* **238,** 1 (2010).
8. V. Khutorsky, *Biophys. J.,* **71**, 2984 (1996).
9. G. Fujii, J.-En Chang, T. Coley, B. Steere, *Biochemistry,* **36**, 4959 (1997).
10. T. M. Koyama, C. R. Stevens, E. J. Borda, K. J. Grobe, D. A. Cleary, *Chem. Educator,* **4**, 12 (1999).
11. S. M. Ohline, M. L. Campbell, M. T. Turnbull, S. J. Kohler, *J. Chem. Ed.*, **78(9)**, 1251 (2001).
12. J. Genova, Z. Slavkova, H. Chamati, M. Petrov, *Phase Transit.,* **92 (4),** 323 (2019).
13. J. Genova, Z. Slavkova, H. Chamati, M. Petrov, *Journal of Surfactants and Detergents,* **22**, 1229 (2019).
14. J. Genova, Z. Slavkova, H. Chamati, *Coll. Surf. A,* **603,** 125090 (2020).

Advances in particle size analysis with transmitted light techniques

D. Wirz, H.-J. Bart

Thermische Verfahrenstechnik, TU Kaiserslautern, Germany

Particle size distributions (PSD) play a key role in many multiphase processes, but a quantitative analysis is a challenging task, especially due to a lack of reliable measurement techniques. The Optical Multimode Online Probe (OMOP) for droplet size analysis based on a shadowgraphic transmitted light approach was further developed for bubbles or solids in liquids or even droplets in sprays. A key problem for laboratory scale measurement techniques are industrial processes conditions like elevated temperature and pressure. This article gives an overview on the developments, for example with a bubble column where pressures up to 5 bar influence the bubble size, a crystallizer where the transient PSD can be a direct property of the product and a stirred pump-mixer-settler where the pumping behavior and impeller design has a direct effect of the droplet size.

INTRODUCTION

Multiphase flows dominate a vast majority of processes in chemical and process industry, while the particulate phase can either be a fluid or a solid and the continuous phase can either be gaseous or liquid. The particulate properties of the disperse phase have an important effect on (reactive) mass transfer, particulate growth, aggregation and breakup. Therefore, the particulate state is important for the performance of a process and the product quality and yield or any product property (size, shape, etc.).

A review on measurement of the PSD is given elsewhere [1, 2] but the majority of measurement techniques uses optical techniques based on laser light or imaging techniques, the latter with the use of a digital camera. Commercial incident light techniques are offered by Mettler Toledo Inc. [3], SOPAT GmbH [4] and Pixact Ltd [5] and as laser-optical probe, the Focus Beam Reflectance Measurement [6], by Mettler Toledo Inc. In this article an alternative shadowgraphic setup with telecentric lenses instead of an incident light technique will be discussed in detail in the following.

Telecentric shadowgraphic technique

A new telecentric shadowgraphic setup was reported in 2013 for the measurement of droplet size distribution (DSD) in extraction columns [7, 8] and is called the Optical Multimode Online Probe (OMOP) [9]. This first version is executed as a flange that is placed between the glass compartments in laboratory scale, as depicted in Fig. 1. The measurement flange consists of two tubes with protection windows in the front that are diametrically inserted in the flange. The tubes are adjustable and provide a flexible measurement volume and position. The LED illumination unit emits a parallel light bundle through a plano-convex lens. The camera with the telecentric lens is positioned in the opposite site and captures the images. The tubes are sealed *via* dynamic sealings and can therefore be adjusted during the process and positioned *via* a fixing screw. This setup delivers pictures with a high contrast between the particles (dark) and the background (bright), examples are given later in Figs. 5, 8 and 12.

In addition, the telecentric lens has a distance-independent magnification (telecentric principle), therefore the shadowgraphic projection of captured particle size is not influenced by their distance to the lens [10]. This is a common drawback with endocentric lenses that are used in commercially available probes, requiring accurate calibration and advanced image algorithm that deals with the distortion in size and blurriness [11, 12]. In addition, telecentric lenses provide high accuracy of 8.2% for droplets down to 8 µm [13]. In addition, telecentric lenses provide higher depth of fields [10] resulting in a better image quality allowing to detect more particles, which are easier to evaluate with image processing tools.

The main advantage of endoscopic probes is their easy integration, as they are inserted in any apparatus *via* a nozzle-spout. Two endoscopic probes (see Fig. 2) were built in the recent years to overcome the drawback of tedious flange integration when using one-sided access. These probes integrate all features of the telecentric shadowgraphic principle and are less invasive and can be designed in any dimension (even as a small laboratory probe [14]) and are

---

* To whom all correspondence should be sent:
E-mail: dominic.wirz@mv.uni-kl.de

completely inline adjustable in terms of depth of field, measurement volume and illumination. Their integration into different processes will be discussed with different case studies.
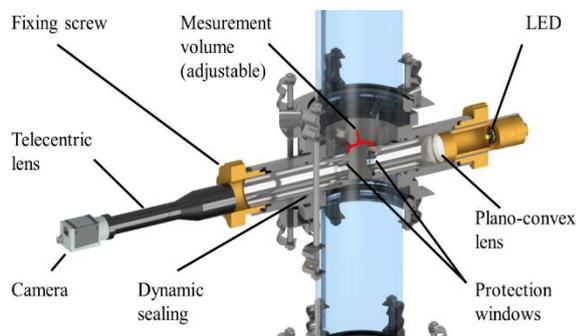
Figure 1. Cut through a DN100 shadowgraphic measurement flange.
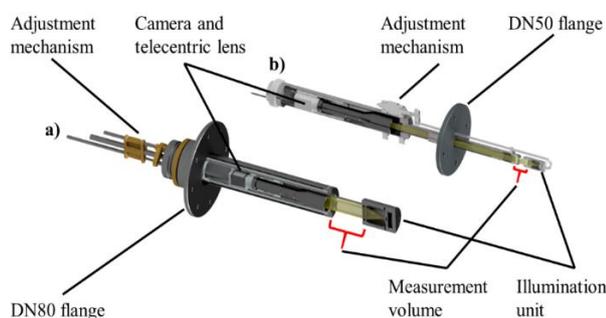
Figure 2. Endoscopic shadowgraphic probes in a) DN80; b) DN50.

Case Studies

Bubble Column

Bubble size distributions (BSD) markedly influence gas-liquid mass transfer area [15] and little is reported besides integral gas holdup for industrial relevant processes. Studies of the BSD are commonly found in lab-scale rectangular bubble columns [16–19] but investigations in closed systems or at industrial relevant conditions are rarely found. In order to demonstrate the applicability of the shadowgraphic principle a semi-batch bubble column with a special measurement flange (see Fig. 3) is built for process conditions up to 100 bar and 650K, with a height of 2100 mm and a perforated plate gas distributor (97 × 700 μm holes in 10 mm distance). The measurement flange is 860 mm above the gas distributor which is delivering in-house pressured air controlled by a mass flow controller (MFC). The liquid phase is demineralized water with an initial liquid height of 1050 mm and equals about 8.2 L and the working pressure that can be adjusted *via* the valve at the column top. Experiments were performed for different superficial gas velocities and overpressure in the homogeneous regime.

The probe head (see Fig. 4) has a smaller diameter than the probe body to minimize invasivity. The front of the probe contains the inspection window made of a thermally toughened glass (Metaglas®, Fa. Huberts Industrieglas) that resists 280°C and 100 bar. The measurement volume is now fixed as no polymer exists allowing a dynamic sealing. Static sealings together with spacers are used for a measurement volume of 12 mm in width.
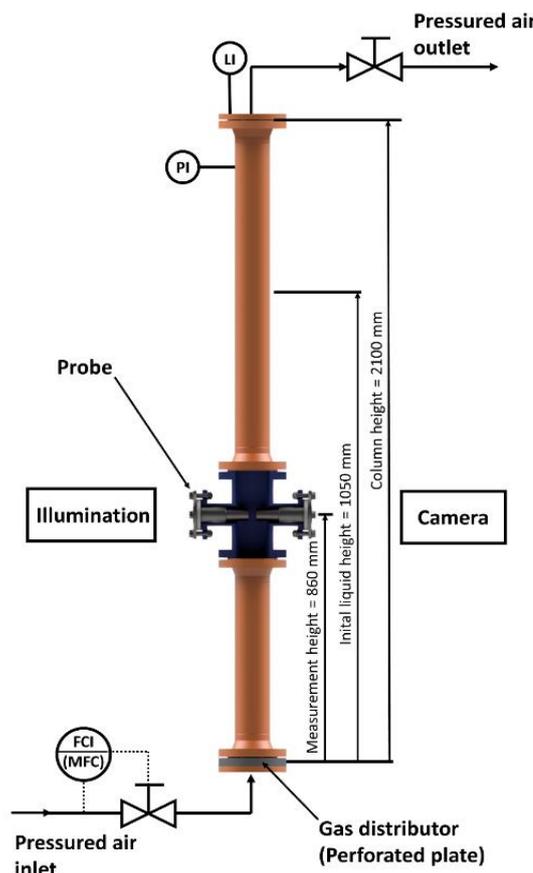
Figure 3. DN100 semi-batch bubble column.
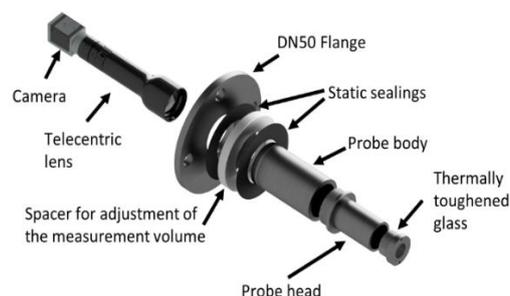
Figure 4. Pressure and temperature stable probe tube with affixed measurement volume.

For the evaluation of the acquired images the following subsequent image algorithm results are given in Fig. 5. The acquired pictures were binarized and the particle areas are blackened with a fill holes

algorithm to prevent segmentation errors in a standard watershed algorithm, where the particles are separated [20].

A size of 1 mm in diameter is the lower threshold for the detection to exclude dust and fragments in the image and additionally a form parameter C_i was used in the range of 0.7 - 1 to exclude non-segmented or erroneous segmented bubbles.
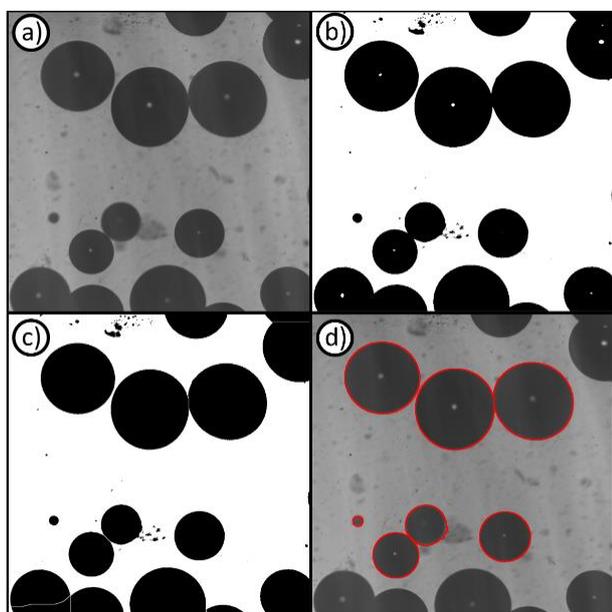
Figure 5. Basic particle detection algorithm based on binary operations. a) original image, b) binary image, c) fill holes and watershed, d) particle detection.

The circularity, C_i, is the roundness of an object and has a value between 0 and 1, where 1 is a perfect circle. It is defined with the perimeter, *U,* and the area, *A:*

$$Ci = 4\pi \frac{A}{U^2} \qquad (1)$$

As can be seen in Fig. 6, at a superficial gas velocity of $u_g = 2.1$ cm/s an increasing pressure results in a closer BSD with a decreasing mean diameter, as was expected. The mean bubble size decreases from about 5.4 mm at 0 bar pressure to 3.8 mm at 5 bar overpressure in the volume distribution. The pressure difference from 0 bar to 1 bar decreased the bubble mean diameter by 9.2%, from 5.4 mm to 4.9 mm. This shows that even small changes in pressure like the hydrostatic pressure in industrial columns can significantly change the bubble diameter [21].

Crystallizer

The crystal size distribution (CSD) and the final crystal form are decisive for the desired product quality [22] and affect, e. g., the downstream

processing [23, 24] but its determination is still a challenge. In regard to this the shadowgraphic probe was inserted in a 25 L double-jacket draft tube crystallizer with a propeller type stirrer with a diameter of 150 mm stirring at 250 rpm as depicted in Fig. 7. In order to ensure that a similar suspension is measured, the bypass inlet is directly above the probe.
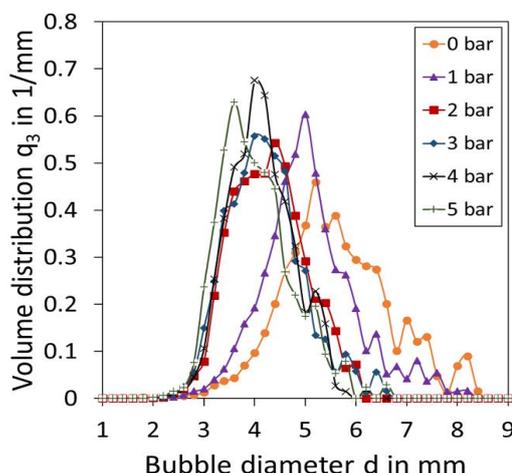
Figure 6. Bubble size distribution; $u_g = 2.1$ cm/s; overpressure between 0 bar and 5 bar.

FTIR was used for concentration measurement and the CSD was detected with a QICPIC online microscope (Fa. Sympatec, Germany) in a bypass and the DN50 shadowgraphic probe (see Fig. 7).
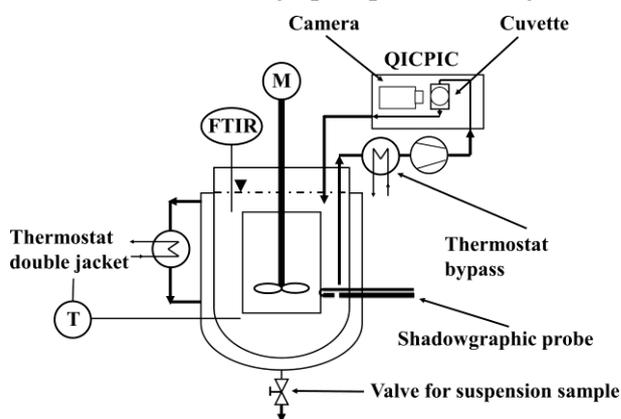
Figure 7. Setup of the 25 L double jacket draft tube crystallizer.

The measurement width in the flow cuvette of the QICPIC and the shadowgraphic probe are both 2 mm. Different experiments were executed in a cooling crystallization with potassium hydrogen phosphate (KH_2PO_4) which was crystallized with seeds from an initial clear aqueous solution. KH_2PO_4 forms resilient bipyramidal crystals, that were already successfully measured with the QICPIC [25, 26]. Suspension samples were taken every 5 min and

at the end of the experiment to have an alternative off-line analysis of the CSD.

Likewise, in Fig. 5 the same procedure in a MATLAB script is used. Binarization with a following background subtraction was used to remove scratches and immobile particles (see Fig. 8b). Morphological closing and fill holes was used to cover the bright areas in the particles and a

segmentation algorithm was not used (see Fig. 8c). Green are detected crystals that fit the form parameters and the red ones are sorted out by the algorithm. The evaluation is based on the body prism width L and a correction factor to consider the rotation of the crystals, as reported elsewhere [27, 28].
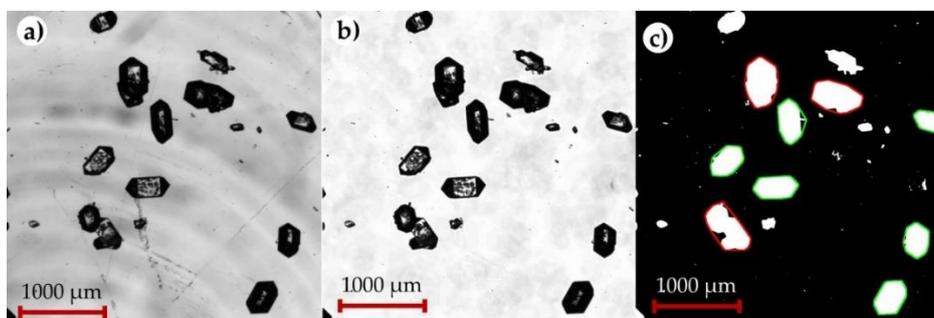
Figure 8. Image processing in MATLAB for crystals. a) original image, b) binary image, c) fill holes and morphological closing with the detection of the convex hull.

In the experiments only single crystals were evaluated, agglomerates and overlapping crystals where excluded. This was realized by using the shape descriptor convexity, *C,* in a range of 0.95-1 and the eccentricity, *ε,* between 0.4 and 1. The transient CSD of KH_2PO_4 is here shown exemplarily in Fig. 9 and more details can be found elsewhere [28]. The shadowgraphic probe and the QICPIC that was successfully applied for KH_2PO_4 in the past, gave the same results. Both diagrams show the same start where a bimodal distribution is present, which is conform with the distribution of the added seeds. With increasing experiment time, a larger fraction has grown from about 250 µm up to 280 µm, while the small number of particles increased due to secondary nucleation. These results are additionally verified by sieve analysis, that was taken during the last measurement point at a suspension density of 7 % (see Fig. 10). The sieve analysis confirms the results of the shadowgraphic probe. It was found that this is valid for different temperatures up to 58°C and suspension densities about 12%. It was also found that the shadowgraphic probe has a wider range of operation, as the bypass of the QICPIC tends to blocking, especially at higher temperatures.
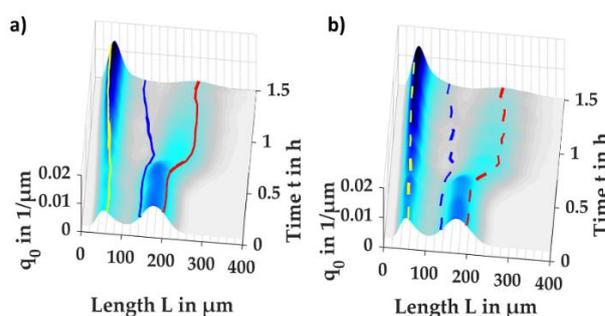
Figure 9. Transient number distribution of a) shadowgraphic probe, b) QICPIC online microscope. The percentiles are shown as following; yellow p_{10}, blue p_{50} and red p_{90}.
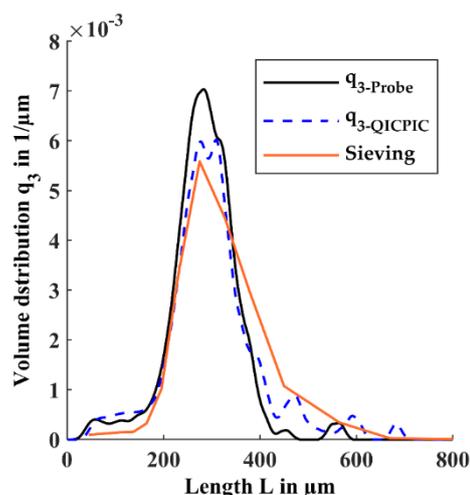
Figure 10. Comparison of the shadowgraphic probe, the online microscope, and the sieve analysis at the end of the experiment.

Pump-mixer

Pump-mixers are continuously operated stirred vessels that are used in mixer-settler cascades in solvent extraction to save pumps [29–31]. The impeller of the vessel is used to mix and pump fluids at the same time. Although these apparatuses are commonly used in industry [32] their scale-up and optimal design is based on rule-of-thumbs. Table 1 gives geometrical details of the DN300 pump-mixer-settler shown in Fig 11.

The liquid feed is controlled by two valves (V1 and V2) and measured by supersonic wave flow indicators (FI), while the two flow rates generate a so-called head Δh in the feed tanks which is measured *via* a scale. Only V2 is used to adjust the phase ratio in order to maximize the flow rate. To measure the DSD the DN50 endoscopic telecentric probe was used (see Fig. 2b). The probe is inserted from the side *via* a single sided flange at the mixer at the position depicted in Fig. 11. Demineralized water (continuous phase) with 50 mmol/L NaCl guarantees a constant electric conductivity of 8800 µS/cm and paraffin oil (FC 2006, Fa. Fauth, Germany) is the disperse phase (viscosity of 9.5 mm²/s, density of 825 kg/m³). The impeller speed was set to 400 rpm at phase ratios of 10%, 15% and 30%. The DSD is evaluated *via* a modified convolutional neuronal network as reported in [33] exemplarily shown in Fig. 12.
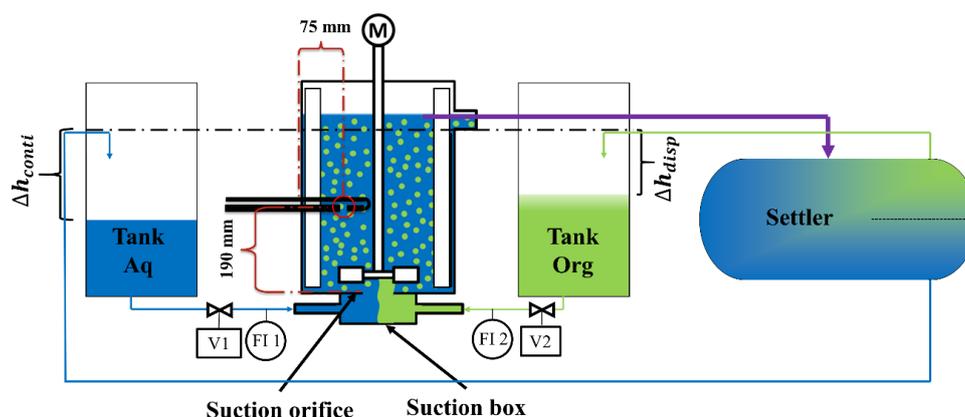
Figure 11. Experimental setup of the DN300 pump-mixer-settler.

Table 1. Pump-mixer dimensions

Tank diameter	T	300 mm
Tank height	H	350 mm
Clearance beneath impeller disc	C	20 mm
Impeller	RT	Rushton turbine (6 blades)
Impeller diameter	D	100 mm (0,3D)
Baffles 4×90°	B	30 mm × 8 mm (width × thickness)
Suction orifice	d	75 mm (0,25T)
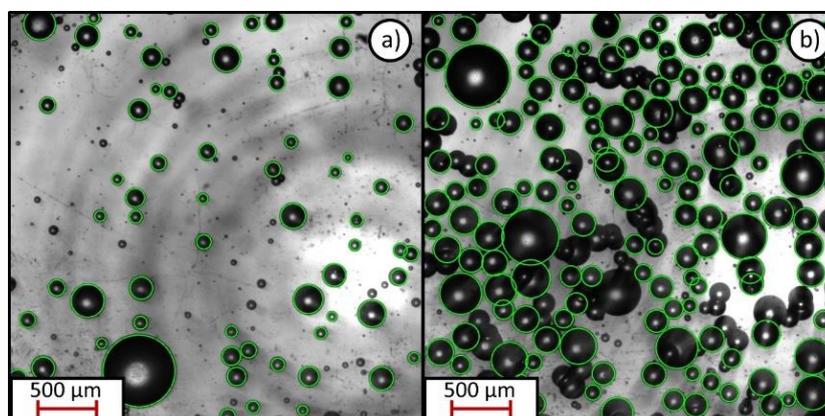
Figure 12. Droplets in the pump-mixer for a) 10% disperse phase, b) 30 % disperse phase.
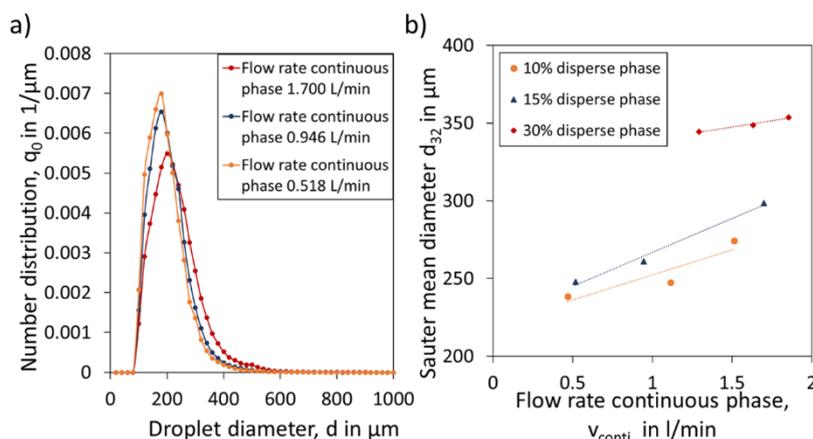
Figure 13. a) DSD for different flow rates at 15% holdup at 400 rpm; b) Sauter mean diameter d_{32} for different phase ratios and flow rates.

The DSD in liquid-liquid dispersions is usually a log-normal-distribution and depends on the flow rate (see Fig. 13a). The impeller produces constant energy dissipation, which leads to droplet breakage. Hence, at low flow rates the energy dissipation per volume of fluid is higher, therefore more droplets break and smaller droplets are produced. On the other hand, higher hold-up leads to more droplet collisions and coalescence, therefore the droplet diameter increases with a higher disperse phase content. As depicted in Fig. 13b, changes in the flow rate at low hold-up lead to significant changes in the Sauter mean diameter, while this effect seems to be less at a higher one. Nevertheless, it could be shown that the shadowgraphic probe can detect even small changes in the DSD. Further on, it was demonstrated that image processing algorithm allows the evaluation of the DSD at industrial relevant disperse phase concentrations up to 30%.

CONCLUSION

The telecentric shadowgraphic probe allows a proper determination of PSD in various apparatuses and processes with an outstanding image quality up to high particle concentrations. Additionally, the telecentric principle provides a constant magnification independent from position, hence, elaborate calibrations or complex image processing algorithms are not needed. It could be shown that this technique can be used for gas-liquid, solid liquid and liquid-liquid systems and can be integrated in different apparatuses with ease, even the applicability for sprays with shadowgraphic methods is reported [34]. The homogeneous bubble column regime and the crystallizer experiments show, that the evaluation of particles can easily be achieved with a simple binary image processing algorithm. This is limited to small disperse phase concentrations (approximately 15 vol.-%), because

the overshadowing of particles leads to erroneous segmentations and therefore false object identifications of the particles. However, the results of the pump-mixer-settler prove that advanced image processing techniques can overcome this drawback and a neuronal network can still properly detect particles at concentrations up to 30 vol. %. In addition, a probe design for the bubble column was presented that allows handling of elevated temperatures and pressures that are omnipresent in industry processes.

This optical inline measurement principle can lead to a better understanding of multiphase flows and helps to reduce the lack of reliable measurement techniques. It was cross-validated with already established measurement techniques, is easy to install and can be used to optimize processes combined with a model predictive control.

REFERENCES

1. M. Lichti, H.-J. Bart, *Chembioeng. Rev.*, **5** (2), 79 (2018).
2. M. Schlüter, *Chem. Ing. Tech.*, **83** (7), 992 (2011).
3. P. Barrett, B. Glennon, *Chem. Eng. Res. Des.*, **80** (7), 799 (2002).
4. A. Amokrane, S. Maaß, F. Lamadie, F. Puel, S. Charton, *Int. J. Chem. Eng.*, **296**, 366 (2016).
5. R. Kopra, H. Mutikainen, O. Dahl, *Tappi J.*, **17** (6), 339 (2018).
6. P. Barrett, B. Glennon, *Part. Part. Syst. Charact.*, **16** (5), 207 (1999).
7. M. Mickler, B. Boecker, H.-J, Bart. *Flow Meas. Instrum.*, **30**, 81 (2013).

8. M. Mickler, H.B. Jildeh, M. Attarakih, H.-J. Bart, *Can. J. Chem. Eng.*, **92** (2), 307 (2014).
9. M. Mickler, H.-J. Bart, *Chem. Ing. Tech.*, **85** (6), 901 (2013).
10. R. Schuhmann, T. Thöniß, *Tech. Mess.*, **65** (4), 131 (1998).
11. S. Maaß, J. Rojahn, R. Hänsch, M. Kraume, *Comput. Chem. Eng.*, **45**, 27 (2012).
12. S. Maaß, S. Wollny, A. Voigt, M. Kraume, *Exp. Fluids*, **50** (2), 259 (2011).
13. J. Schulz, C. Schunk, E. Schleicher, H.-J. Bart, *Chem. Ing. Tech.*, accepted (2020).
14. M. Lichti, H.-J. Bart, C. Roth, EP 3.067.685.A1 (8. Mar.).
15. S. Shu, D. Vidal, F. Bertrand, J. Chaouki, *Renew*, **141**, 613 (2019).
16. R. Krishna, J. M. van Baten, *Int. Commun. Heat Mass*, **26** (7), 965 (1999).
17. V. V. Buwa, V.V. Ranade, *Chem. Eng. Sci.*, **57** (22-23), 4715 (2002).
18. E. Krepper, B. N. Reddy Vanga, A. Zaruba, H.-M. Prasser, M. A. Lopez de Bertodano, *Nucl. Eng. Des.*, **237** (4), 399 (2007).
19. J. Schäfer, M. W. Hlawitschka, M.M. Attarakih, H.-J. Bart, *AIChE J.*, **65** (10) (2019).
20. M. Lichti, H.-J. Bart, *Flow Meas. Instrum.*, **60**, 164 (2018).
21. P. M. Wilkinson, H. Haringa, L. L. van Dierendonck, *Chem. Eng. Sci.*, **49** (9), 1417 (1994).
22. K. Chow, H. H. Y. Tong, S. Lum, A. H. L. Chow, *J. Pharm. Sci.*, **97** (8), 2855 (2008).
23. C. Wibowo, W.-C. Chang, K.M. Ng, *AIChE J.*, **47** (11), 2474 (2001).
24. R. D. Braatz, *Annu. Rev. Control.*, **26** (1), 87 (2002).
25. H. Eisenschmidt, N. Bajcinca, K. Sundmacher, *Cryst. Growth. Des.*, **16** (6), 3297 (2016).
26. C. Borchert, E. Temmel, H. Eisenschmidt, H. Lorenz, A. Seidel-Morgenstern, K. Sundmacher, *Cryst. Growth. Des.*, **14** (3), 952 (2014).
27. C. Borchert, K. Sundmacher, *Chem. Eng. Technol.*, **34** (4), 545 (2011).
28. D. Wirz, M. Hofmann, H. Lorenz, H.-J. Bart, A. Seidel-Morgenstern, E. Temmel, *Crystals*, **10** (9), 740 (2020).
29. K. K. Singh, K. T. Shenoy, A. K. Mahendra, S. K. Ghosh, *Chem. Eng. Sci.*, **59** (14), 2937 (2004).
30. M. V. Tabib, G. Lane, W. Yang, M. P. Schwarz, *Chem. Eng. Sci.*, **80**, 55 (2012).
31. C. Srilatha, V. V. Morab, T. P. Mundada, A.W. Patwardhan, *Chem. Eng. Sci.*, **65** (11), 3409 (2010).
32. A.T. Davis, T.J. Colven. *AIChE J.*, **7** (1), 72 (1961).
33. J. Schäfer, P. Schmitt, M. W. Hlawitschka, H.-J. Bart, *Chem. Ing. Tech.*, **83** (7), 992 (2019).
34. J. Schulz, H.-J. Bart, *Chem. Eng. Res. Des.*, **147**, 624 (2019).

Numerical investigation of hydrodynamics in submerged membrane bioreactor with aeration

V. Iliev, D. Moutafchieva*, R. Doukovski

University of Chemical Technology and Metallurgy, 8 Kl. Ohridski Blvd., 1756 Sofia, Bulgaria

Submerged membrane bioreactors (SMBRs) are an established technology for wastewater treatment, but the efficient fouling reduction by air sparging remains an operating problem and the design rules are still of a purely empirical nature. Therefore, many modeling approaches have been proposed to solve these operating problems and increase the process efficiency. The design of SMBRs is affected by a combination of both hydrodynamic and biological conditions, CFD models and simulations should be performed considering both of these phenomena. The present study focuses on the design of a SMBRs and on the determining of the required aeration rate to achieve a minimum deformation rate of the material in the membrane boundary layer referred to as 0.8 s^{-1}. Following determination of the dimensions and operating parameters of the bioreactor and the membrane module with MATLAB, computer simulations of cell growth have been performed in the selected SMBR with the software ANSYS CFX. The rate of deformation in the boundary layer at inlet air velocities from 0.1 m/s to 0.8 m/s was calculated and dependences for the rate of deformation at the boundary layer on the outer side of the membrane were obtained. It was also found that in order to achieve the set minimum strain rate of 0.8 s^{-1} the minimum aeration velocity should be 0.55 m/s. CFD modeling of SMBRs allowed calculations of the appropriate shear on the membrane surface in order to control sludge filterability and fouling. The adequacy of the computer model used was confirmed by comparing the numerical results obtained by ANSYS CFX with those obtained by MATLAB. The results obtained could be used to clarify the effect of aeration on shear rate in order to achieve more intense turbulence in the reactor that could contribute to the higher efficiency of the membrane module.

Keywords: Submerged membrane bioreactor (SMBR); CFD; Shear stress; Bubble column

INTRODUCTION

Membrane reactors with submerged membrane (SMBR) and aeration of bubble or airlift columns with integrated membrane module use the favorable effect of the two-phase gas-liquid flow on the shear stresses around the membrane. The increasing of the shear stresses to the membrane is considered one of the most effective ways to control its blockage. Therefore, it is important to study the field of tangential stresses and its homogeneity near the surface of the membrane, for which there is no systematic information.

The design of SMBRs is mainly based on knowledge of biokinetics and the conditions under which membrane clogging occurs, although the hydrodynamics in SMBRs are crucial for the operation of these reactors. The influence of the flow regime in the process of design and operation of SMBRs is not sufficiently studied and analyzed. The current methods of designing the desired flow regime within the SMBRs are largely based on empirical techniques (for example: the specific mixing energy). It is difficult to predict how the scaling of the apparatus and the design of industrial installations (size and position of inlets, barriers or

membrane orientation) will affect the hydrodynamics and therefore the overall performance of the membrane reactor. Recently, more and more studies are using CFD (Computational Fluid Dynamics) techniques for studying and modeling of the fluid flow through a membrane module and for studying the factors that cause membrane contamination. CFD is a widely used tool for studying membrane contamination and for studying the mechanisms and factors that influence this process. The computational dynamics of the fluids makes it possible to predict how the geometrical characteristics and operating parameters of the submerged membrane bubble reactor will affect the hydrodynamics and the choice of the optimal design and therefore the performance of the aerated membrane bioreactor.

In the present work a two-step algorithm of SMBR design – e.g. supported by MATLAB and CFD, was verified in a way as to ensure productivity at a reference deformation rate not allowing eventual cell death.

Controlling the hydrodynamic conditions near the membrane is extremely important for the stability of the flow, as well as for minimizing the required membrane surface, reducing the collected

---

* To whom all correspondence should be sent:
E-mail: dessislava_moutafchieva@yahoo.com

sediment on the surface and increasing the transmembrane pressure (TMP) or constant permeate flow. The increasing of the shear stresses to the membrane is considered to be one of the most effective ways to control its blockage.

The shear forces are generated by pumps, by bubbling or by stirring devices to remove the layer formed on the membrane. Of course, care should be taken for possible deactivation of shear-sensitive components. In this sense, the hydrodynamic environment in the MBR (membrane bioreactor) is a compromise between the requirements of the separation process (the area around the membrane surface) and the biochemical reaction (in the reactor volume). From a computational point of view, this means studying the field of velocities and tangential stresses and its homogeneity in these two areas [1, 2].

A large number of studies [4-7] show that the shear stress of the wall is a very important parameter that can be used to indicate the effectiveness of the membrane. It is known that particles accumulated on the surface of the membrane will be washed away when the shear stress increases, as it can increase the reverse transport of the particles away from the membrane. An earlier study of the relationship between membrane contamination and the relationship between permeate flow and wall shear stress was performed by Le Berre and Daufin in 1996 [4]. It shows that the ratio between the permeate flow and the shear stress of the wall can be a useful parameter for predicting the performance of the membrane under different operating conditions. In later studies [5-9], the effect of wall shear stress on membrane contamination during membrane filtration was investigated by digital simulation using CFD [5-8] or investigated experimentally [9].

There are studies that correlate each process resistance to a linear function of the shear stresses on the membrane surface created by the liquid and gas phases. It has been found that the size of the gas bubbles is of significant importance for the shear stresses of the membrane surface. Thus, the aeration of submerged MBR is one of the main topics studied.

The purpose of aeration is to generate small gas bubbles that are evenly distributed across the cross section of the apparatus, thus achieving better mixing of the liquid and more intensive mass transfer. The dispersion of the gas is obtained by passing it through openings, a porous medium or by mixing the gas with a rapid stream of liquid. The rising gas bubbles in contact with the surface of the

membrane affect in the direction of reducing the concentration polarization and, respectively, the formation of a layer of sediment on it. The effect comes from the liquid phase, respectively, from higher actual velocities to the membrane (related to the volume part of the liquid phase in the reactor, 1-ε_G), as well as the mechanical impact of the bubbles on the membrane, which washes away the sediment layer. In submerged MBRs, air dispersion not only delivers oxygen to the biomass, but also retains solids in suspension and is used to reduce membrane contamination by creating a shear stress. The efficient air distribution contributes to the permeability of the membrane, the stability of the applied flow and the reduction of pollution. The appearance of bypass jets and fluid channels, which lead to enhanced sludge removal and high transient shear patterns, is influenced by the interactions between the fluid and the structure. The efficiency parameter of gas bubbling depends on the gas velocity, the size of the nozzle and the concentration of the suspension; the efficiency of the module is affected due to changes in the local flow distribution and suction pressure of the module outlet. [1,16].

The membrane reactors with mechanical stirring combine the hydrodynamic picture created by a certain type of stirrer in the volume of the reactor with that around the surface of the membrane. The size and the direction of the velocity vectors of the fluids to the membrane strongly depend on the stirring rate. The specific design of the agitator and the location of the diaphragm relative to it significantly affect the velocity fields and shear stresses of the diaphragm. The submerged membrane bioreactor allows higher concentrations to be reached relative to the cells and makes it possible to retain the cell mass in the reactor. They are suitable solutions when the goal is to increase the concentration of cell mass in a biomass production reactor.

In the selected type of bioreactors with stirring and aeration, gas bubbles and mechanical stirring jointly affect the uniformity of distribution of velocities and shear stresses to the membrane surface.

The membrane module is placed in the aeration zone to use the beneficial effect of both factors (gas and mechanical stirring) on the reduction of membrane contamination [1, 2].

The optimal operation of the membrane reactor is related to:
• the position of the membrane module in the reactor;

• the gas / liquid ratio;
• the transmembrane pressure;
• the creation of sufficient shear stresses.

Relatively new and few are the attempts to model the process taking into account the dynamics of the relationship between the transmembrane pressure, the shear stresses of the membrane and the flow through the membrane.

EXPERIMENTAL

Description of the bioreactor

For the purpose of the study, based on the literature review, the bioreactor is composed of two chambers (1-outer chamber and 2-inner chamber). The substrate necessary for cell growth passes in the outer chamber through the lower opening (9). It then passes through the membrane surface (5) into the inner chamber, where the cell growth takes place. An agitator (4), driven by an electric motor (13), is mounted in the inner chamber. A toroidal-shaped sparger (3) is placed in the lower part of the outer chamber, through which air for mixing the materials and cleaning the membrane module is introduced. The air required for aeration is introduced through the supply pipe (11), released on the free surface of the solution in chamber 1 and exits through a ventilation opening (12). The membrane module can be dismantled by pre-dismantling the electric drive motor (13) and the gearbox (14) and separating the fastening elements (8) from the bed of the membrane unit (7).
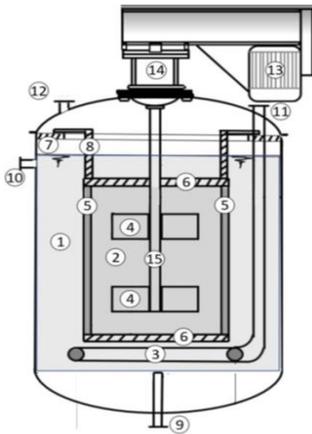
Fig. 1. Submerged membrane bioreactor with stirring and aeration

Numerical experiment for determining the size of the membrane bioreactor

The required volume and height of the membrane bioreactor were determined by a numerical experiment in the programming environment MATLAB, to achieve the desired cell productivity of 6 g/h. To determine the height, the

following ratio H/d = 1.5 was taken for a laboratory reactor with standard geometry and the diameter was calculated from the volume obtained from the experiment. Figure 2 shows the dimensions of the components of the bioreactor.

The cell growth in the inner chamber, as well as the amount of substrate in both chambers was calculated using the ode23 function in the programming environment MATLAB, which allows up to three differential equations to be calculated. The balance equations used are the following (perfect mixing is assumed):

• for the substrate (S_1) in the outer chamber:

$$\frac{dS_1}{dt}V_1 = \dot{v}S_0 - \dot{v}S_1 - Per(S_1 - S_2) \qquad (1)$$

• for the substrate (S_2) in the inner chamber:

$$\frac{dS_2}{dt}V_{12} = Per(S_1 - S_2) - \frac{1}{Yx/s}\mu XV_2 \qquad (2)$$

• for the cells (X):

$$\frac{dX}{dt}V_2 = \mu XV_2 \qquad (3)$$

For the parameters of this model we used experimental data from the literature review (cell growth) [1]: mono kinetics with parameters: μ_{max}=0.5 h^{-1}; Ks=0.12 g/l; $Y_{x/s}$=0.52; initial substrate concentration S_0= 2 g/l; flow rate on the outer chamber $\dot{v}$= 2 l/h and membrane data: Per=0.52 dm/h and A=5.29 dm^2.
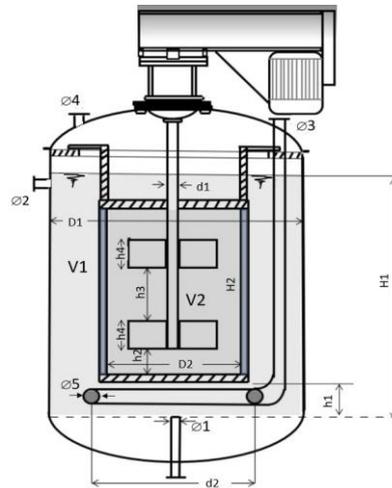
Fig. 2. The bioreactor dimensions. V1 – 0.0014 [m^3]; V2 – 0.0014 [m^3]; D1 – 0.067 [m]; D2 – 0.053 [m]; H1 – 0.201 [m]; H2 – 0.159 [m]; d1 – 0.002 [m]; d2 – 0.116 [m]; h1 – 0.021 [m]; h2 – 0.035 [m]; h3 – 0.056 [m]; h4 – 0.03 [m]; ⌀1 – 0.01 [m]; ⌀2 – 0.005 [m]; ⌀3 – 0.01 [m]; ⌀4 – 0.01 [m]; ⌀5 – 0.01 [m].

From the obtained results it was determined that for achieving the required productivity of 6 g/h, the volume of the membrane module must be 1.4 dm^3 (Fig. 5). Figure 2 shows the dimensions of the

563

components of the bioreactor. The influence of the aeration in the outer chamber and the agitation in the inner chamber were not taken into account during the sizing with MATLAB. These factors were included in the calculation procedure with the program environment ANSYS.

Experiment for determining the minimum aeration velocity

The computer simulation was performed on the working volume of the reactor shown on Figure 3. The immersed membrane is placed at a distance of A = 0.021 m from the base of the reactor and has a height of H = 0.159 m and a diameter of D = 0.053 m. The toroidal sparger, with a diameter of D = 0.01 m and a ring radius of R = 0.058 m, is located at the lower end of the reactor at a distance of B=0.01 m from the base. The agitator is located at a distance of C= 0.056 m from the base of the reactor and the distance between the two propellers is E= 0.03 m. This size also corresponds to their height, and the length is the same for both.
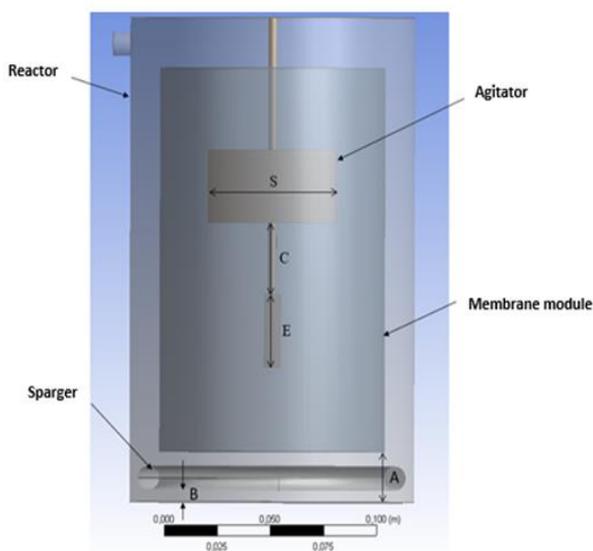
Fig. 3. Schematic representation of the experimental reactor

The inclusion of a sparger in the reactor design increases the turbulence and affects the rate of deformation along the length of the membrane module. The aeration process tends to be highly turbulent, which requires an appropriate model of turbulence. In a computer simulation, the turbulence model k-ε is used to correctly determine the rate of deformation around the membrane wall. This turbulence model is commonly used to model bubble columns, as it is a trade-off between computational accuracy and efficiency [17]. The distribution of the strain rate along the membrane is more homogeneous in the presence of gas. Rising

gas bubbles in contact with the membrane surface affect the direction of reducing the concentration polarization and respectively, the formation of a layer of sediment on it [1]. For the purposes of the present work, it is accepted that the minimum strain rate, at which cake layer formation and membrane clogging is prevented, is 0.8 s^{-1}

The complete modeling of the two-phase flow in the ANSYS programming environment was performed according to the methodology, which includes creating a geometric model of the object, crosslinking the studied object, setting the variables describing the physicochemical behavior of the fluid in the reactor and setting the initial and boundary conditions of the process.

Experimental conditions

Initial conditions of the numerical experiments:
• the amount of air supplied by the sparger is equal to 0.05 volume fractions, which at the specific dimensions of the sparger corresponds to 100 openings, creating bubbles with a diameter of 6 mm;
• the amount of the mixture which includes two solutions - Mixture and Cells, at the entrance, is equal to 0.95 volume fractions;
• the degassing function, which is provided by the software product ANSYS CFX, is used for the gas output;
• the equations 1-3 are used for the calculation of the growth of the cells in the membrane module;
• the water concentration is set to Constant.

The experiment was performed at an air velocity ranging from 0.1 m/s to 0.8 m/s with a step of 0.1 m/s. After each experiment, the average angular strain rate on the surface of the membrane on the side of the outer chamber was calculated using the built-in calculator. Additional cutting planes were constructed to monitor process characteristics as flow rate and reactor pressure.

Experiment for determining the maximum agitator velocity

This experiment was performed under the same conditions as the experiment to determine the minimum aeration velocity. The observations are concentrated on the inner chamber, where the cell growth takes place. The main parameter in this experiment is the angular velocity of the agitator, which varies in the range from 5 rev/min to 35 rev/min with a step of 5 rev/min. To observe the hydrodynamic characteristics of the process, the built-in program calculator and additional intersecting planes were used, as in the previous experiment.

RESULTS AND DISCUSSION

Determining the required reactor volume to achieve the desired cell productivity

Numerical experiments were performed in the MATLAB software environment to determine the operating parameters of the membrane module and the size of the entire reactor, varying the volume of the membrane module from 0.55 dm^3 to 1.6 dm^3 in steps of 0.1 dm^3. A computer simulation with different reactor volumes was performed to monitor cell growth and the results are presented in Figure 4.
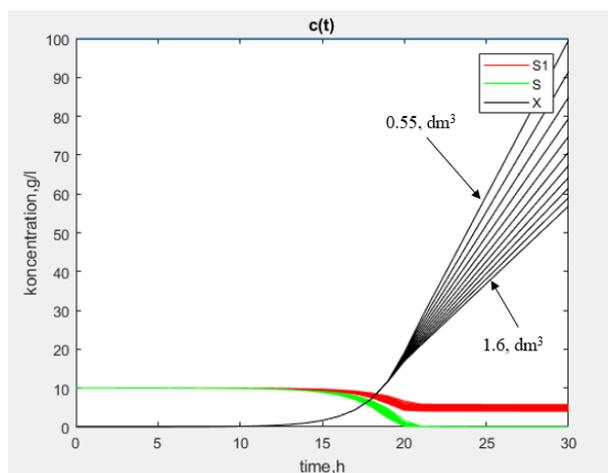
Fig. 4. Cell growth: S1 - concentration of substrate at the outlet of the reactor; S - concentration of substrate necessary for cell growth; X - concentration of cells.

The graph of the figure above shows that as the reactor volume increases, the growth rate of the microorganisms decreases (the slope of the graph lines decreases). The highest concentration of cells is at a membrane module volume of 0.55 dm^3, however, the productivity relative to the reactor volume at this size is too low, which is explained by the smaller volume of the membrane module.

From the graph on Figure 5 it is reported that the set productivity of 6 g/h is achieved at a volume of 1.4 dm^3. The two chambers of the reactor have the same volume, therefore the inner and outer chambers are 1.4 dm^3 and for the volume of the whole reactor we get a volume of 2.8 dm^3.

Determining the rate of deformation by different aeration velocities

Aeration has a significant effect on the shear rate, by increasing the degree of aeration more intense turbulence is achieved inside the bubble column. In addition, aeration contributes to the higher efficiency of the membrane module by reducing the formation of sediment on the membrane surface.

The presented results on Figure 5 show the dependence of the deformation rate at the boundary layer on the outer side of the membrane. The software environment ANSYS CFX is used to calculate the deformation rate at the boundary layer at different velocities of the introduced air from 0.1 m/s to 0.8 m/s.
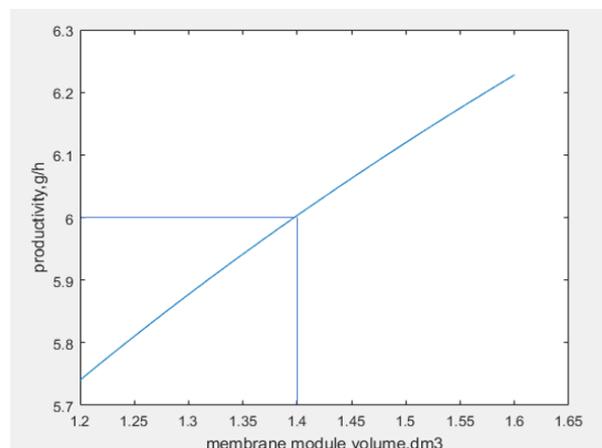
Fig. 5. Performance curve for membrane size between 1.2 dm^3 and 1.6 dm^3
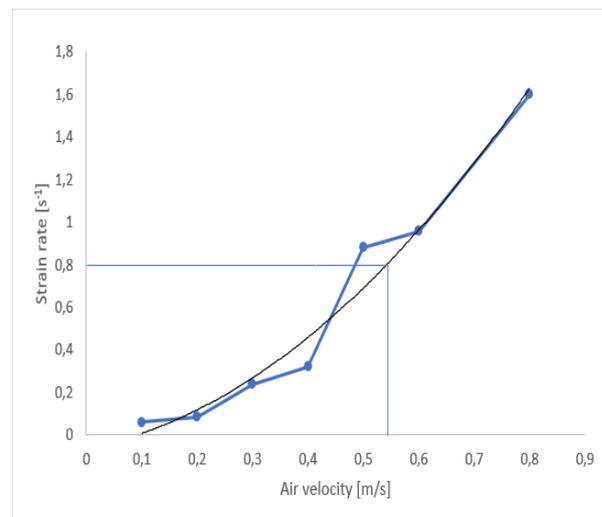
Fig. 6. Deformation rate in the boundary layer

From the graph of Figure 6 it is seen that as the air velocity increases, the strain rate also increases. On one hand, this tendency prevents contamination of the membrane module, but may have a negative effect on the cells that are being developed in the reactor. For the set minimum strain rate of 0.8 s^{-1}, the graph shows a minimum air velocity of 0.55 m/s.

ANSYS CFX allows the obtained numerical results for the strain rate in the outer chamber of the reactor to be presented in vector form, as well as in the form of color contours (Fig. 7).
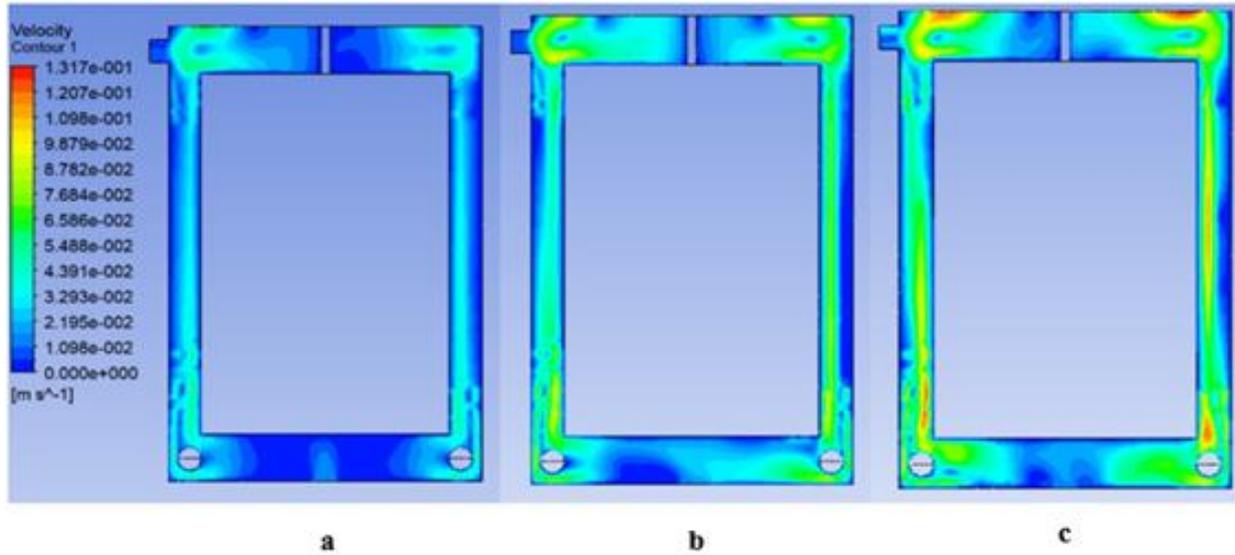
Fig. 7. Shear rate in the outer chamber: at an aeration speed of 0.2 m/s (a); at an aeration speed of 0.4 m/s (b); at an aeration speed of 0.6 m/s (c)

Determination of shear stresses at different agitator speeds

Figure 8 shows the results for the distribution of the shear rate in the inner chamber of the reactor, caused by the agitator at different speeds from 5 rev/min to 30 rev/min.
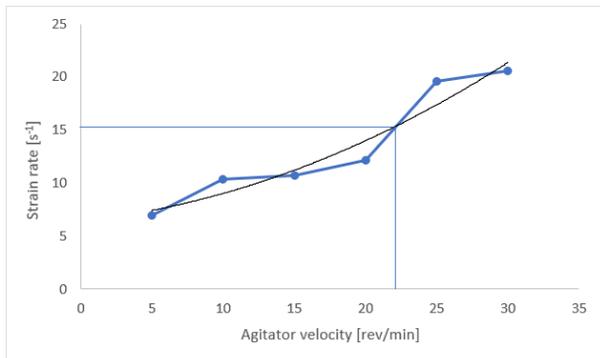
Fig. 8. Deformation rate caused by the agitator
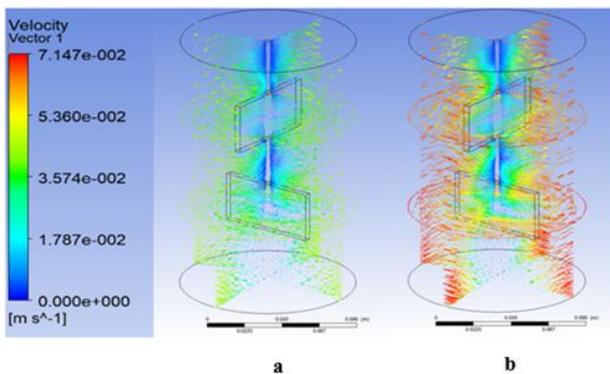
Fig. 9. Deformation rate caused by the agitator: at a stirring speed of 20 rev/min (a); at a stirring speed of 25 rev/min.
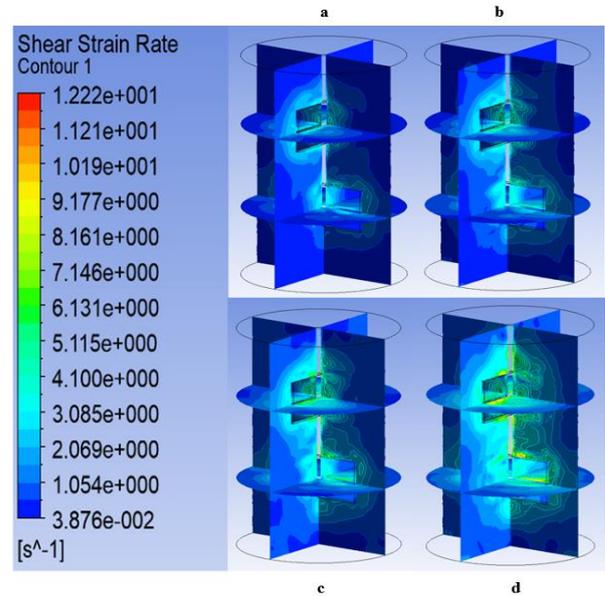
Fig. 10. Deformation rate caused by the agitator at a stirring speed of 10 rev/min (a); at a stirring speed of 15 rev/min (b); at a stirring speed of 20 rev/min (c); at a stirring speed of 25 rev/min (d).

From the graph in Figure 8 it can be seen that in order to reach the set maximum deformation speed of 15 s^{-1} the maximum speed of the agitator must be 22 rev/min.

It can be seen from Figures 9 and 10 that as the stirrer speed increases, the strain rate also increases, which leads to better mixing, but can also lead to the destruction of living cells in the inner chamber of the reactor. The strain rate shown in Figure 10d, when rotating at a fast speed of 25 rpm, is the most pronounced with the highest achieved strain rate being colored in red and the lowest in blue.

566

Comparison between the MATLAB and ANSYS CFX results for cell growth in the inner chamber of the reactor

a

b
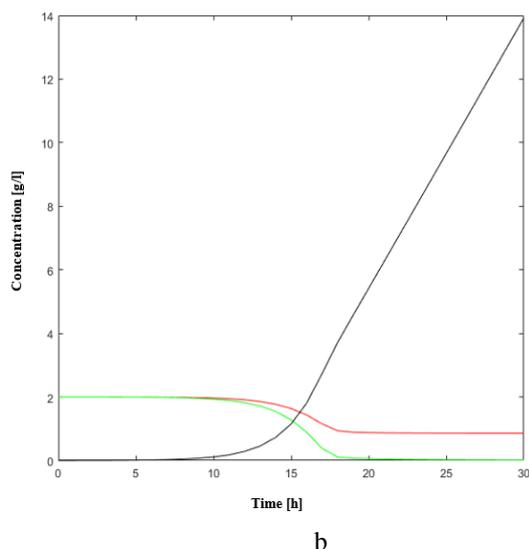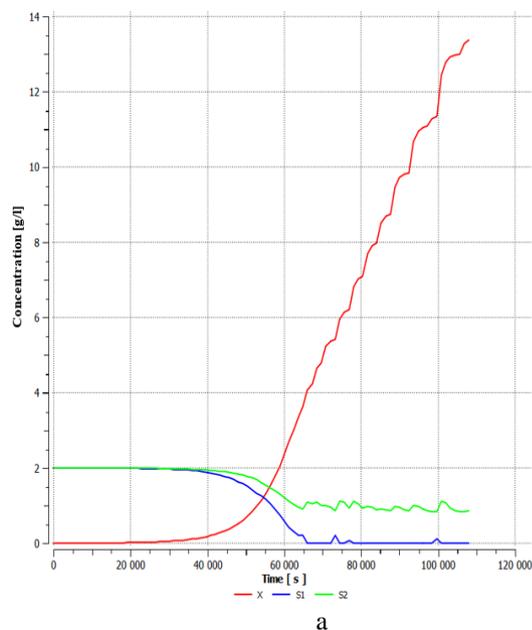
Fig. 11. Cell growth with ANSYS CFX: (a), with MATLAB (b): S1 - concentration of substrate at the outlet of the reactor; S - concentration of substrate necessary for cell growth; X - concentration of cells.

The results obtained are shown in the above figures with different magnitudes in time, as in MATLAB the time is represented in hours, while in ANSYS CFX it is in seconds. The disturbances that are seen on the graph obtained with ANSYS (Fig. 11a) appear after 18 hours. In general, the two graphs are identical, which can be considered as a verification of the computer simulation model used.

CONCLUSION

The two-step procedure combining MATLAB and CFD can be successful in predicting the SMBR design at given productivity and produce visualization of bioreactor fluid dynamics in a way as to avoid pathological condition of cell death. The case study shows that a lab-scale SMBR equipped with a frame membrane could ensure substrate bioconversion of up to 90% for 25 h at zero cell death simulated as reference strain rate less than 0.8 s^{-1} introduced as moderate agitation rate of 22 rev/min. and air velocity of 0.55m/s. The ANSYS CFX software environment makes it possible to formulate a comprehensive computer model and describe the hydrodynamic situation in the bioreactor and around the membrane module in detail. Accordingly, the computer model, thus created, is verified by using the results obtained from calculations with MATLAB.

REFERENCES

1. I. Tsibranska, D. Mutafchieva, Bioreactor technique, Sofia, 2018 (in Bulgarian).
2. J. Simon, C. Judd, The MBR book: principles and applications of membrane bioreactors in water and wastewater treatment, Amsterdam, Elsevier, 2006.
3. C. John, MWH's Water Treatment: principles and design, 3rd edn., Hoboken, New Jersey, John Wiley & Sons Inc., 2012.
4. O. Le Berre, G. Daufin, C. Skimmilk, *Journal of Membrane Science*, **117**(1-2), 261 (1996).
5. C. Chan, P. Bérubé, E. Hall, *Water Research,* **45**(19), 6403 (2011).
6. R. Kaya, G. Deveci, T. Turken, R. Sengur, S. G. Derya, Y. Koseoglu-Imer, I. Koyuncu, *Desalination and Water Treatment,* **351**, 109 (2014).
7. C. Chan, P. R. Bérubé, E. R. Hall, *Journal of Membrane Science,* **297**(1-2), 104 (2007).
8. S. Abdullah, H. E. Wray, P. R. Bérubé, R. C. Andrews, *Desalination and Water Treatment,* **357**, 117 (2015).
9. H. Wray, R. C. Andrews, P. R. Bérubé, *Desalination and Water Treatment,* **330**, 22 (2013).
10. N. Ratkovich, R. Thomas, R. Michael, Energy consumption in terms of shear stress for two types of membrane bioreactors used for municipal wastewater treatment processes, Aalborg, Denmark, 2011.
11. N. Deen, R. Mudde, J.Kuipers, P. Zehner, M. Kraume, Bubble columns, in: Ullmann's Encyclopedia of Industrial Chemistry, 7th edn., Wiley-VCH, 2011.

12. G. Wild, H. Li, S. Poncin, E. Olmos, *International Journal of Chemical Reactor Engineering*, **1**, 1 (2003).

13. M. Ruzicka, J. Drahos M. Fialova, N. Thomas, *Chemical Engineering Science*, **56**(21-22), 6117 (2001).

14. W. Van Benthum, R. Van der Lans, M. Van Loosdrecht, M. Heijnen, *Chemical Engineering Science,* **54**, 3995 (1999).

15. R. Sengur, G. K. Deveci, CFD modeling of submerged membrane bioreactors (sMBRs): a review, Istanbul Technical University, Maslak, 2015.

16. J. Joshi, V. Vitankar, A. Kulkarni, M. Dhotre, K. Ekambara, *Chemical Engineering Science,* **57**, 3157 (2002).

17. D. Mutafchìeva, V. Iliev, *Materials, Methods & Technologies,* **12**, 275 (2018).

AUTHOR INDEX

569

SUBJECT INDEX

Instructions about Preparation of Manuscripts

General remarks: Manuscripts are submitted in English by e-mail The text must be typed on A4 format paper using Times New Roman font size 11, normal character spacing. The manuscript should not exceed 15 pages (about 3500 words), including photographs, tables, drawings, formulae, etc. Authors are requested to use margins of 2 cm on all sides

Manuscripts should be subdivided into labelled sections, e.g. **Introduction, Experimental, Results and Discussion**, *etc*. **The title page** comprises headline, author's names and affiliations, abstract and key words. Attention is drawn to the following:

a) **The title** of the manuscript should reflect concisely the purpose and findings of the work. Abbreviations, symbols, chemical formulas, references and footnotes should be avoided. If indispensable, abbreviations and formulas should be givenin parentheses immediately after the respective full form.

b) **The author**'s first and middle name initials and family name in full should be given, followedby the address (or addresses) of the contributing laboratory (laboratories). **The affiliation** of the author(s) should be listed in detail by numers (no abbreviations!). The author to whom correspondence and/or inquiries should be sent should be indicated by asterisk (*) with e-mail address.

The abstract should be self-explanatory and intelligible without any references to the text andcontaining not more than 250 words. It should be followed by key words (not more than six).

References should be numbered sequentially in the order, in which they are cited in the text. The numbers in the text should be enclosed in brackets [2], [5, 6], [9–12], etc., set on the text line. References are to be listed in numerical order on a separate sheet. All references are to be given in Latin letters. The names of the authors are given without inversion. Titles of journals must be abbreviated according to Chemical Abstracts and given in italics, the volume is typed in bold, the initial page is given and the year in parentheses. Attention is drawn to the following conventions:a) The names of all authors of a certainpublications should be given. The use of "*et al*." inthe list of references is not acceptable.b) Only the initials of the first and middle names should be given. In the manuscripts, the reference to author(s) of cited works should be made without giving initials, e.g. "Bush and Smith [7] pioneered...". If the reference carries the names of three or more authors it should be quoted as "Bush *et al*. [7]", if Bush is the first author, or as "Bush and co-workers [7]", if Bush is the senior author.

Footnotes should be reduced to a minimum. Each footnote should be typed double-spaced at thebottom of the page, on which its subject is first mentioned.**Tables** are numbered with Arabic numerals on the left-hand top. Each table should be referred to inthe text. Column headings should be as short as possible but they must define units unambiguously.The units are to be separated from the preceding symbols by a comma or brackets. Note: The following format should be used when figures, equations, *etc*. are referred to the text (followed by the respective numbers): Fig., Eqns., Table, Scheme.

Schemes and figures. Each manuscript should contain or be accompanied by the respective illustrative material as well as by the respective figure captions in a separate file (sheet).As far as presentation of units is concerned, SI units are to be used. However, some non-SI units are also acceptable, such as °C, ml, l, etc.The author(s) name(s), the title of the manuscript, the number of drawings, photographs, diagrams, etc., should be written in black pencil on the back of the illustrative material (hard copies) inaccordance with the list enclosed. Avoid using more than 6 (12 for reviews, respectively) figures in the manuscript. Since most of the illustrative materials are to be presented as 8-cm wide pictures, attention should be paid that all axis titles, numerals, legend(s) and texts are legible.

The authors are required to submit the text with a list of three individuals and their e-mail addresses that can be considered by the Editors as potential reviewers. Please, note that the reviewers should be outside the authors' own institution or organization. The Editorial Board of the journal is not obliged to accept these proposals.

The authors are asked to submit **the final text** (after the manuscript has been accepted for publication) in electronic form by e-mail. The main text, list of references, tables and figure captions should be saved in separate files (as *.rtf or *.doc) with clearly identifiable file names. It is essential that the name and version of the word-processing program and the format of the text files is clearly indicated. It is recommended that the pictures are presented in *.tif, *.jpg, *.cdr or *.bmp format.

The equations are written using "Equation Editor" and chemical reaction schemes are written using ISIS Draw or ChemDraw programme.

EXAMPLES FOR PRESENTATION OF REFERENCES

REFERENCES
1. D. S. Newsome, *Catal. Rev.–Sci. Eng.*, **21**, 275 (1980).
2. C.-H. Lin, C.-Y. Hsu, *J. Chem. Soc. Chem. Commun.*, 1479 (1992).
3. R. G. Parr, W. Yang, Density Functional Theory of Atoms and Molecules, Oxford Univ. Press, New York, 1989.
4. V. Ponec, G. C. Bond, Catalysis by Metals and Alloys (Stud. Surf. Sci. Catal., vol. 95), Elsevier, Amsterdam, 1995.
5. G. Kadinov, S. Todorova, A. Palazov, in: New Frontiers in Catalysis (Proc. 10th Int. Congr. Catal., Budapest,(1992), L. Guczi, F. Solymosi, P. Tetenyi (eds.), Akademiai Kiado, Budapest, 1993, Part C, p. 2817.
6. G. L. C. Maire, F. Garin, in: Catalysis. Science and Technology, J. R. Anderson, M. Boudart (eds), vol. 6, SpringerVerlag, Berlin, 1984, p. 161.
7. D. Pocknell, *GB Patent* 2 207 355 (1949).
8. G. Angelov, PhD Thesis, UCTM, Sofia, 2001, pp. 121-126.
9 JCPDS International Center for Diffraction Data, Power Diffraction File, Swarthmore, PA, 1991.
10. CA **127**, 184 762q (1998).
11. P. Hou, H. Wise, *J. Catal.*, in press.
12. M. Sinev, private communication.
13. http://www.chemweb.com/alchem/articles/1051611477211.html.

Texts with references which do not match these requirements will not be considered for publication!!!

CONTENTS

Integrated membrane processes for green technologies